

THE UNIVERSITY OF CHICAGO

DYNAMIC MODULATION OF ACTOMYOSIN CONTRACTILITY AND
CORTICAL FLOW BY ACTIN FILAMENT RECYCLING

A DISSERTATION SUBMITTED TO
THE FACULTY OF THE DIVISION OF THE PHYSICAL & BIOLOGICAL
SCIENCES
IN CANDIDACY FOR THE DEGREE OF
DOCTOR OF PHILOSOPHY

DEPARTMENT OF BIOPHYSICAL SCIENCE

BY
WILL MCFADDEN

CHICAGO, ILLINOIS
FEBRUARY 2016

For Claire, you keep me going.

ABSTRACT

Actomyosin-based cortical flow is a fundamental engine for cellular morphogenesis. Cortical flows are generated by cross-linked networks of actin filaments and myosin motors, in which active stress produced by motor activity is opposed by passive resistance to network deformation. Continuous flow requires local remodeling through crosslink unbinding and and/or filament disassembly. But how local remodeling tunes stress production and dissipation, and how this in turn shapes long range flow, remains poorly understood. In this thesis, I attempt to describe the dynamics that underlie cortical flow in a specific cellular system, and extended the observations to a general modeling framework to understand how flows arise in many systems.

To begin, I first characterize the dynamics of cortical flow in the *C. elegans* embryo, and show that existing active fluid theories are adequate to describe the flow behavior of cell polarization and maintenance. I next investigate the turnover of cortical actin by using a recently developed method of monitoring individual actin monomer lifetimes *in vivo*. Additionally, I analyze existing data where filament turnover has been disrupted to show that cortical flows are abrogated. Instead, the networks only transiently contract, indicating that filament turnover is indeed crucial for cortical flows.

I next introduce a computational model for cross-linked networks with active motors based on minimal requirements for production and dissipation of contractile stress, namely asymmetric filament compliance, spatial heterogeneity of motor activity, reversible cross-links and filament turnover.

Finally, I characterize how the production and dissipation of network stress depend, individually, on cross-link dynamics and filament turnover, and how these dependencies combine to determine overall rates of cortical flow. My analysis predicts that filament turnover is required to maintain active stress against external resistance and steady state flow in response to external stress. Steady state stress increases with

filament lifetime up to a characteristic time τ_a , then decreases with lifetime above τ_a . Effective viscosity increases with filament lifetime up to a characteristic time τ_c , and then becomes independent of filament lifetime and sharply dependent on crosslink dynamics. These individual dependencies of active stress and effective viscosity define multiple regimes of steady state flow. In particular my model predicts the existence of a regime, when filament lifetimes are shorter than both τ_c and τ_a , in which dependencies of effective viscosity and steady state stress cancel one another, such that flow speed is insensitive to filament turnover, and shows simple dependence on motor activity and crosslink dynamics. These results provide a framework for understanding how animal cells tune cortical flow through local control of network remodeling. Importantly, we learn that there must be some amount of local control of actomyosin activity in order for cortical flows to persist. As an additional project, I developed a model of upstream regulators of actin and myosin, showing how local recruitment through actin assembly can generate patterns of actomyosin contractility.

ACKNOWLEDGEMENTS

I'd like to thank my advisor, Ed Munro, Birali Runesha, Francois Robin, Patrick McCall, Jon Michaux, Younan Li, Baixue Yao, Shiladitya Banerjee, the University of Chicago Biophysical Sciences program, Michele Wittels, Artifice, Pete Dahlberg, Adam Hammond, James Crooks, the uchicago myCHOICE program, the Insight Data Science Fellowship Program, Color Genomics, Robbie Sliwinski, my fiancee, Claire Stevenson, her family, David Stevenson and Marilyn Lucas, my brother, Andrew McFadden, and my mom, Deb McFadden. Without all of these people and programs, I wouldn't have made it through this work and come out the other side with something of value.

TABLE OF CONTENTS

| | |
|---|-----|
| ABSTRACT | iii |
| ACKNOWLEDGEMENTS | v |
| 1 INTRODUCTION | 1 |
| 1.1 Biological Context of Cortical Flow | 2 |
| 1.2 Introduction to the Cortical Actomyosin Cytoskeleton | 4 |
| 1.3 A physical view of cortical flow | 7 |
| 1.4 Determinants of passive viscoelasticity in actin networks | 9 |
| 1.4.1 Short Timescale Mechanics of Cross-linked Actin Filament Networks | 10 |
| 1.4.2 Long Timescale Stress Relaxation from Transient Cross-link Unbinding | 11 |
| 1.4.3 Elucidating the Importance of Filament Turnover | 13 |
| 1.5 Origins of contractility in disordered contractile networks. | 13 |
| 1.6 Goals of Thesis: Bridging the Theoretical Gap Between Active Fluids and Polymer Models | 16 |
| 2 SINGLE MOLECULE MEASUREMENTS OF ACTIN FILAMENT TURNOVER | 18 |
| 2.1 Preface | 18 |
| 2.1.1 Fitting algorithm for SMPress | 18 |
| 2.1.2 Control experiments to determine the accuracy of SMPress . . | 18 |
| 2.1.3 Taking the proper mean for Par-6 measurements | 19 |
| 2.2 Introduction | 20 |
| 2.3 Results | 21 |
| 2.3.1 Obtaining and verifying single molecule levels for any GFP fusion protein. | 21 |
| 2.3.2 Exploiting intrinsic exchange kinetics to achieve optimized sampling of single molecule mobility and turnover | 23 |
| 2.3.3 SPT analysis reveals distinct classes of Par-6 mobility during maintenance phase | 27 |
| 2.3.4 Measuring spatial and temporal variations in density and turnover | 28 |
| 2.3.5 Measuring spatial variation in Par-6 turnover during maintenance phase. | 29 |
| 2.3.6 Spatiotemporal modulation of actin assembly and turnover during cell division | 30 |
| 2.4 Discussion | 32 |

| | | |
|-------|---|----|
| 3 | FILAMENT RECYCLING AND SUSTAINED CONTRACTILE FLOWS IN AN ACTOMYOSIN NETWORK | 34 |
| 3.1 | Preface | 34 |
| 3.2 | Introduction | 34 |
| 3.3 | Models | 38 |
| 3.3.1 | Asymmetric filament compliance | 40 |
| 3.3.2 | Drag-like coupling between overlapping filaments | 41 |
| 3.3.3 | Active coupling for motor driven filament interactions | 42 |
| 3.3.4 | 2D network formation | 42 |
| 3.3.5 | External applied stress | 43 |
| 3.3.6 | Modeling filament turnover | 44 |
| 3.3.7 | Simulation methods | 44 |
| 3.4 | Results | 46 |
| 3.4.1 | Filament turnover allows and tunes effectively viscous steady state flow. | 46 |
| 3.4.2 | Filament turnover allows persistent stress buildup in active networks | 54 |
| 3.4.3 | Filament turnover tunes the balance between active stress buildup and viscous stress relaxation to generate flows | 61 |
| 3.5 | Discussion | 65 |
| 3.6 | Supplemental Materials | 68 |
| 3.6.1 | Simulation and Analysis Code Available Online | 68 |
| 3.6.2 | Steady-state Approximation of Effective Viscosity | 68 |
| 3.6.3 | Critical filament lifetime for steady state filament extension . | 70 |
| 4 | A MODEL OF UPSTREAM ACTOMYOSIN REGULATORS IN PULSED CONTRACTIONS | 78 |
| 4.1 | Preface | 78 |
| 4.2 | Abstract | 78 |
| 4.3 | Introduction | 79 |
| 4.4 | Results | 81 |
| 4.4.1 | Single-molecule analysis of actomyosin dynamics during pulsed contractions | 81 |
| 4.4.2 | Pulsed activation of RhoA drives the pulsed accumulation of F-actin and Myosin II | 86 |
| 4.4.3 | Pulsed activation of RhoA does not require Myosin II. | 90 |
| 4.4.4 | RhoA feeds back locally to promote its own activity and this is required for pulse initiation. | 91 |
| 4.4.5 | Delayed accumulation of the Rho GAPs RGA-3/4 underlies pulse termination. | 93 |

| | | |
|--------|---|-----|
| 4.4.6 | Fast positive and delayed negative feedback involving RhoA and RGA-3/4 can account quantitatively for locally pulsatile RhoA dynamics. | 97 |
| 4.5 | Discussion | 100 |
| 4.6 | Materials and Methods | 104 |
| 4.6.1 | C. Elegans culture and strains | 104 |
| 4.6.2 | RNA interference | 105 |
| 4.6.3 | Microscopy | 105 |
| 4.6.4 | Single-molecule imaging | 106 |
| 4.6.5 | Analysis of F-actin and Myosin II turnover | 106 |
| 4.6.6 | Measuring local deformations from single molecule data | 107 |
| 4.6.7 | Two-color imaging, pulse tracking, and analysis | 109 |
| 4.6.8 | Kymograph analysis | 111 |
| 4.6.9 | Kinetic analysis | 111 |
| 4.6.10 | Mathematical Modeling | 111 |
| 4.7 | Supplementary Figures | 114 |
| 5 | CONCLUSIONS, OPEN ISSUES, & FUTURE DIRECTIONS | 120 |
| 5.1 | Comparison with Recent Modeling Publications | 120 |
| 5.1.1 | Role of Turnover in Active Stress Generation in a Filament Network by Tetsuya Hiraiwa and Guillaume Salbreux | 120 |
| 5.1.2 | Interplay of active processes modulates tension and drives phase transition in self-renewing, motor-driven cytoskeletal networks by Michael Mak, Muhammad H. Zaman, Roger D. Kamm & Taeyoon Kim | 122 |
| 5.1.3 | Shared conclusion of all three works | 124 |
| 5.2 | Incorporating multi-segment filaments and bending degrees of freedom | 125 |
| 5.3 | Probing more complex mechanisms of turnover | 126 |
| 5.3.1 | Which is more important, filament relocation or stress resetting? | 128 |
| 5.3.2 | Overlooking the subtleties of myosin turnover | 128 |
| 5.4 | A novel cell squishing technique to measure timescales of relaxation <i>in vivo</i> | 129 |
| A | SOURCE CODE AND DOCUMENTATION | 131 |
| A.1 | Practical Implementation of Model Framework | 131 |
| A.1.1 | Launching simulations from the command line | 131 |
| A.1.2 | Package structure of activnet | 135 |
| A.1.3 | ODE Wrapper functions | 135 |
| A.1.4 | Overview of Numerical Integration Implementations | 138 |
| A.1.5 | Left hand side: The mysterious mass matrix | 145 |
| A.1.6 | Line intersection <i>helper</i> Functions | 147 |
| A.1.7 | Visualization code | 147 |

| | | |
|-------|--|-----|
| A.2 | Finding Source Code Online | 147 |
| B | PHASES OF DEFORMATION IN FILAMENT NETWORKS WITH CROSS-LINK SLIP | 148 |
| B.1 | Results | 148 |
| B.1.1 | Steady-state Approximation of Effective Viscosity | 148 |
| B.1.2 | Effects of Filament Compliance | 151 |
| B.1.3 | Alignment at High Strain and Network Tearing | 154 |
| B.1.4 | Phase Diagram of Dominant Behavior | 154 |
| B.1.5 | Frequency dependent modulus | 156 |
| B.1.6 | Strain Memory | 157 |
| B.2 | Summary and Conclusions | 160 |
| B.3 | Network Tearing under Extensional Stress | 161 |
| B.3.1 | Extensional Thinning and Network Tearing | 161 |
| B.3.2 | Tearing Events During Extensional Strain | 161 |
| B.4 | Deriving Molecular Drag Coefficients | 161 |
| C | IMPACT OF FILAMENT RECYCLING ON CORTICAL FLOW IN ANIMAL CELLS | 164 |
| C.1 | Active Fluid Model Fitting of Cortical Flow Measurement in <i>C. elegans</i> embryos | 164 |
| C.1.1 | Obtaining spatially resolved simultaneous measurement of actin and myosin densities | 165 |
| C.1.2 | Obtaining spatially resolved measurement of cortical flow velocities | 165 |
| C.1.3 | Using the data to constrain a basic active fluid model | 166 |
| C.1.4 | Disruption of Flow by Myosin Depletion | 167 |
| C.2 | Stabilization of Filament Turnover with Jasplakinolide Treatment | 168 |
| D | ADDITIONAL INFORMATION ON PULSE MODEL | 170 |
| D.1 | Motivation and experimental context | 170 |
| D.2 | A model for pulsatile actomyosin accumulation in <i>C. elegans</i> | 171 |
| D.2.1 | Analyzing parameter space of the model | 172 |
| D.3 | Simplified model and data fitting | 175 |
| D.3.1 | Fitting techniques | 175 |
| D.4 | Conclusion | 177 |
| E | REDUCING POWER CONSUMPTION IN HIGH PERFORMANCE COMPUTING | 180 |
| E.1 | Introduction | 180 |
| E.1.1 | Alternative Demand Response Options in Data Centers | 181 |
| E.2 | Problem Statement | 183 |
| E.2.1 | Modeling Energy Costs | 183 |

| | | |
|----------|---|------------|
| E.2.2 | Response to a Temporary Price Spike | 185 |
| E.3 | EDEALS: Electricity Demand-response Easy Adjusted Load Shifting | 186 |
| E.4 | Small-Scale Evaluation of EDEALS | 188 |
| E.4.1 | Experimental Setup | 188 |
| E.4.2 | Evaluation of Model Parameters | 188 |
| E.4.3 | Relative Energy Savings and Max Wait Times | 189 |
| E.5 | Conclusion: Implication for An Operational HPC Datacenter | 190 |
| E.6 | Acknowledgments | 191 |
| E.7 | Availability | 192 |
| F | ARTISTIC INTERPRETATIONS OF FILAMENT RECYCLING | 193 |
| F.1 | The ship of Theseus as a metaphor for life | 196 |
| F.2 | Experiments with plastic filament sculpture | 196 |
| G | WORKSHOP ON MODELING IN BIOLOGY | 204 |
| G.1 | Course syllabus | 205 |
| G.1.1 | Course Objective | 205 |
| G.1.2 | Course Design | 205 |
| G.1.3 | Assignments | 205 |
| G.2 | Post-class Student Survey | 207 |
| G.3 | Reflections and Future Ideas | 208 |
| G.4 | Course Materials | 208 |
| G.4.1 | How mathematical models make sense of complex processes . | 209 |
| G.4.2 | Modeling biological systems with differential equations . . . | 209 |
| G.4.3 | Visualizing equations with graphs | 210 |
| G.4.4 | Simplifying models and starting simulations | 211 |
| G.4.5 | Analyzing equations and understanding simulation output . | 212 |
| G.4.6 | Explaining ever more complex systems | 213 |
| G.5 | Quizzes and Project ideas | 213 |

LIST OF FIGURES

23

- 2.2 Exploiting dynamic exchange between cytoplasm and cell surface to obtain long-term tunable and high-density sampling of single molecule behaviors. (a) The basic kinetic principle: During imaging, the level of surface-associated proteins is set by a dynamic balance of: appearance (binding or assembly) at an observable rate k_{app} , disappearance (unbinding or disassembly) at a per-molecule rate k_{off} , and photo-bleaching at a per molecule rate k_{ph} . (b) The predicted response of an initially unobserved cell at steady state to a step change in illumination. For an infinite cytoplasmic pool (cyan), the surface density relaxes to a new illuminated steady state. For a finite cytoplasmic pool (blue), fast relaxation is accompanied by a slower decay caused by irreversible photobleaching. (c) Biphasic response for GFP::Actin under illumination conditions that allow accurate single molecule detection and tracking. (dots) real data; (solid line) model fit; (dashed line) discontinuous jump from $t = 30s$ to $t = 450s$. (d) The fast relaxation to a quasi-stable density during illumination is rapidly reversed when the laser is turned off. (e) Surface density vs time at various laser exposures, shown as a fraction of the initial unobserved density. Error bars indicate standard error of the mean ($n=7,9,6,7$). (f) Estimates of per molecule disappearance (k_{off}) and photobleaching (k_{ph}) rates as a function of laser exposure. Error bars indicate standard deviation, ($n=12,7,8,9,7,6,7,7$). Solid lines show a linear regression against the data. k_{ph} increases linearly with laser exposure, while k_{off} remains constant. 100% laser power $\sim 1.6W/m^2$.

2.3 Analysis of PAR-6::GFP mobility during maintenance phase (a) Distribution of track lengths for 30,558 tracks from $n = 5$ movies taken in one-cell embryos during maintenance phase. (b) Log/log plot of MSD versus lag time () for all 177 tracks with length 80 frames extracted from one of the movies, reveals what appears to be a mixture of brownian and anomalous diffusion. Traces have been assigned colors based on slope (α),(): $\alpha < 0.6$; (): $0.6 < \alpha < 0.9$; (): $\alpha > 0.9$ (c) Scatter plot of diffusion coefficient D versus exponent α , measured by fitting $MSD = 4Dt\alpha$ for the first 10 lag times of the tracks shown in (b), with (): $\alpha < 0.6$; (): $0.6 < \alpha < 0.9$; (): $\alpha > 0.9$. Inset shows two particular trajectories drawn from opposite ends of the scatter plot and indicated by colored circles. Scale bar, 1m. (d) Scatter plot for 177 trajectories obtained by simulating pure brownian diffusion for 80 frames with $D = 0.15 +/- 0.05 m^2.s^{-1}$ and measuring D and α as in (c). (lines) simulated tracks. Note the close match to experimental data for $0.9 < \alpha < 1.2$, but the failure to match points at the bottom left (low D and α).

25

29

- 3.2 Networks with passive cross-links and no filament turnover undergo three stages of deformation in response to an extensional stress. **A**) Three successive time points from a simulation of a $4 \times 6.6 \mu\text{m}$ network deforming under an applied stress of $0.005 \text{ nN}/\mu\text{m}$. Stress (tan arrows) is applied to filaments in the region indicated by the tan bar. In this and all subsequent figures, filaments are color-coded with respect to state of strain (blue = tension, red = compression). Network parameters: $L = 1 \mu\text{m}$, $l_c = 0.3 \mu\text{m}$, $\xi = 100 \text{ nN} \cdot \text{s}/\mu\text{m}$. **B**) Mean filament stress and velocity profiles for the network in (a) at $t=88\text{s}$. Note that the stress is nearly constant and the velocity is nearly linear as predicted for a viscous fluid under extension. **C**) Plots of the mean stress and strain vs time for the simulation in (a), illustrating the three stages of deformation: (i) A fast initial deformation accompanies rapid buildup of internal network stress; (ii) after a characteristic time τ_c (indicated by vertical dotted line) the network deforms at a constant rate, i.e. with a constant effective viscosity, η_c , given by the slope of the dashed line; (iii) at long times, the network undergoes strain thinning and tearing (see inset) 48
- 3.3 Network architecture sets the rate and timescales of deformation. **(a-c)** Comparison of predicted and simulated values for: **A**) the bulk elastic modulus G_0 , **B**) the effective viscosity η_c and **C**) the timescale for transition from viscoelastic to viscous behavior τ_c , given by the ratio of the bulk elastic modulus G_0 to effective viscosity, η_c . Dotted lines indicates the relationships predicted by theory. 49
- 3.4 Filament recycling defines two regimes of effectively viscous flow. **A**) Comparison of $20 \times 12 \mu\text{m}$ networks under $0.001 \text{ nN}/\mu\text{m}$ extensional stress without (top) and with (bottom) filament turnover. Both images are taken when the networks had reached a net strain of 0.04. For clarity, filaments that leave the domain of applied stress are greyed out. **B**) Plots of strain vs time for identical networks with different rates of filament turnover. Network parameters: $L = 5 \mu\text{m}$, $l_c = 0.5 \mu\text{m}$, $\xi = 10 \text{ nN} \cdot \text{s}/\mu\text{m}$. **C**) Plot of effective viscosity vs turnover time derived from the simulations shown in panel b. Square dot is the $\tau_r = \infty$ condition. **D**) Plot of normalized effective viscosity (η/η_c) vs normalized turnover time (τ_r/τ_c) for a large range of network parameters and turnover times. For $\tau_r \ll \tau_c$, the viscosity of the network becomes dependent on recycling time. Red dashed line indicates the approximation given in equation 3.13 for $m = 3/4$ 52

3.5 In the absence of filament turnover, active networks with free boundaries contract and then stall against passive resistance to network compression. **A)** Simulation of an active network with free boundaries. Colors represent strain on individual filaments as in previous figures. Note the buildup of compressive strain as contraction approaches stall between 100 s and 150 s. Network parameters: $L = 5 \mu m$, $l_c = 0.3 \mu m$, $\xi = 1 nN \cdot s/\mu m$, $v = 0.1 nN$. **B)** Plots showing time evolution of total network strain (black) and the average extensional (blue) or compressive (red) strain on individual filaments. **C)** Plots showing time evolution of total (black) extensional (blue) or compressive (red) stress. Note that extensional and compressive stress remain balanced as compressive resistance builds during network contraction.

55

3.6 In the absence of filament turnover, active networks cannot sustain continuous stress against a fixed boundary. **A)** Simulation of an active network with fixed boundaries. Rearrangement of network filaments by motor activity leads to rapid loss of network connectivity. Network parameters: $L = 5 \mu m$, $l_c = 0.3 \mu m$, $\xi = 1 nN \cdot s/\mu m$, $v = 1 nN$. **B)** Simulation of the same network, with the same parameter values, except with ten-fold lower motor activity $v = 0.1 nN$. In this case, connectivity is preserved, but there is a progressive buildup of compressive strain on individual filaments. **C)** Plots of total network stress and the average extensional (blue) and compressive (red) stress on individual filaments for the simulation shown in (a). Rapid buildup of extensional stress allows the network transiently to exert force on its boundary, but this force is rapidly dissipated as network connectivity breaks down. **D)** Plots of total network stress and the average extensional (blue) and compressive (red) stress on individual filaments for the simulation shown in (b). Rapid buildup of extensional stress allows the network transiently to exert force on its boundary, but this force is dissipated at longer times as decreasing extensional stress and increasing compressive stress approach balance. Note the different time scales used for plots and subplots in **C)** and **D)** to emphasize the similar timescales for force buildup, but very different timescales for force dissipation. . .

57

| | |
|--|----|
| 3.10 Flux balance analysis of network density. Qualitative plots of $\rho + \frac{\sigma\tau_r}{\eta_c(\rho)}\rho$ (red curves) vs ρ_0 (green line) for different values of τ_r . For sufficiently large τ_r , there are no crossings. For $\tau_r < \tau_{crit}$, there are two crossings: The rightmost crossing represents a stable steady state. | 71 |
| 3.11 Fast viscoelastic response to extensional stress. Plots of normalized strain vs time during the elastic phase of deformation in passive networks under extensional stress. Measured strain is normalized by the equilibrium strain predicted for a network of elastic filaments without crosslink slip $\gamma_{eq} = \sigma/G_0 = \sigma/(2\mu/l_c)$ | 73 |
| 3.12 Filament turnover rescues strain thinning. a) Plots of strain vs time for different turnover times (see inset in (b)). Note the increase in strain rates with decreasing turnover time. b) Plots of filament density vs strain for different turnover times τ_r . For intermediate τ_r , simulations predict progressive strain thinning, but at a lower rate than in the complete absence of recycling. For higher τ_r , densities approach steady state values at longer times. | 73 |
| 3.13 Mechanical properties of active networks. a) Time for freely contracting networks to reach maximum strain, τ_s , scales with $L\xi/v$. b) Free contraction requires asymmetric filament compliance, and total network strain increases with the applied myosin force v . Note that the maximum contraction approaches an asymptotic limit as the stiffness asymmetry approaches a ratio of ~ 100 . c) Maximum stress achieved during isometric contraction, σ_m , scales approximately with $\sqrt{\mu_e v}/l_c$. d) Time to reach max stress during isometric contraction scales approximately with $L\xi/\sqrt{\mu_e v}$. Scalings for τ_s , σ_m and τ_m were determined empirically by trial and error, guided by dimensional analysis. | 74 |
| 3.14 Filament turnover prevents tearing of active networks. a) An active network undergoing large scale deformations due to active filament rearrangements. b) The same network as in (a) but with a shorter filament turnover time. c) Plots of internal stress vs time for the network in (a). d) Plots of internal stress vs time for the network in (b). | 75 |
| 3.15 Bimodal dependence on turnover time matches bimodal buildup and dissipation of stress in the absence of turnover. a) Bimodal buildup of stress in a network with very slow turnover ($\tau_r = 1000s$). b) Steady state stress for networks with same parameters as in (a), but for a range of filament turnover times. | 76 |
| 3.16 Dynamics of steady state flow. Plots of stress and strain vs position for networks in which motor activity is limited to the right-half domain and filament turnover time is either a) $\tau_r = 10000$ or b) $\tau_r = 10s$. Blue indicates velocity while orange represents total stress, measured as described in the main text. | 76 |

4.1 **Actomyosin pulses in 1 and 2-cell stage embryos.** (A) Schematic view of the zygote P0 during early interphase. Open circles represent the two pronuclei. (B) Micrograph of P0 in early interphase expressing GFP::UTR and NMY-2::RFP. In (A) and (B), white arrowheads indicate individual pulses and magenta arrows indicate membrane invaginations (ruffles). (C) Time evolution of a single pulse in P0. The square region measures $\sim 6.4\mu\text{m}$ by $6.4\mu\text{m}$. The time delay between frames is 6s for the first 6 frames, and 8s thereafter. (D) Schematic of an embryo at the early 2-cell stage, showing the anterior blastomere AB and the posterior blastomere P1. Open circles represent the interphase nuclei. (E) Micrograph of an early two-cell stage embryo expressing GFP::UTR and NMY-2::RFP. White arrowheads indicate individual pulses (F) Time evolution of a single pulse. The square region measures $\sim 6.4\mu\text{m}$ by $6.4\mu\text{m}$. The time delay between frames is 2s for the first 5 frames, and 4s thereafter.

4.2 **Single-molecule analysis of actin network assembly, disassembly and deformation during individual pulsed contractions.** One frame of a time lapse sequence taken from an embryo expressing low levels of Actin::GFP. A patch of cortex undergoing a pulse is identified from the time lapse sequence, and outlined in cyan. (B) Automatic particle detection of single-molecules from the image in (A). (C) Trajectories of the molecules displayed in (B) that were tracked for longer than 2s. (D) A polygonal region of interest identified at time $t = t_{ref}$, in (A) (dashed cyan polygon) is propagated forward and backward in time using the trajectories of tracked particles (see Materials and Methods). (E-H) Simultaneous measurements of single molecule dynamics and patch deformation over time. (E) Strain rate, measured using the particle-based method (see Materials and Methods). (F) Number of actin molecules in the patch. (G-H) Appearance rates (G) and disappearance rates (H) of actin molecules. Red shading in (F-H) indicates the time period in which the cortex is contracting locally (strain rate > 0).

4.3 Spatiotemporal modulation of assembly and disassembly drives transient accumulation of F-actin and Myosin II during pulsed contractions. (A-D) Data from individual pulses, aligned with respect to the onset of contraction and then averaged to display particle-based strain rate (A), numbers of actin molecules (scaled by the average number for each pulse) (B) appearance rate (C), and disappearance rate (D) versus time. (E) Total rate of change in actin density (green) and the individual contributions to rate of change from turnover and surface contraction. (F) Distribution of time delays between the initiation of contraction and actin accumulation. Data in (A-F) were averaged over 42 pulses, collected in 8 embryos. (G-J) Average myosin dynamics synchronized with respect to time at which myosin density reached peak levels during a pulse, displaying particle-based strain rate (G), number of molecules (scaled to the average number for each pulse) (H), appearance rate (I) and disappearance rate (J) versus time. Data were averaged over 30 pulses, collected in 5 embryos. Error bars: 95% confidence interval.

87

4.4 Local pulses of RhoA activation underlie pulsed accumulation and disappearance of F-actin and Myosin II. (A) Micrograph of a 2-cell stage embryo expressing GFP::AHPH as a reporter for RhoA activity, and NMY-2::RFP. (B) Temporal dynamics of GFP::AHPH and NMY-2::RFP accumulation during a single pulse. The square region measures $\sim 5.3\mu\text{m}$ by $5.3\mu\text{m}$. The time between frames is 2s for the first five frames, and 4s thereafter. (C) Above: Normalized fluorescence intensities of GFP::AHPH, and NMY-2::RFP. Below: A kymograph showing that local contraction (concerted movements of myosin puncta) begins after the accumulation of GFP::AHPH. The yellow box below left indicates the region used to generate the kymograph. (D) Comparison of averaged normalized fluorescence intensities vs time for active RhoA (GFP::AHPH), Myosin (NMY-2::GFP) and F-actin (GFP::UTR) from two-color data, co-aligned with respect to a common reference signal (NMY-2::RFP). Data were co-aligned with respect to the time at which NMY-2::RFP reaches 25% threshold. Hued regions report 95% confidence intervals. (E) Distribution of the delays between the onset of accumulation of NMY-2::RFP, and the onset of accumulation of GFP::AHPH, NMY-2::GFP and GFP::UTR. Onset of accumulation was measured as the time at which normalized probe intensity rose above 25% of its maximal level. (F) Distribution of the delays between the onset of disappearance of NMY-2::RFP, and the onset of disappearance of GFP::AHPH, NMY-2::GFP and GFP::UTR. Onset of disappearance was measured as the time at which normalized probe intensity fell below 75% of its maximal level. In boxplots, the central mark represents the median, the box indicates the 25th and 75th percentile, and the whiskers mark the minimum and maximum values

- 4.5 **Myosin II is not required for the pulsed activation of RhoA.** (A) Comparison of pulse dynamics in zygotes expressing GFP::AHPH and NMY-2::mKATE and treated with either *spd-5*(RNAi) or *nmy-2*(RNAi). Top panels show myosin localization (NMY-2::mKATE), middle panels show RhoA activity (GFP::AHPH). Bottom panels are kymographs showing GFP::AHPH dynamics over time. Dashed yellow rectangles in middle panel indicate the regions from which the kymographs were made. Vertical yellow arrows indicate a region undergoing repeated pulses. Intensities were scaled identically for *spd-5*(RNAi) and *nmy-2*(RNAi) zygotes. (B) Top: Mean intensities of NMY-2::mKATE (red) and GFP::AHPH (green) vs time for a single pulse in an *nmy-2*(RNAi) zygote. Bottom: sequential snapshots of the region undergoing the pulse showing NMY-2::mKATE (red) and GFP::AHPH (green) distributions. Yellow arrowheads indicate the 1-2 particles that can be detected in the region undergoing a pulse. (C) Mean intensity of GFP::AHPH over time in *nmy-2*(RNAi) and *spd-5*(RNAi) zygotes, aligned with respect to the time at which the normalized signal reaches 25% of its maximum value. For *spd-5* (RNAi) zygotes, the signal was measured either within the entire boxed region in which each pulse occurred or at its periphery (see Figure 4.12 for details). Hued regions report 95% confidence intervals.
- 4.6 **RhoA activation is autocatalytic.** (A) The time derivative of normalized RhoA activity (GFP::AHPH) plotted vs normalized activity during the early phase of pulse initiation in P0 (top panel, n = 40 pulses) and AB (bottom panel, n = 41 pulses). Error bars: 95% confidence interval. (B-C) Analysis of pulse dynamics in embryos progressively depleted of RHO-1 by RNAi. (B) Top panels show GFP::AHPH distributions in interphase embryos from mothers subjected to no (wild type), 10 hours and 13 hours of *rho-1*(RNAi). Middle panels show kymographs from the same embryos illustrating spatiotemporal dynamics of GFP::AHPH from interphase through cytokinesis. Dashed yellow lines indicate approximate pattern of cortical flow. Cyan arrowheads indicate accumulation of GFP::AHPH just prior to cytokinesis. (C) Timeline indicating the presence (magenta circles) or absence (cyan circles) of pulsing in embryos treated with *rho-1*(RNAi) for the indicated times, revealing an abrupt transition from pulsing to no pulsing at ~12 hours post-treatment.

92

94

4.10 Schematic overview of methods for tracking a moving and deforming patch of cortex from single molecule data. (A) Micrograph of a two-cell stage embryo expressing Actin::GFP at single-molecule levels. Anterior is to the left. Dashed lines indicate the outlines of AB and P1. The blue ellipse identifies a region in which a pulse occurs, from which a reference ROI will be extracted. (B) Method for extracting the reference ROI. Left: Single particles detected in the raw image. The particles shown in red are those contained within the blue ellipse. Middle and right: The reference ROI (solid red line) is the smallest convex polygon containing all red particles. (C) Strategy for iterative propagation of the polygonal ROI from frame to frame (either backwards or forwards in time). The polygons vertices move with the particle that defined that vertex so long as the particle remains visible. When a particle associated with a vertex disappears (dashed magenta particle in middle left panel), the vertex displacement is extrapolated from the motion of the surrounding particles. If an internal particle moves outside the boundaries of the polygon defined by existing vertices (green particle in middle right panel) a new vertex associated with that particle is introduced.

115

4.11 Comparison of different methods to quantify local deformation (strain rate) and to align data across multiple pulses. (A,B) Comparison of different methods used to compute local deformation rates during pulses. (A) Measures of deformation rate vs time for the same data using three different metrics: (top) Rate of change in normalized surface area, (middle) material strain rate and (bottom) particle based strain rate (see materials and methods for details on how these were computed). (B) Measurements of single molecule number (top), appearance rate (middle) and disappearance rate (bottom) were aligned and averaged with respect to the onset of contraction, over 42 pulses, using the three metrics to measure deformation: change in normalized surface area (green), material strain rate (red), and particle-based strain rate (blue). Vertical dashed lines mark lowest actin density preceding the pulse. Horizontal dashed lines in top graph mark, respectively, the minimum number of actin molecules and the number of molecules at the onset of contraction. For all three metrics, the delay from actin minimum to contraction onset is $\delta t \approx 5$ s, and the relative change in number of molecules from minimum to contraction onset is $\delta n \approx 30\%$. (C) Measurements of material strain rate, number of molecules, appearance rate and disappearance rate, aligned and averaged with respect to the end of contraction for the same data shown in A&B. (D) Measurements of particle-based strain rate, number of molecules, appearance rate and disappearance rate, aligned and averaged with respect to the onset of contraction, in wild type (blue, n = 42 pulses) and *arx-2*(RNAi) (red, n = 49 pulses) embryos. (E) Left column: number of molecules relative to average in wild type (blue) and *arx-2*(RNAi) (red) embryos, as previously displayed in (D). The vertical dashed line marks lowest actin density preceding the pulse, delayed respectively by $\delta t \approx 5$ s and $\delta t \approx 6$ s from the contraction onset (gray box). The horizontal dashed line displays the amount of pre-contraction increase in the number of actin molecules, with $\delta n \approx 30\%$ and $\delta n \approx 40\%$, respectively. Right column: a histogram showing the distribution of delays between contraction onset and increase of actin molecules. Staircase line: cumulative distribution function of the delays. Error bars report 95% confidence intervals.

116

4.12 Schematic overview of methodology for measuring and aligning fluorescence intensities from two-color data during pulsed contractions. (A) Method for determining regions of interest in which to measure fluorescence intensities, illustrated for a single pulse. Row 1: raw GFP::AHPH signal. Row 2: raw NMY-2::RFP signal. Row 3: smoothed NMY-2::RFP signal. Row 4: thresholded NMY-2::RFP signal. Row 5: The smallest box containing the largest thresholded domain is the bounding box. In each frame, the center of bounding box is located on the centroid of the thresholded domain. Row 6: A fixed-size peripheral region is the complement of the largest thresholded region within its bounding box. The center of the fixed-size peripheral region is located at the center of the thresholded region in each frame. (B) Normalized fluorescence intensity of GFP::AHPH and NMY-2::RFP versus time for ten representative pulses in AB cells. Time $t = 0$ when NMY-2::RFP rises above 25% of its normalized maximum value. (C) Fluorescence intensities from all pulses in (B) co-aligned relative to time $t = 0$. The bold traces represent the average GFP::AHPH and NMY-2::RFP intensities. (D,E) Alignment of averaged normalized fluorescence intensities for NMY-2::XFP measured for pulses in P0 (D) and AB (E) cells co-expressing the indicated probes (shown in parentheses). Time $t = 0$ is when NMY-2::XFP rises above 25% of its normalized maximum value. (F,G) Averaged normalized fluorescence intensity of GFP::AHPH measured in the bounding box (green) and periphery (gray) for pulses in P0 (F) and AB (G) cells. In (D-G), halos report 95% confidence intervals.

117

4.13 Two color analysis of Myosin II and Anillin dynamics during pulsed contractions in one- and two-cell embryos.(A,E) Micrographs of two-cell (A) and one-cell (E) embryos co-expressing GFP::ANI-1 and NMY-2::RFP. White arrowheads indicate individual pulses. (B,F) Expanded views of single pulses illustrating temporal dynamics of GFP::ANI-1 and NMY-2::RFP accumulation. (C,G) Plots of averaged normalized fluorescence intensities for NMY-2::RFP and GFP::ANI-1 from two-color movies, aligned to the time at which NMY-2::RFP reaches 25% threshold. The averaged normalized fluorescence intensity of GFP::AHPH, co-aligned using the NMY-2::RFP signal, is shown for reference. Halos report 95% confidence intervals. (D,H) Distribution of the delays in the onset of appearance and disappearance of GFP::ANI-1 measured relative to NMY-2::RFP. Onset of appearance and disappearance were measured respectively as the time at which the normalized signal rose above 25% or fell below 75% of the maximum value.

118

4.14 Two color analysis of pulsed contractions in P0. (A) A zygote expressing GFP::AHPH and NMY-2::RFP. White arrowheads indicate individual pulses. (B) Expanded view of a single pulse illustrating temporal dynamics of GFP::AHPH and NMY-2::RFP accumulation. Time delay between frames is 4s for the first 4 frames, and 6s thereafter. (C) Plot of normalized fluorescence intensities of GFP::AHPH and NMY-2::RFP versus time for the pulse displayed in (B). Below: kymograph showing movements of NMY-2::RFP punctae before and during the pulse. Yellow box at left indicates the region used to make kymograph. Yellow arrow at right indicates the onset of contraction. Note that a sharp rise in GFP::AHPH precedes both Myosin accumulation and onset of contraction. (D) Averaged normalized fluorescence intensities for NMY-2::RFP, GFP::AHPH and GFP::UTR from two-color movies, aligned to the time at which NMY-2::RFP reaches 25% threshold. Halos report 95% confidence intervals. (E) Distributions of the delay in onset of accumulation of GFP::AHPH, GFP::UTR, and NMY-2::GFP, measured relative to the onset of accumulation of NMY-2::RFP during pulse initiation for many individual pulses. Onset of accumulation is measured as the time at which each normalized signal exceeds 25% of its maximum value. (F) Distributions of the delay in the onset of disappearance of GFP::AHPH, GFP::UTR, and NMY-2::GFP measured relative to NMY-2::RFP during pulse termination for many individual pulses. Onset of disappearance is measured as the time at which each normalized signal falls below 75% of its maximum value. In (E,F) box plots, the central mark represents the median, the box indicates the 25th and 75th percentile, the whiskers mark the minimum and maximum values and the “+” symbol represents outliers. 119

- B.1 Ratio of effective viscosity measured by shear simulation to predicted effective viscosity as a function of connectivity, L/l_c . Inset: Same measurement for extensional simulations 150
B.2 Network and filament strain for different filament drag coefficient parameters. (top) Plot of total strain normalized by the final mean filament strain, $\delta L/L$. Dashed lines show the amount of strain from affine mechanical stretching. (bottom) Standard deviation of filament extension for the networks in A. Note that the creep compliance in A becomes constant (slope 1) only after the spread in filament extension in B stops increasing. Colors indicate unique experimental conditions. 152

| | | |
|-----|--|-----|
| B.3 | Sublinear network strain ends as change in filament strain decays. (top) Change in standard deviation of filament strain, σ , as a function of strain relative to pure mechanical strain. (bottom) Dependence of strain rate exponent as a function of strain relative to pure mechanical strain, γ_0 . Colors indicate unique experimental conditions. | 153 |
| B.4 | Creep response of a network transitioning to phase D. (top) Strain curves for a network undergoing large scale deformation. Inset shows strain exponent as a function of strain (exponent passes 1). (bottom) Traces for the variance in filament orientation and number of cross links. Vertical dashed line shows the point where the strain exponent becomes greater than one. | 155 |
| B.5 | Schematic of the general creep response of compliant filament networks illustrating the 4 phases of deformation: A) rapid mechanical response, B) combination of slow filament stretching and cross-link slip, C) cross- link slip dominated (line indicates slope of one), D) network tearing from filament alignment. Note that the portion of the curve in section D is only a hypothetical continuation of the actual data. | 156 |
| B.6 | phase diagram of creep response for different filament extension, μ and cross-link friction, ξ . Yellow, green, and purple dots correspond to creep measurements $\gamma \sim t^\alpha$ with $\alpha < 0.92$, $0.92 < \alpha < 0.98$, or $\alpha > 0.98$ respectively. Blue dots represent creep measurements where $\gamma_{total} < 2\gamma_{mechanical}$ | 157 |
| B.7 | Frequency dependent moduli for networks. | 158 |
| B.8 | Creep curves in the presence of reversing applied stress for (a) nonlinear extension or (b) linear extension. Note that for linear filaments the induced strain returns to approximately 0 after a complete cycle, while in the nonlinear case the cycle is not completely reversible. | 159 |
| C.1 | Measurement of myosin intensity and flow profile. These measurements fit a theoretical model of active fluid flow. | 167 |
| C.2 | Measurement of actin distributions and flow profiles for mrck-1 knock- down embryos. MRCK-1 is an upstream regulator of myosin. | 168 |
| C.3 | | 169 |
| D.1 | Reaction pathway with labels for coefficients associated with feedback strengths. | 170 |
| D.2 | Perturbation simulation results plotted on phase planes for a variety of parameters. | 173 |
| D.3 | Phase diagram of for $k_q = 1$ and $k_q q = 100$ | 174 |
| D.4 | | 175 |
| D.5 | Multiple methods of fitting. | 176 |

| | | |
|-----|---|-----|
| D.6 | Simulation results and fitted data for model with $m = 2$ and $k = 0$. Displaying simulation results and the data used to fit the simulation on a phase plane (left) and as pairs of time plots (right). | 177 |
| D.7 | Small variation in simulation parameters can have large qualitative effects. | 178 |
| D.8 | Final figure as it appears in Reference [173]. | 179 |
| E.1 | Average core usage for a 244 node shared HPC partition in the Midway cluster. Insert shows usage statistics histogram. | 181 |
| E.2 | Energy monitoring framework. | 183 |
| E.3 | Diagram of job scheduling during a four node temporary shutdown experiment. Each colored rectangle displays the execution time of a single LAMMPS test job running for approximately 5 minutes. | 184 |
| E.4 | Total power consumed during experiments where variable numbers of machines were shut down during simulated peak pricing. | 184 |
| E.5 | Energy usage of test cluster during partial shutdown experiments. Solid lines indicate power usage during the shutdown, while dashed lines indicate power usage after returning to full operation. | 186 |
| E.6 | Maximum (solid) and mean (dashed) job wait times during partial shutdown experiments. | 187 |
| E.7 | Power data for test cluster (top) and production cluster (bottom) nodes in presence of variable usage. The slope and intercept of the line are used to determine u_v and u_0 respectively. | 189 |
| E.8 | Comparison between node level IPMI measurements and rack level CDU measurements. Best fit shows the model relationship used to convert IPMI data to estimated total power draw. | 190 |
| E.9 | Estimated savings from partial cluster shutdowns. | 191 |
| F.1 | | 197 |
| F.2 | | 197 |
| F.3 | | 198 |
| F.4 | | 199 |
| F.5 | | 200 |
| F.6 | | 201 |
| F.7 | | 202 |
| F.8 | | 203 |
| G.1 | Responses from student survey. Only 2 of 5 students replied. | 207 |

LIST OF TABLES

| | | |
|-----|---|-----|
| 3.1 | Simulation Parameter Values | 45 |
| 3.2 | Simulation Parameter Values | 77 |
| E.1 | Model parameters estimated for medium scale HPC datacenter. | 191 |

CHAPTER 1

INTRODUCTION

1.1 Biological Context of Cortical Flow

Many essential cellular processes, including cytokinesis and cell migration, depend on the fundamental ability of cells to change their shape[200]. Cellular deformation is a complex process because cells contain an intricate array of organelles and cytoskeletal machinery that must be reorganized in a highly coordinated manner. When changing shape, cells must simultaneously facilitate the rearrangements of these internal constituents while maintaining structural stability. A key open question in the field of cell biology is how cells undergo these complex intracellular rearrangements while maintaining their structural integrity.

One fundamental and ubiquitous form of cellular deformation is known as cortical flow: Cortical flows originate within a thin layer of cross-linked actin filaments and myosin motors, called the actomyosin cortex, that lies just beneath the plasma membrane[145]. Cortical flows result in the long range movements of cortical material within a cell[1]. Cortical flows are thought to be driven by gradients of tension originating from imbalances in myosin motor activity, which lead to movements of cortical material from regions of low stress to regions of high stress[22].

Cortical flow plays an essential role in a wide variety of biological processes, including cell polarization, cell division, cell crawling and multicellular tissue morphogenesis [22, 82, 15, 222, 165, 145]. For example, cortical flow was implicated as an important driver for establishing the primary embryonic axis of the single-cell *C. elegans* embryo. In the early *C. elegans* embryo the proteins PAR-3, PAR-6 and PKC-3 are initially distributed evenly around the cortex of the cell, however to establish the antero-posterior axis, these proteins must become enriched at the anterior cortex. Cortical flow generates this asymmetry by actively transporting these proteins to the anterior pole. An asymmetric flow is generated from the sperm entry point, which occurs at the nascent posterior pole of the embryo and causes a local decrease in an upstream regulator of myosin contractility [145]. This small asymmetry leads to a gradient in myosin activity across the embryo and the formation of cortical flow toward the anterior. This process was later shown in [138] to rely on gradients of tension as suggested in [22]. Cortical flows also play an important role in amoeboid motility[213, 226, 156].

Recent work has shown that during migration of Dictyostelium there is a rapid flow of actin and myosin toward the rear of the cell [226]. It is thought that this flow contributes to motility via a clutch hypothesis, in which the actomyosin cortex is attached to the substrate through focal adhesions and this coupling causes the flow to produce traction forces that result in migration[213, 156]. Investigating epithelial spreading during zebrafish epiboly has found that cortical flow can even give rise to shape changes in entire tissues. In the zebrafish embryo, the enveloping cell layer, an epithelial monolayer of cells on the outer surface of the embryo, spreads around the yolk. The small region of yolk just beyond the spreading cells, known as the yolk syncytial layer, was found to be enriched with actomyosin, which also appears to flow in the opposite direction of cell spreading. This exerts forces against the exterior shell of the embryo through a flow-friction mechanisms similar to that of amoeboid movement. Taken together, these examples demonstrate how cortical flows are an important mechanism of cell behavior across a variety of cellular processes in a diversity of species. This range of cellular behaviors is accomplished with the same core mechanism of actomyosin cortical flows. Understanding how these flows arise and are regulated is key to advancing our understanding of their roles in these processes.

To begin to understand how the actomyosin cortex gives rise to cortical flows, we need to synergize knowledge from two distinct scales: the molecular components involved and macroscopic behavior of flows. The molecular components, actin and myosin and crosslinkers, are fairly well understood, but it hasn't been clearly demonstrated how they produce the emergent behavior of cortical flows. A theoretical model exists that explains how long range flows could occur, but it does not take into account the behavior of the molecular players. Ideally, we would like to merge these ideas into a molecular scale model that could be used to derive macroscopic observations. In particular, this model would be composed of polymers and motors that can produce macroscopic flow. The model will need to be capable of generating a domain of contraction as well as a domain of passive resistance. The contracting region will need to persistently deliver force in proportion to the amount of motor activity while the passive side undergoes continuous deformation. The challenge is to understand how macroscopic properties arise from and are controlled by microscopic properties.

This is important for understanding biological functions of cortical flow, but it is also fundamental challenge in soft matter physics that goes beyond biology.

The goal of this thesis is to connect the molecular players of the cortical cytoskeleton within a modeling framework that will allow me to derive a macroscopic theory of cortical flow consistent with previous work in the field [19]. For this research, I'm going to be explicitly limiting the complexity of the molecular model in order to make it tractable enough to derive the macroscopic theory. To do so, I will be making a number of key simplifying assumptions, which aim to balance the realistic behavior of cytoskeletal mechanics with a tractable simplified model. This work will allow me to shed new light on the molecular players that contribute to the physics underlying cortical flows.

1.2 Introduction to the Cortical Actomyosin Cytoskeleton

Decades of research have revealed a great deal about the cellular machinery that sets up and drives cortical flows: the cortical actomyosin cytoskeleton. The cortical actomyosin cytoskeleton is composed of a meshwork of actin filaments that are bound together by cross-linking proteins, and myosin mini-filaments each of which constantly turn over in cycles of polymerization, depolymerization and redistribution. This network serves to provide structural support to the cell, as well as generate and transduce mechanical force to carry out essential functions such as cellular shape change and migration. In the following sections, I will highlight the key structural components and biochemistry of the actomyosin cortex that enables it to drive cortical flows.

Actin Filaments Actin filaments are polarized semi-flexible polymers, composed of chains of actin monomers held together by reversible supramolecular bonds. Actin monomers can spontaneously polymerize in solution or they can be actively nucleated and elongated by factors such as formins, which give rise to long linear filaments, or the ARP2/3 complex, which gives rise to shorter branched networks such as those found in the lamellipodia [?]. Addition of monomers to the actin filament occurs preferentially

from one end of the filament known as the barbed (plus) end due to the difference in binding constants between ATP and ADP bound forms of actin monomers. The barbed end contains an abundance of ATP bound actin compared to the opposite end, known as the pointed (minus) end, which has a greater abundance of ADP bound actin. The binding constant between ATP bound actin monomers is greater than that between ADP bound actin, thus polymerization preferentially occurs from the barbed end and disassembly preferentially occurs from the pointed end. Assembly and disassembly from opposite ends of a filament causes a phenomenon known as actin treadmilling. During treadmilling, filaments are depolymerized from their minus ends as they grow from the plus end, which causes the filament to apparently translocate while turning over. Turnover can also be enhanced by regulators of depolymerization including cofilin and gelsolin [24]. These factors can sever filaments internally, creating new minus ends with ADP bound actin, which leads to a rapid depolymerization of the exposed ends. Experimental studies *in vivo* reveal that these mechanisms of depolymerization can result in rapid turnover of cortical actin filaments on timescales of 5 to 100 seconds, much faster than would occur through actin treadmilling alone [171, 63, 62, 31, 108].

The mechanical properties of the polymerized actin filament is that of a semi-flexible polymer, a polymer that has a non-negligible bending stiffness, giving rise to a persistence length, or a characteristic length, over which the filament will remain approximately straight. This causes the filament to have an asymmetric compliance, as filaments at their relaxed length are able to compress easily and buckle, while extension is more difficult. The physical theory of semi-flexible polymers plays an important role in my work and will discussed in greater detail in Section 1.4.1.

Actin Cross-linkers In cytoskeletal networks, the actin filaments are connected by small cross-linking proteins that physically bind the filaments together through reversible elastic attachments [117]. Importantly, these attachments are reversible meaning that they can bind and unbind on timescales on sub-second timescales [117]. There are many types of filament cross-linkers including filamin, a cross-linker that binds filaments into loose disorganized networks, and alpha-actinin, which binds fil-

aments into tight bundles [117]. These cross linking proteins enable actin networks to form a range of higher order structures that allow them to carry out a variety of functions within the cell. For example, fascin is the main cross-linking protein found in filopodia, where it arranges filaments into aligned bundles with the same polarity, such that all the filament extension will occur in the direction of the leading edge to drive the cell forward [174]. As another example, the leading edge of migrating cells also contains filamin A, which forms the branched networks of the lamellipod [39]. Finally, in the rear of a migrating cell, alpha actinin forms the tightly packed stress fibers that help in trailing edge retraction [227].

Cross-linked actin networks are crucial for regulating the deformation of cells. Network deformation and stress relaxation are thought to occur through the transient binding and unbinding of actin cross-linkers[6] *in vitro* [114]. To better understand this process, one can imagine two filaments that are lying parallel to one another and are bound together with two cross-linkers. If a force were applied to one of the filaments, the cross-linkers would stretch out to sustain the force between the filaments. But if one of those cross linkers was to unbind, then the filaments would be free to slide away from each other by a small amount. Then another cross-linker could come in and bind, and the process could be repeated over and over allowing these filaments to slip past one another, dissipating stress and allowing for large scale deformation. In this way, the transience of filament binding can allow for network deformations to persist permanently and not return elastically to their initial state. The physics of semiflexible networks with transient cross-links is discussed in greater detail in Section 1.4.1.

Myosin Molecular Motors Interspersed among the actin filaments are myosin motors, which not only bind together and connect multiple filaments (functioning as an effective cross-linker), but also exert local forces on the actin [41]. Myosin II is a hexamer composed by joining two 3-mers of myosin heavy chain, myosin essential light chain, and myosin regulatory light chain. This complex is able to generate force by undergoing ATP hydrolysis of the heavy chain, driving a conformational change known as the power stroke. The cycle of binding and exerting force on actin,

referred to as its duty cycle (akin to that terms usage in a macroscopic machine), can vary depending on the specific biochemistry of the myosin isoform. The cycle involves binding actin, a conformational change of the head domain, and releasing actin. When myosin binds to actin it does so in an orientation such that the power stroke can only occur toward the pointed end of the filament. A single myosin attached with one head to an actin filament will therefore propel itself in the direction of the barbed end when it undergoes the power stroke. Although some myosins are capable of walking processively because the binding phase of the motor is relatively long, myosin II is not processive as a lone hexamer due to the short period of attachment in its duty cycle. However, individual myosin II motors polymerize together into bundles called myosin mini-filaments [41], which may together walk processively. These mini-filaments polymerize into bipolar bundles via antiparallel interactions of their coiled-coil tails, such that one set of heads points in one direction and the other set of heads points in the other direction. These bipolar bundles of motor heads can then interact with multiple actin filaments at once to exert force on the network [16]. Two important features of this motion are the gliding speed and the stall force. The gliding speed is the speed of free myosin minifilaments walking unencumbered, which depends largely on the speed of the motor duty cycle and the myosin step size. The stall force is the force that must be applied to prevent the myosins from walking, which arises from the minimum force required to prevent the rotation of the motor head domain during the power stroke. These two features of myosin force generation make up two extremes of what is known as the myosin force-velocity curve, a measurement of the inverse relationship between the velocity of myosin motion and the force applied to prevent its motion. This force velocity curve is a key metric used to understand the levels of force that a given myosin mini-filament can exert.

1.3 A physical view of cortical flow

Local forces produced by bipolar myosin filaments are integrated within cross-linked networks to build macroscopic contractile stress[148, 14, 89]. At the same time, cross-linked networks resist deformation and this resistance must be dissipated by

network remodeling to allow macroscopic deformation and flow. Since the molecular components of the cytoskeleton have now been identified and characterized in great detail, the next great challenge is to integrate these molecular properties into a model that can help us understand how they give rise to macroscopic shape change events, such as cortical flow[1].

One successful approach to modeling cortical flow has relied on coarse-grained phenomenological descriptions of actomyosin networks as active fluids, whose motions are driven by gradients of active contractile stress and opposed by an effectively viscous resistance[138]. Active contractile stress constitutes an effective internal negative pressure of a material, one that pulls inward on surrounding material due to the forces generated within the body of the active material. In the context of biological systems this active stress is thought to arise predominantly by cellular mechanism of ATP hydrolysis, such as myosin or kinesin motor activity or actin polymerization at the leading edge of a cell. In these models, spatial variation in active stress is typically assumed to reflect spatial variation in motor activity and force transmission[19]. The internal viscous resistance is assumed to reflect the internal dissipation of elastic structure due to local remodeling of filaments and/or cross-links[179, 44]. This gives rise to an effective viscosity, which (similar to regular viscosity) sets the degree to which forces are able to produce viscous deformations in the material. Additionally, as active fluids are often considered to be embedded in some surrounding system, some models also propose an effective frictional resistance between the active fluid and the medium in which it is embedded. Since effective viscosity acts to transmit material forces and external friction acts to dampen force transmission, The ratio of the effective viscosity to the external friction gives rise to a hydrodynamic length scale over which forces dissipate. Experimental evidence has suggested that this frictional resistance may be minimal, giving rise to a hydrodynamic length scale on the order of tens of microns [138], which would indicate that internal forces should persist over the length scale of entire cells.

Models combining an active fluid description with simple kinetics for network assembly and disassembly, can successfully reproduce the spatiotemporal dynamics of cortical flow observed during polarization [138], cell division [205, 178], cell motility

[98, 134] and tissue morphogenesis [12]. For example, in the developing *C. elegans* embryo, an initial small asymmetry in stress of the actomyosin cortex is magnified by cortical flow to produce a global polarized cell[145]. Experiments performed in [138], along with an active fluid model, showed that the appearance of this phenomenon was dependent on a gradient in active stress to drive flow and a sufficiently large effective viscosity to produce long range flows. This global polarization from mechanical flow constitutes a mechanism of macroscopic pattern formation beyond the conventional Turing reaction-diffusion mechanism[84].

It remains a challenge to connect this coarse-grained description of cortical flow to the molecular origins of force generation and dissipation within cross-linked actomyosin networks. To understand how cells exert physiological control over cortical deformation and flow, or how to build and tune networks with desired properties *in vitro*, it is essential to connect the theoretical understanding of flow to the molecular players involved. Both active stress and effective viscosity are sensitive to microscopic parameters including densities of filaments, motors and cross-links, force-dependent motor/filament interactions, cross-link dynamics, and network turnover rates. Thus a key challenge is to understand how tuning these molecular parameters controls the dynamic interplay between active force generation and passive relaxation to control the dynamics of cortical flow.

1.4 Determinants of passive viscoelasticity in actin networks

Cross-linked networks of semi-flexible polymers are a class of materials with highly interesting properties. Early studies of semi-flexible polymer networks reconstituted *in vitro* revealed novel, nonlinear rheology, spurring interest from materials scientists[27]. Additionally, cross-linked networks of cytoskeletal polymers have been a subject of great interest to biologists because of their importance as structural components of cells[61, 180]. On shorter timescales, the response of cross-linked polymer networks to applied stress can be well-described theoretically in terms of purely elastic mechanical resistance. On longer timescales, the network's elastic resistance begins to

give way to a viscous relaxation of stored stress, but the mechanisms that govern this viscous relaxation remain poorly understood. It is important to understand the mechanism behind this long timescale relaxation of cross-linked polymer networks to explain their novel material properties as well as how this effect may govern cellular processes[191]. For *in vitro* reconstitutions, this viscous relaxation is thought to result from transient unbinding and rebinding of intermolecular cross-links[212, 26]. Theoretical [26, 143] and computational [101, 116, 113] studies reveal that cross-link unbinding can endow actin networks with complex time-dependent viscoelasticity. However, while cross-link unbinding is sufficient for viscous relaxation (creep) on very long timescales *in vitro*, it is unlikely to account for the rapid cortical deformation and flow observed in living cells [212, 115, 116, 225, 120]. Studies in living cells reveal fluid-like stress relaxation on timescales of 10-100s [138, 82, 22, 83, 56, 11], which is thought to arise through a combination of cross link unbinding and actin filament turnover [44, 43, 179]. Actin filament turnover is thought to play a role in allowing a more rapid remodeling of filament networks than is possible with cross-link unbinding alone[171], and perturbing turnover can lead to changes in cortical mechanics and in the rates and patterns of cortical flow[209, 62].

1.4.1 *Short Timescale Mechanics of Cross-linked Actin Filament Networks*

Early *in vitro* studies of cross-linked actin filament networks revealed strikingly different elastic behaviors compared to the already well-understood flexible polymer gels [198]. The complexity of these behaviors drove a surge in both experimental and theoretical studies of semi-flexible networks of which cross-linked actin is a prime example. For a comprehensive review of this field we recommend [27], but we will shortly repeat some important milestones here.

Diversity and discrepancy in observations led a drive toward systematic *in vitro* experimental explorations of the rheology of cross-linked semi-flexible polymer networks at short timescales. In studies with rigid irreversibly cross-linked networks, it was found that differences in network structure could lead to remarkably different

elastic moduli, suggesting distinct phases of mechanical response [70]. These discoveries in turn begat theoretical work on the basic implications of the semi-flexible nature of filaments on network mechanics.

Prior work on the basic physics of individual semi-flexible polymers [135, 50], and comprehensive theories of semi-flexible filament solutions, [141] laid a groundwork for theoretical considerations of cross-linked networks. Beginning with the so-called mikado model descriptions[78, 221], it was determined that there should exist a minimum rigidity percolation threshold, and that the connectivity of the network determined whether the mechanical response was dominated by non-affine bending or affine stretching of filaments. The mechanics of rigidly cross-linked networks were shown to be well-described in terms of purely elastic stretching of filaments between cross-linked points[192].

Incorporating Effects of Cross-link Compliance

Despite the success of the theory[192] for networks with rigid cross-links, this was not sufficient to account for all the mechanical properties of the networks. Early studies showed that surprising qualitative differences in mechanical response could be traced to differences in the chosen cross-linker[215, 118]. In addition, many studies using more compliant cross-linkers showed that cross-linker compliance could give rise to different nonlinear rheological properties on short timescales[68, 69, 96, 119]. Making matters even more complicated, ongoing research has begun to uncover added complexity from issues such as filament bundling[143, 40]and active cross-linking by molecular motors[102]. Theorists have now built a number of largely successful models that help characterize different aspects of the cross-link dominated response[80, 223, 25].

1.4.2 Long Timescale Stress Relaxation from Transient Cross-link Unbinding

The importance of cross-link dynamics in generating a viscous stress relaxation in semi-flexible polymer networks has been known for at least 20 years[212]. At long

timescales, the purely elastic behavior of cross-linked networks gives way to fluid-like stress relaxation. Additionally, fluid-like flows have been observed in a number of cellular processes[138, 82, 22, 83, 56, 11]. In *in vitro* studies, long timescale creep behaviors are thought to arise predominantly from the transient nature of filament binding for most biologically relevant cross-linkers[115, 116, 225, 120].

The dependence of network rheology on cross-link unbinding is an active subject of theoretical research[143]. Several theoretical methods have addressed cross-link binding and unbinding directly in analytical approaches that allowed well-constrained fits for specific cross-linkers [26, 143]. These theories have focused conceptually at the level of the cross-linked filament and were extended analytically to macroscopic networks. In another approach, modelers have taken cross-links as extended springlike structures [101] that are able to bind and unbind in simulated filament networks. Finally, other more ambitious simulations have even sought to interrogate the effects of cross-link unbinding in combination with the more complex mechanics of filament bundles[116, 113]. However, rheological studies of stress relaxation in actin filament networks suggest that crosslink dynamics are not sufficient to simultaneously relax and transmit stress at the rates observed in cells[44].

Cross-link Slip Approach to Incorporating Cross-link turnover

As a final point, I wish to mention a few previous attempts to incorporate a coarse-grained representation of filament cross-linking in which cross-linked filaments are able to slide past each other as molecular bonds form and rupture, akin to coarse-grained models of molecular friction[210, 190, 60]. This drag-like coupling has been shown to be an adequate approximation in the case of ionic cross-linking of actin[214, 33], and can be found in the theoretical basis of force-velocity curves for myosin bound filaments[10]. Although, this cross-link slip formulation has not yet been used directly to model the effects of cross-linkers on network mechanics, I propose that it will form a suitable bulk approximation in the presence of supra-molecular cross-links as well.

1.4.3 Elucidating the Importance of Filament Turnover

The fundamental importance of actin filament turnover in setting the mechanical properties of a cell has been known to biologists for decades [37]. Nevertheless, theoretical investigators have only begun to explore the role of turnover quite recently [81, 133, 231] (see the final chapter of this thesis for a comparison of my results with these recent publications). A major factor contributing to the slow advancement of our understanding of the role of turnover in cell mechanics is the difficulty in experimentation. However, recent advances in experimental techniques of reconstituted systems should make turnover a viable avenue of study in the near future.

Another major factor preventing the advancement of our understanding of the impact of turnover on cell mechanics and dynamics is the complexity already inherent in our computational models of polymer systems at many length and time scales[132]. For this work I wish to accelerate the interest in filament turnover as a fundamental contributor to cellular mechanics. To do so, I will deemphasize the particularities of the polymer and cross-linker models and create a simplified generic model. With this simplified model we will then be in a position to analyze the fundamental role of filament turnover.

1.5 Origins of contractility in disordered contractile networks.

How force production and dissipation depend on motor activity and network remodeling remains an active subject of study. While it has been made clear in recent work [138], which described the buildup of tension along the A-P axis of a developing *C. elegans* embryo, that myosin force generation is crucial for driving flows, the exact mechanism by which actin and myosin can generate force in two dimensions is only beginning to be elaborated in detail[109]. Therefore, it is unclear whether we fully understand the mechanism by which force is generated to drive cortical flows. More recent work [133] has begun to suggest that dynamic filament turnover may be necessary for sustaining stress on the timescales observed in cells. All of these issues

lead to the conclusion that there is still more to be learned about the exact nature of cortical flow in cells.

The role of actin and myosin in the contraction of muscle cells has been known since the 1950s[85?]. In muscle cells, actin and myosin are aligned into arrays of sarcomeres, structures where rows of actin thin filaments intercalate with myosin thick filaments[86]. This sarcomeric alignment gives rise to a global ordering that enables muscle contraction. During a contraction, myosin motor activity pulls actin thin filaments from both ends of the myosin thick filament towards the center. This shortening leads naturally to a contraction along the axis of the filaments. Since each sarcomeric array is connected to its neighbors, contraction of each unit allows this micron scale shortening to extend to the length of the entire muscle tissue and generate large scale motion. This mechanism is well understood and has been extended to other contractile elements. In particular, recent work has shown that sarcomere-like structures also appear in stress fibers in motile cells [95], generating local contraction in cells lacking a global sarcomeric structure.

To understand active stress generation in completely disordered actomyosin networks, however, is more difficult. The difficulty in understanding contraction in a disordered 2D network arises from the inherent symmetry in myosin contractility. Based on the description of myosin mini-filament activity given in section ??, we know that the direction in which the myosin generates force is dependent solely on the orientation of the actin filaments with which it is engaged. Therefore, in a disordered network (where filaments are isotropically distributed with no global alignment), individual myosins will not exert their forces in any concerted direction. When averaged together the net contribution of the individual motors will approximately cancel out, causing there to be as much extensile force as contractile force in a network. Therefore, the network should not be able to generate force or contract to any appreciable degree.

Nevertheless, disordered actomyosin networks do contract, and this contraction is thought to be due to more subtle mechanical properties. Theoretical studies suggest that spatial heterogeneity in motor activity along individual filaments, and asymmetrical filament compliance (stiffer in extension than in compression), are sufficient for

macroscopic contraction [110, 109], although other routes to contractility may also exist [109]. In [110], Lenz and co-authors explored the mechanisms of contraction in greater detail by exploring idealized linear contractile elements in a 1D bundle model. In this model, the authors subdivide their bundle into small interacting units which can deform according to a filament force-extension relationships and a motor force-velocity relationships. They showed that motors had to present a large enough variation in force differences such that they could probe the nonlinear force-extension of the actin filaments, and that filaments had to exhibit nonlinear force-extension with a weaker compressional modulus than extensional. This allowed the bundle to preferentially contract because the filament force-extension allowed greater deformation in the contracting direction than in the extending direction.

In vitro studies have shown that local interactions among actin filaments and myosin motors are sufficient to drive macroscopic contraction of disordered networks [149]. The kinematics of contraction observed in these studies supports a mechanism based on asymmetrical filament compliance and filament buckling. However, in these studies, the filaments were preassembled and network contraction was transient, because of irreversible network collapse[8], or buildup of elastic resistance[147], or because network rearrangements (polarity sorting) dissipate the potential to generate contractile force [54, 169, 154, 194]. This suggests that network turnover may play an essential role in allowing sustained production of contractile force. Recent theoretical and modeling studies have begun to explore how this might work [81, 133, 231]. Studies are also beginning to explore dynamic behaviors that can emerge when contractile material undergoes turnover [178, 47]. (For a more in depth discussion of these recent studies and how they relate to the work in this thesis, see the Conclusions section.) However, it remains a challenge to understand how force production and dissipation depend individually on the local interplay of network architecture, motor activity and filament turnover, and how these dependencies combine to mediate tunable control of long range cortical flow.

1.6 Goals of Thesis: Bridging the Theoretical Gap Between Active Fluids and Polymer Models

The goal of this work is to build a computational bridge between the microscopic description of cross-linked actomyosin networks and the coarse grained macroscopic description of an active fluid. We seek to capture the essential microscopic features (dynamic cross-links, active motors, semi-flexible actin filaments with asymmetric compliance, and continuous filament recycling), but in a way that is sufficiently simple to allow systematic exploration of how parameters that govern network deformation and flow in active fluid theory depend on microscopic parameters. To this end, we introduce several coarse-grained approximations into our representation of filament networks. First, we represent semi-flexible actin filaments as simple springs with asymmetric compliance (stronger in extension than compression). Second, we replace dynamic binding/unbinding of elastic cross-links with a coarse-grained representation in terms of molecular friction [210, 190, 60], such that filaments can slide past each other against a constant frictional resistance. Third, we used a scheme similar to that used for cross-links to introduce active motors at filament crossover points with a simple linear force/velocity relationship. We introduce dispersion of motor activity by making only a subset of filament overlaps active [10]. Finally, we model filament turnover by allowing entire filaments to appear and disappear with a fixed probability per unit time. Importantly, these simplifications allow us to extend our single polymer models to dynamical systems of larger network models for direct comparison between theory and modeling results. This level of coarse graining will therefore make it easier to understand classes of behavior for varying compositions of cross-linked filament networks. In addition, it allows us to compute a new class of numerical simulations efficiently, which gives us concrete predictions for behaviors in widely different networks with measurable dependencies on molecular details.

We use this model to probe three areas of interest. First we characterize the passive response of a cross-linked network to externally applied stress. Second we examine the buildup and maintenance of active stress against an external resistance. And finally we characterize the steady state flows produced by an asymmetric distribution of

active motors in which active stress and passive resistance are dynamically balanced across the network. Our results reveal how network remodeling can tune cortical flow through simultaneous effects on active force generation and passive resistance to network deformation.

CHAPTER 2

SINGLE MOLECULE MEASUREMENTS OF ACTIN

FILAMENT TURNOVER

2.1 Preface

This chapter has been submitted to Nature Methods with the following citation:
Franois B Robin, William M McFadden, Baixue Yao, and Edwin M Munro. Single-molecule analysis of cell surface dynamics in *Caenorhabditis elegans* embryos. 11(6):677682, June 2014.

This work was done in collaboration with François Robin and Baixue Yao in Edwin Munro's lab at the University of Chicago. François and Baixue performed the majority of the experiments and analysis. My contribution consisted of three parts outlined in the following sections.

2.1.1 Fitting algorithm for SMPeSS

The SMPeSS technique works by fitting timecourses of counts of single molecules. The equation to which it is fit gives estimates of the model parameters. Francois Robin and I worked to devise the form of the model equation to be fit. Francois created one simplification for computation, and I found another one that was easier to use because it used fewer unique fitting parameters. I implemented the fitting function and implemented techniques to extract the error estimates from the curve fitting results in MATLAB. This code was delivered with the resulting paper.

2.1.2 Control experiments to determine the accuracy of SMPeSS

Using the SMPeSS technique, we believed it was possible to independently measure the disassociation constant and the photobleaching rate of the system. To test this,

Francois and I set out to systematically vary the laser intensity and determine if our fitting scheme found changes in the photobleaching rate, but not the disassociation constant. I collected and processed the majority of the data for these control experiments, which found, indeed, that the photobleaching rate varied linearly with laser intensity while the disassociation rate remained constant across different experimental conditions.

2.1.3 Taking the proper mean for Par-6 measurements

We wished to use measurements of Par-6 disassociation constants as a benchmark with which to compare our technique to prior measurement techniques used in literature. Originally, the group was taking a pure mean of single molecule lifetime over the total number of events, which led to an estimate of the lifetime that was far shorter than what had been measured previously by FRAP. Our measurements were confirmed numerous times, each with the same result.

The problem was that the mean was being taken wrong. In a given period of time, many more particles with a short lifetime will appear compared to relatively few with a long lifetime. Meanwhile if you were to observe at a single instance, there would be closer to an exponential distribution of short and long time events. Taking the average over a wide swath of time therefore, skews the measurement to including more and more short duration events while only counting the long duration events once (even though they appear in many time bins).

The correct way to take the mean is to weight the count of each event by the duration of the event. Another way to put this is that you want to add the mean of the long time over and over for every observed timepoint that you have. After I incorporated this correction, our measurement lined up with previous measurements for the disassociation constant for Par-6, and we were able to publish this result as a corroboration of our technique's validity.

2.2 Introduction

Dynamic remodeling of the embryonic cell surface is essential for the control of cell polarity, division, shape change and movement during early development. This remodeling involves the dynamic interplay of local exchange and movement of proteins that reside at the interface between the plasma membrane and the actin-rich cell cortex. However, quantifying these processes in embryonic cells remains a significant challenge. One promising approach is single molecule imaging combined with single particle tracking (SPT), which can yield quantitative measurements of local mobilities, binding states and exchange kinetics that are inaccessible to ensemble measurements [188, 196, 55]. Combining these approaches with powerful genetic tools in a classical model organism could be a powerful way to investigate subcellular dynamics in embryonic cells, but this has yet to be achieved.

One key limitation has been the lack of simple and reliable methods for tunable and non-invasive labeling of target molecules. Optimal labeling densities are different for each target and must balance the need for high-density sampling of molecular behavior in space and time against practical requirements for accurate and unbiased single molecule detection and tracking. Methods based on microinjection of fluorescently labeled probes [36, 3], or transfection using crippled promoters [152, 5, 4, 2] are cumbersome and inherently hard to optimize. Methods based on surface labeling of transmembrane proteins [129, 195, 91, 66] may be easier to tune, but cannot be generalized to intracellular targets. A more promising approach for intracellular targets uses genetically encoded photoswitchable fluorescent protein fusions to create a renewable supply of single molecules [176, 51, 107]. However, this approach does not report on spatiotemporal variations in density or assembly/binding kinetics of the endogenous protein. Moreover, its use in *C. elegans* would require de novo creation of a transgenic strain for each new target of interest.

Here we describe a simple, versatile and minimally invasive method for single molecule imaging at the cell surface in *C. elegans* embryos that can be applied to any of the large and growing collection of transgenic strains expressing GFP-tagged fusion proteins [127]. We combine sequence-specific inhibition of GFP transgene expression

with selective photobleaching and simple *in vivo* standards to achieve and verify single molecule densities of GFP-fusions over normal levels of the endogenous protein. We exploit the intrinsic exchange dynamics of surface-associated proteins to obtain long term (

>

5000 frames) sampling of single molecule trajectories at signal-to-noise ratios (SNR), frame rates and densities that can be optimized to measure local mobility and turnover for a given molecule. In particular, we show how these data can be used to extract quantitative information about surface density and turnover through two complementary methods: The first involves direct inference from single particle trajectories. The second method, which we refer to as smPReSS for single molecule Photobleaching Relaxation to Steady State, estimates turnover rates by fitting simple kinetic models to measurements of single molecule densities over time and is therefore insensitive to particle tracking errors. To demonstrate the power of this approach, we quantify spatiotemporal variations in mobility and turnover for the polarity protein Par-6 and for actin filaments during asymmetric cell division in the one-cell *C. elegans* embryo.

2.3 Results

2.3.1 Obtaining and verifying single molecule levels for any GFP fusion protein.

In *C. elegans*, a 200nm thick eggshell [57, 30] makes it difficult to image subsurface dynamics with true TIRF optics. To overcome this, we used near-TIRF illumination [128], optimizing laser angle and intensity to achieve ~even illumination across the field of view while maintaining adequate SNR for robust single particle detection and tracking (Fig. 2.1a; Supplementary Fig. 2.1; below and Supplementary Note 6). For any given transgenic strain expressing GFP fused to a target protein, we used a two-step method to achieve densities of GFP-tagged proteins suitable for single molecule imaging (Fig. 2.1b). First, we directed RNA interference (RNAi) against the GFP sequence to selectively reduce maternal expression of the transgene, yielding low levels

of GFP-tagged protein over normal levels of the endogenous protein. For more than a dozen strains tested, we could readily tune exposure times to obtain transgene expression levels at which diffraction limited-speckles could be observed at the cell surface by near-TIRF microscopy (Fig. 2.1c, bottom). In a second step, we used photobleaching to further reduce speckle densities (#speckles/m²) and mean speckle intensity towards single molecule levels (Fig. 2.1d), with no adverse consequences for cell viability (see Supplementary Note 4).

Next we established a general method to verify single molecule levels for any GFP fusion strain that can be readily extended across labs and imaging platforms. We focused on polarity maintenance phase in the one-cell embryo when the densities and distributions of many surface proteins are essentially stationary. Concentrating initially on a strain expressing GFP::Actin, we reduced transgene levels as above until the average intrinsic speckle intensity ($I_{int} = I_{speckle} - I_{background}$) reached a minimum value and the distribution of intensities was well-fit by a single Gaussian (Fig. 2.1d). Then we imaged at high laser power such that speckle disappearance was dominated by photobleaching, rather than disassembly. Under these conditions, the majority of disappearance events occurred in single-steps, confirming that the minimum intensity speckles we observe correspond to single GFP molecules (Fig. 2.1e). Strikingly, when we reduced expression levels in 5 other GFP fusion strains to minimize the mean speckle intensity, we measured speckle intensity distributions during maintenance phase that were indistinguishable from one another and from those measured for GFP::Actin under the same imaging conditions (Fig. 2.1f). Moreover, by fitting multiple Gaussians (for 1,2,N fluorophores/particle) to the distribution of I_{int} , we could readily detect when more than 5% of speckles contain multiple fluorophores (Fig. 2.1d, Supplementary Fig. 2.3a). Thus for any given strain, it is possible to pinpoint a characteristic speckle density below which a pure population of single molecules can be reliably observed, which can subsequently be used to calibrate single molecule imaging on other platforms.

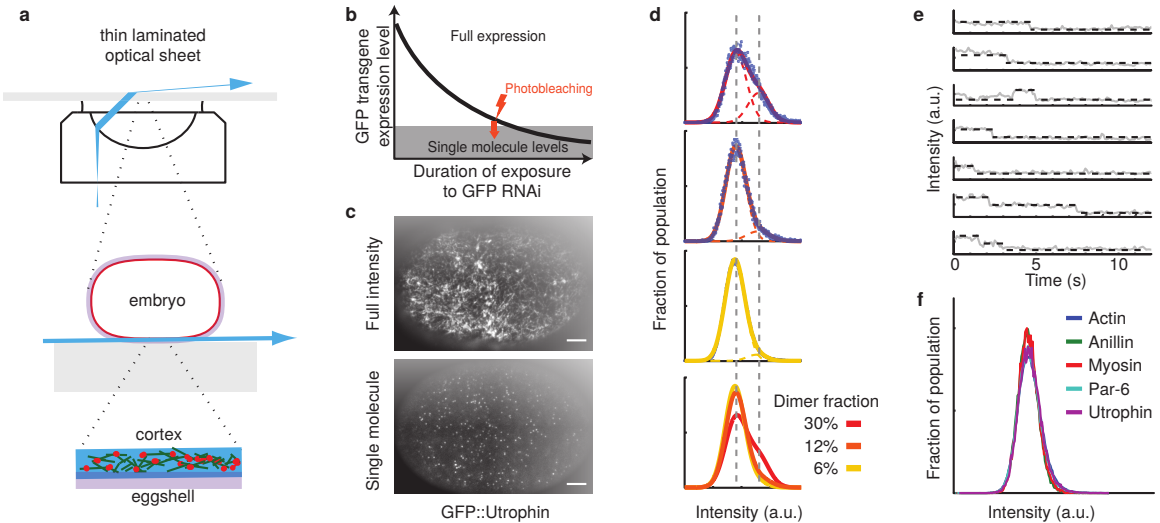


Figure 2.1: Imaging single molecules at the cortex in living embryos. (a-c) Schematic overview of the Near-TIRF imaging approach. (a) Top: Incident laser angle at the cover glass/specimen interface is tuned to create a thin and narrowly inclined laminar sheet (blue) of laser light. At cell (middle) and subcellular (bottom) scales, the laminar sheet is nearly parallel to the coverslip/specimen interface, and is thick enough to illuminate the entire cell cortex in the field of view. (b) Basic approach to achieve single molecule levels for any GFP-fusion strain in *C. elegans*, using a combination of RNAi against GFP and photobleaching. (c) Near-TIRF micrographs of a one-cell embryo expressing GFP::Utrophin showing full intensity and single molecule levels. Scale bar = 5 μ m. (d) Distribution of intrinsic speckle intensities (average particle intensity - local average background) in a strain expressing GFP::PAR-1 for a range of depletion levels. Fits to a sum of two Gaussians representing one and two-molecule speckles measure a decrease in the proportion of doublets from 12% to 5%. Bottom panel compares directly all three previous panels. Images were obtained using identical imaging conditions. (e) Direct verification of single molecule levels by single step photobleaching in an embryo expressing GFP::Actin. Multiple step photobleaching can be readily detected at higher expression levels (last two panels). (f) Intrinsic speckle intensity at low particle densities is essentially identical across all GFP strains tested.

2.3.2 Exploiting intrinsic exchange kinetics to achieve optimized sampling of single molecule mobility and turnover

We sought to exploit the intrinsic exchange dynamics of surface-associated proteins to create a self-renewing pool of GFP-tagged single molecules at the cell surface that could be followed over time to measure mobility and turnover. To establish a kinetic

basis for this approach, we consider a GFP-tagged protein that exchanges dynamically between the bulk cytoplasm and a region of the cell surface, which is observed by near-TIRF microscopy (Fig. 2.2a). The number of molecules $N(t)$ within this region over time is governed by:

$$\frac{dN}{dt} = k_{app} - (k_{off} + k_{ph})N \quad (2.1)$$

where k_{app} is an observable appearance rate that depends on the cytoplasmic concentration of GFP-tagged protein ($k_{app} = k_{on} Y$, where Y is the cytoplasmic concentration) and the nature of the binding process, and k_{off} and k_{ph} are pseudo-first order rate constants such that $k_{off} \times N$ is the rate (in molecules per second) at which particles disappear due to unbinding or disassembly, and $k_{ph} \times N$ is the rate (in molecules per second) at which they disappear due to irreversible photobleaching. (Fig. 2.2a). Prior to illumination, $k_{ph} = 0$ and the steady state density is $N_{ss} = k_{app}/k_{off}$. During illumination, k_{ph} becomes non-zero; if the cytoplasmic pool were infinite, the system would approach a new steady state density given by $N_{ssobs} = k_{app}/(k_{off}+k_{ph})$, which is a fixed fraction of the initial unobserved value (Fig. 2.2b). In practice, irreversible photobleaching will gradually deplete a finite cytoplasmic pool. A variant of the kinetic model that accounts for this depletion (see Supplementary Note 8) predicts a biphasic response to the onset of illumination: a fast relaxation towards $\sim N_{ssobs}$, followed by a slower decay towards 0, at a rate which depends on the photobleaching rate and the size of the cytoplasmic pool (Fig. 2.2b). For a given target molecule, k_{off} is fixed. However, k_{ph} depends on imaging conditions (i.e. the intensity and duty ratio of the laser illumination, while k_{app} can be adjusted by tuning the initial size of the GFP-tagged pool. Thus by co-tuning these factors, it should be possible to target a desired density at quasi-steady state for a range of imaging conditions.

To test this approach, we chose two representative strains expressing GFP::Actin and PAR-6::GFP. Actin monomers exchange dynamically with the cell surface through local filament assembly and disassembly, and based on previous work, we expected GFP::F-Actin to be relatively immobile at the cell surface and to turn over in a

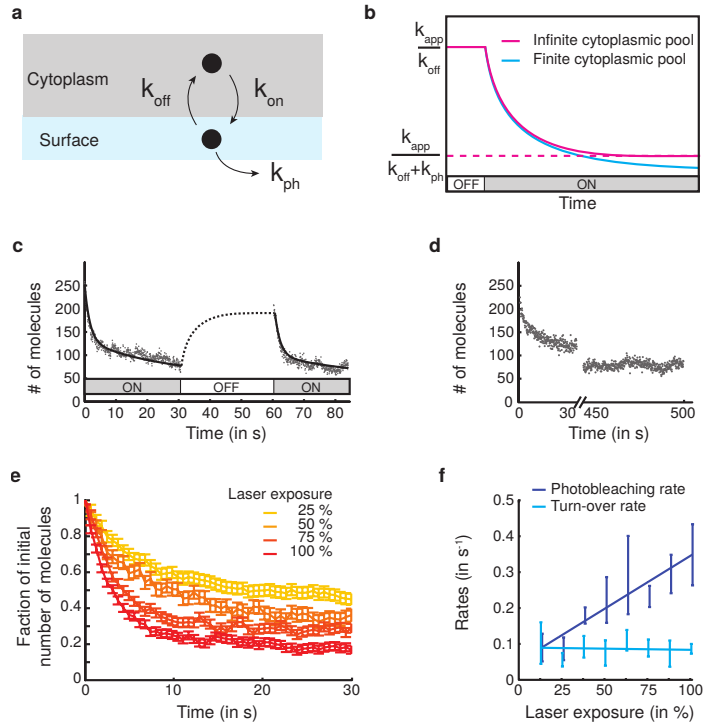


Figure 2.2: Exploiting dynamic exchange between cytoplasm and cell surface to obtain long-term tunable and high-density sampling of single molecule behaviors. (a) The basic kinetic principle: During imaging, the level of surface-associated proteins is set by a dynamic balance of: appearance (binding or assembly) at an observable rate k_{app} , disappearance (unbinding or disassembly) at a per-molecule rate k_{off} , and photobleaching at a per molecule rate k_{ph} . (b) The predicted response of an initially unobserved cell at steady state to a step change in illumination. For an infinite cytoplasmic pool (cyan), the surface density relaxes to a new illuminated steady state. For a finite cytoplasmic pool (blue), fast relaxation is accompanied by a slower decay caused by irreversible photobleaching. (c) Biphasic response for GFP::Actin under illumination conditions that allow accurate single molecule detection and tracking. (dots) real data; (solid line) model fit; (dashed line) discontinuous jump from $t = 30\text{s}$ to $t = 450\text{s}$. (d) The fast relaxation to a quasi-stable density during illumination is rapidly reversed when the laser is turned off. (e) Surface density vs time at various laser exposures, shown as a fraction of the initial unobserved density. Error bars indicate standard error of the mean ($n=7,9,6,7$). (f) Estimates of per molecule disappearance (k_{off}) and photobleaching (k_{ph}) rates as a function of laser exposure. Error bars indicate standard deviation, ($n=12,7,8,9,7,6,7,7$). Solid lines show a linear regression against the data. k_{ph} increases linearly with laser exposure, while k_{off} remains constant. 100% laser power $\sim 1.6\text{W/m}^2$.

few 10s of seconds (see [67] for review), while fast-diffusing monomers of GFP::Actin should produce highly blurred images and thus escape detection under our imaging conditions [152]. Par-6 is a conserved polarity protein that binds dynamically to sites on the plasma membrane [126, 224, 170] and recent FRAP measurements suggest that it diffuses rapidly at the cell surface and dissociates very slowly, with an effective dissociation rate constant $k_{off} = 5.4 * 10^{-3} \text{ s}^{-1}$ [155]. Focusing again on polarity maintenance phase, we reduced densities to single molecule levels, allowed the system to equilibrate unobserved, and then recorded data for a range of laser intensities and exposure times (Fig. 2.2c-e, Supplementary Fig. 2.3b). For both strains, we observed the predicted biphasic response to a step change in illumination - a rapid initial decrease in the number of molecules to a quasi-stable value followed by slower decay (Fig. 2.2c,d, Supplementary Fig. 2.2,3a, also Supplementary Video 1). Importantly, the initial decrease was reversed with equally rapid kinetics when the laser was turned off (Fig. 2.2c) confirming that the quasi-steady state is set by a dynamic balance of exchange and photobleaching. For both strains, we could therefore obtain robust estimates for effective dissociation and photobleaching rate constants k_{off} and k_{ph} , by fitting the predicted biphasic kinetics to the change in single molecule density over time; for each strain, we optimized fitting conditions by adjusting laser exposure (intensity and duty ratio; see below and Supplementary Note 9). As expected, estimates of k_{ph} varied linearly with laser exposure while estimates of k_{off} remained fixed over a range of exposures (Fig. 2.2f). Significantly, our estimates of k_{off} for Par-6 in the anterior cortex ($k_{off} = 7.4 * 10^{-3} \text{ s}^{-1}$) are consistent with those previously obtained by FRAP ($k_{off} = 5.4 * 10^{-3} \text{ s}^{-1}$, [155]). We refer to this approach as smPReSS for single-molecule Photobleaching Relaxation to Steady State. Because smPReSS relies directly on counting single molecules, it is relatively insensitive to non-specific fluorescence and can be applied at very low fluorophore densities that would be inaccessible using ensemble methods like FRAP and its variants. Moreover, because it does not rely on particle tracking, it is insensitive to particle tracking errors.

Next, we assessed the potential for long-term high-density sampling of single molecule trajectories, as previously achieved with photoswitchable fluorophores. To this end, we set laser intensities to ensure signal-to-noise ratios and frame rates suit-

able for robust particle tracking using standard SPT algorithms and software (Supplementary Video 1-3, [207, 90], Supplementary Note 6, Supplementary Table 1). Under these conditions, we measured effective photobleaching rate constants $k_{ph} \sim 0.1 \text{ s}^{-1}$ for GFP::Actin and $k_{ph} \sim 0.3 \text{ s}^{-1}$ for PAR-6::GFP, resulting in less than 30% loss in density over 5000 frames (Fig. 2.2d, Supplementary Fig. 2.2, 3a). When we pre-tuned the initial size of the cytoplasmic pool to optimize quasi-stable densities towards maximal values consistent with robust SPT, we were able to recover for GFP::Actin (resp. PAR-6::GFP) $\sim 30,000$ (resp. $\sim 7,500$) individual trajectories over the 5000-frame interval, with an average duration of 35 (resp. 15) frames, and ~ 5000 (resp. ~ 250) trajectories lasting longer than 80 frames. We observed comparable results with several other strains (data not shown). Thus, the intrinsic exchange dynamics of GFP-tagged proteins can be exploited to achieve continuous long-term single molecule imaging, and these imaging conditions can be tuned to optimize single particle tracking analysis or estimates of bulk turnover by smPReSS.

2.3.3 SPT analysis reveals distinct classes of Par-6 mobility during maintenance phase

The ability to rapidly sample large numbers of individual trajectories makes it possible to analyze surface dynamics during well-defined and short-lived windows of developmental time. To illustrate this, we tracked local movements of PAR-6::GFP molecules at the cell surface during maintenance phase in one-cell embryos. To get a rough classification of Par-6 mobilities, we measured mean-square-displacement (MSD) vs lag time for 1086 trajectories with lifetimes larger than 80 frames (Fig. 2.3a,b). Then we fit the first 10 time points to $\text{MSD} = 4D\alpha$ to estimate the anomalous diffusion exponent α and a short-term diffusivity D. This analysis revealed what appears to be at least two distinct mobility classes (Fig. 2.3b,c, Supplementary Video 1,4,5). Approximately 43% of Par-6 molecules undergo what appears to be simple diffusion, with $0.9 < \alpha < 1.2$ and short term diffusivity $D = 0.17 \text{ m}^2\text{s}^{-1}$ (red traces and dots in Fig. 2.3b,c), which is comparable to previous measurements by FRAP ($0.28 \text{ m}^2/\text{s}$, 25). Another $\sim 22\%$ of Par-6 molecules undergo what appears to be slower sub-diffusive

motion, with $\alpha < 0.6$ and short term $D = 0.008$ (blue traces and dots in Fig. 2.3b,c). The remaining 35% of the tracks undergo intermediate behavior, with short term $D = 0.057$ for $0.6 \leq \alpha \leq 0.9$ (gray traces and dots in Fig. 2.3b,c). Simulating Brownian diffusion for 177 particles with diffusivities chosen randomly from the range $D = 0.15$ m².s⁻¹ and then analyzing trajectories as above reproduced a distribution of short term D and alpha values very similar to the distribution observed for the subset of real particles with $0.9 < \alpha < 1.2$ (Fig. 2.3d). In contrast (and as expected) for no values of D did simulated Brownian diffusion reproduce the class of trajectories for $\alpha < 0.6$ observed for single molecules of Par-6 (Supplementary Fig. 2.4). These observations are consistent with previous studies documenting two populations of Par-6, punctate and diffuse, with distinct localizations and genetic requirements, and which likely reflect different binding modes and binding partners for Par-6 [126]. Further analyses combining the sampling methods introduced here with e.g. Bayesian trajectory analysis [151, 58] and genetic manipulation should yield further information about these different binding states and their regulation.

2.3.4 Measuring spatial and temporal variations in density and turnover

A key advantage of our approach is that the GFP-tagged proteins sample the same kinetics as the underlying pool. Thus, they report not just on mobilities, but also on spatiotemporal variation in densities, appearance rates (k_{app}) and per molecule turnover rates (k_{off}). In principle, k_{app} and k_{off} can be measured either directly from single molecule trajectories or by smPReSS as described above. However practical considerations constrained the choice of method as illustrated by analysis of Par-6 turnover during polarity maintenance and actin turnover during cell division.

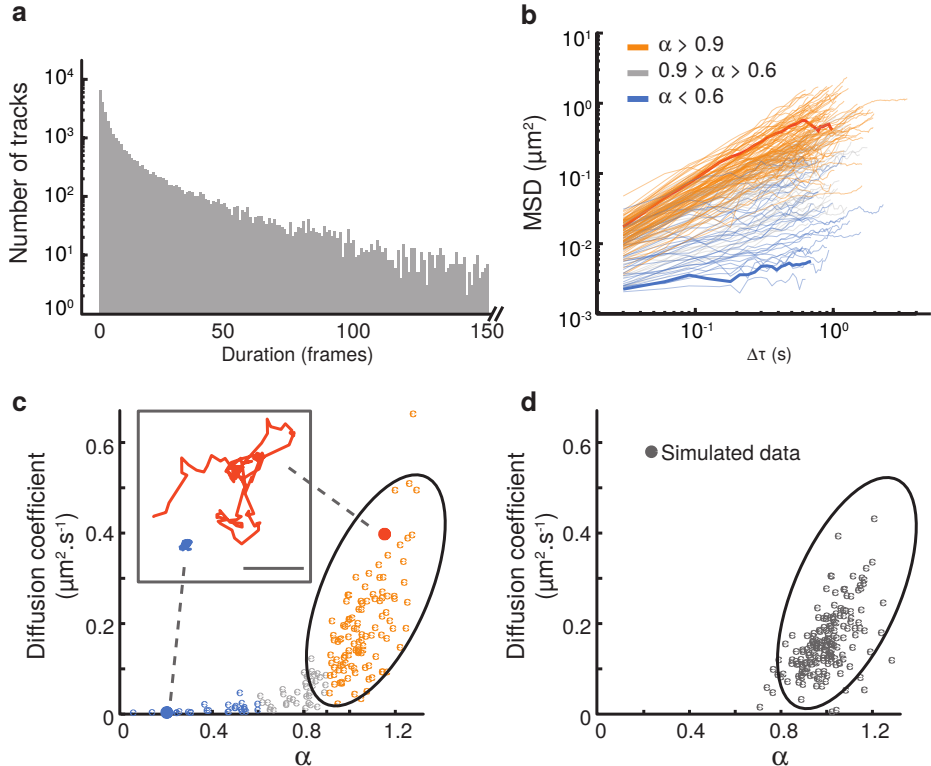


Figure 2.3: Analysis of PAR-6::GFP mobility during maintenance phase (a) Distribution of track lengths for 30,558 tracks from $n = 5$ movies taken in one-cell embryos during maintenance phase. (b) Log/log plot of MSD versus lag time ($\Delta\tau$) for all 177 tracks with length ≥ 80 frames extracted from one of the movies, reveals what appears to be a mixture of brownian and anomalous diffusion. Traces have been assigned colors based on slope (α): (blue) $\alpha < 0.6$; (grey) $0.6 < \alpha < 0.9$; (orange) $\alpha > 0.9$ (c) Scatter plot of diffusion coefficient D versus exponent α , measured by fitting $\text{MSD} = 4D\Delta\tau^\alpha$ for the first 10 lag times of the tracks shown in (b), with (blue) $\alpha < 0.6$; (grey) $0.6 < \alpha < 0.9$; (orange) $\alpha > 0.9$. Inset shows two particular trajectories drawn from opposite ends of the scatter plot and indicated by colored circles. Scale bar, 1m. (d) Scatter plot for 177 trajectories obtained by simulating pure brownian diffusion for 80 frames with $D = 0.15 \pm 0.05 \text{ m}^2.\text{s}^{-1}$ and measuring D and α as in (c). (lines) simulated tracks. Note the close match to experimental data for $0.9 < \alpha < 1.2$, but the failure to match points at the bottom left (low D and α).

2.3.5 Measuring spatial variation in Par-6 turnover during maintenance phase.

Par-6 is highly enriched at the anterior cortex in polarized one-cell embryos. These differences are thought to be caused by more rapid dissociation of Par-6 in the pos-

terior [29]. However, anterior vs posterior differences in dissociation rate cannot be detected by conventional FRAP analysis because the densities of Par-6 in the posterior are too low. Unfortunately, the photobleaching rates ($k_{ph} \sim 0.3 \text{ s}^{-1}$) required for accurate particle tracking are ~ 40 -fold higher than the dissociation rates ($k_{off} = 7.4 * 10^{-3} \text{ s}^{-1}$) measured by smPReSS. Thus resolving A vs P differences in turnover by particle tracking would be difficult or impossible because photobleaching will dominate small differences in k_{off} . Instead, we exploited the tunability of our approach, setting laser exposure and image acquisition (100% laser, 30ms exposure at 1 second intervals) to maintain accurate detection while reducing photobleaching rates to $k_{ph} \sim 0.005$. Under these conditions, smPReSS yielded robust estimates of k_{off} for anterior and posterior regions. Combined with measurements of relative density, this allowed us to infer relative values for k_{app} . Interestingly, our results suggest that the majority of the A vs P difference in density is due to differences in recruitment rates, consistent with the enrichment of several known binding partners for Par-6 (Cdc-42 and Par-3) at the anterior [105, 126].

2.3.6 Spatiotemporal modulation of actin assembly and turnover during cell division

As a second example, we measured spatiotemporal modulation of actin assembly and disassembly during the first cell division (Fig. 2.4a, Supplementary Video 2,3). Both actin assembly and disassembly are thought to be modulated during cytokinesis [197], but their relative contributions to actin filament accumulation are not well understood. We performed these experiments in embryos depleted of non-muscle Myosin II to remove the confounding effects of surface deformations and flow and remove myosin-dependent effects on turnover [55, 36]. We verified strong depletion of Myosin II by the complete failure of cytokinesis and a complete absence of local surface deformation and cortical flow during early anaphase. In the case of GFP::Actin, the turnover rates measured by smPReSS ($k_{off} \sim 0.1 \text{ s}^{-1}$) were similar to the photobleaching rates ($k_{ph} \sim 0.1 \text{ s}^{-1}$) required for accurate particle tracking, and agreed well with estimates of k_{off} from particle tracking (Fig. 2.4b; Supplementary Fig. 5),

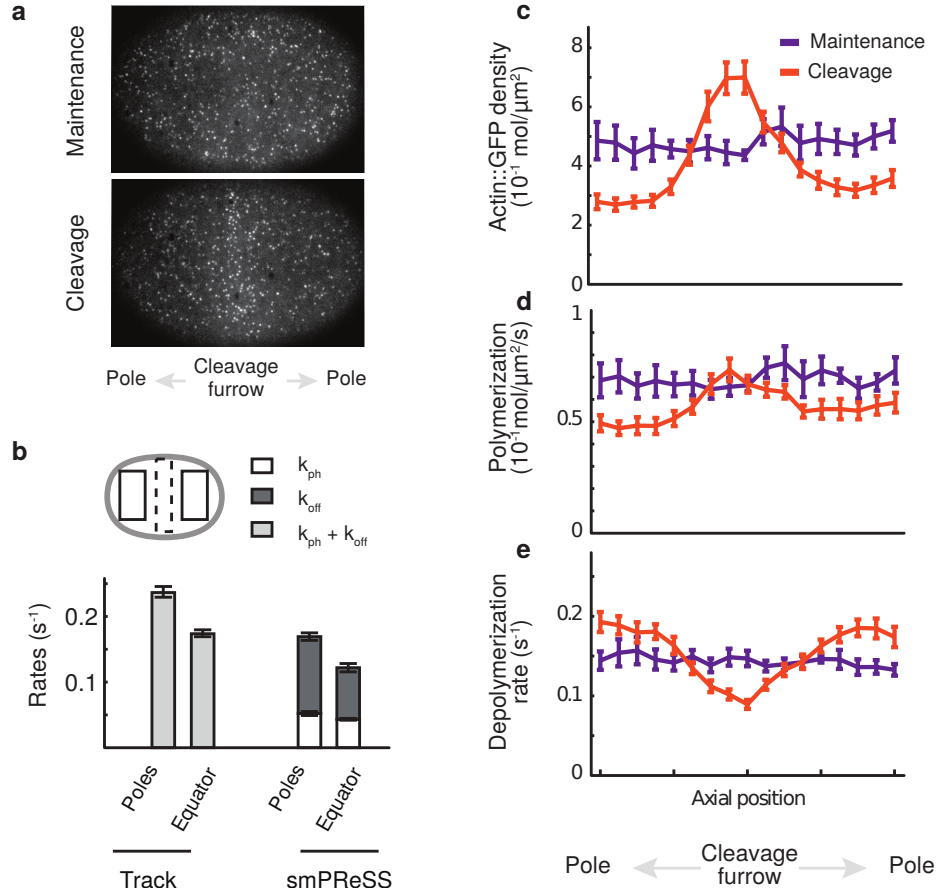


Figure 2.4: Spatial and temporal analysis of actin dynamics in *nmy-2* RNAi embryos. (a) Near-TIRF micrographs of GFP::Actin during maintenance phase (top) and cleavage (bottom). (b) Measurements of turnover at the equator and poles during anaphase using tracking (left) or smPReSS (right). Schematic at top left indicates the equatorial (purple) and polar (red) regions in which the measurements were made. For tracking, the sum of k_{off} and k_{ph} is displayed; for smPReSS, the values for k_{ph} and k_{off} are stacked. (c-e) Spatial variation in actin density and turnover kinetics during maintenance phase (purple) and cleavage (red), measured by tracking and binned along the antero-posterior axis. (c) cortical density, (d) polymerization rate; (e) depolymerization rate (instantaneous disappearance rate minus estimated photobleaching rate). In b-e, error bars indicate cell to cell SEM ($n=7,16$).

suggesting that in this case, we could use SPT to measure spatiotemporal variations in turnover, using the smPReSS measurements of k_{ph} to correct for photobleaching. We measured roughly uniform values for k_{app} and k_{off} along the AP axis during maintenance phase (Fig. 2.4c-e), consistent with a lack of cortical asymmetry at

this stage in myosin-depleted embryos (data not shown). During the transition into anaphase, when the contractile ring normally assembles, we observed a net increase in actin density at the equator as anticipated, and we also observed a net decrease at the poles (Fig. 2.4a,c). Surprisingly, these changes involved strong modulation of both filament assembly and disassembly (Fig. 2.4d,e). The equatorial increase was associated with a small increase in assembly rate and a larger decrease in turnover, while the polar decrease in density was associated with both a decrease in assembly and an increase in turnover. Thus our ability to simultaneously resolve assembly, disassembly and density revealed an unappreciated dimension to the control of cortical microfilaments during cell division.

2.4 Discussion

Here we describe for the first time a simple and tunable method to monitor single molecule mobility and exchange dynamics at the cell surface in embryonic cells of a genetic model organism - *C. elegans*. By tuning the size of the GFP-tagged pool and photobleaching rates, we obtained continuous long term sampling of single molecule trajectories at densities and track lengths that are limited mainly by the photostability of GFP and by well-known constraints on the accurate detection and tracking of single molecules. We focused here on single molecule imaging and analysis. However brighter (multi-molecule) speckles may be optimal for some analyses [65], and can be readily achieved through a slightly different tuning of the cytoplasmic pool. Our approach is minimally invasive because it relies on sampling very low levels of GFP fusions over normal levels of the endogenous protein, with no detectable phototoxicity, even at very high laser power. Because we rely on the intrinsic exchange of GFP fusion proteins between the cytoplasm and the cell surface, no additional methods or reagents are required to target fluorophores to the protein of interest, and the method can be readily implemented by anyone with access to a TIRF microscope equipped for GFP excitation and a sufficiently sensitive (e.g. back-thinned EM-gain CCD) camera.. Our approach thus leverages the large collection of existing fusion strains in *C. elegans* [127], plus recently developed methods for the rapid production of new

strains by genome editing [49], and can be readily combined with any of the large arsenal of molecular genetic tools available in this model organism.

Our approach is immediately compatible with a growing array of tools, based on SPT, to analyze local heterogeneity and spatiotemporal variation in mobility and binding states [151, 58]. Under conditions in which photobleaching rates do not dominate turnover (e.g. low mobility and fast turnover as for GFP::Actin), it is possible to measure spatiotemporal variation in turnover directly from single particle trajectories. As an alternative, we introduced a new method called smPReSS that estimates bulk turnover rates by fitting single molecule counts vs time to kinetic exchange models. smPReSS relies only on single molecule detection and thus is insensitive to particle tracking errors. As illustrated by our analysis of Par-6 turnover, smPReSS can be tuned to measure turnover rates under conditions that are inaccessible to SPT analysis or to ensemble-based measurements like FRAP and its variants. A key assumption underlying both approaches is that the kinetics remain stationary during the time it takes to measure them; the validity of this assumption must be assessed on a case-by-case basis.

Finally, we developed and optimized the methods described here for use in *C. elegans*. However sequence specific inhibition of GFP expression in transgenic strains expressing GFP fusions proteins could be implemented in other model organisms through a variety of methods, in particular RNA interference and targeted protein degradation. Likewise, the use of intrinsic turnover to sample single molecule dynamics is a general principle that could be readily applied in other organisms and cell types. Combining these methods with molecular genetic tools already available in model organisms offers a promising new avenue to study cell surface dynamics in developing embryos.

CHAPTER 3

FILAMENT RECYCLING AND SUSTAINED CONTRACTILE FLOWS IN AN ACTOMYOSIN NETWORK

3.1 Preface

This chapter has been submitted to the arXiv preprint server with the following citation: W. M. McFadden, P. M. McCall, and E. M. Munro. Filament turnover is essential for continuous long range contractile flow in a model actomyosin cortex. ArXiv e-prints, December 2016. [140]

This work was done in collaboration with Patrick McCall in Margaret Gardel’s lab and with Edwin Munro at the University of Chicago. Ed and Patrick directed the outcomes of the project and gave valuable feedback. Patrick’s contributions to the work include 1) *in vivo* experiments, which were at one time considered for inclusion in the manuscript but eventually withheld; 2) frequent discussion and brainstorming with me about actin dynamics, polymer physics, mechanics, interpretation of simulation results and analysis, and the appropriate direction for the project; 3) careful vetting of both a) derivations of analytic results and b) scaling relations derived from the simulations, which uncovered some inconsistencies that we were eventually able to resolve. My contribution was all of the simulation and analysis code.

3.2 Introduction

Cortical flow is a fundamental and ubiquitous form of cellular deformation that underlies cell polarization, cell division, cell crawling and multicellular tissue morphogenesis[22, 82]. These flows arise within the actomyosin cortex, a thin layer of cross-linked actin filaments and myosin motors that lies just beneath the plasma membrane [179]. The

active forces that drive cortical flows are thought to be generated by myosin motors pulling against individual actin filaments [145]. These forces must be integrated within cross-linked networks to build macroscopic contractile stress. At the same time, cross-linked networks resist deformation and this resistance must be dissipated by network remodeling to allow macroscopic network deformation and flow. How force production and dissipation depend on motor activity, network architecture and remodeling remains poorly understood.

Current models for cortical flow rely on coarse-grained descriptions of actomyosin networks as active fluids, whose motions are driven by gradients of active contractile stress and opposed by an effectively viscous resistance[138]. In these models, gradients of active stress are assumed to reflect spatial variation in motor activity and viscous resistance is assumed to reflect the internal dissipation of elastic resistance due to local remodeling of filaments and/or cross-links [19]. A key virtue of these models is that their behavior is governed by a few parameters (active stress and effective viscosity). By coupling an active fluid description to simple kinetic models for network assembly and disassembly and making active stress and effective viscosity depend on e.g network density and turnover rates, it is possible to capture phenomenological descriptions of cortical flow. Models based on this active fluids description can successfully reproduce spatiotemporal dynamics of cortical flow observed during polarization [138], cell division [205, 178], cell motility [98, 134] and tissue morphogenesis [79].

However, to understand how cells exert physiological control over cortical deformation and flow, or to build and tune networks with desired properties *in vitro*, it is essential to connect this coarse-grained description to the microscopic origins of force generation and dissipation within cross-linked actomyosin networks. Both active stress and effective viscosity depend sensitively on microscopic parameters including densities of filaments, motors and cross-links, force-dependent motor/filament interactions, cross-link dynamics and network turnover rates. Thus a key challenge is to understand how tuning these microscopic parameters controls the dynamic interplay between active force generation and passive relaxation to control macroscopic dynamics of cortical flow.

Studies in living cells have documented fluid-like stress relaxation on timescales of 10-100s of seconds [138, 82, 22, 83, 56, 11]. These modes of stress relaxation are thought to arise both from the transient binding/unbinding of individual cross-links and from the turnover (assembly/disassembly) of actin filaments (ref). Studies of cross-linked and/or bundled actin networks *in vitro* suggest that cross-link unbinding may be sufficient to support viscous relaxation (creep) on very long timescales[212, 115, 116, 225, 120], but is unlikely to explain the rapid large scale cortical deformation and flow observed in living cells. It has been proposed in the field that rapid actin turnover must play a significant role as well. Indeed, photokinetic and single molecule imaging studies reveal rapid turnover of cortical actin filaments in living cells on timescales of 10-100 seconds [171]. Previous theoretical models have explored the dependence of stress relaxation on cross-link binding and unbinding analytically [26, 143] and others have explicitly modeled reversible cross-linking in combination with complex mechanics of filament bundles [101, 116, 113], leading to complex viscoelastic stress relaxation. However, until very recently [133] very little attention has been paid to actin turnover as mechanism of stress relaxation.

Recent work has also begun to reveal insights into mechanisms that govern active stress generation in disordered actomyosin networks. *In vitro* studies have confirmed that local interactions among actin filaments and myosin motors are sufficient to drive macroscopic contraction of disordered networks [149]. Theoretical studies suggest that asymmetrical compliance of actin filaments (stiffer under extension than compression) and spatial differences (dispersion) in motor activity are sufficient conditions for contraction in one [110] and two [109] dimensional networks, although other routes to contractility may also exist [109]. Further work has explored how modulation of network architecture, cross-link dynamics and motor density, activity and assembly state can shape rates and patterns of network deformation [103, 8, 9] or network rheology [122, 102].

Significantly, *in vitro* models for disordered actomyosin networks have used stable actin filaments, and these networks support only transient contraction, either because of network collapse[8], or buildup of elastic resistance[147], or because network rearrangements (polarity sorting) dissipate the potential to generate contractile force

[154, 194]. This suggests that continuous turnover of actin filaments may play a key role in allowing sustained deformation and flow. Recent theoretical and modeling studies have begun to explore how this could work [81, 133, 231], and to explore dynamic behaviors that can emerge in contractile material with turnover [47]. However, there is much to learn about how the buildup and maintenance of contractile force during continuous deformation and flow depends on the local interplay of network architecture, motor activity and filament turnover.

The goal of this work is to build a computational bridge between the microscopic description of cross-linked actomyosin networks and the coarse grained macroscopic description of an active fluid. We seek to capture the essential microscope features (dynamic cross-links, active motors and semi flexible actin filaments with asymmetric compliance and continuous filament recycling), but in a way that is sufficiently simple to allow systematic exploration of how parameters that govern network deformation and flow in an active fluid theory depend on microscopic parameters. To this end, we introduce several coarse-grained approximations into our representation of filament networks. First, we represent semi-flexible actin filaments as simple springs with asymmetric compliance (stronger in extension than compression). Second, we replace dynamic binding/unbinding of elastic cross-links with a coarse-grained representation in terms of molecular friction [210, 190, 60], such that filaments can slide past each other against a constant frictional resistance. Third, we used a similar scheme to introduce active motors at filament crossover points with a simple linear force/velocity relationship, and we introduce dispersion of motor activity by making only a subset of filament overlaps active [10]. Finally, we model filament turnover by allowing entire filaments to appear and disappear with a fixed probabilities per unit time. Importantly, these simplifications allow us to extend our single polymer models to dynamical systems of larger network models for direct comparison between theory and modeling results. This level of coarse graining will therefore make it easier to understand classes of behavior for varying compositions of cross-linked filament networks. In addition, it allows us to compute a new class of numerical simulations efficiently, which gives us concrete predictions for behaviors in widely different networks with

measurable dependencies on molecular details.

3.3 Models

Our motivation is to model essential microscope features of cross-linked actomyosin networks (semi flexible actin filaments with asymmetric compliance, dynamic cross-links, active motors and continuous filament recycling), in a way that is simple enough to allow systematic exploration of how tuning these microscopic features controls macroscopic network deformation and flow. We focus on 2D networks for computational tractability and because they capture a reasonable approximation of the quasi-2D cortical actomyosin networks that govern flow and deformation in many eukaryotic cells[138, 35], or the quasi-2D networks studied recently in vitro[149, 181].

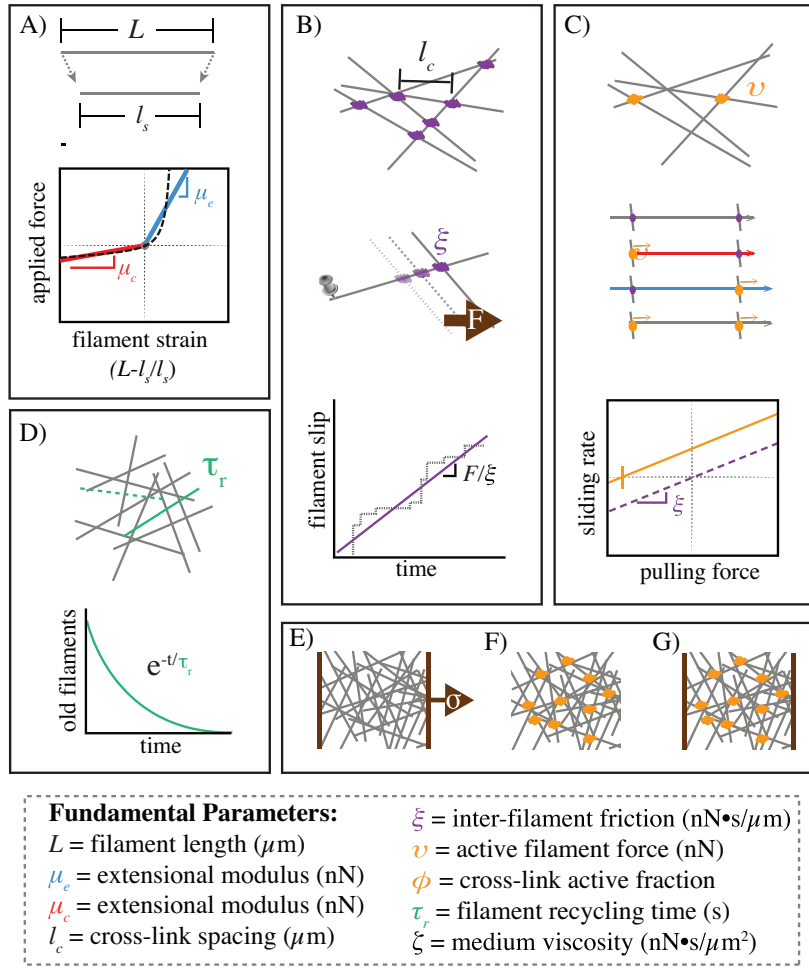


Figure 3.1: Schematic of modeling framework. a) Asymmetric filament compliance. Filaments have smaller spring constant for compression than for extension. b) Cross-link slip. Cross-links are coupled by an effective drag, such that their relative motion is proportional to any applied force. c) Motor activity. Filament activity manifests as a basal sliding rate even in the absence of an external force. Fractional activity. Only a subset of filament cross-links are active, resulting in differential force exertion along the filament. d) Filament recycling. Filaments are turned over at a constant rate, leading to a refreshing in the strain state of all filaments after a characteristic timescale. e) Applied stress. In simulations with passive cross-links, and external stress is applied as force field acting on a fixed spatial domain.

3.3.1 Asymmetric filament compliance

We model individual filaments as chains of springs with relaxed length l_s . Filaments can therefore be represented as a sequence of nodes with positions \mathbf{x}_i , where the index i enumerates over all nodes of all segments. The internal elastic resistance of filament segments gives rise to nearest neighbor force interactions, $\mathbf{F}_{i,i+1}^\mu$, of the form

$$\mathbf{F}_{i,i+1}^\mu = \mu \frac{|\mathbf{x}_{i+1} - \mathbf{x}_i| - l_s}{l_s} \left(\frac{\mathbf{x}_{i+1} - \mathbf{x}_i}{l_s} \right) \quad (3.1)$$

where the modulus, μ , is a composite quantity representing both filament and cross-linker compliance in a manner similar to a proposed effective medium theory [25]. To model asymmetric filament compliance, we assign a different value to the modulus μ , depending on whether the strain on a given filament segment, $(|\mathbf{x}_{i-1} - \mathbf{x}_i| - l_s)/l_s$, is greater or less than 0. In the limit of highly rigid cross-links and flexible filaments, our model reduces to the pure semi-flexible filament models of [78, 221]. In the opposite regime of nearly rigid filaments and highly flexible cross links, our model is essentially the same as that of [25] in small strain regimes before any nonlinear cross link stiffening. In a departure from those previous models, we assume here that the magnitude of the force on interior cross-links is the same as those on the exterior. This approach ignores the variation in strain on these two sets of cross-links as addressed in [25], but we choose to ignore this variation in favor of an approximated, global mean approach.

Because we are dealing with semi-flexible filaments we also introduce a bending modulus between our filament segments such that the restoring force is proportional to the angle between the filament segments and points in the direction orthogonal to the filament direction, $\mathbf{u}_i = (\mathbf{x}_{i-1} - \mathbf{x}_i)/|\mathbf{x}_{i-1} - \mathbf{x}_i|$.

The total internal force on a filament node i can therefore be written as:

$$\mathbf{F}_i^{\text{int}} = \mathbf{F}_{i-1,i}^\mu + \mathbf{F}_{i,i+1}^\mu \quad (3.2)$$

Introducing a filament bending stiffness adds another mode of asymmetric compliance since filaments can bend/buckle internally under compression. For the majority

of the work presented here, we have set $l_s = L$ to obviate dependence on bending driven asymmetries. However, the major points of the paper are still valid for $l_s < L$ under the condition that $\kappa/l_s \gg \mu_c$.

3.3.2 Drag-like coupling between overlapping filaments

Previous models represent cross-linkers as elastic connections between pairs of points on neighboring filaments that appear and disappear with either fixed or force-dependent probabilities [101, 25]. Here, we introduce a simpler coarse-grained model for dynamic cross-links by replacing many transient elastic interactions with an effective drag-like coupling between every pair of overlapping segments.

$$\mathbf{F}_{\mathbf{i}-1,\mathbf{i}}^\xi = \xi \sum_j \frac{l_s - |s_{ij} - s_i|}{l_s} (\mathbf{v}_{\mathbf{i}-1,\mathbf{i}} - \mathbf{v}_{\mathbf{j}-1,\mathbf{j}}) \quad (3.3)$$

where s_i is the location (in arc length) of node i , $\mathbf{v}_{\mathbf{n}-1,\mathbf{n}}$ represent the average velocity of the filament segment spanning nodes $n - 1$ and n , and the sum is taken over all filament segments such that the segment from node $j - 1$ to node j intersects the segment from $i - 1$ to i at the location s_{ij} .

$$\mathbf{F}_\mathbf{i}^{\text{coup}} = \mathbf{F}_{\mathbf{i}-1,\mathbf{i}}^\xi + \mathbf{F}_{\mathbf{i},\mathbf{i}-1}^\xi \quad (3.4)$$

This model assumes a linear relation between the drag force and the velocity difference between attached segments. This drag-like coupling has been shown to be an adequate approximation in the case of ionic cross-linking of actin[214, 33], and can be found in the theoretical basis of force-velocity curves for myosin bound filaments[10]. Although non-linearities can arise through force dependent detachment kinetics and/or non-linear force extension of cross-links, we assume that inhomogeneities from non-linear effects are of second or higher order. With this assumption, the motion of filaments can be described by a deterministic dynamical equation of the form

$$0 = -l_s \zeta \mathbf{v}_\mathbf{i} - \mathbf{F}_\mathbf{i}^{\text{coup}} + \mathbf{F}_\mathbf{i}^{\text{int}} \quad (3.5)$$

Here, the first term is the filament’s intrinsic drag through its embedding fluid, ζ , while the second comes from the drag-like coupling between filaments, ξ .

3.3.3 Active coupling for motor driven filament interactions

To add motor activity we select a subset of cross-linked points and impose an additional force of magnitude v on each of the overlapping filament segments, directed towards the (+) end of that segment, $\mathbf{u}_i = (\mathbf{x}_{i-1} - \mathbf{x}_i)/|\mathbf{x}_{i-1} - \mathbf{x}_i|$. Thus, the total “active” force on a given filament segment is

$$\mathbf{F}_{i-1,i}^v = v\mathbf{u}_i \sum_j \frac{l_s - |s_{ij} - s_i|}{l_s} q_{ij} \quad (3.6)$$

where q_{ij} equals 0 or 1 depending on whether there is an “active” cross-linker at this location. To model dispersion of motor activity, we set $q_{ij} = 1$ on a randomly selected subset of cross-link points at the beginning of the simulation, such that $\bar{q} = \phi$, where \bar{q} indicates the mean of q .

Finally, for each active force, $\mathbf{F}_j^{\text{act}}$, imparted by filament j , we must also impart the opposite force onto the filament between i and $i+1$ as well. Therefore, the entire equation for activity will appear as

$$\mathbf{F}_i^{\text{act}} = \mathbf{F}_{i-1,i}^v + \mathbf{F}_{i,i+1}^v - \sum_j \mathbf{F}_{j-1,j}^v q_{ij} \quad (3.7)$$

This will leave us with a full equation of motion given by the sum of each of the parts defined above.

$$0 = -L\zeta\mathbf{v}_i - \mathbf{F}_i^{\text{coup}} + \mathbf{F}_i^{\text{int}} + \mathbf{F}_i^{\text{act}} \quad (3.8)$$

3.3.4 2D network formation

We used a mikado model approach [206] to initialize a minimal network of connected unstressed linear filaments in a rectangular 2D domain. We generate 2D networks of these semi-flexible filaments by laying down straight lines of length, L , with random

position and orientation. We then assume that overlapping filaments become cross-linked at their points of overlap. Although real cytoskeletal networks may form with non-negligible anisotropy, for simplicity, we focus on isotropically initialized networks. We define the density using the average distance between cross-links along a filament, l_c . A simple geometrical argument can then be used to derive the number of filaments filling a domain as a function of L and l_c [78]. Here, we use the approximation that the number of filaments needed to tile a rectangular domain of size $D_x \times D_y$ is $2D_x D_y / L l_c$, and that the length density is therefore simply, $2/l_c$. In the absence of cross-link slip, we expect the network to form a connected solid with a well defined elastic modulus[78, 221].

3.3.5 External applied stress

We can model our active networks as a coupled system of differential equations satisfying 3.12. However, to probe the passive response of the network, we also wish to incorporate externally applied stresses. Although the general passive mechanical response of this system may be very complex, we focus our attention on low frequency deformations and the steady-state creep response of the system to an applied stress. To do this we introduce a fixed stress, σ along a fixed domain at one edge of the network. The stress is applied via individual forces to the filaments lying within a patch of size D_w such that the sum of individual forces is equal to the applied stress times the height of the domain. These forces point in the direction, $\hat{\mathbf{x}}$, producing an extension of the patch. The region of applied stress does not move as the network deforms, allowing us to more easily focus our attention on a fixed sized domain.

Finally, we add a 0 velocity constraint at the other edge of our domain of interest. We assume that our network is in the “dry,” low Reynold’s number limit, where inertial effects are so small that we can equate our total force to 0. Therefore, we have a dynamical system of wormlike chain filaments satisfying

$$0 = -L\zeta \mathbf{v}_i - \mathbf{F}_i^{\text{coup}} + \mathbf{F}_i^{\text{int}} + \mathbf{F}_i^{\text{act}} + \sigma \hat{\mathbf{u}}(\mathbf{x}_i) \quad (3.9)$$

subject to constraints such that $\mathbf{v}_i(\mathbf{x})$ is 0 with $x = 0$. This results in an implicit

differential equation for filament segments which can be integrated in time to produce a solution for the motion of the system.

3.3.6 Modeling filament turnover

In living cells, actin filament assembly is governed by multiple factors that control nucleation, elongation, and filament branching. Likewise filament disassembly is governed by multiple factors that promote filament severing and monomer dissociation at filament ends. Here, we focus on a lowest order model for filament recycling in which entire filaments appear with a fixed rate per unit area, k_{app} and disappear at a rate $k_{diss}\rho$, where ρ is a filament density. With this assumption, in the absence of network deformation, the density of filaments will equilibrate to a steady state density, k_{app}/k_{diss} , with time constant $\tau_r = 1/k_{diss}$. In deforming networks, the density will be set by a competition between strain thinning ($\gamma > 0$) or thickening ($\gamma < 0$), and density equilibration via turnover. To implement this assumption, at fixed time interval $\tau_s < 0.01 \cdot \tau_r$ (i.e. 1% of the equilibration time), we selected a fraction, τ_s/τ_r , of existing filaments (i.e. less than 1% of the total filaments) for degradation. We then generated a fixed number of new unstrained filaments $k_{app}\tau_s D_x D_y$ at random positions and orientations within the original domain. This method ensures that there is a constant fixed number of filaments present throughout the simulation. We refer to this continuous turnover as filament recycling, to $k_{diss} = 1/\tau_r$ as the recycling rate, and to τ_r as the recycling time.

3.3.7 Simulation methods

Details of our simulation approach and references to our code can be found in the Appendix. Briefly, equations 3.1,3.4,3.6 and 3.9 define a coupled system of ordinary differential equations for the velocities of the endpoints of filament segments, $\dot{\mathbf{x}}$. These equations are coupled by the effective cross-link friction on segment overlap points, yielding a system of the form:

$$\mathbf{A} \cdot \dot{\mathbf{x}} = \mathbf{f}(\mathbf{x}) \quad (3.10)$$

where \mathbf{A} represents a coupling matrix between endpoints of filaments that overlap, and $\mathbf{f}(\mathbf{x})$ is the spring force between pairs of filament segment endpoints. We numerically integrate this system of equations to find the time evolution of the positions of all filament endpoints. We generate a network of filaments with random positions and orientations as described above within a domain of size D_x by D_y . For all simulations, we imposed periodic boundaries in the y -dimension. When imposing an extensional stress, we constrained all filament segment endpoints within a fixed distance $0.05 \cdot D_x$ from the left edge of the domain to be non-moving, then we imposed a rightwards force on all segment endpoints within a distance $0.05 \cdot D_x$ from the left edge of the patch. To simulate free contraction, we removed all constraints at boundaries; to assess buildup of contractile stress under isometric conditions, we used periodic boundary conditions in both x and y dimensions.

We smoothed all filament interactions, force fields, and constraints by allowing forces to decay linearly over small regions such that the equations contained no sharp discontinuities. The nominal units for length, force, and time are μm , nN, and s, respectively. We explored parameter space around an estimate of biologically relevant parameter values given in Table 3.1.

Table 3.1: Simulation Parameter Values

| parameter | symbol | physiological estimate |
|-----------------------------|------------------|---|
| extensional modulus | μ_e | 1nN |
| compressional modulus | μ_c | 0.01nN |
| cross-link drag coefficient | ξ | <i>unknown</i> |
| solvent drag coefficient | ζ | $0.0005 \frac{\text{nNs}}{\mu\text{m}^2}$ |
| filament length | L | $5\mu\text{m}$ |
| cross-link spacing | l_c | $0.5\mu\text{m}$ |
| active filament force | v | 0.1nN |
| active cross-link fraction | ϕ | $0.1 < 0.9$ |
| domain size | $D_x \times D_y$ | $20 \times 50\mu\text{m}$ |

3.4 Results

The goal of this study is to understand how cortical flow is shaped by the simultaneous dependencies of active stress and effective viscosity on filament turnover, crosslink drag and on “network parameters” that control filament density, elasticity and motor activity. We approach this in three steps: First, we analyze the passive deformation of a cross-linked network in response to an externally applied stress; we identify regimes in which the network response is effectively viscous and characterize the dependence of effective viscosity on network parameters and filament turnover. Second, we analyze the buildup and dissipation of active stress in cross-linked networks with active motors, as they contract against an external resistance; we identify conditions under which the network can produce sustained stress at steady state, and characterize how steady state stress depends on network parameters and filament turnover. Finally, we confirm that the dependencies of active stress and effective viscosity on network parameters and filament turnover are sufficient to predict the dynamics of networks undergoing steady state flow in response to spatial gradients of motor activity.

3.4.1 Filament turnover allows and tunes effectively viscous steady state flow.

Networks with passive cross-links and no filament turnover undergo three stages of deformation in response to an extensional force. To characterize the passive response of a cross-linked filament network without filament recycling, we simulated a simple uniaxial strain experiment in which we pinned the network at one end, imposed an external stress at the opposite end, and then quantified network strain and internal stress as a function of time (Fig. 3.1E). The typical response occurred in three qualitatively distinct phases (Fig. 3.2A,C). At short times the response was viscoelastic, with a rapid buildup of internal stress and a rapid \sim exponential approach to a fixed strain (3.11A), which represents the elastic limit in the absence of cross-link slip predicted by [78]. At intermediate times, the local stress and strain rate were approximately constant across the network (Fig. 3.2B),

and the response was effectively viscous; internal stress remained constant while the network continued to deform slowly and continuously with nearly constant strain rate (shown as dashed line in Fig. 3.2C) as filaments slip past one another against the effective cross-link drag. In this regime, we can quantify effective viscosity, η_c , as the ratio of applied stress to the measured strain rate. Finally, as the network strain approached a critical value ($\sim 30\%$ for the simulation in Fig. 3.2), strain thinning lead to decreased network connectivity, local tearing, and rapid acceleration of the network deformation (see inset in Fig. 3.2C).

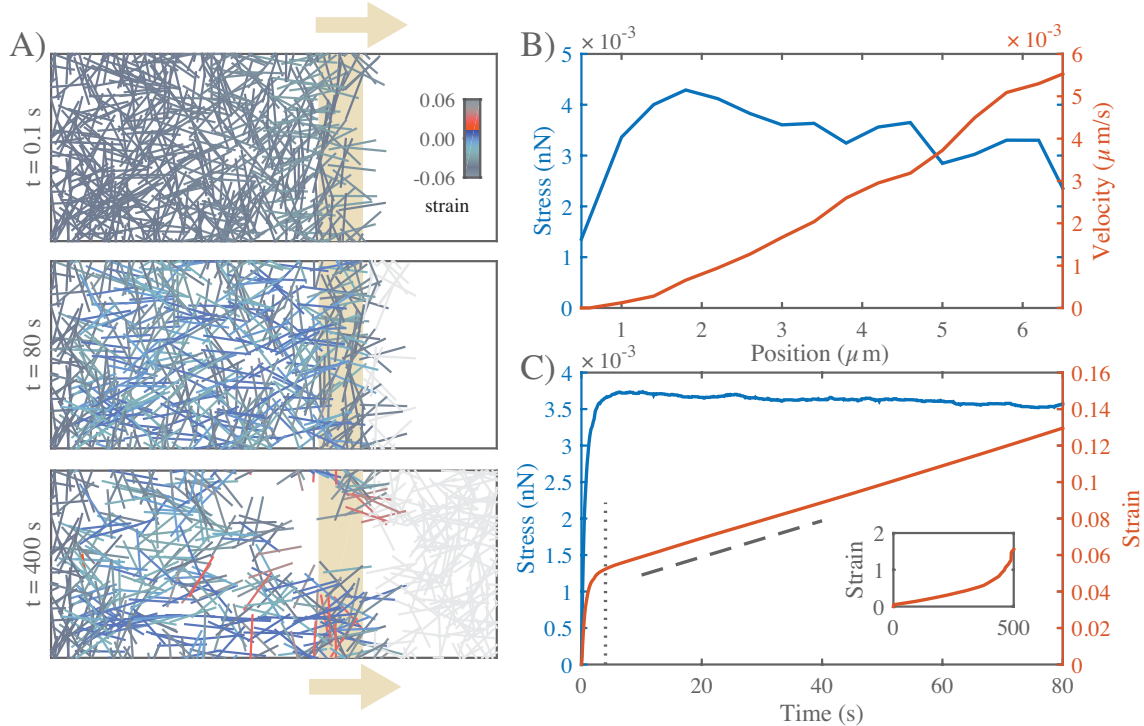


Figure 3.2: Networks with passive cross-links and no filament turnover undergo three stages of deformation in response to an extensional stress. **A)** Three successive time points from a simulation of a $4 \times 6.6 \mu\text{m}$ network deforming under an applied stress of $0.005 \text{ nN}/\mu\text{m}$. Stress (tan arrows) is applied to filaments in the region indicated by the tan bar. In this and all subsequent figures, filaments are color-coded with respect to state of strain (blue = tension, red = compression). Network parameters: $L = 1 \mu\text{m}$, $l_c = 0.3 \mu\text{m}$, $\xi = 100 \text{ nN} \cdot \text{s}/\mu\text{m}$. **B)** Mean filament stress and velocity profiles for the network in (a) at $t=88\text{s}$. Note that the stress is nearly constant and the velocity is nearly linear as predicted for a viscous fluid under extension. **C)** Plots of the mean stress and strain vs time for the simulation in (a), illustrating the three stages of deformation: (i) A fast initial deformation accompanies rapid buildup of internal network stress; (ii) after a characteristic time τ_c (indicated by vertical dotted line) the network deforms at a constant rate, i.e. with a constant effective viscosity, η_c , given by the slope of the dashed line; (iii) at long times, the network undergoes strain thinning and tearing (see inset)

Network architecture sets the rate and timescales of deformation. To characterize how effective viscosity and the timescale for transition to effectively viscous behavior depend on network architecture and cross-link dynamics, we simulated a uniaxial stress test, holding the applied stress constant, while varying filament length L , density l_c , elastic modulus μ_e and cross link drag ξ (see Table 3.2). We measured the elastic modulus, G_0 , the effective viscosity, η_c , and the timescale τ_c for transition from viscoelastic to effectively viscous behavior, and compared these to theoretical predictions. We observed a transition from viscoelastic to effectively viscous deformation for the entire range of parameter values that we sampled. Our estimate of G_0 from simulation agreed well with the closed form solution $G_0 \sim \mu/l_c$ predicted by a previous theoretical model [78] for networks of semi-flexible filaments with irreversible cross-links (Fig. 3.3B).

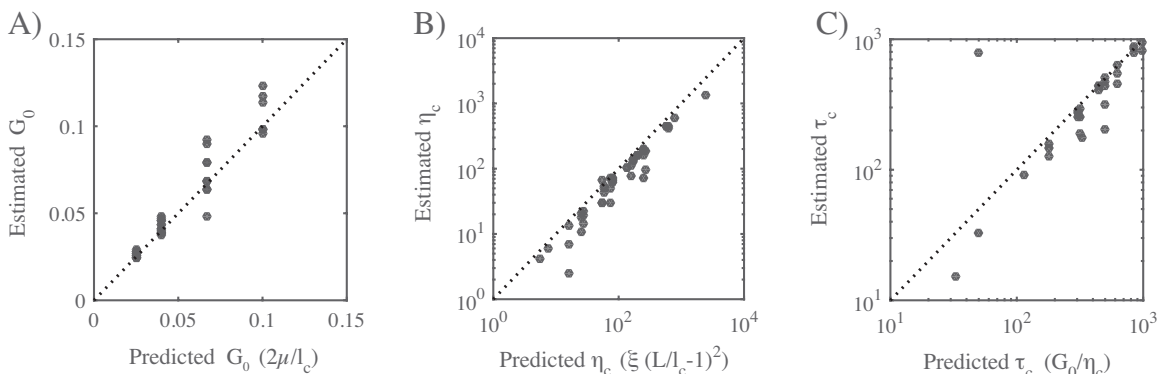


Figure 3.3: Network architecture sets the rate and timescales of deformation. **(a-c)** Comparison of predicted and simulated values for: **A)** the bulk elastic modulus G_0 , **B)** the effective viscosity η_c and **C)** the timescale for transition from viscoelastic to viscous behavior τ_c , given by the ratio of the bulk elastic modulus G_0 to effective viscosity, η_c . Dotted lines indicates the relationships predicted by theory.

A simple theoretical analysis of filament networks with frictional cross link slip, operating in the intermediate viscous regime (see Section B.1.1), predicted that the effective viscosity η_c should be proportional to the cross-link drag coefficient and to the square of the number of cross-links per filament:

$$\eta_c = 4\pi\xi \left(\frac{L}{l_c} - 1 \right)^2 \quad (3.11)$$

As shown in Fig. 3.3B, our simulations agree well with this prediction for a large range of sampled network parameters. Finally, for many linear viscoelastic materials, the ratio of effective viscosity to the elastic modulus η_c/G_0 sets the timescale for transition from elastic to viscous behavior[139]. Combining our approximations for G_0 and η_c , we predict a transition time, $\tau_c \approx L^2\xi/l_c\mu$. Measuring the time at which the strain rate became nearly constant (i.e. $\gamma \sim t^n$ with $n > 0.8$) yields an estimate of τ_c that agrees well with this prediction over the entire range of sampled parameters (Fig. 3.3C). Thus the passive response of filament networks with frictional cross link drag is well-described on short (viscoelastic) to intermediate (viscous) timescales by an elastic modulus G_0 , an effective viscosity η_c , and a transition timescale τ_c , with well-defined dependencies on network parameters. However, without filament turnover, strain thinning and network tearing limits the extent of viscous deformation to small strains.

Filament turnover allows sustained large-scale viscous flow and defines two distinct flow regimes. To characterize how filament turnover shapes the passive network response to an applied force, we introduced a simple form of turnover in which entire filaments disappear at a rate $k_{diss}\rho$, where ρ is the filament density, and new unstrained filaments appear with a fixed rate per unit area, k_{app} . In a non-deforming network, filament density will equilibrate to a steady state value, $\rho_0 = k_{ass}/k_{diss}$, with time constant $\tau_r = 1/k_{diss}$. However, in networks deforming under extensional stress, the density will be set by a competition between strain thinning and density equilibration via turnover.

We simulated a uniaxial stress test for different values of τ_r , while holding all other parameters fixed (Fig. 3.4A-C). For large τ_r , as described above, the network undergoes strain thinning and ultimately tears. Decreasing τ_r increases the rate at which the network equilibrates towards a steady state density ρ_0 . However, it also increases the rate of deformation and thus the rate of strain thinning (Fig. 3.4B). We found that the former effect dominates, such that below a critical value $\tau_r = \tau_{crit}$, the network can achieve a steady state characterized by a fixed density and a constant strain rate (3.12). Simple calculations (see Section 3.6.3) show that the critical value

of τ_r is approximately:

$$\tau_{crit} = \frac{\xi \left(\sqrt{\frac{L}{l_c}} - 1 \right)^3}{\sigma}. \quad (3.12)$$

where σ is the applied stress, L/l_c the linear cross link density, and ξ is the effective crosslink drag.

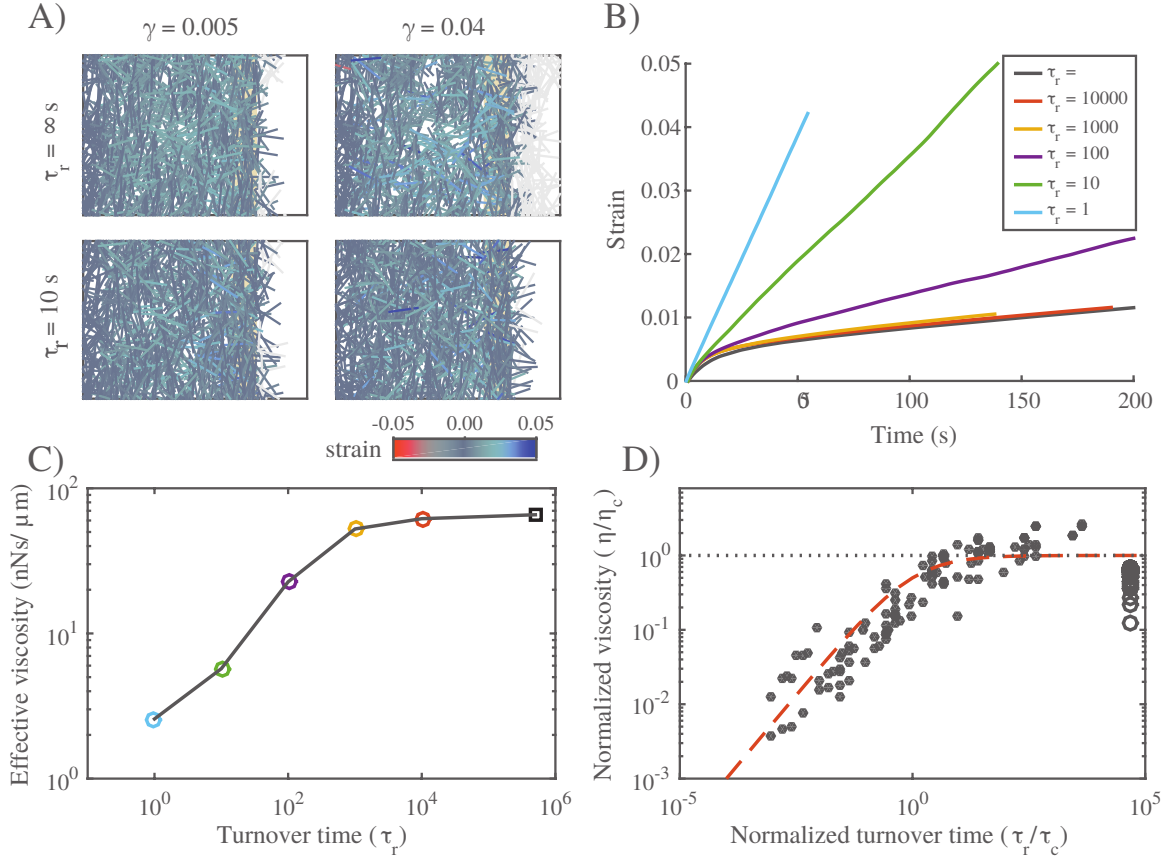


Figure 3.4: Filament recycling defines two regimes of effectively viscous flow. **A)** Comparison of $20 \times 12 \mu\text{m}$ networks under $0.001 \text{ nN}/\mu\text{m}$ extensional stress without (top) and with (bottom) filament turnover. Both images are taken when the networks had reached a net strain of 0.04. For clarity, filaments that leave the domain of applied stress are greyed out. **B)** Plots of strain vs time for identical networks with different rates of filament turnover. Network parameters: $L = 5 \mu\text{m}$, $l_c = 0.5 \mu\text{m}$, $\xi = 10 \text{ nN} \cdot \text{s}/\mu\text{m}$. **C)** Plot of effective viscosity vs turnover time derived from the simulations shown in panel b. Square dot is the $\tau_r = \infty$ condition. **D)** Plot of normalized effective viscosity (η/η_c) vs normalized turnover time (τ_r/τ_c) for a large range of network parameters and turnover times. For $\tau_r \ll \tau_c$, the viscosity of the network becomes dependent on recycling time. Red dashed line indicates the approximation given in equation 3.13 for $m = 3/4$.

For $\tau_r < \tau_{crit}$, we observed two distinct steady state flow regimes (Fig. 3.4B,C). For intermediate values of τ_r , effective viscosity remains constant with decreasing τ_r . However, below a certain value of τ_r ($\approx 10^3$ for the parameters used in Fig. 3.4C), effective viscosity decreased monotonically with further decreases in τ_r . To

understand what sets the timescale for transition between these two regimes, we measured effective viscosity at steady state for a wide range of network parameters (L, μ, l_c), crosslink drags (ξ) and filament turnover times (Fig. 3.4D). Strikingly, when we plotted the normalized effective viscosity η_r/η_c vs a normalized recycling rate τ_r/τ_c for all parameter values, the data collapsed onto a single curve, with a transition at $\tau_r \approx \tau_c$ between an intermediate turnover regime in which effective viscosity is independent of τ_r and a high turnover regime in which effective viscosity falls monotonically with decreasing τ_r/τ_c (Fig. 3.4D).

This biphasic dependence of effective viscosity on filament turnover can be understood intuitively as follows: As new filaments are born, they become progressively stressed as they stretch and reorient under local influence of surrounding filaments, eventually reaching an elastic limit where their contribution to resisting network deformation is determined by effective crosslink drag. The time to reach this limit is about the same as the time, τ_c , for an entire network of initially unstrained filaments to reach an elastic limit during the initial viscoelastic response to uniaxial stress, as shown in Fig. 2b. For $\tau_r < \tau_c$, individual filaments do not have time, on average, to reach the elastic limit before turning over; thus the deformation rate is determined by the elastic resistance of partially strained filaments, which increases with lifetime up to $\tau_r = \tau_c$. For $\tau_r > \tau_c$, the deformation rate is largely determined by cross-link resistance to sliding of maximally strained filaments, and the effective viscosity is insensitive to further increase in τ_r .

These results complement and extend a previous computational study of irreversibly cross-linked networks of treadmilling filaments deforming under extensional stress[100]. Kim et al identified two regimes of effectively viscous deformation: a “stress-dependent” regime in which filaments turnover before they become strained to an elastic limit and deformation rate is proportional to both applied stress and turnover rate; and a “stress-independent” regime in which filaments reach an elastic limit before turning over and deformation rate depends only on the turnover rate. The fast and intermediate turnover regimes that we observe here correspond to the stress-dependent and independent regimes described by Kim et al, but with a key difference. Without filament turnover, Kim et al’s model predicts that a network

cannot deform beyond its elastic limit. In contrast, our model predicts viscous flow at low turnover, governed by an effective viscosity that is set by cross-link density and effective drag. Thus our model provides a self-consistent framework for understanding how crosslink unbinding and filament turnover contribute separately to viscous flow and connects these contributions directly to previous theoretical descriptions of cross-linked networks of semi-flexible filaments.

In summary, our simulations predict that filament turnover allows networks to undergo viscous deformation indefinitely, without tearing, over a wide range of different effective viscosities and deformation rates. For $\tau_r < \tau_{crit}$, this behavior can be summarized by an equation of the form:

$$\eta = \frac{\eta_c}{1 + (\tau_c/\tau_r)^m} \quad (3.13)$$

For $\tau_r \gg \tau_c$, $\eta \approx \eta_c$: effective viscosity depends on crosslink density and effective crosslink drag, independent of changes in recycling rate. For $\tau_r \ll \tau_c$, effective viscosity is governed by the level of elastic stress on network filaments, and becomes strongly dependent on filament lifetime: $\eta \sim \eta_c(\tau_r/\tau_c)^m$. The origins of the $m = 3/4$ scaling remains unclear (see Discussion).

3.4.2 Filament turnover allows persistent stress buildup in active networks

In the absence of filament turnover, active networks with free boundaries contract and then stall against passive resistance to network compression. Previous work [110, 149, 102] identifies asymmetric filament compliance and spatial heterogeneity in motor activity as minimal requirements for macroscopic contraction of disordered networks. To confirm that our simple implementation of these two requirements (see Models section) is sufficient for macroscopic contraction, we simulated active networks that are unconstrained by external attachments, varying filament length, density, crosslink drag and motor activity. We observed qualitatively similar results for all choices of parameter values: Turning on motor activity in an initially unstrained network induced rapid initial contraction, followed by a slower buildup

of compressive stress (and strain) on individual filaments, and an \sim exponential approach to stall (Fig. 3.5). The time to stall, τ_s , scaled as $L\xi/v$ (3.13A). On even longer timescales, polarity sorting of individual filaments, as previously described [169, 147, 154, 194] lead to network expansion (see 3.5).

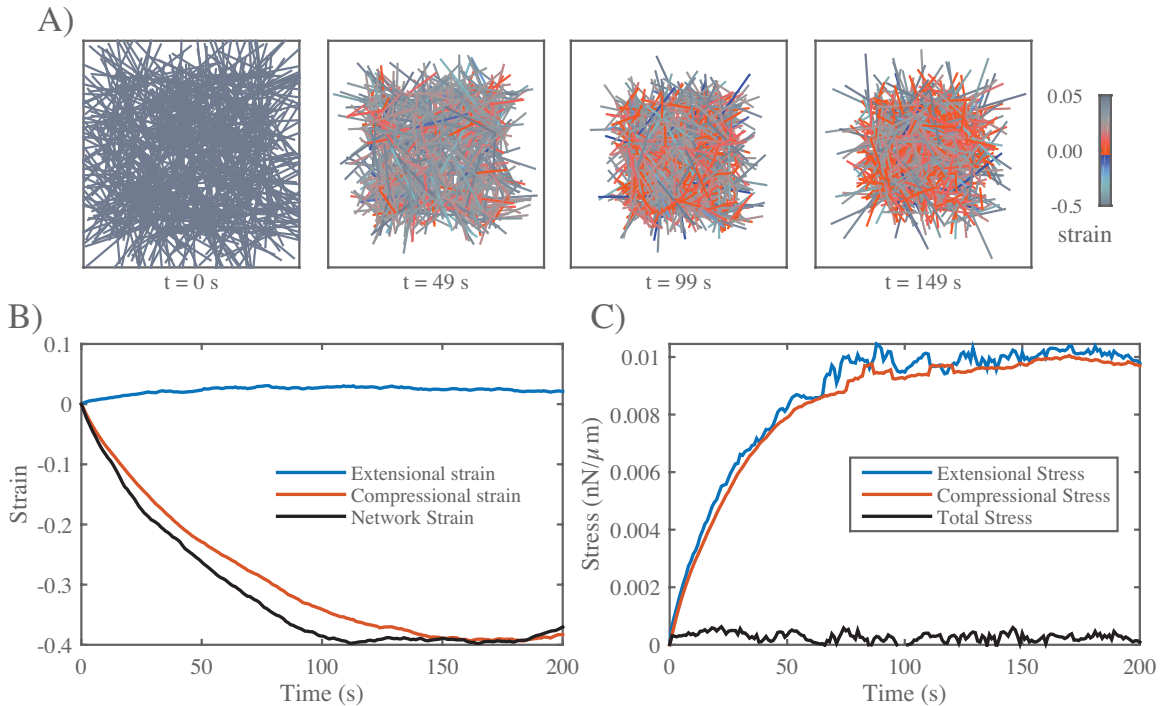


Figure 3.5: In the absence of filament turnover, active networks with free boundaries contract and then stall against passive resistance to network compression. **A)** Simulation of an active network with free boundaries. Colors represent strain on individual filaments as in previous figures. Note the buildup of compressive strain as contraction approaches stall between 100 s and 150 s. Network parameters: $L = 5 \mu\text{m}$, $l_c = 0.3 \mu\text{m}$, $\xi = 1 \text{nN} \cdot \text{s}/\mu\text{m}$, $v = 0.1 \text{nN}$. **B)** Plots showing time evolution of total network strain (black) and the average extensional (blue) or compressive (red) strain on individual filaments. **C)** Plots showing time evolution of total (black) extensional (blue) or compressive (red) stress. Note that extensional and compressive stress remain balanced as compressive resistance builds during network contraction.

During the rapid initial contraction, the increase in network strain closely matched the increase in mean compressive strain on individual filaments Fig. 3.5B, as predicted theoretically [110, 109] and observed experimentally[149]. Contraction required asymmetric filament compliance and spatial heterogeneity of motor activity ($\mu_e/\mu_c > 1$,

$\phi < 1$, 3.13B). Thus our model captures a minimal mechanism for bulk contractility in disordered networks through asymmetric filament compliance and dispersion of motor activity. However, in the absence of turnover, contraction is limited by internal buildup of compressive resistance and the dissipative effects of polarity sorting.

Active networks cannot sustain stress against a fixed boundary in the absence of filament turnover. During cortical flow, regions with high motor activity contract against a passive resistance from neighboring regions with lower motor activity. To understand how the active stresses that drive cortical flow are shaped by motor activity and network remodeling, we analyzed the buildup and maintenance of contractile stress in active networks contracting against a rigid boundary. We simulated active networks contracting from an initially unstressed state against a fixed boundary (Fig. 3.6A,B), and monitored the time evolution of mean extensional (blue), compressional (red) and total (black) stress on network filaments (Fig. 3.6C,D). We focused initially on the scenario in which there is no, or very slow, filament turnover, sampling a range of parameter values controlling filament length and density, motor activity, and crosslink drag.

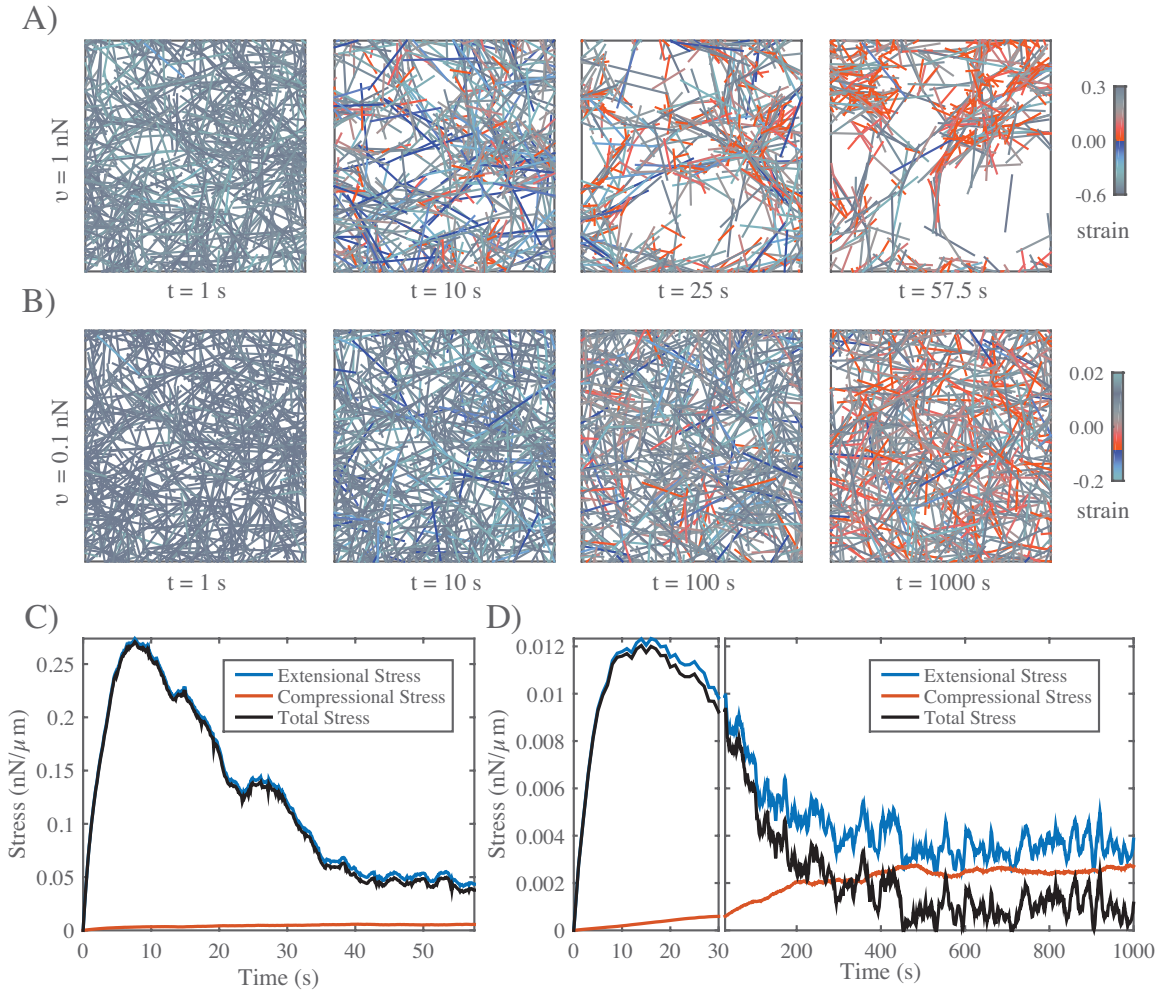


Figure 3.6: In the absence of filament turnover, active networks cannot sustain continuous stress against a fixed boundary. **A)** Simulation of an active network with fixed boundaries. Rearrangement of network filaments by motor activity leads to rapid loss of network connectivity. Network parameters: $L = 5 \mu\text{m}$, $l_c = 0.3 \mu\text{m}$, $\xi = 1 \text{ nN} \cdot \text{s}/\mu\text{m}$, $v = 1 \text{ nN}$. **B)** Simulation of the same network, with the same parameter values, except with ten-fold lower motor activity $v = 0.1 \text{ nN}$. In this case, connectivity is preserved, but there is a progressive buildup of compressive strain on individual filaments. **C)** Plots of total network stress and the average extensional (blue) and compressive (red) stress on individual filaments for the simulation shown in (a). Rapid buildup of extensional stress allows the network transiently to exert force on its boundary, but this force is rapidly dissipated as network connectivity breaks down. **D)** Plots of total network stress and the average extensional (blue) and compressive (red) stress on individual filaments for the simulation shown in (b). Rapid buildup of extensional stress allows the network transiently to exert force on its boundary, but this force is dissipated at longer times as decreasing extensional stress and increasing compressive stress approach balance. Note the different time scales used for plots and subplots in **C)** and **D)** to emphasize the similar timescales for force buildup, but very different timescales for force dissipation.

We observed a similar behavior in all cases: total stress built rapidly to a peak value σ_m , and then decayed towards zero (Fig. 3.6C,D). The rapid initial increase in total stress was determined largely by the rapid buildup of extensional stress (Fig. 3.6C,D) on a subset of network filaments (Fig. 3.6A,B $t = 10s$). The subsequent decay involved two different forms of local remodeling: under some conditions, e.g. for higher motor activity (e.g. Fig. 3.6A,C), the decay was associated with rapid local tearing and fragmentation, leading to global loss of network connectivity as described previously both in simulations[133] and *in vitro* experiments [8]. However, for many parameters, (e.g. for higher motor activity as in Fig. 3.6B,D), the decay in stress occurred with little or no loss of global connectivity. Instead, local filament rearrangements changed the balance of extensile vs compressive forces along individual filaments, leading to a slow decrease in the average extensional stress, and a correspondingly slow increase in the compressional stress, on individual filaments (see Fig. 3.6D).

Combining dimensional analysis with trial and error, we were able to find empirical scaling relationships describing the dependence of maximum stress σ_m and the time to reach maximum stress τ_m on network parameters and effective crosslink drag ($\sigma_m \sim \sqrt{\mu_e v}/l_c$, $\tau_m \sim L\xi/\sqrt{\mu_e v}$, 3.13C,D). Although these relationships should be taken with a grain of salt, they are reasonably consistent with our simple intuition that the peak stress should increase with motor force (v), extensional modulus (μ_e) and filament density ($1/l_c$), and the time to reach peak stress should increase with crosslink drag (ξ) and decrease with motor force (v) and extensional modulus (μ_e).

Filament turnover allows active networks to exert sustained stress on a fixed boundary. Regardless of the exact scaling dependencies of σ_m and τ_m on network parameters, these results reveal a fundamental limit on the ability of active networks to sustain force against an external resistance in the absence of filament turnover. To understand how this limit can be overcome by filament turnover, we simulated networks contracting against a fixed boundary from an initially unstressed state, for increasing rates of filament turnover (decreasing τ_r), while holding all other parameter values fixed (Fig. 3.7A-C). While the peak stress decreased monotonically

with decreasing τ_r , the steady state stress showed a biphasic response, increasing initially with decreasing τ_r , and then falling off as $\tau_r \rightarrow 0$. We observed a biphasic response regardless of how stress decays in the absence of turnover, i.e. whether decay involves loss of network connectivity, or local remodeling without loss of connectivity, or both (3.14 and not shown). Significantly, when we plot normalized steady state stress (σ/σ_m) vs normalized recycling time (τ_r/τ_m) for a wide range of network parameters, the data collapse onto a single biphasic response curve, with a peak near $\tau_r/\tau_m = 1$ (Fig. 3.7D). In particular, for $\tau_r < \tau_m$, the scaled data collapsed tightly onto a single curve representing a linear increase in steady state stress with increasing τ_r . For $\tau_r > \tau_m$, the scaling was less consistent, although the trend towards a monotonic decrease with increasing τ_r was clear. These results reveal that filament turnover can rescue the dissipation of active stress during isometric contraction due to network remodeling, and they show that, for a given choice of network parameters, there is an optimal choice of filament lifetime that maximizes steady state stress.

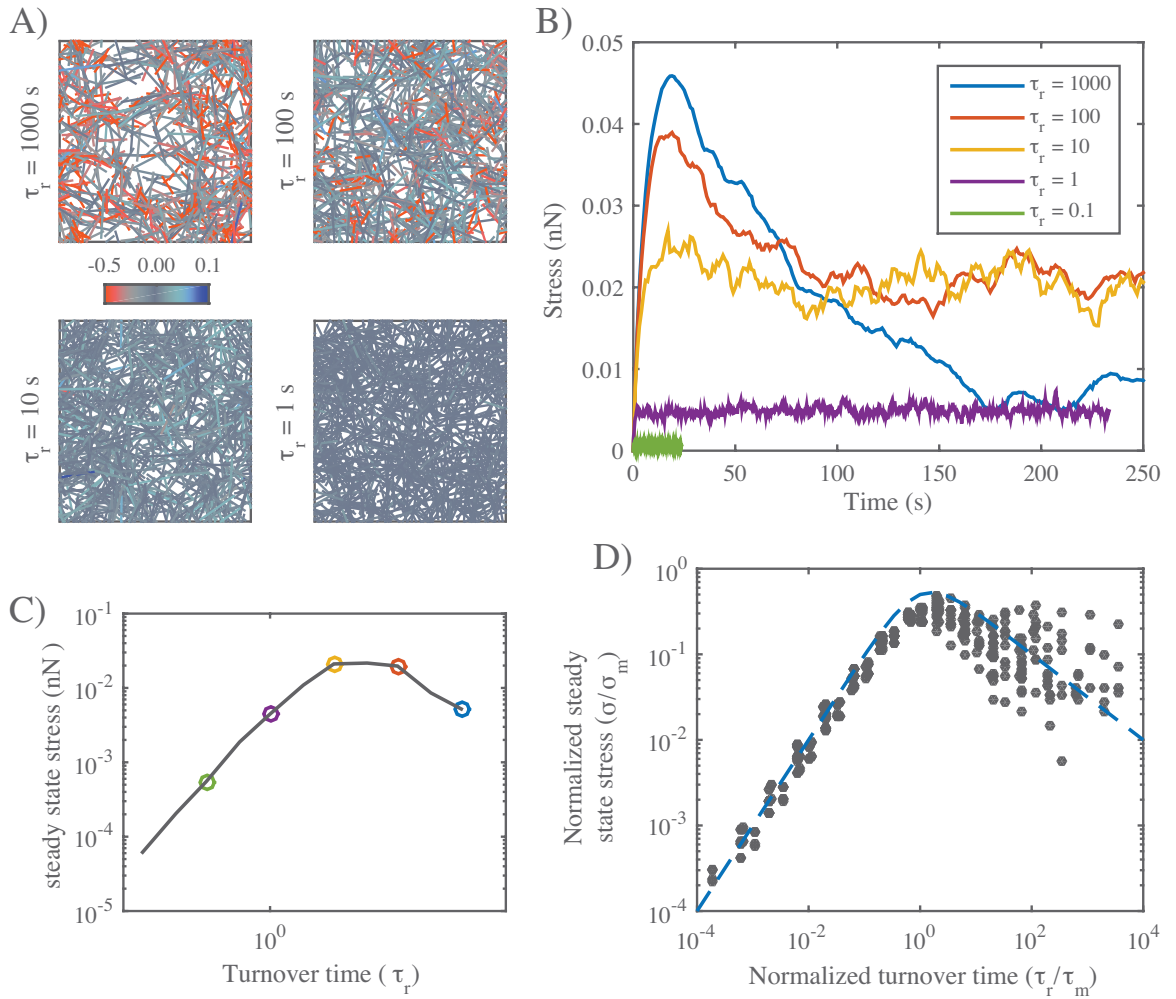


Figure 3.7: Filament turnover allows active networks to exert sustained stress on a fixed boundary. **A)** Snapshots from simulations of active networks with fixed boundaries and different rates of filament turnover. All other parameter values are the same as in Fig. 3.6A. Note the significant buildup of compressive strain and significant remodeling for longer, but not shorter, turnover times. **B)** Plots of net stress exerted by the network on its boundaries for different recycling times; for long-lived filaments, stress is built rapidly, but then dissipates. Decreasing filament lifetimes reduces stress dissipation by replacing compressed with uncompressed filaments, allowing higher levels of steady state stress; for very short lifetimes, stress is reduced, because individual filaments do not have time to build stress before turning over. **C)** Plots of \approx steady state stress estimated from the simulations in **B**) vs turnover time. **D)** Plot of normalized steady state stress vs normalized recycling time for a wide range of network parameters and turnover times. Steady state stress is normalized by the predicted maximum stress σ_m achieved in the absence of filament turnover. Turnover time is normalized by the predicted time to achieve maximum stress τ_m , in the absence of filament turnover. Predictions for σ_m and τ_m were obtained from the phenomenological scaling relations shown in (Fig. 3.13C,D). Dashed blue line indicates the approximation given in equation 3.14 for $n = 1$.

We can understand the biphasic dependence of steady state stress on filament lifetime using the same reasoning applied to the case of passive flow: During steady state contraction, the average filament should build and dissipate active stress on approximately the same schedule as an entire network contracting from an initially unstressed state (Fig. 3.7B). Therefore for $\tau_r < \tau_m$, increasing lifetime should increase the mean stress contributed by each filament. For $\tau_r > \tau_m$, further increases in lifetime should begin to reduce the mean stress contribution. Directly comparing the time-dependent buildup and dissipation of stress in the absence of turnover, with the dependence of steady state stress on τ_r , supports this interpretation (3.15)

As for the passive response (i.e. Equation 3.13), we can describe this biphasic dependence phenomenologically with an equation of the form:

$$\sigma_{ss} = \frac{\sigma_m}{(\tau_r/\tau_m)^n + \tau_m/\tau_r} \quad (3.14)$$

where the origins of the exponent n remain unclear.

3.4.3 Filament turnover tunes the balance between active stress buildup and viscous stress relaxation to generate flows

Thus far, we have considered independently how network remodeling controls the passive response to an external stress, or the steady state stress produced by active contraction against an external resistance. We now consider how these two forms of dependence will combine to shape steady state flow produced by spatial gradients of motor activity. We consider a simple scenario in which a network is pinned on either side and motor activity is continuously patterned such that the right half network has uniformly high levels of motor activity (controlled by v , with $\psi = 0.5$), while the left half network has none. Under these conditions, the right half network will contract continuously against a passive resistance from the left half network. Because of asymmetric filament compliance, the internal resistance of the right half network to active compression should be negligible compared to the external resistance of the left half network. Thus the steady state flow will be described by:

$$\dot{\gamma} = \frac{\sigma_{ss}}{\eta} \quad (3.15)$$

where σ_{ss} is the active stress generated by the right half-network (less the internal resistance to filament compression), η is the effective viscosity of the left half network and strain rate $\dot{\gamma}$ is measured in the left half-network. Note that strain rate can be related to the steady state flow velocity v at the boundary between right and left halves through $v = \dot{\gamma}Dx$. Therefore, we can understand the dependence of flow speed on filament turnover and other parameters using the approximate relationships summarized by equations 3.13 and 3.14 for η and σ_{ss} . As shown in Fig. 3.8, there are two qualitatively distinct possibilities for the dependence of strain rate on τ_r , depending on the relative magnitudes of τ_m and τ_c . In both cases, for fast enough turnover ($\tau_r < \min(\tau_m, \tau_c)$), we expect weak dependence of strain rate on τ_r ($\dot{\gamma} \sim \tau_r^{1/4}$). For all parameter values that we sampled in this study (which were chosen to lie in a physiological range), $\tau_m > \tau_c$. Therefore we predict the dependence of steady state strain rate on τ_r shown in Fig. 3.8A.

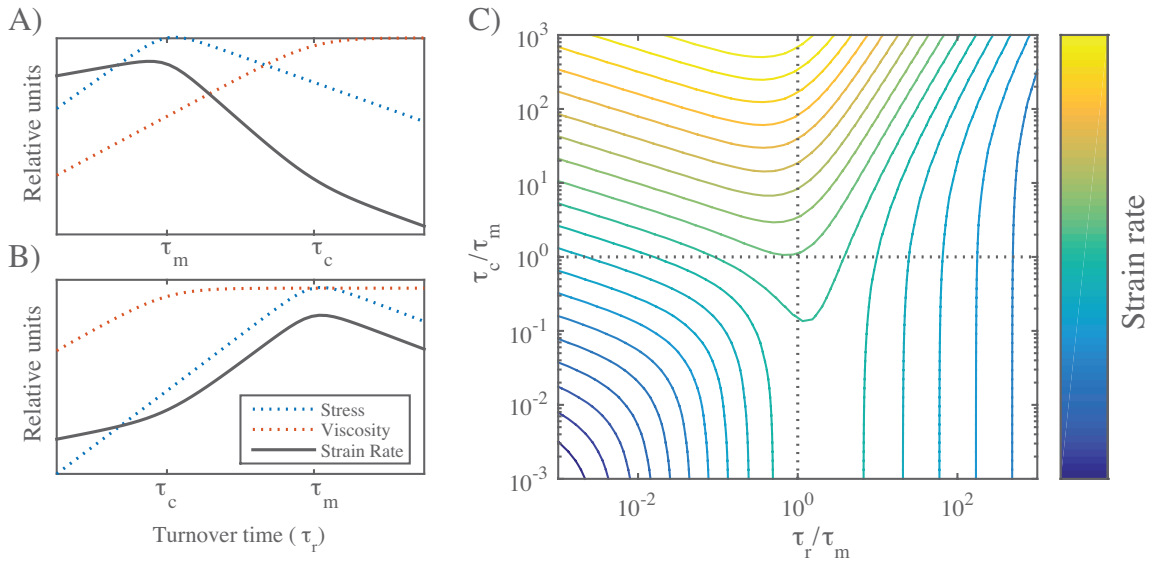


Figure 3.8: Filament recycling tunes the magnitudes of both effective viscosity and steady state stress. **A)** Dependence of steady state stress, effective viscosity, and resulting strain rate on recycling time τ_r under the condition $\tau_m < \tau_c$. **B)** Same as a) but for $\tau_c < \tau_m$. **C)** State space of flow rate dependence relative to the two relaxation timescales, τ_r and τ_c normalized by the stress buildup timescale, τ_m .

To confirm this prediction, we simulated the simple scenario described above for a range of values of τ_r , with all other parameter values initially fixed. As expected, we observed a sharp dependence of steady state flow speeds on filament recycling rate (Fig. 3.9B,C). For very long recycling times, ($\tau_r = 1000s$, dark blue line), there was a rapid initial deformation (contraction of the active domain and dilation of the passive domain), followed by a slow approach to a steady state flow characterized by slow contraction of the right half-domain and a matching dilation of the left half-domain (see 3.16). However, with decreasing values of τ_r , steady state flow speeds increased steadily, before reaching an approximate plateau on which flow speeds varied by less than 15 % over more than two decades of variation in τ_r (Fig. 3.9C).

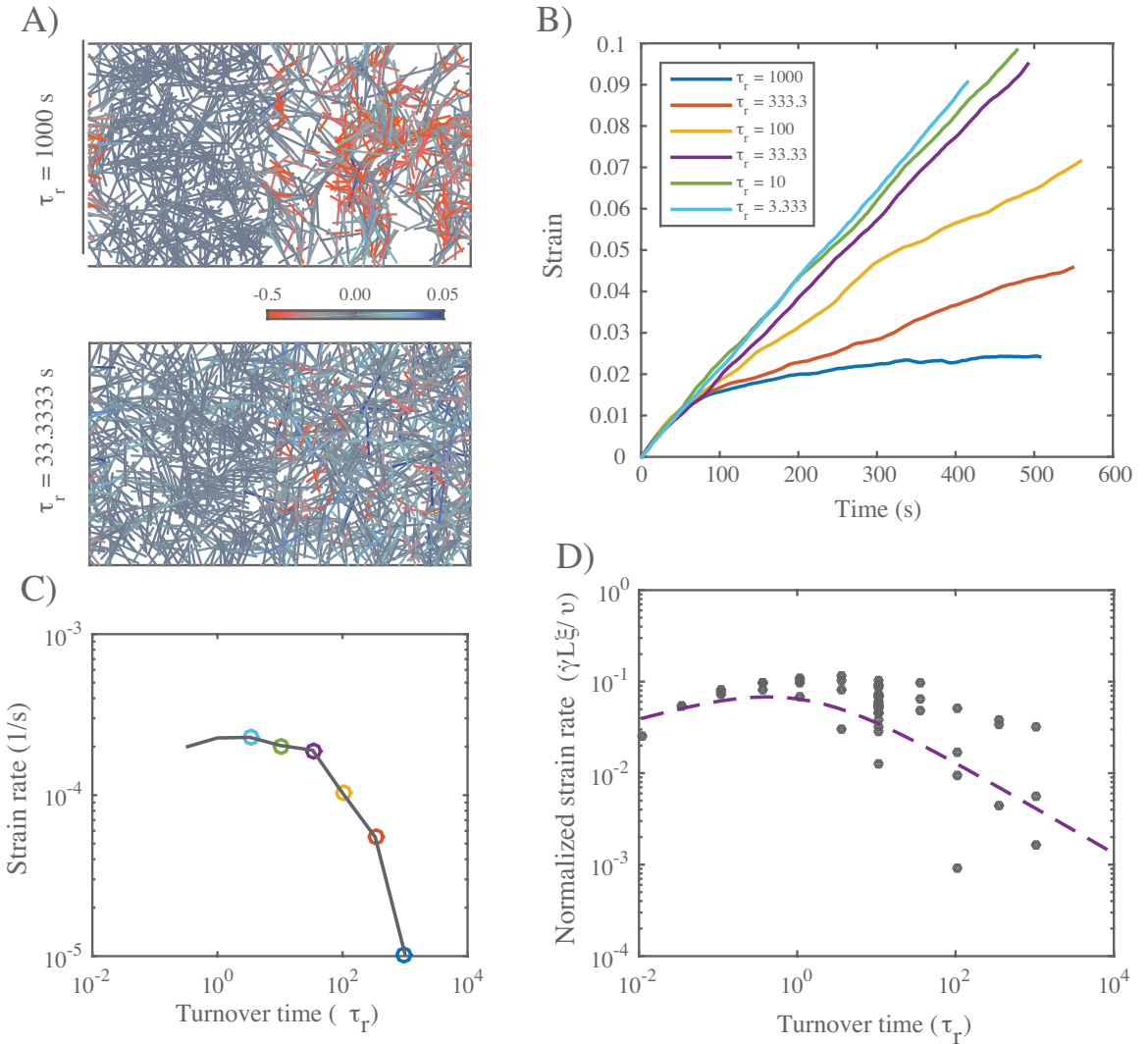


Figure 3.9: Filament recycling allows sustained flows in networks with non-isotropic activity. **A)** Example simulations of non-isotropic networks with long ($\tau_r = 1000$) and short ($\tau_r = 33$) recycling timescales. In these networks the left half of the network is passive while the right half is active. Network parameters are same as in Figs 3.6 and 3.7. Importantly, in all simulations $\tau_m < \tau_c$. **B)** Graph of strain for identical networks with varying recycling timescales. With long recycling times, the network stalls; reducing the recycling timescale allows the network to persist in its deformation. However, for the shortest recycling timescales, the steady state strain begins to slowly return to 0 net motion. Measurements are based on the passive side of the network. **C)** Steady state strain rates for the networks in (b). **D)** Graph of network's long-term strain rate as a function of recycling timescale. Dashed line is form of dependence predicted by the theoretical arguments shown in Fig. 3.8.

We repeated these simulations for a wider range of parameter values, and saw similar dependence of $\dot{\gamma}$ on τ_r in all cases. Using equation 3.13 with $\tau_r < \tau_c$ and equation 3.14 with $\tau_r < \tau_m$, and the theoretical or empirical scaling relationships found above for η_c , τ_c , σ_m and τ_m , we predict a simple scaling relationship for $\dot{\gamma}$ (for small τ_r):

$$\dot{\gamma} = \frac{v}{\xi L} (\tau_r)^{1/4} \quad (3.16)$$

Indeed, when we plot the steady state measurements of $\dot{\gamma}$, normalized by $v/\xi L$, for all parameter values, the data collapse onto a single curve for small τ_r . Thus, our simulations identify a flow regime, characterized by sufficiently fast filament turnover, in which the steady state flow speed is buffered against variation in turnover, and has a relatively simple dependence on other network parameters.

3.5 Discussion

Cortical flows arise through a dynamic interplay of force production and dissipation within cross-linked actomyosin networks. Here we combined computer simulations with simple theoretical analysis to explore how this interplay depends on motor activity, crosslink dynamics, network architecture and filament turnover. Our results reveal two essential requirements for filament turnover during cortical flow: (a) to allow the continuous relaxation of elastic resistance without catastrophic loss of network connectivity and (b) to prevent the dissipation of active stress through local network rearrangements. We find that biphasic dependencies of active stress and passive relaxation on filament lifetime define multiple modes of steady state flow with distinct dependencies on network parameters and filament turnover.

We identify two distinct modes of passive response to uniaxial stress: a low turnover mode in which filaments strain to an elastic limit before turning over, and effective viscosity depends on crosslink density and effective crosslink friction, and a high turnover mode in which filaments turn over before reaching an elastic limit and effective viscosity is proportional to elastic resistance and \approx proportional to filament

lifetime. We note that the weakly sub-linear dependence of effective viscosity on filament lifetime that we observe in the high turnover regime may simply reflect a failure to capture very local modes of filament deformation, since a previous study [100] in which filaments were represented as connected chains of smaller segments predicted linear dependence of effective viscosity on filament lifetime. While previous studies have emphasized individual roles for cross-link unbinding or filament turnover in stress relaxation [44, 43, 179], here we have capture their distinct contributions within a single self-consistent modeling framework.

Our simulations confirm the theoretical prediction [110, 149, 102] that spatial heterogeneity of motor activity and asymmetric filament compliance are sufficient to support macroscopic contraction of unconstrained networks. However, under isometric conditions, and without filament turnover, our simulations predict that active stress cannot be sustained. On short timescales, motor forces drive local buildup of extensional stress, but on longer timescales, active local filament rearrangements drive local changes in connectivity that lead, invariably, to a decay in active stress. Under some conditions, contractile forces drive networks towards a critically connected state, leading to tearing and fragmentation, as previously described [8, 133]. However, we find that stress decay can also occur without any global loss of connectivity, through a gradual decrease in extensile force and a gradual increase in compressive force along individual filaments. Our results suggest that when filaments can slide relative to one another, the motor forces that produce active stress will inevitably lead to local changes in connectivity that decrease active stress. Thus for contractile networks to maintain isometric tension on long timescales, they must either form stable crosslinks to prevent filament rearrangements, or they must continuously recycle network filaments (or active motors) to renew the local potential for production of active stress.

Indeed, our simulations predict that filament turnover is sufficient for maintenance of active stress. As in the passive case, they predict biphasic dependence of steady state stress on filament turnover: For short-lived filaments ($\tau_r < \tau_m$), steady state

stress increases linearly with filament lifetime because filaments have more time to build towards peak extensional stress before turning over. For longer lived filaments ($\tau_r > \tau_m$), steady state stress decreases monotonically with filament lifetime because local rearrangements decrease the mean contributions of longer lived filaments. These findings imply that for cortical networks that sustain contractile stress under approximately isometric conditions, tuning filament turnover can control the level of active stress, and there will be an optimal turnover rate that maximizes the stress, all other things equal. This may be important, for example in early development, where contractile forces produced by cortical actomyosin networks maintain, or drive slow changes in, cell shape and tissue geometry [179, 74].

For cortical networks that undergo steady state flows driven by spatial gradients of motor activity, our simulations predict that the biphasic dependencies of steady state stress and effective viscosity on filament lifetime define multiple regimes of steady state flow, characterized by different dependencies on filament turnover (and other network parameters). In particular, the \sim linear dependencies of steady state stress and effective viscosity on filament lifetime for short-lived filaments define a fast turnover regime in which steady state flow speeds are buffered against variations in filament lifetime, and are predicted to depend in a simple way on motor activity and crosslink resistance. Measurements of F-actin turnover times in cells that undergo cortical flow [199, 150, 216, 75, 64, 171] suggests that they may indeed operate in this fast turnover regime, and recent studies in *C. elegans* embryos suggests that cortical flow speeds are surprisingly insensitive to depletion of factors (ADF/Cofilin) that govern filament turnover [138], consistent with our model's predictions. Stronger tests of our model's predictions will require more systematic analyses of how flow speeds vary with filament and crosslink densities, motor activities, and filament lifetimes.

S1 Video. Extensional strain in passive networks. Movie of simulation setup shown in Fig. 3.2. Colors are the same as in figure.

S2 Video. Active networks contracting with free boundaries. Movie of simulation setup shown in Fig. 3.5. Colors are the same as in figure.

3.6 Supplemental Materials

3.6.1 Simulation and Analysis Code Available Online

All of the simulation and analysis code for generating the figures in this paper is available online. To find the source code please visit our Github repository at
<https://github.com/wmcfadden/activnet>

3.6.2 Steady-state Approximation of Effective Viscosity

We begin with a calculation of a strain rate estimate of the effective viscosity for a network described by our model in the limit of highly rigid filaments. We carry this out by assuming we have applied a constant stress along a transect of the network. With moderate stresses, we assume the network reaches a steady state affine creep. In this situation, we would find that the stress in the network exactly balances the sum of the drag-like forces from cross-link slip. So for any transect of length D, we have a force balance equation.

$$\sigma = \frac{1}{D} \sum_{\text{filaments}} \sum_{\text{crosslinks}} \xi \cdot (\mathbf{v}_i(\mathbf{x}) - \mathbf{v}_j(\mathbf{x})) \quad (3.17)$$

where $\mathbf{v}_i(\mathbf{x}) - \mathbf{v}_j(\mathbf{x})$ is the difference between the velocity of a filament, i , and the velocity of the filament, j , to which it is attached at the cross-link location, \mathbf{x} . We can convert the sum over cross-links to an integral over the length using the average density of cross-links, $1/l_c$ and invoking the assumption of (linear order) affine strain rate, $\mathbf{v}_i(\mathbf{x}) - \mathbf{v}_j(\mathbf{x}) = \dot{\gamma}x$. This results in

$$\begin{aligned}\sigma &= \frac{1}{D} \sum_{filaments} \int_0^L \xi \cdot (\mathbf{v}_i(\mathbf{s}) - \mathbf{v}_j(\mathbf{s})) \frac{ds \cos \theta}{l_c} \\ &= \sum_{filaments} \frac{\xi \dot{\gamma} L}{l_c} \cos \theta \cdot (x_l + \frac{L}{2} \cos \theta)\end{aligned}\quad (3.18)$$

Here we have introduced the variables x_l , and θ to describe the leftmost endpoint and the angular orientation of a given filament respectively. Next, to perform the sum over all filaments we convert this to an integral over all orientations and endpoints that intersect our line of stress. We assume for simplicity that filament stretch and filament alignment are negligible in this low strain approximation. Therefore, the max distance for the leftmost endpoint is the length of a filament, L , and the maximum angle as a function of endpoint is $\arccos(x_l/L)$. The linear density of endpoints is the constant $D/l_c L$ so our integrals can be rewritten as this density over x_l and θ between our maximum and minimum allowed bounds.

$$\sigma = \frac{1}{D} \int_0^L dx_l \int_{-\arccos(\frac{x_l}{L})}^{\arccos(\frac{x_l}{L})} \pi d\theta \frac{\xi \dot{\gamma} L}{l_c} \cdot \frac{D}{L l_c} \cdot (x_l \cos \theta + \frac{L}{2} \cos^2 \theta) \quad (3.19)$$

Carrying out the integrals and correcting for dangling filament ends leaves us with a relation between stress and strain rate.

$$\sigma = 4\pi \left(\frac{L}{l_c} - 1 \right)^2 \xi \dot{\gamma} \quad (3.20)$$

We recognize the constant of proportionality between stress and strain rate as a viscosity (in 2 dimensions). Therefore, our approximation for the effective viscosity, η_c , at steady state creep in this low strain limit is

$$\sigma = 4\pi \left(\frac{L}{l_c} - 1 \right)^2 \xi \quad (3.21)$$

3.6.3 Critical filament lifetime for steady state filament extension

We seek to determine a critical filament lifetime, τ_{crit} , below which the density of filaments approaches a stable steady state under constant extensional strain. To this end, let ρ be the filament density (i.e. number of filaments per unit area). We consider a simple coarse grained model for how ρ changes as a function of filament assembly k_{ass} , filament disassembly k_{diss} , ρ and strain thinning $\dot{\gamma}\rho$. Using $\rho_0 = \frac{k_{ass}}{k_{diss}}$, $\tau_r = \frac{1}{k_{diss}}$, and $\dot{\gamma} = \frac{\sigma}{\eta_c}$.

$$\frac{d\rho}{dt} = \frac{1}{\tau_r} \left(\rho_0 - \rho - \frac{\sigma\tau_r}{\eta_c(\rho)}\rho \right) \quad (3.22)$$

where $\eta_c = \eta_c(\rho)$ on the right hand side reflects the dependence of effective viscosity on network density. The strength of this dependence determines whether there exists a stable steady state, representing continuous flow. Using $\eta_c(\rho) \sim \xi \left(\frac{L}{l_c(\rho)} - 1 \right)^2$ from above (ignoring the numerical prefactor) and $\rho \sim \frac{2}{Ll_c(\rho)}$, we obtain:

$$\frac{d\rho}{dt} = \frac{1}{\tau_r} \left(\rho_0 - \rho - \frac{\sigma\tau_r}{\xi(\rho L^2/2 - 1)^2}\rho \right) \quad (3.23)$$

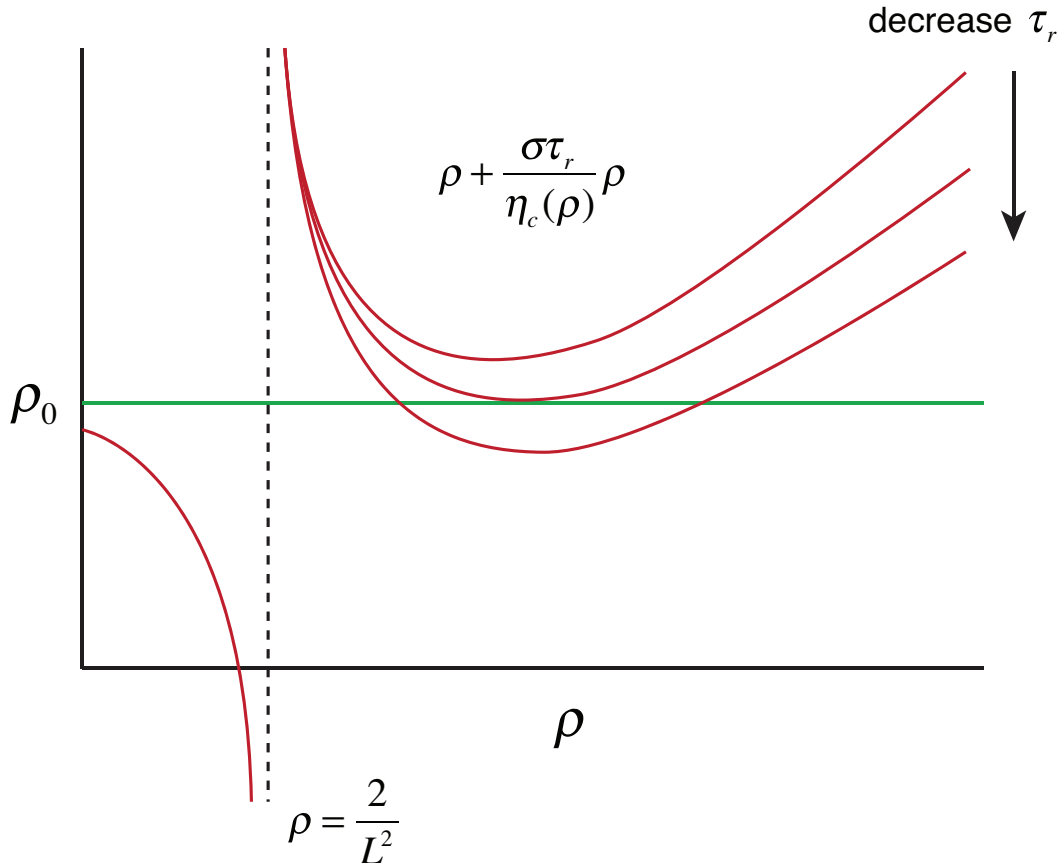


Figure 3.10: Flux balance analysis of network density. Qualitative plots of $\rho + \frac{\sigma\tau_r}{\eta_c(\rho)}\rho$ (red curves) vs ρ_0 (green line) for different values of τ_r . For sufficiently large τ_r , there are no crossings. For $\tau_r < \tau_{crit}$, there are two crossings: The rightmost crossing represents a stable steady state.

Figure 3.10 sketches the positive (ρ_0) and negative ($\rho + \frac{\sigma\tau_r}{\eta_c(\rho)}\rho$) contributions to the right hand side of Equation 6 for different values of τ_r . For sufficiently large τ_r , there is no stable state, i.e. strain thinning will occur. However, as τ_r decreases below a critical value τ_{crit} , a stable steady state appears. Note that when $\tau_r = \tau_{crit}$, $\rho + \frac{\sigma\tau_r}{\eta_c(\rho)}\rho$ passes through a minimum value ρ_0 at $\rho = \rho^*$. Accordingly, to determine τ_{crit} , we solve:

$$0 = \frac{d}{d\rho} \left(\rho + \frac{\sigma\tau_r}{\eta_c(\rho)} \rho \right) = 1 - \frac{\sigma\tau_r}{\xi(\rho L^2/2 - 1)^3} \quad (3.24)$$

From this, with some algebra, we infer that

$$\rho^* = \frac{2}{L^2} \left(1 + \left(\frac{\sigma\tau_r}{\xi} \right)^{1/3} \right) \quad (3.25)$$

and

$$\frac{\sigma\tau_r}{\eta_c(\rho^*)} = \left(\frac{\sigma\tau_r}{\xi} \right)^{1/3} \quad (3.26)$$

We seek a value for $\tau_r = \tau_{crit}$ at which

$$\rho^* + \frac{\sigma\tau_{crit}}{\eta_c(\rho^*)} \rho^* = \rho_0 \quad (3.27)$$

Substituting from above, and using $\rho_0 = \frac{2}{Ll_c}$, we have:

$$\frac{2}{L^2} \left(1 + \left(\frac{\sigma\tau_{crit}}{\xi} \right)^{1/3} \right) \left(1 + \left(\frac{\sigma\tau_{crit}}{\xi} \right)^{1/3} \right) = \frac{2}{Ll_c} \quad (3.28)$$

Finally, rearranging terms, we obtain

$$\tau_{crit} = \frac{\xi}{\sigma} \left(\sqrt{\frac{L}{l_c}} - 1 \right)^3 \quad (3.29)$$

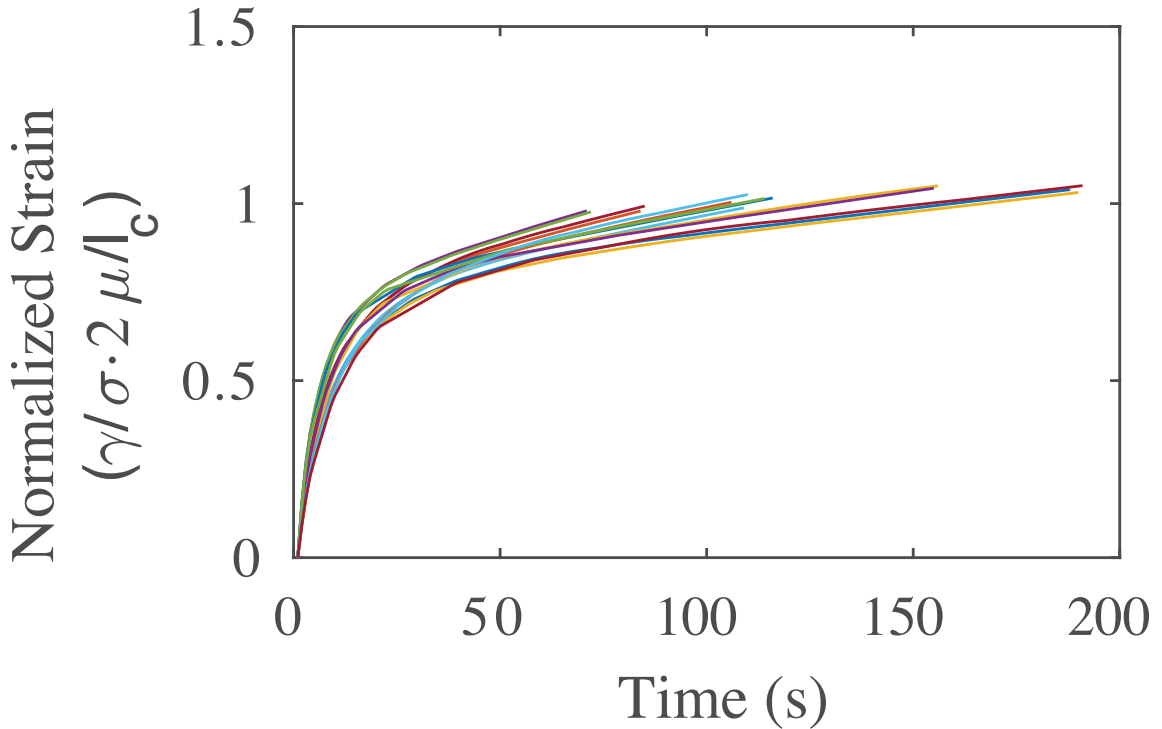


Figure 3.11: Fast viscoelastic response to extensional stress. Plots of normalized strain vs time during the elastic phase of deformation in passive networks under extensional stress. Measured strain is normalized by the equilibrium strain predicted for a network of elastic filaments without crosslink slip $\gamma_{eq} = \sigma/G_0 = \sigma/(2\mu/l_c)$.

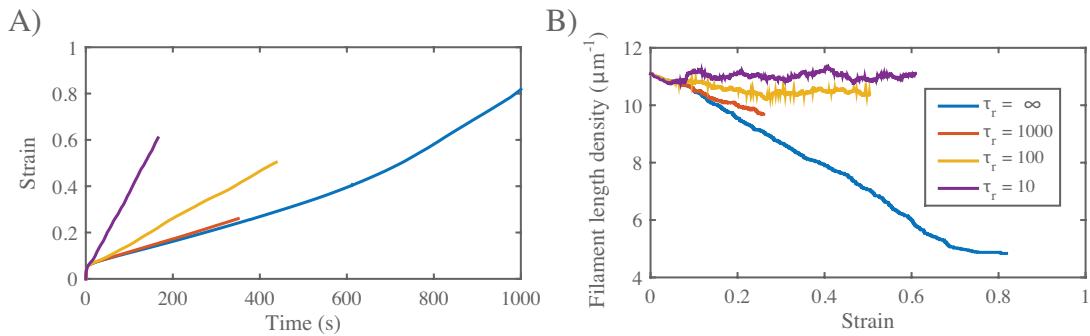


Figure 3.12: Filament turnover rescues strain thinning. **a)** Plots of strain vs time for different turnover times (see inset in (b)). Note the increase in strain rates with decreasing turnover time. **b)** Plots of filament density vs strain for different turnover times τ_r . For intermediate τ_r , simulations predict progressive strain thinning, but at a lower rate than in the complete absence of recycling. For higher τ_r , densities approach steady state values at longer times.

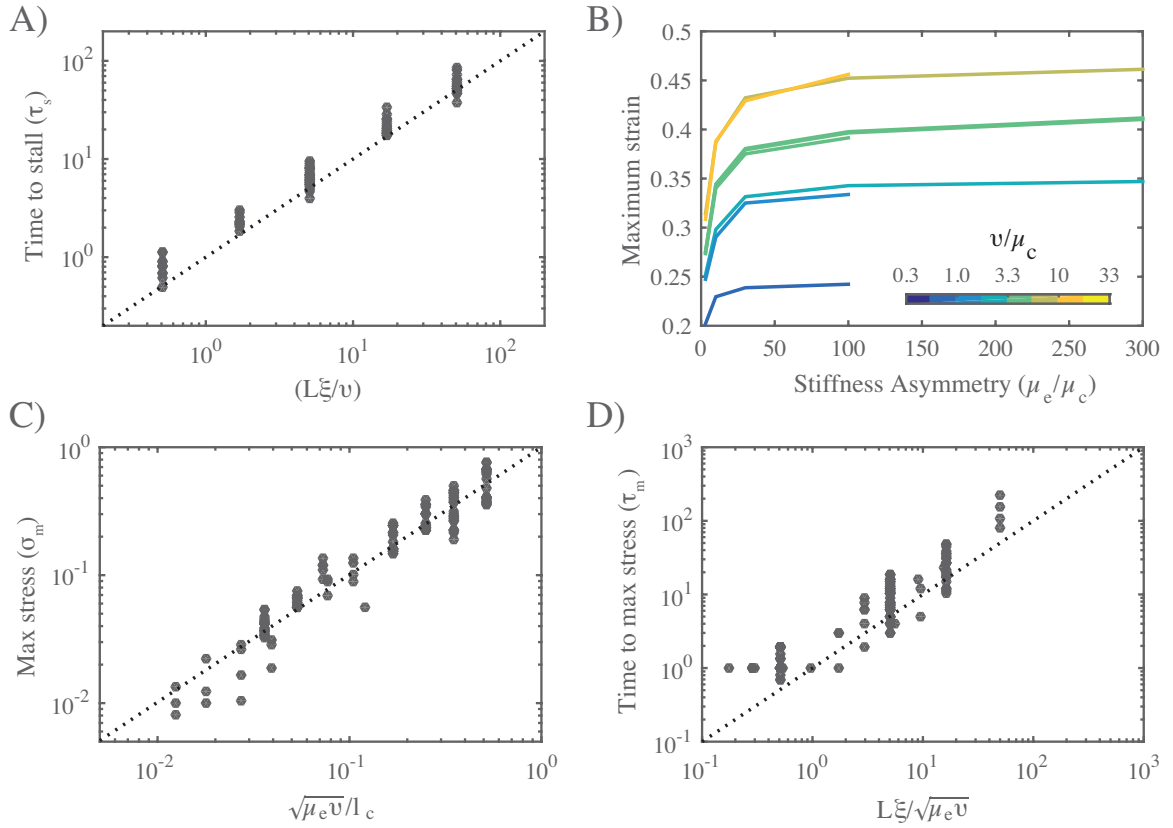


Figure 3.13: Mechanical properties of active networks. **a)** Time for freely contracting networks to reach maximum strain, τ_s , scales with $L\xi/v$. **b)** Free contraction requires asymmetric filament compliance, and total network strain increases with the applied myosin force v . Note that the maximum contraction approaches an asymptotic limit as the stiffness asymmetry approaches a ratio of ~ 100 . **c)** Maximum stress achieved during isometric contraction, σ_m , scales approximately with $\sqrt{\mu_e v}/l_c$. **d)** Time to reach max stress during isometric contraction scales approximately with $L\xi/\sqrt{\mu_e v}$. Scalings for τ_s , σ_m and τ_m were determined empirically by trial and error, guided by dimensional analysis.

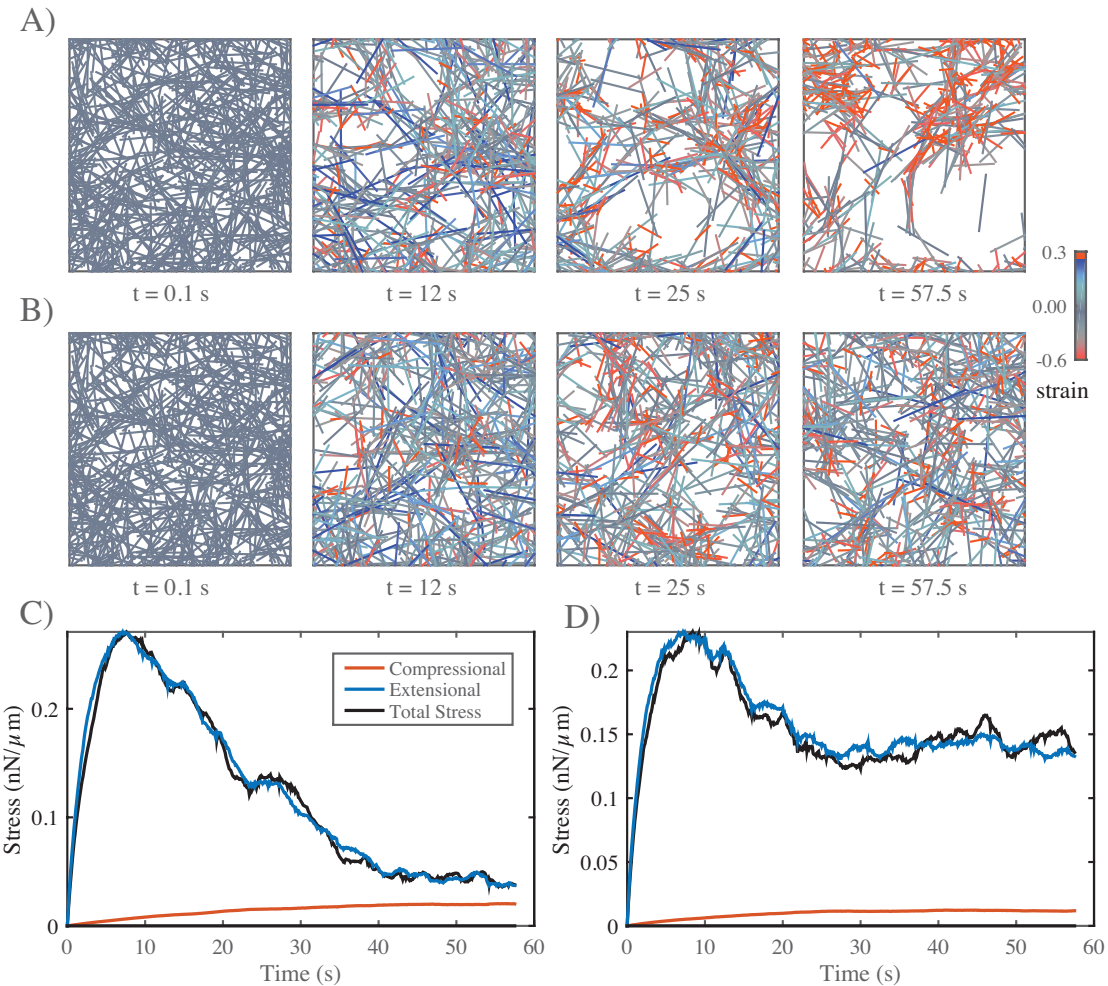


Figure 3.14: Filament turnover prevents tearing of active networks. **a)** An active network undergoing large scale deformations due to active filament rearrangements. **b)** The same network as in (a) but with a shorter filament turnover time. **c)** Plots of internal stress vs time for the network in (a). **d)** Plots of internal stress vs time for the network in (b).

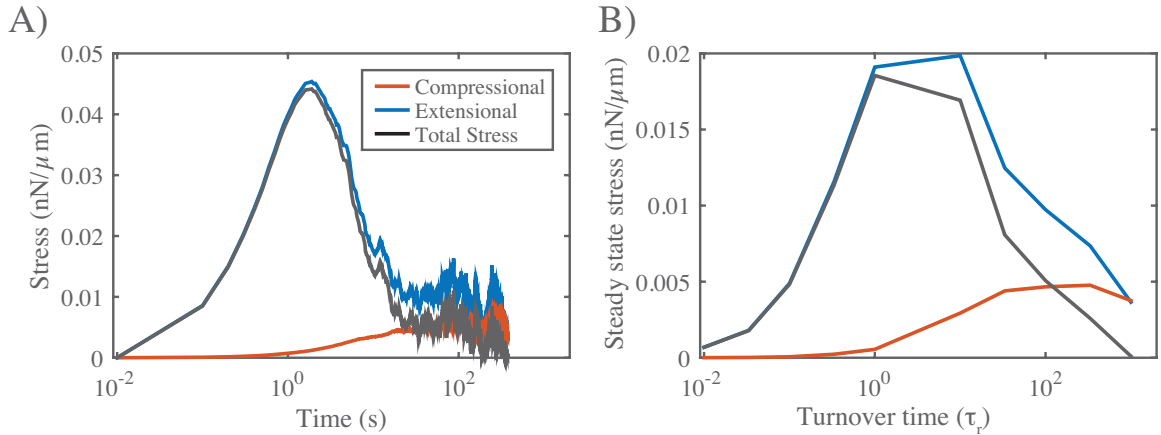


Figure 3.15: Bimodal dependence on turnover time matches bimodal buildup and dissipation of stress in the absence of turnover. **a)** Bimodal buildup of stress in a network with very slow turnover ($\tau_r = 1000\text{s}$). **b)** Steady state stress for networks with same parameters as in (a), but for a range of filament turnover times.

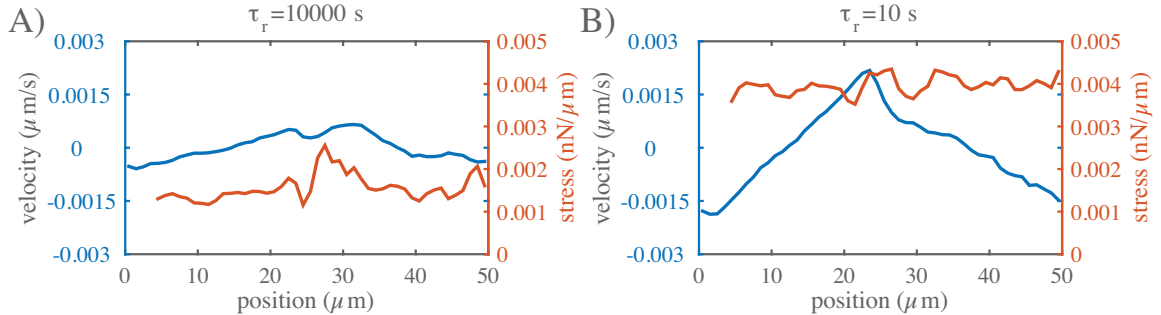


Figure 3.16: Dynamics of steady state flow. Plots of stress and strain vs position for networks in which motor activity is limited to the right-half domain and filament turnover time is either **a)** $\tau_r = 10000\text{s}$ or **b)** $\tau_r = 10\text{s}$. Blue indicates velocity while orange represents total stress, measured as described in the main text.

Table 3.2: Simulation Parameter Values

| Parameter | Fig 3 | Fig 4 | Fig S2a,b | Fig S2c,d | Fig 7 | Fig 9 |
|---------------|--------------------|-----------------------|------------------|---------------------|------------------------|------------------------|
| L | 1, 3, 5, 7, 10 | 3 | 3, 5 | 3, 5 | 5 | 3, 5, 8 |
| l_c | 0.2, 0.3, 0.5, 0.8 | 0.3, 0.5 | 0.3 | 0.15, 0.2, 0.3, 0.4 | 0.2, 0.3 | 0.15, 0.2, 0.3, 0.4 |
| μ_e/μ_c | 100 | 100 | 3 – 300 | 100 | 100 | 100 |
| μ_c | 0.01 | 0.01 | 0.01 – 0.3 | 0.001 – 0.03 | 0.01 | 0.01 |
| ξ | 0.1, 1 | 0.05, 0.1, 1 | 0.01, 0.1, 1 | 0.1, 1 | 0.1, 1, 3, 3 | 0.1, 1 |
| v | | | 0.1, 0.3, 1 | 0.1, 1 | 0.1, 1, 3 | 0.1 |
| ϕ | | | 0.25 | 0.5 | 0.25, 0.75 | 0.25 |
| τ_r | 0.0002 – 0.01 | 0.1 – 10 ⁴ | | | 0.01 – 10 ³ | 0.01 – 10 ³ |
| σ | | 0.00003 – 0.005 | | | | |

CHAPTER 4

A MODEL OF UPSTREAM ACTOMYOSIN REGULATORS IN PULSED CONTRACTIONS

4.1 Preface

This chapter has been submitted to the BioRxiv preprint server with the following citation: Robin FB, Michaux JB*, McFadden W, Munro EM. Excitable RhoA dynamics drive pulsed contractions in the early *C. elegans* embryo. BioRxiv (2016) Published online September 21, 2016. <http://dx.doi.org/10.1101/076356>.

This work was done in collaboration with François Robin and Jonathan Michaux in Edwin Munro's lab at the University of Chicago. François performed the single-molecule imaging experiments, particle tracking, and statistical analyses documented in Figures 2.2, 2.3, 2.10, and 2.11. Jon performed the remainder of experiments.

My contribution was the analysis of the mathematical model presented in Figure 4.9 and Section 4.4.6. In addition, I wrote the code for fitting the model parameters using pulse time-series data, via either a piece-wise fitting approach or fitting the full function. For a more detailed analysis of the modeling and fitting work the reader may refer to the Appendix D.

4.2 Abstract

Pulsed actomyosin contractility underlies diverse modes of tissue morphogenesis, but the mechanisms that generate pulsed contractions are still poorly understood. Here, we combine quantitative imaging with genetic perturbations and mathematical modeling to identify a core mechanism for pulsed contractility in early *C. elegans* embryos. We show that pulsed accumulation of actomyosin is governed almost entirely by local control of assembly and disassembly downstream of RhoA. Pulsed activation and

inactivation of RhoA precedes, respectively, the accumulation and disappearance of actomyosin, and persists in the near complete absence of Myosin II. Autocatalytic activation of RhoA underlies rapid pulse initiation, while delayed accumulation of the RhoA GTPase activating proteins (GAPs) RGA-3/4 provides negative feedback to terminate each pulse. Mathematical models, tightly constrained by our experiments, confirm that this combination of positive and negative feedback is sufficient to generate locally pulsatile RhoA dynamics and reproduce the observed waveform of RhoA activation and RGA-3/4 accumulation. We propose that excitable RhoA dynamics are a common driver for pulsed contractility that can be tuned or coupled to actomyosin dynamics in different ways to produce a diversity of morphogenetic outcomes.

4.3 Introduction

Pulsed contractility is a widespread mode of actomyosin contractility expressed by many non-muscle cells in which transient accumulations of F-actin and Myosin II accompany local contractions of the cell surface. Pulsed contractions were first identified in the polarizing *C.elegans* zygote [146], and have now been documented in a wide variety of embryonic and extra-embryonic epithelia [? 17, 166, 42, 136, 189] and mesenchymal cells [99]. A similar phenomenon known as cell shape oscillations have been observed in many cultured cells [186, 177, 94]. Pulsed contractions produce transient shape changes that can be biased or rectified in different ways to produce distinct morphogenetic outcomes such as tissue invagination [136], tissue elongation [166, 112?], epithelial tissue closure [189] and wound healing [167]. During embryonic development, pulsed contractions may represent an adaptation to accommodate rapid cell and tissue deformations while maintaining overall tissue integrity [211]. In other contexts, such as in many cultured cells, shape oscillations may represent an aberrant behavior that manifests when cells lose normal adhesion to their substrates [177, 158], or when microtubules are depolymerized [93, 94, 164, 219, 160, 21] or when contractile tension is very high during cytokinesis [186].

Despite their widespread occurrence and increasing evidence for their functional relevance, the mechanisms that initiate and terminate pulsed contractions remain

poorly understood. From a dynamical perspective, pulsed contractions represent a form of excitable behavior, exemplified by action potentials in neuronal cells [87] or pulses of intracellular calcium release observed in many cell types [72]. Theoretical studies highlight two key ingredients for excitability: positive feedback to drive rapid upswing in activity, and delayed negative feedback to bring it back down again. A key challenge is to identify the specific modes of positive and negative feedback that drive pulsed contractions.

Multiple forms of positive feedback could contribute to initiating pulsed contractions. For example, local actomyosin-based contraction could promote further accumulation of actomyosin through mechanosensitive motor-filament binding [? 59, 168, 53, 182], by enhancing actin filament assembly and/or stability [77, 45], or by transporting and concentrating actomyosin and/or its upstream activators [144, 48]. Alternatively, dynamic clustering of F-actin and/or Myosin II by scaffolding proteins such as Anillin could promote Myosin II recruitment and focal contraction [131]. Finally, autocatalytic activation of upstream regulators such as RhoA could drive local excitation, independent of, or in addition to, myosin-based tension or network contraction [229, 144, 13]. Similarly, multiple forms of delayed negative feedback could contribute to terminating pulses, including progressive buildup of steric or elastic resistance to further contraction [48], or contraction-mediated disassembly, or delayed recruitment of disassembly factors or inhibitors of Myosin II or RhoA [144, 97, 13].

Here we combine quantitative imaging with experimental manipulations and mathematical modeling to identify the dynamical basis for pulsed contractility in the early *C.elegans* embryo. Using single-molecule imaging and particle tracking analysis, we provide definite evidence that the initiation of pulsed contractions does not involve or require local redistribution of actomyosin or its upstream activators. Instead, pulsed contractions are driven by local pulses of RhoA activity, which feed forward to control local accumulation of downstream targets F-actin, Myosin II and Anillin. We present evidence that pulsed accumulation of RhoA is governed by locally excitable RhoA dynamics: local autocatalytic activation of RhoA drives the rapid upswing of RhoA activity during pulse initiation, while F-actin-dependent recruitment of the redundantly acting RhoA GTPase activating proteins (GAPs) RGA-3/4 provide delayed

negative feedback to terminate the pulse. A minimal model, sharply constrained by our experimental data, suggests that this combination of feedback is sufficient to generate locally excitable or oscillatory RhoA dynamics and to explain quantitatively the temporal dynamics of RhoA activation and RGA-3/4 accumulation during each pulse. We propose that excitable RhoA dynamics defines a core mechanism for pulsed contractility and suggest that this mechanism may be tuned or filtered through downstream effectors to control the size or spacing or lifetime of pulsed contractions.

4.4 Results

Pulsed contractions were originally described in *C.elegans* during interphase in the polarizing zygote P0 (Figure 4.1A-C, individual pulses indicated by white arrowheads in Figure 4.1B; [146]). In these cells, pulsed contractions are associated with transient deep invaginations of the cell surface (magenta arrows in Figure 4.1A,B); this makes it more difficult to quantify local changes in density of cortical factors during individual pulses, because these measurements could be confounded by movements of the cortex in/out of the plane of focus. Therefore, we focused on pulsed contractions that occur at the two-cell stage in the anterior blastomere known as AB (Figure 4.1D-F, individual pulses indicated by white arrowheads in Figure 4.1E). As in P0, pulsed contractions in AB involve transient accumulations of F-actin and Myosin II; they are associated with transient local contractions of the actomyosin cortex (Figure 4.1F), but they are not associated with pronounced invaginations of the cell surface.

4.4.1 Single-molecule analysis of actomyosin dynamics during pulsed contractions

As a key step towards distinguishing different mechanisms for pulsed contractions, we used single-molecule imaging and single-particle tracking analysis to quantify the relative contributions of local turnover and redistribution to changes in F-actin and Myosin II density during individual pulses. As described previously [172], we used RNAi against GFP to obtain embryos expressing single molecule levels of Actin::GFP

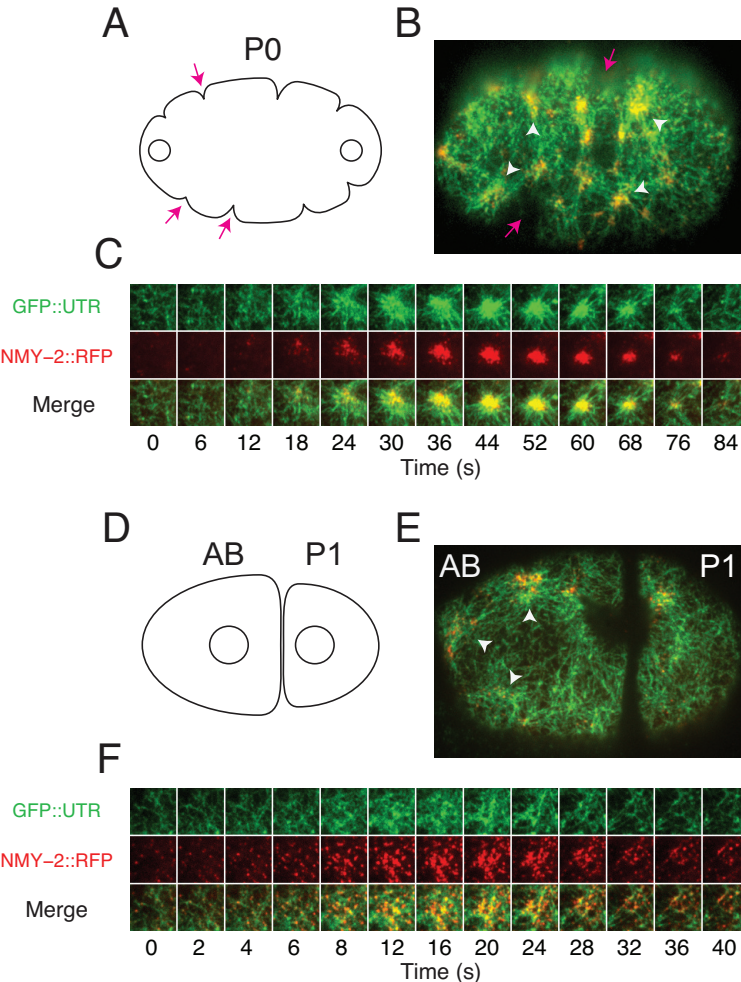


Figure 4.1: Actomyosin pulses in 1 and 2-cell stage embryos. (A) Schematic view of the zygote P0 during early interphase. Open circles represent the two pronuclei. (B) Micrograph of P0 in early interphase expressing GFP::UTR and NMY-2::RFP. In (A) and (B), white arrowheads indicate individual pulses and magenta arrows indicate membrane invaginations (ruffles). (C) Time evolution of a single pulse in P0. The square region measures $\sim 6.4\mu\text{m}$ by $6.4\mu\text{m}$. The time delay between frames is 6s for the first 6 frames, and 8s thereafter. (D) Schematic of an embryo at the early 2-cell stage, showing the anterior blastomere AB and the posterior blastomere P1. Open circles represent the interphase nuclei. (E) Micrograph of an early two-cell stage embryo expressing GFP::UTR and NMY-2::RFP. White arrowheads indicate individual pulses (F) Time evolution of a single pulse. The square region measures $\sim 6.4\mu\text{m}$ by $6.4\mu\text{m}$. The time delay between frames is 2s for the first 5 frames, and 4s thereafter.

or of the non-muscle myosin heavy chain fused to GFP (NMY-2::GFP) over the endogenous proteins (Figure 4.2A). We combined near-total internal reflection fluorescence (TIRF) imaging with single-molecule detection and tracking to measure the appearance, motion and disappearance of single-molecule speckles (Figure 4.2A-C, [172]). We assumed, with others [217, 208], that single molecule appearance and disappearance events report directly on local rates of filament assembly and disassembly. We have shown previously that rates of turnover measured by single-molecule tracking agree well with those measured from single-molecule data by fitting kinetic models to photobleaching curves ([172], Materials and Methods).

We then devised new methods to measure simultaneously: (a) single molecule appearance rates, disappearance rates and densities, and (b) local rates of cortical deformation, on a moving and deforming patch of cortex during individual pulsed contractions (Figure 4.10; see Materials and Methods for details). Briefly, we identified a reference frame for each pulse near the onset of contraction; within that frame, we identified a polygonal region of interest containing the contracting patch (dashed blue polygon in Figure 4.2A; hereafter the patch); we propagated the patch forward and backwards in time by extrapolating the displacements of tracked particles on or near its boundary (Figure 2.2D, Figure 4.10). We then measured local deformation of the patch as frame-to frame changes in patch area, or by estimating a local strain rate from frame-to-frame displacements of the individual particles, with similar results in both cases (Figure 2.2E; Figure 4.11A-C; Materials and Methods). At the same time, we measured the number of molecules and single-molecule appearance and disappearance rates within the patch over time (Figure 2.2F-H). Finally, we aligned single-molecule measurements with respect to the onset or termination of individual contractions to produce a dynamical signature of actin assembly, disassembly and deformation over the lifetime of a pulse (Figure 4.3A-D; Figure 4.11D-F). These measurements allowed us to distinguish, cleanly, changes in single-molecule densities due to local assembly and disassembly from those due to local contraction (or expansion) of the cortical patch.

If pulses are initiated by positive feedback in which local contraction concentrates actomyosin and/or its upstream regulators, then the onset of actomyosin accumula-

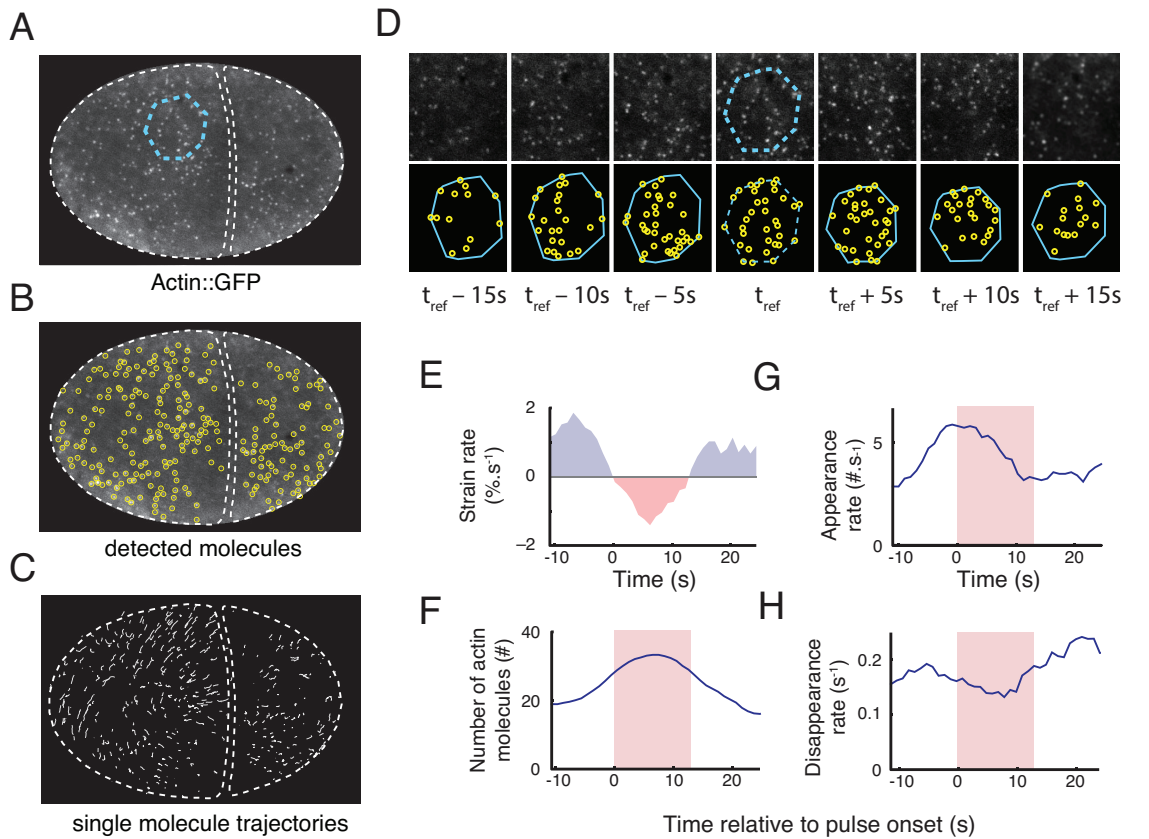


Figure 4.2: Single-molecule analysis of actin network assembly, disassembly and deformation during individual pulsed contractions. One frame of a time lapse sequence taken from an embryo expressing low levels of Actin::GFP. A patch of cortex undergoing a pulse is identified from the time lapse sequence, and outlined in cyan. (B) Automatic particle detection of single-molecules from the image in (A). (C) Trajectories of the molecules displayed in (B) that were tracked for longer than 2s. (D) A polygonal region of interest identified at time $t = t_{ref}$, in (A) (dashed cyan polygon) is propagated forward and backward in time using the trajectories of tracked particles (see Materials and Methods). (E-H) Simultaneous measurements of single molecule dynamics and patch deformation over time. (E) Strain rate, measured using the particle-based method (see Materials and Methods). (F) Number of actin molecules in the patch. (G-H) Appearance rates (G) and disappearance rates (H) of actin molecules. Red shading in (F-H) indicates the time period in which the cortex is contracting locally (strain rate > 0).

tion should coincide with the onset of contraction. Contradicting this expectation, we found that, on average, Actin:GFP began to accumulate ~ 5 s before the onset of contraction (Figure 4.3B,F; Figure 4.11A-C), during a period of time in which the cortex was locally expanding (Figure 4.3A). Approximately 30% of the total increase in Actin::GFP single molecule density measured during a pulse occurred before the onset of contraction (Figure 4.11A-C). This initial accumulation was due entirely to a net imbalance of assembly and disassembly (Figure 4.3E): Before the onset of contraction, assembly rates increased (Figure 4.3C) and disassembly rates decreased (Figure 4.3D), leading to a sharp increase in the net rate of single molecule accumulation that peaked at the onset of contraction (Figure 4.3E). During the contraction phase itself, the rate of change in single-molecule densities was determined almost entirely by a net imbalance of assembly/disassembly, with a very minor ($\pm 6\%$) contribution from contraction itself (Figure 4.3E). Assembly rates decreased steadily, and disassembly rates increased steadily, such that a transition from net assembly to net disassembly (and from increasing density to decreasing density) occurred ~ 7 s sec after the onset of contraction (Figure 4.3E). We obtained very similar results in embryos depleted of ARX-2, an essential subunit of the ARP2/3 complex (Figure 4.12), suggesting that our results are not biased by selective incorporation of Actin::GFP into branched vs unbranched F-actin [34].

Single-molecule analysis of GFP-tagged Myosin II (NMY-2::GFP) revealed local assembly/disassembly dynamics that were strikingly similar to those measured for GFP::Actin. (Figure 4.3G-J). On average, the density of single molecules of NMY-2::GFP began to increase ~ 6 s before the onset of contraction during a period of local cortical expansion (Figure 4.3H), and approximately 50% of this increase occurred before the onset of contraction. As observed for GFP::Actin, the upswing in Myosin II before the onset of a contraction was associated with both a sharp increase in appearance rates and a sharp decrease in disappearance rates (Figure 4.3I,J); the net rate of increase peaked at the onset of contraction, and during the contraction phase, the appearance and disappearance rates returned steadily towards baseline levels. In summary, we find that changes in actomyosin density during pulsed contractions are governed primarily by dynamic local imbalance of F-actin and Myosin II appearance

and disappearance rates. A large fraction of the increase in F-actin and Myosin II density during each pulse occurs before the onset of contraction, and local contraction accounts for only a minor fraction of the subsequent density increase during the contraction phase itself. We conclude that changes in actomyosin density during pulsed contractions are governed primarily by dynamic modulation of assembly and disassembly, not by local clustering of these factors or by dynamical coupling of contraction and advection.

4.4.2 Pulsed activation of RhoA drives the pulsed accumulation of F-actin and Myosin II

The observation that F-actin and Myosin II accumulate with very similar kinetics during pulsed contractions suggests that their accumulation is driven by a common upstream regulator. An obvious candidate is the small GTPase RhoA (encoded by *rho-1* in *C.elegans*), which recruits and/or activates downstream effectors including formins, Rho Kinase (ROCK) and Anillin to control F-actin assembly and Myosin II activation in a variety of cell types [88, 160]. RhoA activity is required for pulsed contractions in P0 [142, 184, 204], and a biosensor for active RhoA derived from the RhoA binding domain of Anillin (henceforth GFP::AHPH) localizes to contractile foci in the zygote [203].

To determine if pulsed activation of RhoA accompanies pulsed contractions, we used a strain co-expressing GFP::AHPH [204] with an RFP-tagged version of the myosin heavy chain (NMY-2::RFP) to co-monitor RhoA activity and Myosin II accumulation during individual pulses in AB. We observed a striking correlation between pulsed accumulation of GFP::AHPH and NMY-2::RFP during individual pulsed contractions (Figure 4.4A-C). GFP::AHPH accumulated rapidly within a broad domain that prefigured the initial accumulation of NMY-2::RFP, reached a peak near the onset of visible contraction, and then began to disappear before NMY-2::RFP (Figure 4.4B,C). The initial accumulation of GFP::AHPH was diffuse, whereas NMY-2::RFP accumulated as discrete particles that increased in number and size before contracting together into a smaller and tighter central domain. During the falling phase of

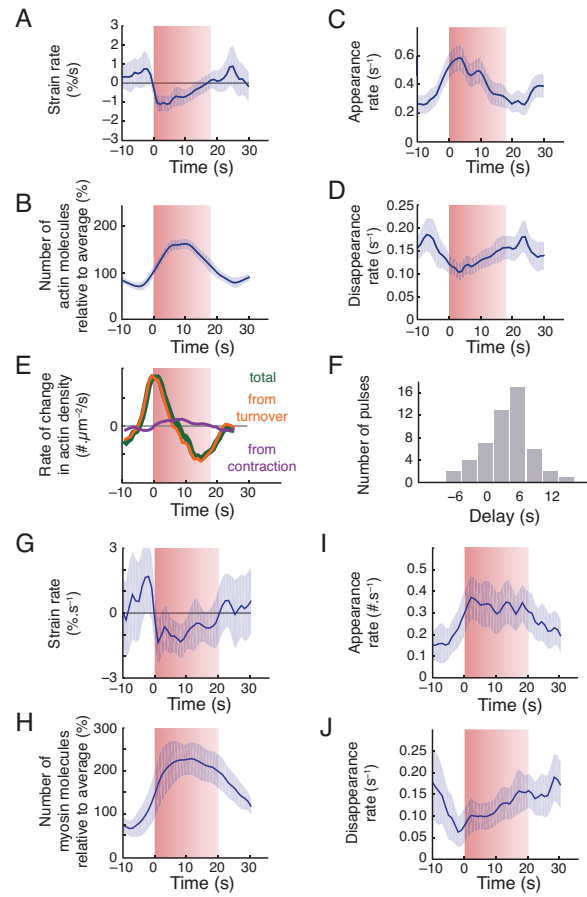


Figure 4.3: Spatiotemporal modulation of assembly and disassembly drives transient accumulation of F-actin and Myosin II during pulsed contractions. (A-D) Data from individual pulses, aligned with respect to the onset of contraction and then averaged to display particle-based strain rate (A), numbers of actin molecules (scaled by the average number for each pulse) (B) appearance rate (C), and disappearance rate (D) versus time. (E) Total rate of change in actin density (green) and the individual contributions to rate of change from turnover and surface contraction. (F) Distribution of time delays between the initiation of contraction and actin accumulation. Data in (A-F) were averaged over 42 pulses, collected in 8 embryos. (G-J) Average myosin dynamics synchronized with respect to time at which myosin density reached peak levels during a pulse, displaying particle-based strain rate (G), number of molecules (scaled to the average number for each pulse) (H), appearance rate (I) and disappearance rate (J) versus time. Data were averaged over 30 pulses, collected in 5 embryos. Error bars: 95% confidence interval.

each pulse, the diffuse pool of GFP::AHPH at the outer edges of the initial domain disappeared rapidly, while a smaller and more persistent fraction of GFP::AHPH co-localized with NMY-2::RFP particles in the central domain (yellow arrows in Figure 4.4B; Figure 4.13).

To quantify these observations, we aligned data for multiple pulses from embryos co-expressing NMY-2::RFP and GFP::AHPH (see Materials and Methods). For each pulse, we smoothed and thresholded the NMY-2::RFP signal to identify a region of interest (ROI) containing high levels of NMY-2::RFP just before the onset of contraction (Figure 4.12A; Materials and Methods). We propagated this ROI forward and backwards in time (see Figure 4.12A, Materials and Methods), and then measured the mean intensities of the RFP and GFP signals within the ROI before, during and after the pulse (Figure 4.12B,C). We normalized these data with respect to the minimum (pre-contraction) and maximum intensities measured during this interval, then aligned data for multiple pulses with respect to the time point at which NMY-2::RFP reached 25% of its maximum intensity (Figure 4.4D, Materials and Methods). These aligned data confirm that sharp increases and decreases in RhoA activity precede, respectively, the appearance and disappearance of NMY-2::RFP (Figure 4.4D). On average, GFP::AHPH reaches 25% of its maximum intensity 8.6 +/- 3.9 seconds before NMY-2::RFP (Figure 4.4E), and falls below 75% of its maximum intensity 11.1 +/- 3.5 seconds before NMY-2::RFP (Figure 4.4F).

We used the same approach to align data for embryos co-expressing NMY-2::RFP and either the F-actin binding domain of Utrophin fused to GFP (GFP::UTR); a marker for F-actin [28, 204], or GFP::Anillin [?]. Using NMY-2::RFP as the common reference to co-align data for NMY-2::RFP, GFP::AHPH, GFP::UTR and GFP::Anillin, we found that like Myosin II, F-actin and Anillin accumulate and dissipate during pulsed contractions with a significant delay relative to GFP::AHPH (Figure 4.4D-F, Figure 4.13A-D). Thus local activation and inactivation of RhoA precedes and times the accumulation and disappearance of its downstream targets.

Finally, we used the time points at which NMY-2::RFP intensities (Figure 4.4D) and single molecule densities of Myosin::GFP (Figure 4.3H) reached 25% of their peak values to align the time course of RhoA activation with respect to the onset of

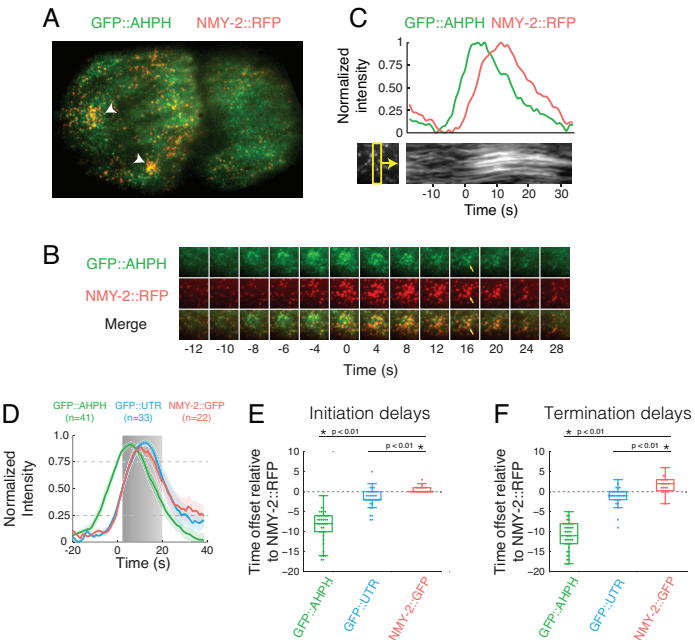


Figure 4.4: Local pulses of RhoA activation underlie pulsed accumulation and disappearance of F-actin and Myosin II. (A) Micrograph of a 2-cell stage embryo expressing GFP::AHPH as a reporter for RhoA activity, and NMY-2::RFP. (B) Temporal dynamics of GFP::AHPH and NMY-2::RFP accumulation during a single pulse. The square region measures $\sim 5.3\mu\text{m}$ by $5.3\mu\text{m}$. The time between frames is 2s for the first five frames, and 4s thereafter. (C) Above: Normalized fluorescence intensities of GFP::AHPH, and NMY-2::RFP. Below: A kymograph showing that local contraction (concerted movements of myosin puncta) begins after the accumulation of GFP::AHPH. The yellow box below left indicates the region used to generate the kymograph. (D) Comparison of averaged normalized fluorescence intensities vs time for active RhoA (GFP::AHPH), Myosin (NMY-2::GFP) and F-actin (GFP::UTR) from two-color data, co-aligned with respect to a common reference signal (NMY-2::RFP). Data were co-aligned with respect to the time at which NMY-2::RFP reaches 25% threshold. Hued regions report 95% confidence intervals. (E) Distribution of the delays between the onset of accumulation of NMY-2::RFP, and the onset of accumulation of GFP::AHPH, NMY-2::GFP and GFP::UTR. Onset of accumulation was measured as the time at which normalized probe intensity rose above 25% of its maximal level. (F) Distribution of the delays between the onset of disappearance of NMY-2::RFP, and the onset of disappearance of GFP::AHPH, NMY-2::GFP and GFP::UTR. Onset of disappearance was measured as the time at which normalized probe intensity fell below 75% of its maximal level. In boxplots, the central mark represents the median, the box indicates the 25th and 75th percentile, and the whiskers mark the minimum and maximum values

contraction as measured by single molecule imaging. This analysis shows that RhoA activity peaks just before the onset of contraction (indicated by gray box in Figure 4.4D) and thus local concentration of active RhoA by advection-contraction [144] cannot explain the rising phase of RhoA activation in *C.elegans* embryos. By extension, the same analysis reveals that RhoA activity peaks and begins to fall at a point where F-actin and Myosin II disappearance rates are at a minimum (Figure 4.3D,J); thus factors other than cortical actomyosin disassembly drive the disappearance of active RhoA at the end of a pulse.

Using the same two-color image analysis, we confirmed that pulses of RhoA activity accompany pulsed contractions in the zygote P0. To remove the potentially confounding effects of large scale cortical flows that occur during zygotic polarization, we performed these measurements in embryos depleted of the centrosomal factor SPD-5 [146, 76], which exhibit pulsed contractions but lack cortical flows. In *spd-5*(RNAi) P0 zygotes, as in wild-type AB cells, increases and decreases in local GFP::AHPH intensity preceded the rise and fall of NMY-2::RFP (Figure 4.14A-F) and to a lesser extent GFP::UTR (Figure 4.14D-F) and GFP::Anillin (Figure 4.13E-H). As in AB, the initial accumulation of GFP::AHPH was broad and diffuse while a more persistent pool of GFP::AHPH remained concentrated within punctae that co-localized with NMY-2::RFP within a more central region of the initial domain (yellow arrows in Figure 4.14B).

4.4.3 Pulsed activation of RhoA does not require Myosin II.

Recent studies suggested that active RhoA and Myosin II accumulate with similar timing during pulsed apical contractions in the *Drosophila* germband, and that Myosin II activity is required for pulsed accumulation of active RhoA [144]. Our observation that active RhoA peaks before the onset of contraction rules out models in which local contraction concentrates RhoA, or its upstream activators, to initiate pulses. However, it remains possible that Myosin II activity is otherwise required for pulsed activation of RhoA. To test this possibility, we used RNAi to deplete the Myosin heavy chain NMY-2 in a strain co-expressing transgenic GFP::AHPH and

NMY-2 tagged with mKate2 at the endogenous locus by CRISPR-mediated homologous recombination (NMY-2::mKate2, a kind gift of Dan Dickinson). We used RNAi against NMY-2 to deplete NMY-2::mKate2 to the point where only a few single NMY-2::mKate particles could be detected at the P0 cortex using imaging conditions that allow robust detection of single molecules (Figure 4.5A). Under these conditions, in *nmy-2* RNAi zygotes, we still observed transient focal accumulations of GFP::AHPH (Figure 4.5A,B). These accumulations were roughly similar in size and spacing to those observed in *spd-5* (RNAi) zygotes during polarity establishment, and many occurred on patches of cortex in which fewer than two discrete particles of NMY-2::mKate were detected, excluding any possible contribution from contractile tension generated by Myosin II (Figure 4.5B). Aligning GFP::AHPH intensities vs time across many pulses in *nmy-2*(RNAi) zygotes revealed a mean time course for AHPH accumulation and dissipation that is comparable to that measured for the diffuse pool of GFP::AHPH in *spd-5* (RNAi) zygotes (Figure 4.5C). Indeed, pulses terminated more rapidly in *nmy-2*(RNAi) than in *spd-5* (RNAi) zygotes, implying that neither Myosin II activity nor its inhibition is required for rapid pulse termination. We conclude that Myosin II is not required for locally pulsatile activation of RhoA in *C.elegans* embryos, although myosin activity may shape spatiotemporal pulse dynamics (see Discussion).

4.4.4 RhoA feeds back locally to promote its own activity and this is required for pulse initiation.

A recent study described propagating cortical waves of RhoA activity in echinoderm oocytes and frog embryos; these appear to be driven by locally excitable RhoA dynamics in which RhoA feeds back positively to promote its own activation and negatively, through local F-actin assembly, to promote delayed inactivation [13]. We hypothesized that a similar combination of positive and negative feedbacks could drive local pulses of RhoA activity in *C.elegans* embryos. Plotting the rate of change in GFP::AHPH intensity vs intensity during the rising phase of individual pulses in either P0 or AB cells revealed a sharp increase in the rate of RhoA activation with increasing RhoA (Figure 4.6A). This is consistent with a scenario in which active

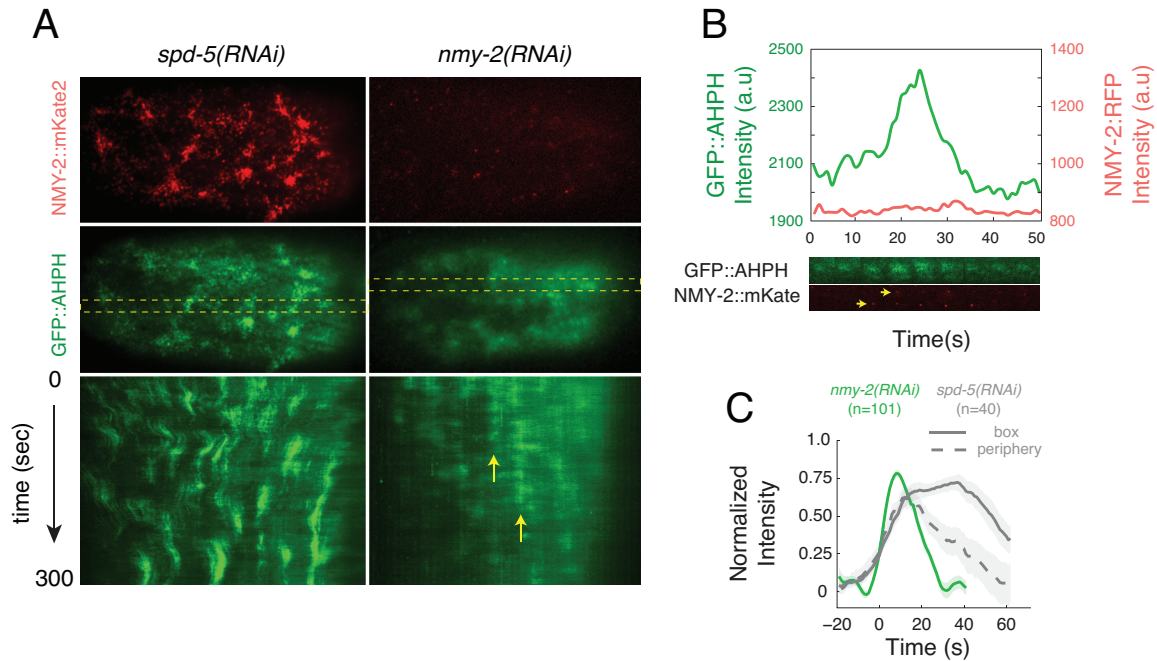


Figure 4.5: Myosin II is not required for the pulsed activation of RhoA.

(A) Comparison of pulse dynamics in zygotes expressing GFP::AHPH and NMY-2::mKATE and treated with either *spd-5(RNAi)* or *nmy-2(RNAi)*. Top panels show myosin localization (NMY-2::mKATE), middle panels show RhoA activity (GFP::AHPH). Bottom panels are kymographs showing GFP::AHPH dynamics over time. Dashed yellow rectangles in middle panel indicate the regions from which the kymographs were made. Vertical yellow arrows indicate a region undergoing repeated pulses. Intensities were scaled identically for *spd-5(RNAi)* and *nmy-2(RNAi)* zygotes.

(B) Top: Mean intensities of NMY-2::mKATE (red) and GFP::AHPH (green) vs time for a single pulse in an *nmy-2(RNAi)* zygote. Bottom: sequential snapshots of the region undergoing the pulse showing NMY-2::mKATE (red) and GFP::AHPH (green) distributions. Yellow arrowheads indicate the 1-2 particles that can be detected in the region undergoing a pulse.

(C) Mean intensity of GFP::AHPH over time in *nmy-2(RNAi)* and *spd-5(RNAi)* zygotes, aligned with respect to the time at which the normalized signal reaches 25% of its maximum value. For *spd-5* (*RNAi*) zygotes, the signal was measured either within the entire boxed region in which each pulse occurred or at its periphery (see Figure 4.12 for details). Hued regions report 95% confidence intervals.

RhoA feeds back positively to promote further activation of RhoA. However, it could also reflect pulsed activation of RhoA (without feedback) by an upstream activator. To distinguish these possibilities, we used RNAi to progressively deplete embryos of RhoA. If the time course of RhoA activation is dictated by an upstream activator, we should observe pulsed accumulation of GFP::AHPH as long as it remains detectable at the cortex. In contrast, if positive feedback of RhoA onto itself drives pulse initiation, then there should be an abrupt loss of pulsing below a threshold level of RhoA. Consistent with the latter expectation, we observed an abrupt transition from pulsed to non-pulsed RhoA accumulation after \sim 12 hours of feeding (Figure 4.6B,C). In zygotes that lacked pulsed RhoA accumulation, we could still readily detect robust RhoA-dependent cortical flows [142, 185] during polarity establishment (dashed yellow lines in Figure 4.6B) and localized accumulation of active RhoA prior to cytokinesis (cyan arrowheads in Figure 4.6B). Together, these observations support the idea that RhoA feeds back positively to amplify its own activation and that sufficiently strong feedback is required to generate local pulses of high RhoA activity.

4.4.5 Delayed accumulation of the Rho GAPs RGA-3/4 underlies pulse termination.

What terminates RhoA activity during each pulse? Our results imply that local termination of RhoA activity at the end of a pulses does not require Myosin II activity or (by extension) its local inhibition by Myosin phosphatase [162, 161?], nor is it timed by cortical disassembly. Previous studies identified the redundant RhoA GAPs RGA-3 and RGA-4 as inhibitors of RhoA activity during polarization and cytokinesis [184, 228, 183, 204]. A YFP-tagged RGA-3 transgene accumulates at the cortex in early embryos [184], and simultaneous depletion of RGA-3 and RGA-4 leads to hyper activation of RhoA and hypercontractility during zygotic polarization [184, 183, 204]. We wondered, therefore, if RGA-3/4 could provide negative feedback to terminate RhoA activity during individual pulses. To test this possibility, we first imaged embryos co-expressing GFP::RGA-3 and NMY-2::mKATE. Focusing on AB, and using 2-color analysis as above, we confirmed that GFP::RGA-3 is present

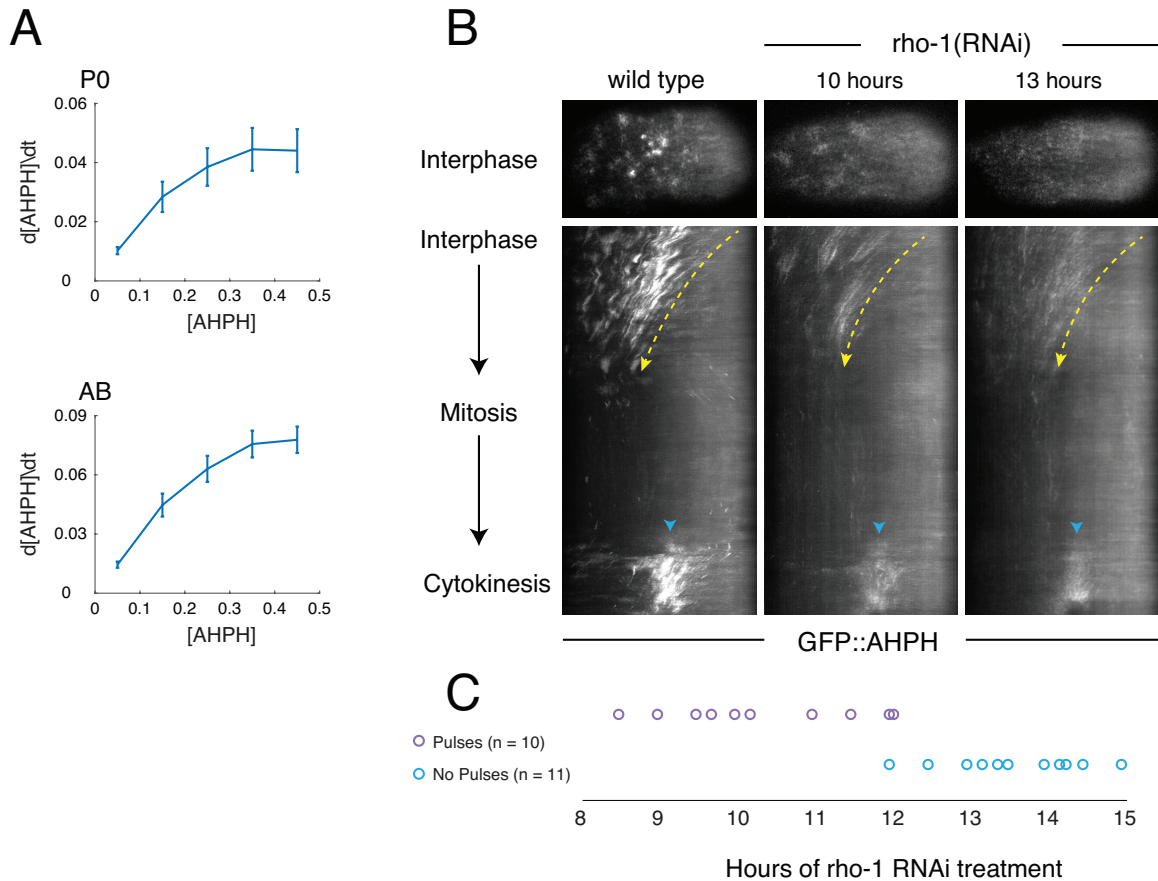


Figure 4.6: RhoA activation is autocatalytic. (A) The time derivative of normalized RhoA activity (GFP::AHPH) plotted vs normalized activity during the early phase of pulse initiation in P0 (top panel, $n = 40$ pulses) and AB (bottom panel, $n = 41$ pulses). Error bars: 95% confidence interval. (B-C) Analysis of pulse dynamics in embryos progressively depleted of RHO-1 by RNAi. (B) Top panels show GFP::AHPH distributions in interphase embryos from mothers subjected to no (wild type), 10 hours and 13 hours of $\rho\text{-}1$ (RNAi). Middle panels show kymographs from the same embryos illustrating spatiotemporal dynamics of GFP::AHPH from interphase through cytokinesis. Dashed yellow lines indicate approximate pattern of cortical flow. Cyan arrowheads indicate accumulation of GFP::AHPH just prior to cytokinesis. (C) Timeline indicating the presence (magenta circles) or absence (cyan circles) of pulsing in embryos treated with $\rho\text{-}1$ (RNAi) for the indicated times, revealing an abrupt transition from pulsing to no pulsing at ~ 12 hours post-treatment.

throughout the cortex, but accumulates locally during individual pulsed contractions (Figure 4.7A-C). Significantly, GFP::RGA-3 and NMY-2::mKATE accumulated with very similar timing (Figure 4.7B). Using NMY-2::mKATE and NMY-2::RFP as common signals to co-align data for GFP::AHPH and GFP::RGA-3, we inferred that, on average, GFP::RGA-3 accumulates with a ~6 sec delay relative to GFP::AHPH. The rate of RhoA activation peaks before the onset of GFP::RGA-3 accumulation, and rapid accumulation of GFP::RGA-3 coincides with deceleration and then reversal of RhoA activation (Figure 4.7C, bottom). Together, these observations suggest that delayed accumulation of RGA-3/4 plays a key role in terminating each pulse of RhoA activity. To test this further, we created a strain in which GFP::AHPH and NMY-2::mKATE were co-expressed in *rga-3;rga-4* (hereafter *rga-3/4*) double mutant embryos [228]. Consistent with previous reports [184, 228, 183, 204], during polarity establishment in P0 in *rga-3/4* double mutant embryos, we observed hyper-accumulation of GFP::AHPH and hypercontractility that was characterized by a sequence of convulsive contractions of the anterior cortex and rapid anterior directed cortical flows (Figure 4.7D, 2nd column). However, we could no longer detect local pulses of GFP::AHPH in these embryos. In principle, this could be because rapid flows sequester factors required for pulsed contractility to the extreme anterior pole. To exclude this possibility, we used partial depletion of the myosin regulatory light chain (MLC-4) to attenuate contractility and cortical flows in *rga-3/4* double mutant zygotes or in control zygotes that were doubly heterozygous for *rga-3* and *rga-4* (Figure 4.7D). In control zygotes partially depleted of MLC-4, cortical flows were sharply reduced, but pulsed accumulation of GFP::AHPH could be readily detected (Figure 4.7D, 3rd column). By contrast, in *rga-3/4* double mutant zygotes partially depleted of MLC-4, cortical flows during polarity establishment phase were slower than observed in wild type embryos; GFP::AHPH was uniformly enriched, but we did not observe local pulses of GFP::AHPH accumulation (Figure 4.7D, 4th column). Together, these data suggest that negative feedback through delayed accumulation of RGA-3/4 plays a key role in terminating local pulses of RhoA activity.

Recent work suggests that F-actin accumulation mediates delayed inhibition of RhoA activity in echinoderm and frog oocytes and embryos [13]. We wondered if

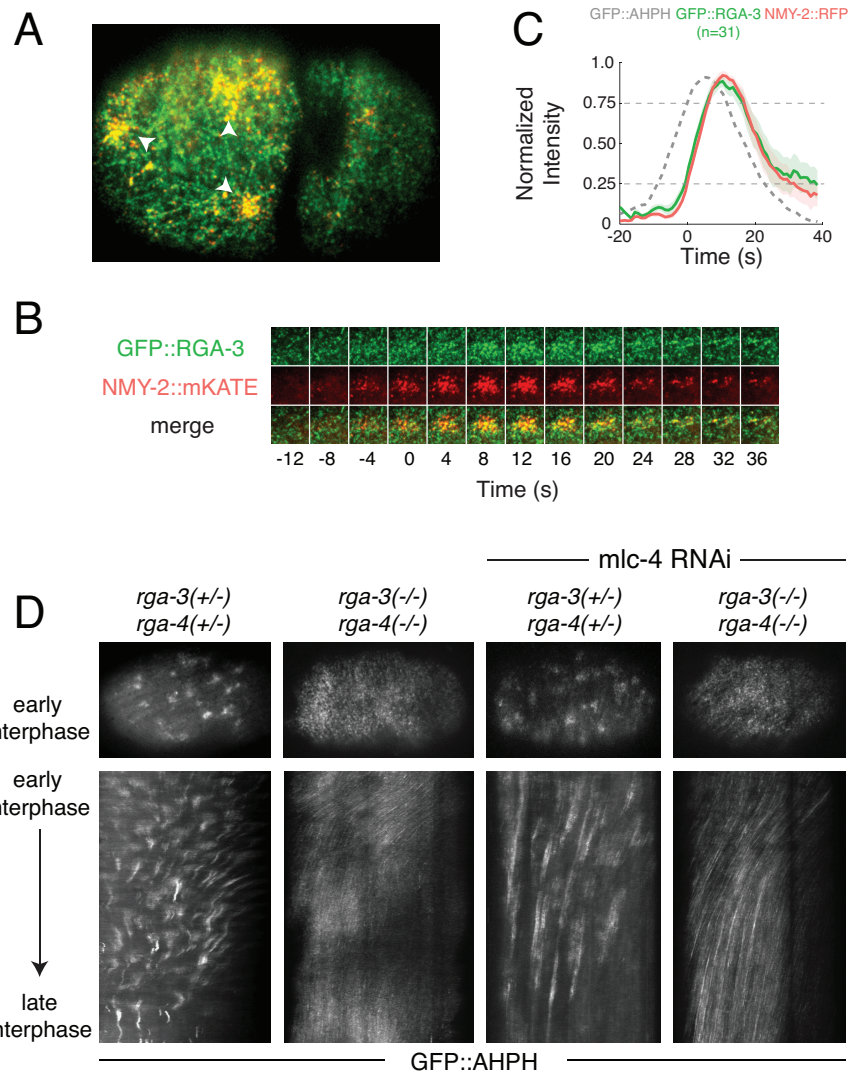


Figure 4.7: Delayed accumulation of RGA-3/4 mediates negative feedback required for pulse termination. (A) Micrograph of a 2-cell stage embryo expressing GFP::RGA-3 (green) and NMY-2::RFP (red). (B) Temporal dynamics of a single pulse. The square region measures 6.4 μ m by 6.4 μ m. (C) Top: Averaged normalized fluorescence intensities vs time for NMY-2::RFP and GFP::RGA-3 from two-color data, co-aligned with respect to the time at which NMY-2::RFP reaches 25% threshold. The averaged normalized fluorescence intensity of GFP::AHPH, co-aligned with NMY-2::RFP. Bottom: The averaged time derivative of the normalized GFP::AHPH intensity, again co-aligned using NMY-2::RFP. Hued regions report 95% confidence intervals. (D) (top panels) Distributions of GFP::AHPH during interphase in zygotes with the indicated genotypes. (bottom panels) Kymographs showing patterns of GFP::AHPH distribution and redistribution during interphase for the same genotypes. Micrographs of 1-cell stage embryos expressing GFP::AHPH. RhoA exhibits pulsatile activity in *rga-3/4(+/-)* embryos (control n=4 embryos, *mlc-4* RNAi n=6 embryos) but not *rga-3/4(-/-)* embryos (control n=9 embryos, *mlc-4* RNAi n=8 embryos).

F-actin might play a similar role in *C.elegans* embryos by mediating recruitment of RGA-3/4. Consistent with this possibility, two-color imaging of GFP::RGA-3 and mCherry::Lifeact (a marker for F-actin [163]) revealed extensive co-localization of RGA-3 and F-actin in both P0 and AB (Figure 4.8A). A substantial fraction of GFP::RGA-3 co-localized with mCherry::Lifeact in extended linear structures that presumably represent actin filaments and/or small filament bundles. Treating permeabilized zygotes [32, 157] with Latrunculin A to depolymerize F-actin lead to a profound loss of cortical GFP::RGA-3, supporting the idea that F-actin plays a key role in recruiting RGA-3/4 to the cortex during individual pulses (Figure 4.8B).

4.4.6 Fast positive and delayed negative feedback involving RhoA and RGA-3/4 can account quantitatively for locally pulsatile RhoA dynamics.

Our data suggest that locally excitable RhoA dynamics could arise independently of myosin activity through a combination of fast positive feedback on RhoA activity and delayed negative feedback via local recruitment of RGA-3/4 (Figure 4.9A). To ask if this combination of feedback loops is sufficient to generate locally pulsatile activity, we formulated a simple ordinary differential equation model, describing local rates of change in RhoA and RGA-3/4, based on the following assumptions: (a) RhoA is activated at a basal rate, and feeds back positively to promote further RhoA activation, (b) RhoA feeds forward through F-actin assembly to promote local, reversible, association of RGA-3/4 with the cortex and (c) RGA-3/4 acts as a GAP to promote local inactivation of RhoA. Consistent with our experimental observations (Figure 4.6A), we assumed that autoactivation of RhoA is a saturating function of RhoA activity, represented by a Hill function with Hill coefficient $n = 1$. We assumed that inactivation of RhoA by RGA-3/4 obeys Michaelis-Menten kinetics. To account for the observed delay between an increase in RhoA and the sharp onset of RGA-3/4 accumulation (Figure 4.7C), we assumed ultrasensitive dependence of RGA-3/4 accumulation rate on RhoA, with the steepness of the response governed by an exponent m (see Materials and Methods for mathematical details).

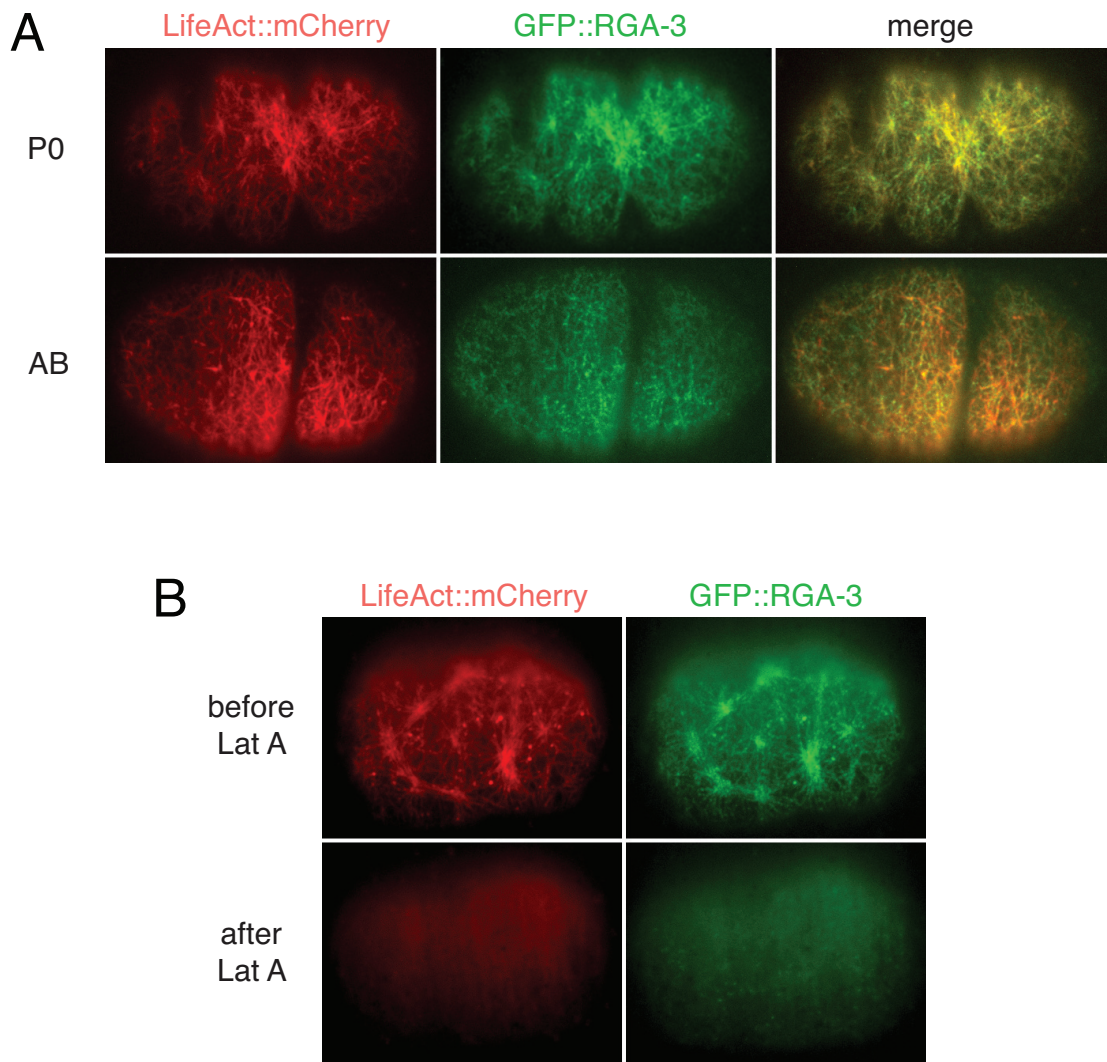


Figure 4.8: **Cortical RGA-3/4 localization depends on F-actin** (A) Micrographs of P0 (top) and AB (bottom) embryos co-expressing GFP::RGA-3 and mCherry::LifeAct. (B) Zygote co-expressing GFP::RGA-3 and mCherry::LifeAct before (top) and \sim 90s after (bottom) treatment with 10M Latrunculin A.

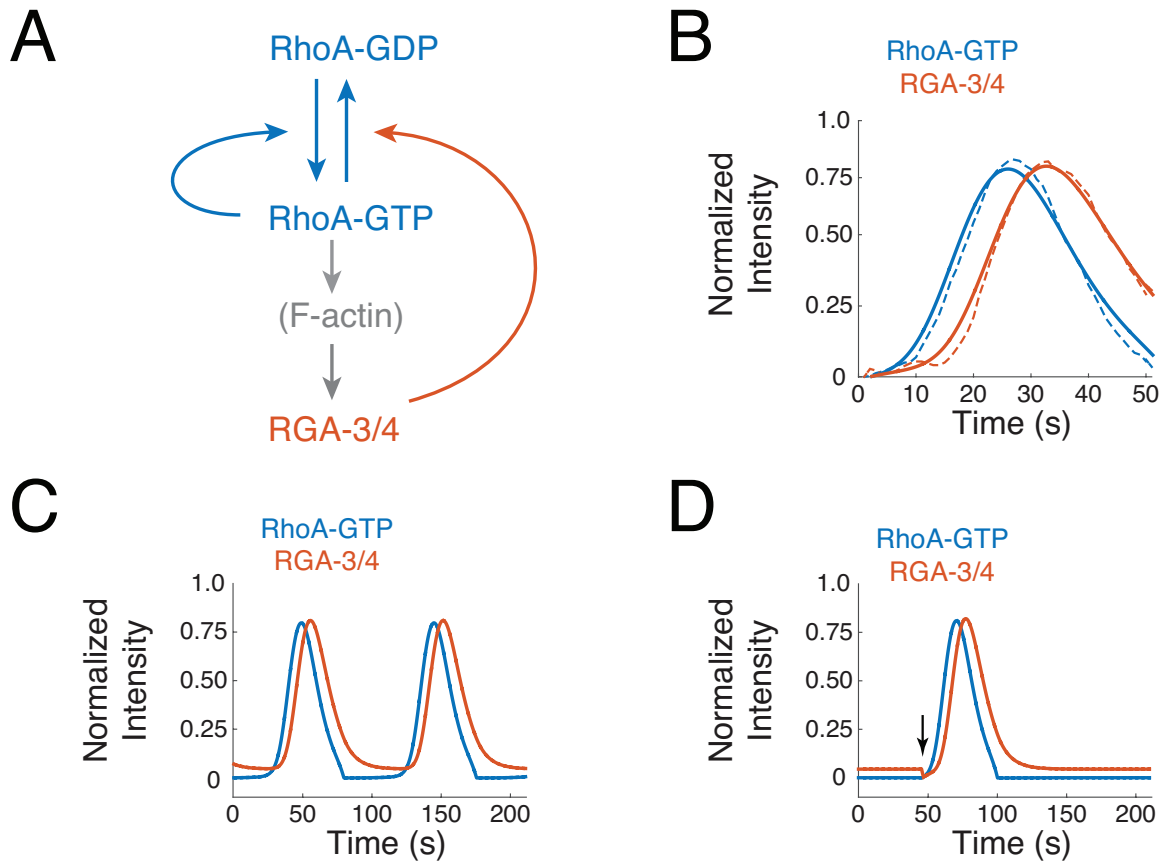


Figure 4.9: Autocatalytic RhoA activation and delayed negative feedback through RGA-3/4 is sufficient to produce locally excitable RhoA dynamics.

(A) Schematic representation of the simple mathematical model used to model RhoA pulse dynamics. (B) Comparison between measured (dashed lines) and simulated (solid lines) pulse dynamics for the case in which $n = 1$, $k_r^0 = 0.005$, $k_p^0 = 0.006$. The remaining model parameters were estimated by fitting data ($m = 1.5289$, $K_{fb} = 0.4581$, $K_{GAP} = 0.001$, $k_r^{ass} = 0.1592$, $k_r^{diss} = 0.1101$; see Materials and Methods for details). (C) Simulation dynamics for the parameter values in (B) are oscillatory, with pulses occurring at regular intervals. (D) A small change in the basal RhoA activation rate from $k_p^0 = 0.006$ to $k_p^0 = 0.004$ results in excitable dynamics in which a stable rest state can be destabilized by a transient reduction of RGA-3/4 (vertical black arrow) to trigger a single pulse of RhoA activity.

We set values for basal RhoA activation and RGA-3/4 recruitment rates based on the slow rates of increase in GFP::AHPH and GFP::RGA-3 observed before the sharp upswing of each pulse (Figure 4.7C). Then we estimated values for the models remaining parameters by fitting the relationships between the local rates of RhoA activation and RGA-3/4 recruitment and the local densities of RhoA and RGA-3/4 inferred from averaged and co-aligned GFP::AHPH and GFP::RGA-3 intensities (Figure 4.7C; see Materials and Methods for details). For these choices of parameters, without any further adjustments, the model predicts oscillatory dynamics, with a pulse waveform that matches closely that measured for pulses in AB cells (Figure 4.9B,C).

Interestingly, the dynamics could be tuned by small decreases in the basal RhoA activation rate (Figure 4.9D) or small increases in the basal RGA-3/4 recruitment rate (not shown), into a regime in which the dynamics are excitable - i.e., there is a stable state and a transient local input is required to trigger a pulse of RhoA activity (Figure 4.9D). This is consistent with our observations in *nmy-2*(RNAi) embryos that some patches of cortex are quiescent while others exhibit repeated pulses of activity at regular intervals (yellow arrows in Figure 4.5A). We conclude that a simple combination of positive and negative feedback loops, coupling local RhoA activity and RGA-3/4 accumulation, is in principle sufficient to explain pulsatile RhoA dynamics in early *C.elegans* embryos, independent of actomyosin contractility.

4.5 Discussion

Pulsed contractility is a widespread mode of actomyosin contractility, but its mechanistic basis has remained poorly understood [111, 73]. Current models for pulsed contractility invoke mechanochemical feedback in which contractile forces produced by Myosin II couple in different ways with actomyosin assembly/disassembly to drive excitable or oscillatory dynamics. Proposed feedback mechanisms include tension-dependent motor binding kinetics [168, 53? , 125], tension-dependent filament assembly/stabilization [77, 45] or disassembly [130], tension-dependent activation of Myosin II via Ca++ [94] or RhoA [104], or modes of feedback in which local contraction

advects and concentrates actomyosin and/or its upstream activators [20, 106, 144]. Here, we have identified a mechanism for pulse generation that does not require force production or redistribution of cortical factors by Myosin II. Using single molecule imaging and particle tracking analysis, we have shown that the rapid initial accumulation of F-actin and Myosin II begins well before the onset of contraction, at a time when the cortex is locally expanding; Redistribution of actomyosin by local contraction makes a minor contribution to the overall accumulation of actomyosin during each pulse. Instead, our data show that pulsed accumulation and disappearance of F-actin and Myosin II are determined primarily by local modulation of their assembly/recruitment and disassembly. Using two-color imaging, we have shown that during each pulse, active RhoA begins to accumulate well before its downstream targets F-actin, Myosin II and Anillin. Active RhoA nearly reaches its peak level before the onset of contraction (Figure 4.4D), and then it begins to disappear well before its downstream targets. Significantly, locally pulsed activation of RhoA continues to occur on patches of cortex that contain only a few (1-2) particles of Myosin II, which presumably are insufficient to produce local contractile stress. Thus a Myosin-independent RhoA pulse-generator underlies pulsed contractility in early *C.elegans* embryos.

The pulses of RhoA activity described here and in other contexts [144, 13, 137] are strikingly reminiscent of excitable behaviors found in other systems, such as action potentials in neuronal [87] or cardiac cells [124], or transient pulses of intracellular calcium release [72], or pulses of actin assembly observed in motile cells [218]. Theoretical studies highlight two key ingredients for excitable dynamics: fast positive feedback and delayed negative feedback [193]. The sharp acceleration of active RhoA accumulation that we observe during the early rising phase of individual pulses is a dynamical signature of fast positive feedback in which RhoA promotes its own activity. Stronger evidence that RhoA participates in a positive feedback loop that is essential for pulsing comes from our observation that depletion of RhoA below a certain threshold leads to an abrupt loss of pulsed contractions, while having minimal effects on other RhoA-dependent functions such as cortical flow during polarization[142, 185] or cytokinesis [123].

The mechanism for this feedback remains unclear. Because the initial acceleration of RhoA activation occurs before any visible accumulation of Myosin II, Anillin or F-actin, it is unlikely that accumulation of these downstream targets makes a significant contribution to positive feedback. A more likely possibility is that RhoA feeds back through one or more of its upstream activators, such as ECT-2, CYK-4 and NOP-1 [204]. For example, during cytokinesis, active RhoA can act as a cofactor to promote transactivation of the RhoGEF ECT-2 by the RhoGAP CYK-4 [229]. While CYK-4 is not required for pulsed activation of RhoA during polarization [204], it is possible that RhoA could feedback through NOP-1, a protein of unknown activity that is required for RhoA activation during interphase in P0 and AB [204]. Identifying the molecular mechanism(s) for this feedback is an important goal for future studies.

Our data suggest that the redundantly acting RhoGAPs RGA-3/4 play a key role in providing the delayed negative feedback that terminates RhoA pulses. RGA-3/4 act as GAPs towards RHO-1 in vitro [184], and loss of RGA-3/4 leads to hyperactivation of RhoA in vivo [204]. We find that during each pulse, RGA-3 accumulates with a delay of \sim 6 seconds relative to active RhoA. Significantly, *the rate* of active RhoA accumulation peaks, and begins to fall, just as GFP::RGA-3 begins to accumulate, suggesting that rapid accumulation of RGA-3/4 plays a key role in timing the end of each RhoA pulse. Consistent with this possibility, pulsatile RhoA activation is completely abolished in *rga-3/4* double mutant zygotes, even when contractility is attenuated to prevent sequestration of RhoA activators by hyperactive cortical flow. A similar dependence of pulsatility on a RhoA GAP has recently been reported in the context of ventral furrow invagination in *Drosophila* [137].

Together, these data suggest a model for locally excitable RhoA dynamics in which RhoA feeds back positively to promote its own activation, and feeds back negatively with a delay through RGA-3/4 to promote its own inactivation. Indeed, when we formulate this model mathematically, and constrain model parameter values to match the local dependencies of RhoA and RGA-3/4 accumulation rates on levels of RhoA and RGA-3/4 inferred from two-color imaging data, the model predicts locally pulsatile RhoA dynamics, and small tunings of the models parameters mediate interconversion between excitable dynamics and spontaneous oscillations. This

simple modeling exercise establishes an internally consistent hypothesis for pulsatile contractility that can be confirmed and extended by future experiments.

What governs the recruitment of RGA-3/4 during each pulse? We have found that GFP::RGA-3 co-localizes broadly and extensively with cortical F-actin in both P0 and AB. RGA-3/4 accumulates with the same timing as F-actin during each pulse, and depolymerizing F-actin abolishes this accumulation. This suggests a specific mechanism for delayed recruitment of RGA-3/4 in which RhoA promotes increased local F-actin assembly (potentially through the formin CYK-1 [187]), and F-actin in turn recruits RGA-3/4. Interestingly, a recent study[13] suggests that RhoA and cortical F-actin form an excitable circuit, with RhoA as activator and F-actin as inhibitor, that propagates cortical waves of RhoA activity and F-actin assembly in oocytes and embryonic cells of frogs and echinoderms. The mechanism(s) by which F-actin feeds back to inactivate RhoA in these cells remains unknown, but our observations in *C.elegans* support to the idea, proposed by Bement et al, 2015, that a RhoGAP homologous (or analogous) to RGA-3/4 may be recruited by F-actin to mediate negative feedback in frog and echinoderm cells. A similar circuit design may underlie the propagation of actin waves observed in many motile cells (reviewed in [7]).

It is also interesting to compare our observations to those made recently in the *Drosophila* germband [144]. In germband cells, pulsed accumulation of a RhoA biosensor appears to coincide with the local accumulation of F-actin and Myosin II, and with the onset of contraction, and it is abolished by inhibition of Rho Kinase, an upstream activator of Myosin II. In *C.elegans*, by contrast, pulsed accumulation of the analogous biosensor (based on a fragment of Anillin that binds active RhoA) precedes actomyosin accumulation and the onset of contraction by many seconds and persist in the almost complete absence of Myosin II.

To some extent, these differences could reflect the imaging methods used to detect the RhoA biosensor. Using near-TIRF imaging in *C.elegans* embryos, we detect two pools of the biosensor: a diffuse pool that begins to accumulate well before Myosin II, and a second more punctate pool whose distribution strongly overlaps with Myosin II (Figure 4.4B, Figure 4.12F&G, Figure 4.14. Based on studies in other cells [218],

the diffuse pool may be more difficult to detect using confocal microscopy. Thus it remains possible that a diffuse pool of active RhoA accumulates before actomyosin in the *Drosophila* germband, but escapes detection by confocal microscopy.

An alternative idea is that pulsed contractility is governed by locally excitable RhoA dynamics in both systems, but that different forms of positive feedback may contribute differently to driving the rapid upswing of RhoA activity, and that different mechanisms may operate to trigger pulses (by driving RhoA activity above a threshold for excitation). For example, in the *Drosophila* germband, a mode of feedback in which local contraction advects and concentrates active RhoA (or upstream activators) may be required to initiate pulses, whereas in *C.elegans*, local fluctuations in RhoA or RGA-3/4 levels may be sufficient to do so in the absence of contractility. Importantly, in the *Drosophila* germband, as in *C.elegans*, advection/contraction coupling accounts for only a fraction of the total accumulation of active RhoA during each pulse; thus other modes of positive feedback must also make a significant contribution. More generally, we hypothesize that the different modes of RhoA excitability that have been described in frog, echinoderm, *C.elegans* and *Drosophila* embryos share a deeper underlying mechanistic origin. We suggest that a comparative analysis of mechanisms for pulsing in these and other systems will be a very fruitful way to uncover core conserved circuitry for pulse generation and to understand the ways in which this core circuitry is tuned or accessorized in different contexts to achieve different functional outcomes.

4.6 Materials and Methods

4.6.1 *C. Elegans culture and strains*

We cultured *C. elegans* strains at 22°C under standard conditions [23] Table 2.1 lists the mutations and transgenes used in this study. Unless otherwise specified, strains were provided by the Caenorhabditis Genetics Center, which is funded by the National Institutes of Health (NIH) National Center for Research Resources.

4.6.2 RNA interference

RNAi was performed by the feeding method as previously described [201]. Bacteria targeting *nmy-2*, *spd-5*, *rho-1*, *perm-1*, *arx-2* and *mlc-4* were obtained from the Kamath feeding library [92]. The L4417 plasmid targeting the entire GFP sequence (generated by the Fire lab and available at <http://www.addgene.org/1649/>) was transformed into HT115(DE3) bacteria. For the Myosin depletion experiments, L4 larvae co-expressing GFP::AHPH and NMY-2::mKate2 were transferred to *nmy-2* RNAi feeding plates 24-30 hours before imaging. Strong depletion of myosin was verified by strong loss of cortical NMY-2::mKate2. For experiments involving *spd-5* RNAi, L4 larvae were transferred to feeding plates for 24-30 hours before imaging. For the RhoA depletion experiments, synchronized young adults were transferred to *rho-1* RNAi plates 8-16 hours before imaging. For experiments involving *mlc-4* RNAi, synchronized young adults were transferred to feeding plates for 12-16 hours before imaging. For the latrunculin A experiments, late L4 larvae were transferred to *perm-1* RNAi plates 16-24 hours before imaging. For experiments involving *arx-2* RNAi, L4 larvae were transferred to feeding plates for 30-36 hours before imaging.

4.6.3 Microscopy

We mounted embryos as described previously [172] on glass slides under #1.5 coverslips in 3-5 μ l of standard Egg Salts containing \sim 100 uniformly sized polystyrene beads ($18.7 \pm 0.03 \mu\text{m}$ diameter, Bangs labs, NT29N). The beads acted as spacers and allowed us to achieve uniform compression of the embryo surface across experiments [172].

We performed all imaging on a Nikon ECLIPSE-Ti inverted microscope equipped with a Ti-ND6-PFS Perfect Focus Unit. A laser merge module (Spectral Applied Research) controlled fast, tunable delivery of 481nm and 561 nm laser excitation from 50mW solid state lasers (Coherent Technology) to a motorized TIRF illuminator. We adjusted laser illumination angle to achieve near-TIRF illumination [202]. We collected images using a Nikon CFI Apo 1.45 NA oil immersion TIRF objective combined with 1.5 intermediate magnification onto an Andor iXon3 897 EMCCD camera.

All image acquisition was controlled using Metamorph software.

4.6.4 Single-molecule imaging

We performed single molecule imaging as described previously [172]. For NMY-2::GFP, we used a combination of RNAi against GFP and mild photobleaching in wide field illumination mode to reduce surface densities of GFP-tagged transgenic proteins to single molecule levels. For GFP::Actin, which is expressed at very low levels in the strain that we used, we used mild photobleaching alone. For GFP::Actin and NMY-2::GFP, we imaged single molecules using 10% laser power ($\sim 0.16 \mu W m^{-2}$), with 100ms exposures in continuous streaming mode (GFP::Actin and NMY-2::GFP), yielding an approximate photobleaching rate of $\sim 0.05 s^{-1}$ [172].

4.6.5 Analysis of F-actin and Myosin II turnover

In previous work, we compared two methods for estimating local F-actin disassembly rates from single molecule data [172]. The first method (smPReSS) estimates average disassembly rates in a local region by fitting kinetic models to the approximately exponential decay in particle densities measured during photobleaching, assuming steady state conditions. The second method relies on single molecule detection and tracking and infers appearance and disappearance events directly from single molecule trajectories. We showed that under steady state conditions, and when Myosin II is inhibited to remove the effects of local contraction and cortical flow, these two methods yield estimates of local disassembly that agree to within 20%. During pulsed contractions, the steady state assumption is not valid and the effects of cortical flow cannot be ignored. Therefore, in this work, we relied exclusively on the particle tracking method to measure local appearance, disappearance and motion of single molecules.

In preliminary analyses, we found that single molecules of GFP::Actin and NMY-2::GFP move sufficiently slowly during pulsed contractions that we could obtain marginally better results by pre-averaging ten consecutive frames of raw data to produce sequences of images at one-second intervals. We performed single molecule

detection and tracking on this pre-averaged data using a Matlab implementation (<http://people.umass.edu/kilfoil/downloads.html>) of the Crocker-Grier method [38, 159]. We then inferred single molecule appearance and disappearance events and frame-to-frame single molecule displacements directly from the single molecule trajectories.

4.6.6 Measuring local deformations from single molecule data

The key goal of our single molecule analysis was to distinguish the relative contributions of local assembly/disassembly and local deformation/flow to changes in local density during pulsed contractions. To do so, it was essential to follow dynamic changes in assembly/disassembly on a moving and contracting patch of cortex, i.e. in a material (Lagrangian) frame of reference. We used single molecule displacements to identify and track regions of cortex undergoing pulsed contractions as follows:

For each pulse, we identified a reference time point at/near the onset of contraction by visual inspection of the time lapse sequence. At this time point, we identified manually an elliptical region containing the patch of cortex undergoing contraction (Figure 4.10A). We computed the smallest polygon (the convex hull) containing all the particles detected within the elliptical region (Figure 4.10B). Each vertex of the reference polygon was thus associated with a single molecule detected on the cell surface. To propagate the polygonal ROI forwards and backwards in time, we computed the frame-to-frame displacement of each of its vertices, either from the displacement of a vertex-associated molecule or (once the molecule disappears) from a weighted average of the frame-to-frame displacements of nearby particles (Figure 4.10C). We then measured local deformation and turnover within this polygonal ROI as follows:

We compared three different measures of local compression (or dilation) within the polygonal ROI from frame to frame (Figure 4.11A): the change in normalized surface area, a particle-based strain rate and a material strain rate. We computed the change in surface area sA as the time-derivative of the normalized area of the polygonal ROI:

$$s_A(t) = \frac{A_{t+1} - A_t}{\langle A \rangle}$$

where $\langle A \rangle$ is the mean surface area taken over all frames in the pulse sequence. To compute a particle-based strain rate, for each particle in the polygonal ROI, we computed the average normalized change in distance between that particle and its near-neighbors:

$$s_p^i(t) = \frac{1}{M} \sum_{j=1 \dots M} \frac{d_{ij}^{t+1} - d_{ij}^t}{d_{ij}^t}$$

where d_{ij}^t is the distance between particle i and a near neighbor particle j at time t and the sum is taken over all neighbor particles within a disk of radius 20 pixels centered on particle i. We then averaged over all particles in the ROI to obtain a particle-based strain rate for the entire ROI:

$$s_p(t) = \frac{1}{N} \sum_{i=1 \dots N} s_p^i(t)$$

Finally, to compute a material strain rate s_M , we used a linear least squares regression method to estimate the local gradient of particle velocities [?]. We then decomposed the resulting velocity gradient tensor into anti-symmetric (rotation) and symmetric (strain rate) components. We then took one half the trace of the symmetric strain rate tensor as a measure of local compressive strain. In practice, we found that all three methods yielded very similar results regarding the magnitude and timing of contractions (Figure 4.11A). We report results based on the particle-based strain rate in Figures 2.2 and 2.3.

To quantify turnover rates for F-actin or Myosin II within the polygonal ROI, for each time point t, we measured the area of the ROI (A_t), the number of particles N_t , their density $D_t = \frac{N_t}{A_t}$, and the number of appearance and disappearance events that occurred within the ROI between time t and $t + \Delta t$ ($\Delta N_t^+, N_t^-$). We quantified the mean appearance rate and the mean disappearance rates within the ROI as: $k_i^+ = \frac{\Delta N_t^+}{\Delta t}$ and $k_i^- = \frac{\Delta N_t^-}{N_t \Delta t}$. We computed the change in actin density within a polygonal ROI at time t as $\Delta D_t = D_{t+\Delta t} - D_t$. We estimated the contribution to the

change in density from deformation of the ROI to be $\Delta D_{deformation} = -D_t \frac{A_{t+\Delta t} - A_t}{A_{t+\Delta t}}$ and the contribution from turnover (i.e. a net imbalance of appearance and disappearance) to be $\Delta D_{turnover} = \frac{N_{t+\Delta t} - N_t}{A_{t+\Delta t}}$, such that $\Delta D_t = \Delta D_{deformation} + \Delta D_{turnover}$. We note that this method for measuring the differential contributions of deformation and turnover to changes in density does not rely on single molecule tracking and is thus insensitive to tracking errors.

4.6.7 Two-color imaging, pulse tracking, and analysis

We performed two-color imaging using the imaging system described above with near-TIRF illumination. We performed the initial steps of image processing, pulse identification and extraction, using the software package ImageJ (<http://imagej.nih.gov/ij/>). For all subsequent steps, including pulse tracking, intensity measurements, data normalization and alignment across multiple pulses, we used custom functions written in MATLAB (<http://www.mathworks.com>).

We imaged embryos co-expressing GFP- and RFP-tagged transgenes by alternating 100 ms exposures with 488nm and 561nm excitation, thus giving 5 two-color frames per second. We used 25% maximum laser power ($\approx 0.4\mu\text{W}\mu\text{m}^{-2}$) for each channel. For subsequent analysis, we averaged over five consecutive frames to obtain a single image for each channel at one-second intervals. We limited our analysis to individual pulses that moved very little during the period leading up to the onset of contraction. We used ImageJ to extract a subregion containing each pulse of interest. With the exception of Myosin-depleted embryos, we used NMY-2::RFP as a reference signal to track the location of the pulse through time. For the analysis of Myosin-depleted embryos, we used GFP::AHPH as the reference signal.

We used the reference signal to identify and track a moving region of interest associated with each pulse as follows (Figure 4.13A): First, we smoothed each frame of the image sequence using a gaussian filter, $\sigma = 2-3 \mu\text{m}$. We then thresholded the smoothed image to identify regions of interest (ROIs) associated with the pulse in consecutive frames. We used the same value of σ and the threshold for all frames and chose these values such that each ROI in the sequence was simply connected and

such that the largest ROI in the sequence was approximately the same size as the region of strong signal accumulation near the peak of the pulse in the unprocessed data, as viewed by eye.

To measure signal intensity vs time during a pulse, we first used MATLAB to determine the centroid of each ROI to obtain a sequence of centroid positions $C_t = (x_t, y_t)$. We then extended this sequence backwards in time using the first measured centroid position C_{first} and extended it backwards in time using the last measured centroid position C_{last} . We then used a single reference ROI, centered on positions $[C_{first-N}, \dots, C_{last+N}]$, to measure a sequence of GFP and RFP intensities over time. We compared three different reference ROIs: (i) the largest ROI measured in the sequence, which corresponds roughly to peak accumulation of Myosin II, (ii) a bounding box = the smallest square region containing the largest ROI, and (iii) an annular region obtained by subtracting the largest ROI from the bounding box.

We normalized the intensity data for individual pulses using the equation $I_{norm}(t) = \frac{I_{mean}(t) - I_{min}}{I_{max} - I_{min}}$, where $I_{mean}(t)$ is the mean intensity of the ROI at time t, I_{min} is the minimum mean intensity of the ROI before the onset of contraction, and I_{max} is the maximum mean intensity of the ROI measured over the entire sequence $[C_{first-N}, \dots, C_{last+N}]$. Finally, we aligned data across multiple pulses with respect to the time point at which NMY-2::RFP crossed 25% of its normalized maximum intensity (Figure 4.13). The mean was calculated with a 95% confidence interval.

We performed a number of additional controls to assess the sensitivity of our results to variation across strains, or the details of pulse identification, tracking and intensity measurements. First, we compared the kinetics of Myosin II accumulation during pulses in embryos co-expressing NMY-2::GFP and NMY-2::RFP and confirmed that the dynamics of accumulation were essentially identical after normalizing for differences in expression level and probe brightness (Figure 4.4E,4F, Figure 4.12D,S3E). Second, we confirmed that the the dynamics of Myosin::RFP accumulation was essentially identical across the different two-color strains that we used (Figure 4.12D ; Figure 4.12E). Finally, we verified that our measurements of the rate and relative timing of accumulation of different signals were largely insensitive to differences in the size of the box/blobs used (Figure 4.12, data not shown).

4.6.8 Kymograph analysis

To produce the kymographs shown in Figures 4-7 and Figure 4.13, we aligned images so that the AP axis of the embryo coincided with the horizontal (x) image axis. We selected rectangular regions aligned with the x image axis, whose width (in x) coincided with the embryonic region of interest and whose height (in y) was 10-20 pixels. From the original image stack, we extracted an xyt substack corresponding to this rectangular region; we used ImageJ's reslice tool to reslice this stack with respect to the xt plane, then we used a maximum intensity projection to collapse the individual slices in y to obtain a kymograph in x vs t.

4.6.9 Kinetic analysis

For the kinetic analysis (Figure 4.6A), normalized intensity values were first smoothed using custom MATLAB software. The time derivatives of $\frac{d[AHPH]}{dt}$ were calculated from smoothed normalized intensity values using MATLAB's built in difference method. The data were then binned, and the average and standard deviation were calculated per bin.

4.6.10 Mathematical Modeling

We built a simple ordinary differential equation model for RhoA pulse generation at a single point in space based on autocatalytic activation of RhoA and delayed negative feedback via RhoA-dependent recruitment of RGA-3/4. We started with the following assumptions:

1. RhoA is activated at a constant basal rate.
2. Active RhoA feeds back to promote further RhoA activation at a rate that can be described as a Hill function of RhoA density.
3. RGA-3 and RGA-4 can be treated as a single species (RGA-3/4) that acts as a GAP to promote local inactivation of RhoA.

4. Active RhoA promotes local F-actin assembly; RGA-3/4 binds F-actin from an abundant cytoplasmic pool, and dissociates from F-actin at a constant rate. Because RGA-3 and F-actin accumulate with very similar kinetics, we did not model F-actin directly. Instead, we assumed that RGA-3/4 binds the cortex at a constant basal rate plus a rate that depends on the local density of active RhoA, and that RGA-3/4 dissociates from the cortex at a constant rate.
5. To capture the observed delay between the sharp upswing in RhoA activity and the onset of F-actin and RGA-3/4 accumulation (Figure 4.4D, Figure 4.7B), we assumed ultrasensitive dependence of RGA-3/4 recruitment rate on RhoA activity.

With these assumptions, letting p represent the density of RhoA and r represent the density of RGA-3/4, we write a pair of ordinary differential equations (ODEs) for p and r :

$$\begin{aligned}\frac{dp}{dt} &= k_p^0 + k_p^{fb} \frac{p^n}{K_{fb} + p^n} - k_{GAP} \frac{p}{K_{GAP} + p} r \\ \frac{dr}{dt} &= k_r^0 + k_r^{ass} p^m - k_r^{diss} r\end{aligned}\quad (4.1)$$

To estimate the values for model parameters, we extracted empirical relationships between RGA-3/4, active RhoA and their time derivatives from intensity data for GFP::RGA-3 and GFP::AHPH that was normalized, averaged and aligned over many individual pulses, and then co-aligned using Myosin::RFP as a common reference (Materials and Methods, Figure 4.7B). Then we used these data to constrain the values of parameters in equations (1) as follows. First, we set $n = 1$, based on the observed form of dependence of $\frac{d[AHPH]}{dt}$ on AHPH in Figure 4.6A, and we set values for basal RhoA activation ($k_p^0 = 0.006$) and basal RGA-3/4 recruitment ($k_r^0 = 0.005$) based on the slow rates of increase in GFP::AHPH and GFP::RGA-3 observed before the sharp upswing of each pulse. Then, we used a non-linear least squares regression to fit the right hand sides of equations (1.1) to the intensity data, to estimate values for the remaining parameters.

In our initial efforts to fit the equation for RhoA, the values estimated for K_{GAP} were consistently negative and very close to zero, corresponding to a scenario in which RGA-3/4 operates near saturation on active RhoA. Therefore, in all subsequent analyses, we set K_{GAP} to a small constant positive value ($K_{GAP} = 0.001$) and used non-linear least squares fits to choose values for k_p^{fb} and K_{fb} as described above.

For each set of parameters determined as above, we set the initial values for r and p to zero, simulating a scenario in which RhoA is minimally active and a small perturbation reduces RGA-3/4 to a minimally observed level. We then solved the equations numerically using Matlab to determine if this initial perturbation would result in either a single pulse of RhoA activity, followed by a return to a stable inactive state (excitability) or a train of pulses (oscillatory dynamics).

4.7 Supplementary Figures

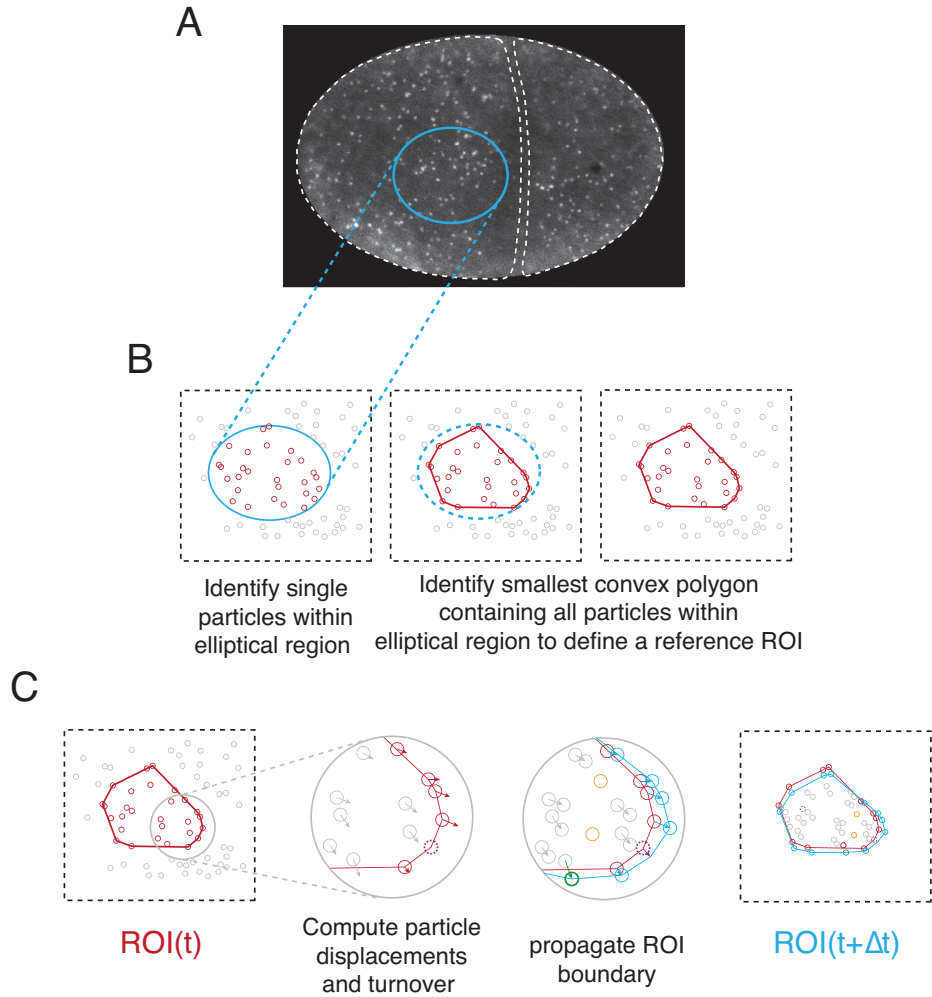


Figure 4.10: Schematic overview of methods for tracking a moving and deforming patch of cortex from single molecule data. (A) Micrograph of a two-cell stage embryo expressing Actin::GFP at single-molecule levels. Anterior is to the left. Dashed lines indicate the outlines of AB and P1. The blue ellipse identifies a region in which a pulse occurs, from which a reference ROI will be extracted. (B) Method for extracting the reference ROI. Left: Single particles detected in the raw image. The particles shown in red are those contained within the blue ellipse. Middle and right: The reference ROI (solid red line) is the smallest convex polygon containing all red particles. (C) Strategy for iterative propagation of the polygonal ROI from frame to frame (either backwards or forwards in time). The polygons vertices move with the particle that defined that vertex so long as the particle remains visible. When a particle associated with a vertex disappears (dashed magenta particle in middle left panel), the vertex displacement is extrapolated from the motion of the surrounding particles. If an internal particle moves outside the boundaries of the polygon defined by existing vertices (green particle in middle right panel) a new vertex associated with that particle is introduced.

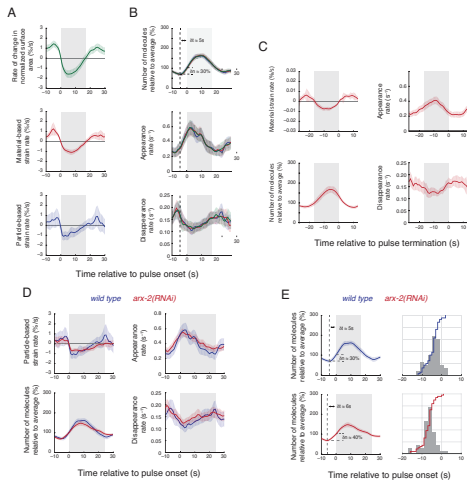


Figure 4.11: Comparison of different methods to quantify local deformation (strain rate) and to align data across multiple pulses. (A,B) Comparison of different methods used to compute local deformation rates during pulses. (A) Measures of deformation rate vs time for the same data using three different metrics: (top) Rate of change in normalized surface area, (middle) material strain rate and (bottom) particle based strain rate (see materials and methods for details on how these were computed). (B) Measurements of single molecule number (top), appearance rate (middle) and disappearance rate (bottom) were aligned and averaged with respect to the onset of contraction, over 42 pulses, using the three metrics to measure deformation: change in normalized surface area (green), material strain rate (red), and particle-based strain rate (blue). Vertical dashed lines mark lowest actin density preceding the pulse. Horizontal dashed lines in top graph mark, respectively, the minimum number of actin molecules and the number of molecules at the onset of contraction. For all three metrics, the delay from actin minimum to contraction onset is $\delta t \approx 5$ s, and the relative change in number of molecules from minimum to contraction onset is $\delta n \approx 30\%$. (C) Measurements of material strain rate, number of molecules, appearance rate and disappearance rate, aligned and averaged with respect to the end of contraction for the same data shown in A&B. (D) Measurements of particle-based strain rate, number of molecules, appearance rate and disappearance rate, aligned and averaged with respect to the onset of contraction, in wild type (blue, $n = 42$ pulses) and *arx-2*(RNAi) (red, $n = 49$ pulses) embryos. (E) Left column: number of molecules relative to average in wild type (blue) and *arx-2*(RNAi) (red) embryos, as previously displayed in (D). The vertical dashed line marks lowest actin density preceding the pulse, delayed respectively by $\delta t \approx 5$ s and $\delta t \approx 6$ s from the contraction onset (gray box). The horizontal dashed line displays the amount of pre-contraction increase in the number of actin molecules, with $\delta n \approx 30\%$ and $\delta n \approx 40\%$, respectively. Right column: a histogram showing the distribution of delays between contraction onset and increase of actin molecules. Staircase line: cumulative distribution function of the delays. Error bars report 95% confidence intervals.

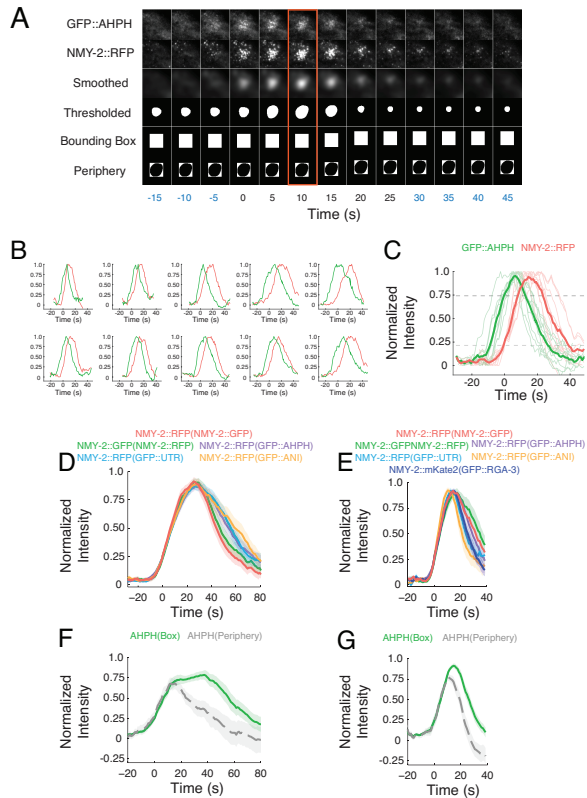


Figure 4.12: Schematic overview of methodology for measuring and aligning fluorescence intensities from two-color data during pulsed contractions.

(A) Method for determining regions of interest in which to measure fluorescence intensities, illustrated for a single pulse. Row 1: raw GFP::AHPH signal. Row 2: raw NMY-2::RFP signal. Row 3: smoothed NMY-2::RFP signal. Row 4: thresholded NMY-2::RFP signal. Row 5: The smallest box containing the largest thresholded domain is the bounding box. In each frame, the center of bounding box is located on the centroid of the thresholded domain. Row 6: A fixed-size peripheral region is the complement of the largest thresholded region within its bounding box. The center of the fixed-size peripheral region is located at the center of the thresholded region in each frame. (B) Normalized fluorescence intensity of GFP::AHPH and NMY-2::RFP versus time for ten representative pulses in AB cells. Time $t = 0$ when NMY-2::RFP rises above 25% of its normalized maximum value. (C) Fluorescence intensities from all pulses in (B) co-aligned relative to time $t = 0$. The bold traces represent the average GFP::AHPH and NMY-2::RFP intensities. (D,E) Alignment of averaged normalized fluorescence intensities for NMY-2::XFP measured for pulses in P0 (D) and AB (E) cells co-expressing the indicated probes (shown in parentheses). Time $t = 0$ is when NMY-2::XFP rises above 25% of its normalized maximum value. (F,G) Averaged normalized fluorescence intensity of GFP::AHPH measured in the bounding box (green) and periphery (gray) for pulses in P0 (F) and AB (G) cells. In (D-G), halos report 95% confidence intervals.

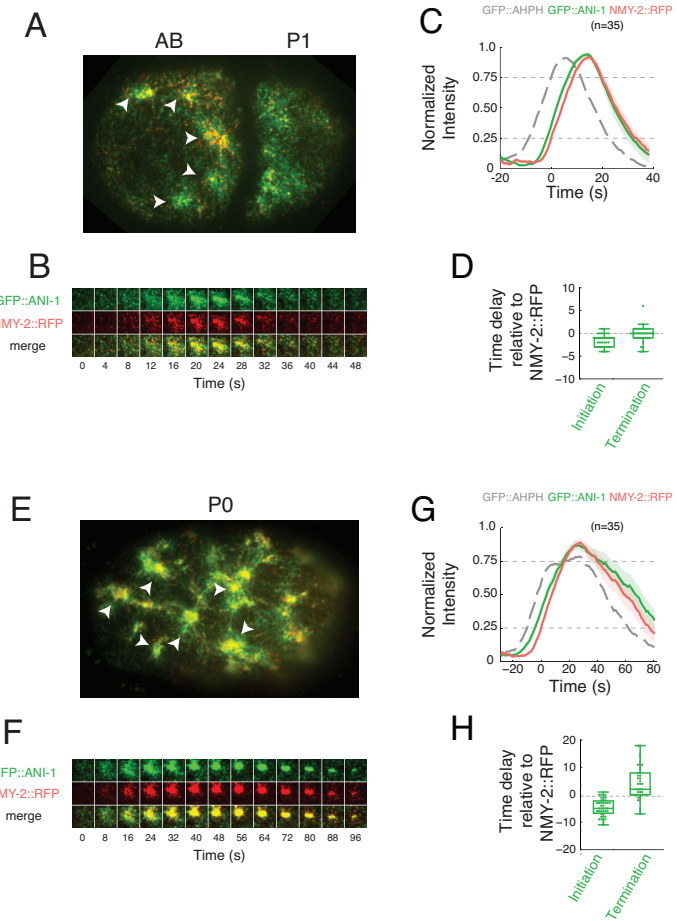


Figure 4.13: Two color analysis of Myosin II and Anillin dynamics during pulsed contractions in one- and two-cell embryos. (A,E) Micrographs of two-cell (A) and one-cell (E) embryos co-expressing GFP::ANI-1 and NMY-2::RFP. White arrowheads indicate individual pulses. (B,F) Expanded views of single pulses illustrating temporal dynamics of GFP::ANI-1 and NMY-2::RFP accumulation. (C,G) Plots of averaged normalized fluorescence intensities for NMY-2::RFP and GFP::ANI-1 from two-color movies, aligned to the time at which NMY-2::RFP reaches 25% threshold. The averaged normalized fluorescence intensity of GFP::AHPH, co-aligned using the NMY-2::RFP signal, is shown for reference. Halos report 95% confidence intervals. (D,H) Distribution of the delays in the onset of appearance and disappearance of GFP::ANI-1 measured relative to NMY-2::RFP. Onset of appearance and disappearance were measured respectively as the time at which the normalized signal rose above 25% or fell below 75% of the maximum value.

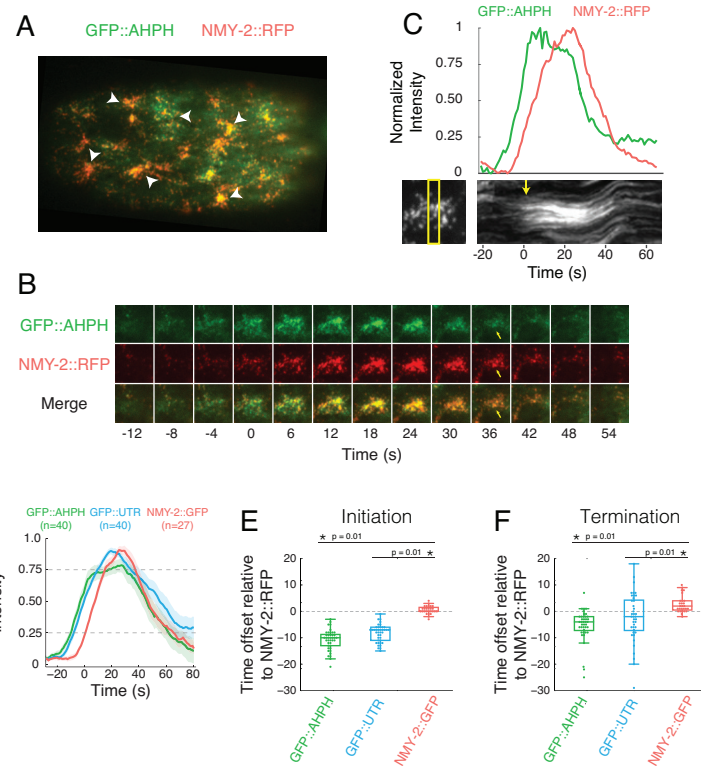


Figure 4.14: Two color analysis of pulsed contractions in P0. (A) A zygote expressing GFP::AHPH and NMY-2::RFP. White arrowheads indicate individual pulses. (B) Expanded view of a single pulse illustrating temporal dynamics of GFP::AHPH and NMY-2::RFP accumulation. Time delay between frames is 4s for the first 4 frames, and 6s thereafter. (C) Plot of normalized fluorescence intensities of GFP::AHPH and NMY-2::RFP versus time for the pulse displayed in (B). Below: kymograph showing movements of NMY-2::RFP punctae before and during the pulse. Yellow box at left indicates the region used to make kymograph. Yellow arrow at right indicates the onset of contraction. Note that a sharp rise in GFP::AHPH precedes both Myosin accumulation and onset of contraction. (D) Averaged normalized fluorescence intensities for NMY-2::RFP, GFP::AHPH and GFP::UTR from two-color movies, aligned to the time at which NMY-2::RFP reaches 25% threshold. Halos report 95% confidence intervals. (E) Distributions of the delay in onset of accumulation of GFP::AHPH, GFP::UTR, and NMY-2::GFP, measured relative to the onset of accumulation of NMY-2::RFP during pulse initiation for many individual pulses. Onset of accumulation is measured as the time at which each normalized signal exceeds 25% of its maximum value. (F) Distributions of the delay in the onset of disappearance of GFP::AHPH, GFP::UTR, and NMY-2::GFP measured relative to NMY-2::RFP during pulse termination for many individual pulses. Onset of disappearance is measured as the time at which each normalized signal falls below 75% of its maximum value. In (E,F) box plots, the central mark represents the median, the box indicates the 25th and 75th percentile, the whiskers mark the minimum and maximum values and the “+” symbol represents outliers.

CHAPTER 5

CONCLUSIONS, OPEN ISSUES, & FUTURE DIRECTIONS

5.1 Comparison with Recent Modeling Publications

There have been several recent publications incorporating various mechanisms of turnover in cross-linkers, filaments, and motors, while probing timescales of stress generation and dissipation. In the following two sections, I will compare my work with the results found in the two most pertinent recent papers.

5.1.1 Role of Turnover in Active Stress Generation in a Filament Network by Tetsuya Hiraiwa and Guillaume Salbreux

In their paper from May of 2016, Hiraiwa and Salbreux[81] showed that their model networks of filaments and active and passive cross-linkers were capable of generating transient stresses, and that adding filament turnover was able to cause those stresses to be maintained indefinitely. They also showed that there needed to be a critical number of cross-linkers present in order for the network to generate stress. The specifics of how and why these conclusions were dependent on the specific model they used so I will next explain the specifics of their model and how it differed from my own.

Their model consisted of rigid filaments and rigid motors in the presence of passive cross-linkers. The passive cross-linkers were considered to be point-like and to bind the rigid filaments together directly at their point of contact. From this it follows that the cross-linking constraint only allows deformation through filaments rotating around their points of contact. In addition, it should be clear in this mechanical picture that 3 filaments attached into a triangle will not be able to undergo any

deformation. According to the paper, the main driver of force generation is when a motor filament walks along two actin filaments that are cross-linked together at one point. The motor filament exerts a force on the two filaments which can serve to either contract or extend the filaments relative to each other. Averaging over the total number of configurations before the motor detaches, they find that one motor with two filaments has a net contractile effect. In contrast, in my simulations, this effect would not take place at all. The geometrical argument requires myosin motors to be fairly large relative to the actin filaments in order for this effect to be significant as was shown in [109]. In my simulations, the contractile asymmetry followed directly from the asymmetry between the spring constant of extension vs. compression.

Next, their model predicted that there would be a minimum number of cross-linkers required before there could be a net stress generated within the network. Their critical number of cross-linkers turned out to be equal to the number of filaments. This seems reasonable, as with fewer cross-linkers, there would on average be less than one cross-linker per filament, meaning that most filaments would on average only be attached to one other filaments and would therefore be unable to transmit force between two filaments. In my model, cross-linking was assumed to take place at every filament overlap point, but if I relaxed this requirement of my model, I presume that reducing the number of cross-linking points would result in very nearly the same effect as was found in this study.

These networks generated and maintained their stress, but the addition of cross-linker turnover prevented stresses from persisting. Once cross-links were allowed to turn over, filaments and motors were able to freely rearrange. The authors showed that this free rearrangement led to loss of connectivity and clumping of filaments and motors which prevented the sustainment of stress. This is highly similar to the result from my work where a form of viscous cross-link slipping also resulted in a global loss of stress buildup over time. In my work, however, this was baked into the form of the cross-linking from the beginning so all that could be varied was the timescale over which stress dissipation took place. Entirely preventing stress dissipation by making the cross-link binding permanent was not possible in my framework.

The most pertinent conclusion from this paper was that the addition of filament

turnover into the network restored the ability to maintain a non-zero stress indefinitely even when cross-links were turning over. Their explanation for this is similar to the reasoning from my paper: active motors rearrange filaments, which causes a loss of connectivity, but this can be prevented by putting filaments back into the rarefied regions of the network. They show examples of this to suggest that this is indeed the case, and continue to show that their finding for the critical number of cross-linkers qualitatively holds for the case of turnover as well.

The authors were able to present a phase diagram that summarized their main conclusions. In the diagram, they essentially just showed that there was an optimum in turnover time and that the optimum varied with the number of cross-linkers. The more cross-linkers the network contained, the faster the turnover had to occur in order to reach the optimum. Because the number of cross-linkers was not varied in my simulations there was no similar conclusion in my paper.

The authors in this paper did not look at the passive dissipation of stress in the absence of active stress generation. However, it seems safe to assume that at least two conclusions from their work would hold in their simulation framework if they were to probe the passive properties using an external force as I did. First, the network would not be able to maintain global connectivity if the number of cross-linkers was less than the number of filaments. The reasoning is identical to the active case where having fewer than one cross-link per filament will almost certainly lead to a global loss of connectivity over a large enough spatial scale. Second, in the presence of cross-link turnover the network would not retain global connectivity.

5.1.2 Interplay of active processes modulates tension and drives phase transition in self-renewing, motor-driven cytoskeletal networks by Michael Mak, Muhammad H. Zaman, Roger D. Kamm & Taeyoon Kim

The model of Mak et al.[133] is probably one of the most intricate models used to simulate actomyosin mechanics in the field. As such, it is very useful for suggesting the

origins of emergent properties in these networks. On the other hand, its complexity can make it difficult to pin down precisely which effects lead to which outcomes. Nevertheless, in this paper, the authors were able to draw conclusions about what mechanisms led to their observations and bulk measurements. Importantly, this was the first work to show that networks without turnover can only generate transient net stress and that turnover allows the network to persistently maintain stress.

Their modeling framework consists of segmented actin filaments where each filament has an extensional and a bending spring constant. These filaments are connected by cross-linkers that are also small springs, which can bind and unbind randomly with a characteristic timescale. Finally, motors are implemented as cross-linkers with the ability to periodically hop from one location to the next along the filament. This modeling framework is very useful due to its high molecular similarity with a number of known properties about actin and myosin networks. In particular, the model tries to base its conclusions firmly on a realistic picture of actin and myosin mechanics by choosing simulation parameters that match closely with real measured values.

Their work presents many modeling scenarios where the end result is a network with a short-term buildup of stress followed by a global loss of connectivity and a falloff in the global stress generation. They vary a number of physiologically relevant parameters and monitor the sustainability of stress. Similar to the above work by Hiraiwa and Salbreux, they focus on varying the number of cross-linkers and the filament turnover rate, but they also explicitly vary the percent of crosslinkers that are active. By doing this they were able to map a phase diagram, which showed that the ability to sustain force was possible in one region of parameter space and that the sustained stress was only large in another region of parameter space. Taken together, the overlap of those two domains shows where the network is able to sustain large stresses. This occurs in a confined domain similar to that shown in the work of Hiraiwa and Salbreux. Their explanation for the inability of some networks to sustain stress is that networks deform and generate clusters of material which prevent global stresses to be sustained. They measure the clustering and show that it is important.

They end their work with a generalization of their findings to a so-called active spring model of network contraction. This model represents a simplified view of their

simulation results, and recapitulates the rising and falling timecourse of network stress buildup. Finally, they address a handful of experiments that loosely corroborate their findings. It will be interesting to see more in-depth experimental validations of these models in the future.

This work did not include an analysis of the passive properties of the network, but the authors had already inspected the network in the passive case in their prior work [100]. In fact, their prior conclusions of the importance of filament turnover for tuning the viscosity of simulated networks was the main influence on my current work.

5.1.3 Shared conclusion of all three works

I think it is important to point out that all three of these works (the two previously published as well as my own) have shown that there is in some sense an optimal turnover time for producing a maximal steady state stress. Because the methods of producing the simulations took account of different assumptions, the exact form of the maximal time is different, however, it is remarkable that this property was found to be general to all three modeling forms. It is fairly clear from a mechanical perspective why this would be the case in hindsight, but it appears that this outcome wasn't predicted before these attempts were made at generating models.

However, it should be pointed out that in contrast to the other two papers, my model allows for a subtler mechanism underlying the transience of stress generation in networks without filament turnover. In my work, I attempted to emphasize that the global loss of stress will occur even if the network does not undergo visible thinning and tearing. In particular, there can be a persistent global stress coming from contractile and extensile segments in the network, but these effects will cancel each other to generate no net stress. This observation goes a long way to show that the absence of a permanent stress buildup is not possible even when tearing doesn't occur and that indeed it is reasonable to believe that there should be no way to maintain a permanent stress

5.2 Incorporating multi-segment filaments and bending degrees of freedom

For simplicity, notable aspects of semi-flexible polymer mechanics have been ignored throughout the entirety of this thesis. In developing this work, I chose to limit my analysis to single springlike filaments in order to focus attention on the most prominent properties of semi-flexible polymers. In effect, I took the minimal number of model elements (and accompanying free parameters) that would suffice to produce the 2D network flows of interest.

While this choice greatly simplified the analyses performed and allowed me to focus my results, it does ignore aspects of filament mechanics that may play an observable role in macroscopic cell mechanics. In particular, there are two clear oversimplifications that are introduced by using single springs: uniform strain along filaments and absence of bending.

Uniform strain along filaments results from the model's current insistence that forces add to produce a net strain in the filament. Because all forces are transmitted merely to the ends of each spring, there can be no internal regions of variable strain anywhere else along the filament. This necessarily overlooks the local deformations that could be driven by internal motor forces. The net result will be that deformations on small length scales. As such, certain measurements that were made in the above analysis are most probably over-averaged and not indicative of what would be found in a real system. It is still unclear what impact this will have on the macroscopic dynamics of the system, but nevertheless, this is one of the largest missing pieces that could invalidate some of the model predictions.

The absence of bending degrees of freedom is probably of less concern than the imposition of uniform filament strain. To begin, the fact that bending causes filament stiffness asymmetries has already been incorporated in the asymmetric extensional stiffness imposed on filaments in this model. Thus, adding bending will only serve to double count this asymmetry and will probably not provide much benefit. A second aspect of filament network mechanics is more problematic. It has been shown previously that the mechanical picture of 2D networks can transition from extension

dominated to bending dominated when network densities are sufficiently sparse. The net result of this is that at low enough densities, the main mechanical resistance will be dependent on filaments resisting bending. My model will neglect this transition to bending dominated mechanics, and therefore, the model network should become completely pliable despite the fact that the real network will still maintain some resistance to deformation. However, analyzing networks at such sparse densities will present numerous challenges to the continuum models presented in this work so worrying about the specifics of bending dominated mechanics may be of lesser concern.

Nevertheless, it is important to note that the current implementation can easily allow the introduction of multisegment bending elements. If one uses segment sizes that are shorter than the total filament length, joints will automatically be introduced that separate the filament into multiple regions that are free to deform on their own. However, with $\kappa = 0$, these joints will be free to rotate, which will cause the model to create effectively separated springs that are merely forced to share one attached end. However, $\kappa > 0$, the model will introduce a bending spring that tries to keep individual filaments straight. The magnitude of the bending modulus can then be varied to change the bending stiffness of the filament.

5.3 Probing more complex mechanisms of turnover

Another notable simplification in this work is the method of incorporating filament turnover by causing entire filaments to be reset at random. This is actually not the microscopic means by which filaments are depolymerized and repolymerized in the cell. In fact, both filament depolymerization and repolymerization are governed by more complex and intricate processes that have been studied to painstaking detail. The net result of these events does cause rapid and complete strain resetting on long enough timescales, but there can be subtleties that change the exact form of the strain and orientation resetting of filaments.

The actual mechanism for filament depolymerization relies on a balance of slow filament treadmilling, accompanied by faster timescale filament severing events. The combined action of these two mechanisms should cause a quite rapid removal of the

filament from the physically connected network and thus cause an effectively immediate stress dissipation much like the one demonstrated in our model. Nevertheless, there may be all kinds of regulatory factors which act to make the stress dissipation less idealized than in the simplified model. One such complicating factor would be stress dependent severing rates, which would cause non-uniform dissipation of stress or preservation of stress depending on whether filaments were preferentially severed based on being high stress or low stress state, respectively. Any mechanism could in principle be added to this model, however, it would add to the difficulty of interpreting results and therefore should be incorporated only if some aspect of the model is found to be deficient in its explanatory ability of a specific result.

In addition, to regulation causing non-uniformity in depolymerization, there are molecular details that impact our assumptions about repolymerization as well. In cells, much of the structural actin cytoskeleton is aided in polymerization by formins, which recruit actins to rapidly accelerate the polymerization process. While many aspects of the polymerization are still under active study there is at least some preliminary evidence that the specific nature of formin polymerization provides biases in the orientation of newly polymerized filaments. Specifically, formins appear to follow existing actin filaments preferentially, thereby serving to lay down new actin along a template of existing actin. In addition, crosslinking proteins can preferentially align newly polymerized actin as well. This may be an important part of regulating stress assymetries and as such may need to be incorporated into some aspects of active network models in the future.

The end result of these complex processes allows stress resetting to occur independently from orientational resetting. In this sense, the simplifications in the current implementation tend to conflate the processes of stress resetting and orientation resetting. In effect, there may be different timescales over which different aspects of network memory relax. As such this may be an important avenue of future work.

5.3.1 Which is more important, filament relocation or stress resetting?

It seems very clear that the global disruption of connectivity will necessarily lead to an inability to maintain global net stresses. However, in this work, I've argued that one need not develop global loss of connectivity in order for the net. I found that it was possible for networks to remain macroscopically connected, but for local rearrangements and the internal balance of extension and compression to cause the global stress to dissipate. Therefore, there are actually two distinct activities occurring when filaments are recycled in my model: 1) they are relocated to locations where there may be fewer filaments, and 2) they are reset to have 0 net strain. From this basis, Ron Rock on my committee asked an interesting question: Which is more important, filament relocation or stress resetting.

In my opinion, it is stress resetting which is ultimately more important than filament relocation. Overall, if the thinning from global rearrangement was apparent, then one would have to relocate filaments to maintain connectivity. However, without resetting strain, the filaments would still be able to reach internal balance between extension and compression. In other scenarios, where there is no global thinning, the net stress is still lost over time due to the local rearrangements and extensional and compressive balancing.

It would be easy to test this with the framework I have put in place. One could decouple the two mechanisms by relocating filaments without changing their strain state, and to reset their strain without moving them to new areas. If I were to relocate filaments to regions where connectivity was being lost, but I was to retain them in their stressed state, I predict that the net stress would be lost. This might be useful for future work although it appears pretty clear how it would work out.

5.3.2 Overlooking the subtleties of myosin turnover

My model notably lacks any direct mechanism by which motor turnover can be implemented—i.e. any pair of segments that interact actively at the beginning of the simulation will continue to do so any time they meet each other throughout the

simulation. In a more realistic scenario it should be possible for an intersection of two filaments to undergo intermittent transitions from active to passive interaction. This would mean that the over time filaments would be able to be driven to be stressed and then even without local rearrangement, start to dissipate that stress after the myosin turns off.

Importantly, this oversight leaves the possibility that filament turnover is not actually required to allow stresses to persist. Instead, it would be possible for the filament stresses to be reset by the constant deactivation and reactivation of motor activity. In principle, this could give rise to a form of stress resetting similar to the mechanism found with filament recycling. As such, filament recycling could end up being redundant. Nevertheless, it's possible that myosin turnover would not be capable of completely resetting filament stress because the filament stress relaxation would not be instantaneous as it is with filament recycling.

It would be easy to address this concern by modifying the simulation framework. When originally contemplating this modeling framework I considered incorporating a time varying active force, but decided this would be too contrived to use. Perhaps a better implementation would simply allow random switching of motor activity on and off with yet another characteristic timescale, say τ_τ . In this case, it would seem reasonable that the stress state of the network would be dependent on the minimum of the filament recycling timescale mentioned above (τ_r) and the myosin turnover timescale (τ_τ).

5.4 A novel cell squishing technique to measure timescales of relaxation *in vivo*

At the moment, there are very few possible experiments to probe the stress relaxation possible from filament turnover. I have developed a proposed experiment, which would allow a reasonable measurement of the timescale of deformation of the cell's cytoskeleton. By squishing the cell into a hot dog shape and then letting it freely relax to a sphere, one can approximate the viscosity of the cell's surface. This is because the timescale of relaxation to spherical for a purely viscous droplet embedded in a

medium with much lower viscosity is $\tau \sim T/\eta$ where T is the surface tension and η is the droplet viscosity.

My preliminary experiments showed that this technique was highly reproducible, and could be used to determine reliable timescales by fitting the cell's deformation profile for the time constant of relaxation. In addition, by carrying out the experiments in rooms with different temperatures, I was able to get a consistent shift in the relaxation timescale between sets of samples. Finally, in an experiment with Latrunculin A, a factor that largely depolymerizes the entire actin cytoskeleton, I could determine that the timescale of relaxation for cells in the absence of cortical structure was effectively instantaneous. Thus, changes in cortical viscosity should be easily assessed.

I made several attempts to perform the experiment myself, but, alas, my experimental chops were not up to the task. When treating with jasplakinolide to stabilize the cortex, the embryos underwent a global irreversible contraction. This is to be expected from our earlier observations where myosin acting on a network without turnover causes network contraction and tearing of the cortex (see Appendix). Therefore, in order to perform the experiments properly, one needs to first knock down myosin in the cortex. This presents some experimental difficulty, but can easily be overcome by anyone with sufficient training in *C. elegans* biology.

APPENDIX A

SOURCE CODE AND DOCUMENTATION

A.1 Practical Implementation of Model Framework

Although the prior description is useful for communicating the mathematical principles underlying my modeling framework, I also want to provide a practical explanation of the logic of the code structure. This will help to clarify the implementation details that may be ambiguous in the above formulation and make it easier for others to approach and modify my code.

The simulation code is entirely built on top of MATLAB's ode solving functions. Therefore, at the highest level, the entire simulation framework simply boils down to providing functions to define the ode's left and right hand side, along with the initial conditions for the system. However, because MATLAB's solvers do not allow discontinuities, discontinuous filament recycling events cannot be implemented directly in the ODE. Effectively, it is necessary to stop the simulation solver at fixed times, reset some subset of filaments, and restart the solver with the new state every time a turnover event happens.

In the following sections, I'll walk through the code's logic in more detail, emphasizing the packages and files that modularly summarize the core functions. First I will begin with an explanation of the command line interface used to set model parameters and deploying simulations.

To find the *activnet* simulation code, visit:

<https://github.com/wmcfadden/activnet/tree/master/simulation>

A.1.1 Launching simulations from the command line

The *activnet* package includes a function called *activnet_gen.m*, which can be used to launch simulations on any MATLAB system. The following is the documentation of

the parameters passed to this function.

```

function p = activnet_gen(zet,L,mu,kap,lc,xi,ups,phi,psi,
                           r,sig,Dx,Dy,Df,Dw,ls,lf,tinc,tfin,nonlin)
% generates an active network simulation and prints node positions
% at time steps. Parameters are defined as follows:
%
%   zet - medium viscosity
%   L - length of the filament
%   mu - compressional modulus of the filament
%   kap - bending modulus of a filament if ls<L
%   lc - average distance between filament overlaps
%   xi - frictional resistance between two overlapping segments
%   ups - motor force at filament overlaps
%   phi - fraction of overlaps that receive a motor force
%   psi - spatial variation in motor force
%           (if external force applied, psi sets the periodicity of
%           force application, and psi<0 sets square wave.)
%   r - recycling rate
%   sig - applied stress in the x direction applied at Df*Dx
%           (sig<0 sets stress to be applied in y direction)
%   Dx - x-dimension of domain
%   Dy - y-dimension of domain
%   Df - position at which external force is applied
%           (if Df<0, also position in x dimension where network stops)
%   Dw - width of window in x-dimension where forces are applied
%   ls - length of filament segments
%   lf - length of force falloff at end of filament
%           (just ensures continuous forces)
%   tinc - time increment to return solutions
%           (will be decreased automatically if r is too large)

```

```
% tfin - end time of simulation
% nonlin - factor by which to make filament stiffer for extension
%           (if nonlin<0, add spacing so filaments dont reach edge)
```

These parameters will be explained in more detail below, but here I'll provide a brief practical explanation for their use in setting up simulations. The parameters `zet`, `L`, `mu`, `kap`, `lc`, `xi`, `ups`, `phi`, `r`, `sig`, `Dx`, and `Dy` are defined in the mathematical methods section above as ζ , L , μ_c , κ , l_c , ξ , v , ϕ , $1/\tau_r$, σ , D_x , and D_y , respectively. The parameter `nonlin` is used to internally calculate the extensional modulus $\mu_e = \text{nonlin} \times \mu_c$ (i.e. if `mu` is 1 and `nonlin` is 100, then $\mu_c = 1$ and $\mu_e = 100$). The parameter `psi` is used to generate a spatial gradient in internal activity or temporal periodicity if an external force is applied. The spatial gradient is linear with a maximum at the center of the domain. The parameter `Df` defines the fraction along the x-domain where any external stress will be applied (i.e. stress is applied at Df^*Dx).

All of these terms are positive by definition so setting certain terms negative is used to trigger certain behavior in the simulation environment:

- Setting `mu` < 0 enables the extensional spring constant to be different than the compressive.
- Setting `sig` < 0 causes the external stress to be applied in the y direction rather than the x direction, resulting in shear stress simulations.
- Setting `nonlin` < 0 results in space being added to the edge of the domain so that no filaments intersect with the boundaries of the simulation, allowing the network to undergo unconstrained contraction.
- Setting `psi` < 0 results in oscillating positive and negative stresses being applied to the network (as opposed to a sinusoidal pattern regularly).
- Setting `Df` < 0 will cause the rightward edge of the initially generated network to end at the location where the force is applied.

The parameter `ls` sets the segment size of the filament. Theoretically this segment size is very small (the size of a single actin monomer perhaps), but for computational

reasons this value is set much larger. The parameters `Dw` and `lf` set the regions over which forces will fall off for the domain and individual filaments, respectively. These are just there to ensure there are no discontinuous changes in the ODE equation as filaments move around, and should be set to some smallish number, like 0.05, but don't affect the results too much overall. Finally, `tfin` and `tinc` set the end time of the simulation and the timesteps at which to print results, respectively. The program will automatically shrink `tinc` if the recycling rate, `r` is large enough that manual position updates must occur on timescales smaller than `tinc`.

To run a simulation with an external stress the following code could be used.

```
activnet_gen(0.001, 1, -0.01, 0, 0.8, 10, 0, 0, 0,
             0, -0.002, 20, 4, -0.33, 0.05, 1, 0.025, 1, 10000, 100)
```

To run a simulation with internal filament activity the following code could be used.

```
activnet_gen(0.001, 5, -0.01, 0, 0.3, 10, 0.1, 0.25, 0,
             0.001, 0, 25, 25, 0.5, 0.05, 5, 0.025, 1, 10000, -100)
```

Both of these have nonlinear filament extension because the third argument (`mu`) is less than 0. The results will be printed to the MATLAB console.

The currently deployed package can also be used to launch simulations on any linux system with MATLAB 2014b or the MATLAB 2014b Compiler Runtime installed (you will need to have a \$MATLAB environment variable enabled. Please contact your sysadmin.). In addition, the package can be recompiled on any system running MATLAB to create a new deployment that will run on the compiled MATLAB version and operating system (see the README.txt file for more information about deployment).

```
./run_activnet_gen.sh $MATLAB 0.001 1 -0.01 0 0.8 10 0 0 0 0
-0.002 20 4 -0.33 0.05 1 0.025 1 10000 100 > output.file
```

A.1.2 Package structure of activnet

To understand the high-level overview of this code, you can analyze the basic package structure and the small number of important top level packages.

- activnet_gen.m: topmost wrapping function to call for running simulations; confirms input, generates initial conditions, and calls activnet.m
- activnet.m: Chooses between which ODE implementation to run; stops ODE solver execution to perform filament recycling.
- odes folder: Contains all the ODE computation internals.
- helpers folder: Some additional functions written to perform line intersection tests.
- analysis folder: All the code used to generate the figures in the accompanying publication.

Note: the rest of this documentation is most useful if one is looking over the internals of the code. Trying to understand this without working with the code is probably not very useful.

A.1.3 ODE Wrapper functions

As mentioned above, the initialization and launch of the simulation takes place using the function activnet_gen.m. This function is quite simple. It just ensures proper input parameters, builds a randomized network of filaments, prints the network node positions, and then calls the function activnet.m to compute the simulation results. From there, activnet.m takes care of pausing solvers to update filament position for recycling as well as choosing between solvers depending on the type of problem being solved.

Generating Initial Conditions

Before an ODE solve can be called one needs to set up the initial conditions of the network. Every solver implementation in MATLAB operates on 1D vectors where every element represents a variable to be integrated. Therefore, the data structure for this model is going to need to be set up to be encoded as a 1D vector of numbers. Because the model framework is based around the 2D position of points, I will continually be shifting between the 1D vector, z and the 2D vector p using the following transformations.

```
p = reshape(z0,[],2); % z -> p
z0 = reshape(p,1,[]); % z -> p
```

To select the number of filaments, N , to generate using the input parameters, we use the approximating formula $N \approx \text{floor}(2*Dx*Dy/lc/L)$. This formula is derived from the tiling of a $Dx \times Dy$ domain with lines of length L and spacings between lines lc . This diverges from the exact number of filaments needed when L/lc is small, but we ignore this discrepancy because we mostly operate in the regime where $L/lc > 10$.

We therefore begin by creating an initial set of filament segment endpoints p , where we want to have N total filaments each with $ncnt$ segment endpoints. We do this by selecting a random starting point in our domain (Dx by Dy) with random orientation (thet).

```
p = zeros(N*ncnt,2); %initialize all endpoints to 0
for i=1:N
    p((i-1)*ncnt+1,:) = [Dp*Dx*rand Dy*rand]; %random starting location
    thet = rand*2*pi; %random direction
    for j = 2:ncnt % iterate through remaining segments to add endpoints
        p((i-1)*ncnt+j,:) = p((i-1)*ncnt+j-1,:)+L/(ncnt-1.0)*[cos(thet) sin(thet)];
    end
end
```

In most cases, the network should be assembled such that the domain is filled entirely in the y dimension ($y = 0$ and $y = Dy$) and filled to the left edge ($x = 0$)

and up to the position $x = Dp * Dx$ in the x-dimension. However, in the case that the parameter `nonlin` is less than 0, we set the initial conditions such that there is an empty space of size $0.2Dx$ and $0.2Dy$ at the x and y boundaries.

To keep our density the same we should adjust our calculation of N above, however, in the current implementation this adjustment is not made. This is a known bug that was corrected for after-the-fact in the publication by multiplication of l_c by a constant factor depending on the simulation setup.

Choosing between active and driven simulations

During development I noticed that there were some cases where I could skip certain sections of the computation to speed up integration of the ODEs. In particular, when there is no internal forces generated by filament activity, the right hand side of the differential equation is easier to compute (see below). Therefore, in any situation where internal activity is set to 0, we use the more efficient code. The `activnet.m` code makes this decision by determining if there is pulling of filaments rather than internal force generation.

```
pull = (isempty(nu)&&sig^=0)
```

In this case it runs a different pair of functions to compute the ODE right hand side and mass matrix (see below).

Implementing Filament Recycling

The core function of `activnet.m` is to serve as a wrapper for the ODE solvers mentioned above and described in greater detail below. However, since the ODE solvers won't allow discontinuous changes to the positions of nodes, `activnet.m` must also carryout the task of stitching together smaller simulations and manually updating positions in between. The code in `activnet.m` implements a repeated loop with calls to the underlying ode solvers. If $r > 0$, a solver computes the integral between two adjacent time points in the vector of all time points to evaluate, tt . Then the positions are updated and the solver is used to evaluate integral for the next time interval. Logic

implemented in activnet_gen.m ensures that the timesteps are selected small enough so that there will not be too many filaments disappearing at once.

The following code chunk implements the position update for a randomly selected subset of nodes whenever the recycling rate, r , is greater than 0. The logic implemented in activnet_gen.m ensures that the timesteps are not so large that more than 5% of filaments will be undergoing a discontinuous jump at any one time (i.e $r * istep * tinc < 0.05$).

```
% % select random indices
i = randi(N,floor(r*istep*tinc*N)+(rand<mod(r*istep*tinc*N,1)),1);
% % reset the position of the first segment endpoint
p((i-1)*ncnt+1,:) = [Dp*Dx*rand(size(i)) Dy*rand(size(i))];
% % pick random orientation for each filament
thet = rand(size(i))*2*pi;
for j = 2:ncnt % % iterate over rest of endpoints
    p((i-1)*ncnt+j,:) =
        p((i-1)*ncnt+j-1,:)+L/(ncnt-1.0)*[cos(theta) sin(theta)];
end
```

A.1.4 Overview of Numerical Integration Implementations

As mentioned above, the solution is numerically integrated using MATLAB's built-in ODE solvers. The ODE equation is the low-Reynolds limit of Newton's equation of motion for all the filaments. So to implement, I simply supply an ode solver with a function to compute the right hand side of a system of differential equations ($\mathbf{f}(\mathbf{x})$) along with a function to compute the mass matrix (\mathbf{A}) that connects the derivatives on the left hand side of the ODE system.

$$\mathbf{A} \cdot \dot{\mathbf{x}} = \mathbf{f}(\mathbf{x}) \quad (\text{A.1})$$

With those two matrices the system of differential equations can then be integrated to the desired level of precision by one of MATLAB's implicit ode solvers (e.g. ode15s

or `ode23`). In that equation, \mathbf{x} simply represents the positions of filament endpoints (nodes). Therefore $\dot{\mathbf{x}}$ is just a way to represent the velocity of every endpoint.

The right hand side represents the forces (external or internal) driving the motion of the filaments. The mass matrix \mathbf{A} represents the coupling of filaments to each other (off diagonal elements) and to the solvent in which they are embedded (diagonal elements). Once those are provided, MATLAB's solvers take care of the integration (see MATLAB ode solver documentation for more info).

Right hand sides: *activnet_act_ode.m* vs. *activnet_pull_ode.m*

The right hand side of the equation constitutes all the non-viscous forces in the simulation. The most important and fundamental forces are those of the intrafilament spring mechanics. In these simulations, filaments are represented by chains of filament segments that act as springs with particular properties. As described above, each segment has a compressive (`mu`) and extensional (`mu * nonlin`) spring constant that governs the motion between endpoints along the length of each filament. There is also a bending spring constant (`kap`) which effectively tries to straighten adjoining segments if they are not already colinear. The internal mechanical forces of all filaments in the simulation is represented in the following code snippet.

```
%% compute intrafilament forces
10 = L/(ncnt-1); % length of segment
dp = zeros(size(p));
for n=1:ncnt:length(p)
    va_orth=[0 0];
    va = [0 0];
    la = 0;
    for i=0:ncnt-2
        % % custom subtraction minding boundaries
        vb = mydiff(p(n+i,:),p(n+i+1,:),Dx,Dy);
        lb = sqrt(vb*vb');
        gam = (lb-10)/10; % extension of the segment
```

```

f = mu*vb/lb*gam;           % longitudinal spring force
if(mu<0)                   % allow nonlinearity
    f = -f*(1+(muN-1)*double(gam>0));
end
dp(n+i,:) = dp(n+i,:) + f;
dp(n+i+1,:) = dp(n+i+1,:) - f;

% % below is for bending stiffness

vb_orth = [-vb(2) vb(1)];
if(i>0)
    if(va_orth*vb'>0)
        va_orth = -va_orth;
    end
    if(vb_orth*va'<0)
        vb_orth = -vb_orth;
    end
    tor = kap/10^2*acos(max(min(va*vb'/la/lb,1),0));
    dp(n+i-1,:)=dp(n+i-1,:)+tor*va_orth/la;
    dp(n+i,:)=dp(n+i,:)-tor*va_orth/la;
    dp(n+i+1,:)=dp(n+i+1,:)+tor*vb_orth/lb;
    dp(n+i,:)=dp(n+i,:)-tor*vb_orth/lb;
end
va = vb;
va_orth = vb_orth;
la = lb;
end
end

```

The code loops over every `ncnt` nodes, which constitute the nodes of a single filament. Next the code loops through each node of the individual filament. First, the

code evaluates the extensional force on each node given by $f = \mu * v_b / l_b * \gamma$ with the modification that if $\mu < 0$ and $\gamma < 0$, the force constant is modified to incorporate the nonlinear extensional stiffness. Next, the code evaluates the bending forces for adjacent segments that are not aligned using

```
tor = kap/l0^2*acos(max(min(va*vb'/la/lb,1),0)).
```

The `max(min(...))` is used simply to ensure that there are no aberrantly large values due to errors in evaluation of `acos` with arguments very slightly greater than 1 or less than 0. The two vectors `va_orth` and `vb_orth` are calculated to direct the force orthogonal to the orientation of the filament segment. Finally, it should be noted that a bending force is generated from both the segment behind and the segment in front of the current node of interest and that the force from these need to be assigned at both the current node and the equal and opposite force assigned at the other end of each filament.

After the basic mechanical properties of the filament are accounted for, we need to add extra forces (otherwise the simulations won't be any more interesting than just a bunch of inert springs). What we do depends on whether the simulation is meant to represent active motors or a passive network with an external driver. In the next two sections we cover the specifics of the force equations for both of these cases.

Active ODE

For the ODE with internal activity, we need to compute a very different force on each node. In particular, we have to check for intersections and add forces to filaments that intersect as if they are being pulled on by an active motor at their overlap point. To do this we will use one of the helper functions described below to return all of our overlapping lines. After that we will step through all pairs of intersecting lines and add the appropriate force in the appropriate direction. The following code snippet shows the process with documentation.

```
g = lineSegmentGrid(indL,XY,Dx,Dy,10); % find instersecting lines
```

```
% find distance of intersections from endpoints
```

```

f = min(1,max(0,(g-lf/2)/(1-lf)));
for ind=1:size(g,1)
    i = g(ind,3);
    j = g(ind,4);

    vm = mydiff(p(j,:),p(j+1,:),Dx,Dy);
    lm = sqrt(vm*vm');

    edg = 1;    % this will be used to reduce the force
    % as it gets closer to the edge of a filament

    if(g(ind,1)<lf)
        edg = edg*g(ind,1)/lf;
    elseif((1-g(ind,1))<lf)
        edg = edg*(1-g(ind,1))/lf;
    end

    if(g(ind,2)<lf)
        edg = edg*g(ind,2)/lf;
    elseif((1-g(ind,2))<lf)
        edg = edg*(1-g(ind,2))/lf;
    end

    mul = 1;    % this will be used to modulate the force if
    % psi says there should be a spatial gradient

    if(psi>0)
        mul = double(g(ind,5)>=psi*abs(-Dx*Df));
    end

tnu = nu(ceil(i/ncnt),ceil(j/ncnt))*mul;  % variation in

```

```
% filament force (phi)

dp(i:i+1,:) = dp(i:i+1,:)+edg*tnu/lm*[vm*(1-f(ind,1));vm*f(ind,1)];
dp(j:j+1,:) = dp(j:j+1,:)-edg*tnu/lm*[vm*(1-f(ind,2));vm*f(ind,2)];

end
```

The last line shows the net force that is added to both pairs of nodes that are intersecting ($i:i+1$ and $j:j+1$) with one positive and the other negative to conserve the net force to be 0. The term f is calculated as the distance of the overlap point between the two nearest node locations, and is used to set how much force is applied to the first vs second node. For each iteration of the loop, the force is calculated for the $j:j+1$ filament, and each interaction is stepped through twice (once with each filament in the $j:j+1$ role). The vm calculation determines the direction in which the forces will be applied. The terms edg and tnu simply modify the applied force by scalar quantities based on closeness to the end of the filament and spatial variation in motor force intensity.

Pulling ODE

For the case of the system with an external stress, we will need to add forces at the desired location of stress, and we will need to constrain the filaments located at the edge of the domain. The following two code snippets show these two behaviors.

```
%% add external force at centerline
if(psi>0)
val = sig*sin(psi*t);
elseif(psi<0)
val = sig*round(mod(0.5+-psi*t,1)).*(round(mod(0.55+-psi*t/2,1))-0.5)*2;
else
val = sig;
end
```

```

subp = p(:,1)>(Df-Dw)*Dx&p(:,1)<(Df+Dw)*Dx;
ff = 1-abs(p(subp,1)-Df*Dx)/Dw/Dx;
if(sig<0)
    dp(subp,1)=dp(subp,1) - Dy*val.*ff/sum(ff);
else
    dp(subp,2)=dp(subp,2) - Dy*val.*ff/sum(ff);
end

```

The top section of this code calculates stress that should be applied and sets that as `val`. If `psi` is nonzero then we are looking to have a temporally varying applied stress. If `psi > 0`, then we want a sinusoidally varying stress with frequency `psi`. If `psi < 0`, then we want a square wave with frequency `psi`. The max stress in each case is still `sig`.

The bottom section selects the nodes that will have force added to them in `subp`. The force to be applied to each node is not equally distributed, but instead, `ff` sets the fraction of force to be proportional to the distance to the center of the region of applied stress (set by the width `Dw`). This distribution function is normalized so that the total amount of force is equal to the amount of force needed to set the stress to `val` (i.e. $F_{total} = val \times Dy$). Finally the force is applied in the x direction or the y direction based on whether `sig` is greater or less than 0.

```

% % constrain edges
subp = p(:,1)<Dw*Dx;
dp(subp,:)=dp(subp,:).*repmat(4*p(subp,1)/Dw/Dx-3,1,2);

subp = p(:,1)>Dx*(1-Dw);
dp(subp,:)=dp(subp,:).*repmat(4*abs(p(subp,1)-Dx)/Dw/Dx-3,1,2);

subp = p(:,1)<3*Dx/4*Dw|p(:,1)>Dx-3*Dx/4*Dw;
dp(subp,:)=0;

```

This last segment merely constrains the force at the far left and right edges of the domain to be 0 (within $0.75D_w \times D_x$ from each edge). There is a linear transition to $dp=0$ in the remaining 25% of the region.

It should be noted that in the pulling simulations, there is no need to compute the intersection of filaments. This means that there are far fewer computations than in the active case. I wrote two separate functions for each of the different cases simply to avoid having to perform redundant checks on the cases repeatedly (i.e. the choice is made once in the outer wrapping functions rather than having to repeatedly make the choice for which code to run on each iteration of the solver).

A.1.5 Left hand side: The mysterious mass matrix

To understand the logic of coupling filaments together by their velocities it might be helpful to look at a simple example. Imagine that you have a single particle in some one-dimensional fluid with viscosity, ζ , and with a force, F , acting on it. Assuming low Reynolds limit so there is no acceleration of the particle, the equation of motion would look like the following.

$$\zeta \dot{x} = F \quad (\text{A.2})$$

Now assume you have two particles in that fluid, but (for now) we assume the particles can't interact in any way. Therefore, we can express the equation of motion for both particles pretty simply with the following equation.

$$\zeta \dot{\mathbf{x}} = \mathbf{F} \quad (\text{A.3})$$

Obviously, all we did was replace the scalars with vectors. To make things a little neater we could replace the scalar ζ with a so called mass matrix that would simply look like the following matrix.

$$\mathbf{A} = \begin{bmatrix} \zeta & 0 \\ 0 & \zeta \end{bmatrix} \quad (\text{A.4})$$

Now, if we had some drag-like coupling between the velocities of our two particles with a drag coefficient, ξ , we could simply add a term to the off diagonal.

$$\mathbf{A} = \begin{bmatrix} \zeta & -\xi \\ -\xi & \zeta \end{bmatrix} \quad (\text{A.5})$$

And carrying out our math we can see that this just gives a frictional coupling between the two particles.

$$\begin{aligned} \zeta v_1 - \xi v_2 &= F_1 \\ \zeta v_2 - \xi v_1 &= F_2 \end{aligned} \quad (\text{A.6})$$

This is the entire logic behind the construction of the `activnet_mass.m` function. After finding which filament segments are overlapping, I simply add off-diagonal terms to the mass matrix that couple the nodes of those filament segments together.

Similar to the previous section, there are computational efficiencies to be gained in computing the mass matrix, \mathbf{A} , if the system is being driven externally (as opposed to being driven by internal activity).

activnet_mass.m vs. activenet_mass_sp.m

When we are constraining filaments to remain motionless we run into one little problem with our mass matrix formulation as presented thus far. Essentially, the right hand side of the equation is being set to 0, but the left hand side still has cross terms. To remedy this, in the case where an external stress is applied, I need to manually decouple filaments that lie along the $x = 0$ boundary of the domain. This is carried out in `activenet_mass_sp.m`, but it is not implemented in `activenet_mass.m` because that code only runs in the case where there is internal activity of the filaments and no external constraints.

Additionally, in `activenet_mass_sp.m`, I utilize a sparse matrix for reasons that I honestly don't exactly remember. I assume that I found in that condition I could get some kind of marginal speedup by using a sparse matrix instead of the full matrix.

A.1.6 Line intersection helper Functions

There are a series of helper functions that are called to aid in the calculations of filament intersections. You can analyze the code directly for more detail but briefly, the lineSegmentIntersect.m implementation manually computes the intersection between all pairs of segments while lineSegmentGrid.m first bins lines into grids before testing intersection just on those in the bin. I saw a significant improvement when I moved to lineSegmentGrid even though asymptotically they both perform worst case $O(n^2)$, which I believe is due to the uniformity of the line segment distribution. Some mathematician might be able to prove that. It is interesting to note that the classical best-case line scanning algorithm (i.e. sweep line) is $O(n \log n)$.

A.1.7 Visualization code

In the analysis package, I have included some code called netplot_str.m to aid with visualizing the output of the simulations. This code opens the output file and an accompanying script file to get the parameters passed to the function. The code then goes on to render all the lines in a MATLAB plot. It could be modified easily to render the output in whatever format you may need. However, it is important to note that you need the input parameters to correctly associate output nodes to their correct filament.

A.2 Finding Source Code Online

Source code and up-to-date documentation are available online for the projects described in this dissertation.

- <https://github.com/wmcfadden/smPress>
- <https://github.com/wmcfadden/activnet>
- <https://github.com/munrolab/pulse-reaction-dynamics>

APPENDIX B

PHASES OF DEFORMATION IN FILAMENT NETWORKS WITH CROSS-LINK SLIP

B.1 Results

B.1.1 Steady-state Approximation of Effective Viscosity

We begin with a calculation of a strain rate estimate of the effective viscosity for a network described by our model in the limit of highly rigid filaments. We carry this out by assuming we have applied a constant stress along a transect of the network. With moderate stresses, we assume the network reaches a steady state affine creep. In this situation, we would find that the stress in the network exactly balances the sum of the drag-like forces from cross-link slip. So for any transect of length D , we have a force balance equation.

$$\sigma = \frac{1}{D} \sum_{\text{filaments}} \sum_{\text{crosslinks}} \xi \cdot (\mathbf{v}_i(\mathbf{x}) - \mathbf{v}_j(\mathbf{x})) \quad (\text{B.1})$$

where $\mathbf{v}_i(\mathbf{x}) - \mathbf{v}_j(\mathbf{x})$ is the difference between the velocity of a filament, i , and the velocity of the filament, j , to which it is attached at the cross-link location, \mathbf{x} . We can convert the sum over cross-links to an integral over the length using the average density of cross-links, $1/l_c$ and invoking the assumption of (linear order) affine strain rate, $\mathbf{v}_i(\mathbf{x}) - \mathbf{v}_j(\mathbf{x}) = \dot{\gamma}x$. This results in

$$\begin{aligned} \sigma &= \frac{1}{D} \sum_{\text{filaments}} \int_0^L \xi \cdot (\mathbf{v}_i(\mathbf{s}) - \mathbf{v}_j(\mathbf{s})) \frac{ds \cos \theta}{l_c} \\ &= \sum_{\text{filaments}} \frac{\xi \dot{\gamma} L}{l_c} \cos \theta \cdot (x_l + \frac{L}{2} \cos \theta) \quad (\text{B.2}) \end{aligned}$$

Here we have introduced the variables x_l , and θ to describe the leftmost endpoint and the angular orientation of a given filament respectively. Next, to perform the sum over all filaments we convert this to an integral over all orientations and endpoints that intersect our line of stress. We assume for simplicity that filament stretch and filament alignment are negligible in this low strain approximation. Therefore, the max distance for the leftmost endpoint is the length of a filament, L , and the maximum angle as a function of endpoint is $\arccos(x_l/L)$. The linear density of endpoints is the constant $D/l_c L$ so our integrals can be rewritten as this density over x_l and θ between our maximum and minimum allowed bounds.

$$\sigma = \frac{1}{D} \int_0^L dx_l \int_{-\arccos(\frac{x_l}{L})}^{\arccos(\frac{x_l}{L})} \frac{d\theta}{\pi} \frac{\xi \dot{\gamma} L}{l_c} \cdot \frac{D}{L l_c} \cdot (x_l \cos \theta + \frac{L}{2} \cos^2 \theta) \quad (\text{B.3})$$

Carrying out the integrals and correcting for dangling filament ends leaves us with a relation between stress and strain rate.

$$\sigma = \frac{(L - 2l_c)^2 \xi}{4\pi l_c^2} \dot{\gamma} \quad (\text{B.4})$$

We recognize the constant of proportionality between stress and strain rate as a viscosity. Therefore, our approximation for the effective viscosity, η_{eff} , at steady state creep in this low strain limit is

$$\eta_{eff} = \frac{(L - 2l_c)^2 \xi}{4\pi l_c^2}. \quad (\text{B.5})$$

As illustrated in Figure B.1, under moderate strains ($\gamma < 0.2$), our simulations show that in the high density limit, our theoretical approximation from Eqn B.5 is highly accurate at explaining the network behavior. Aside from a geometrical factor, our approximation is valid for both shear and extensional stresses applied to the network.

As the density of the network approaches the breakdown limit, the effective viscosity diverges from our expected value. At the low connectivities, our expected viscosity goes to 0, but the medium viscosity begins to take over as we cross the percolation threshold at $L/l_c \sim 6$.

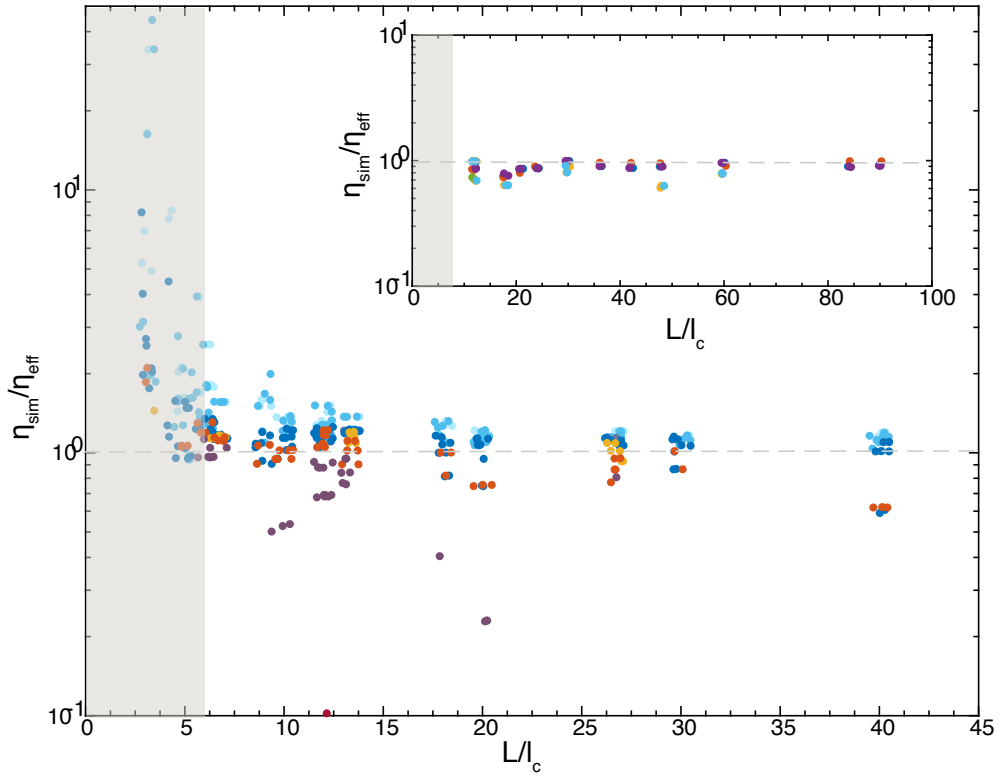


Figure B.1: Ratio of effective viscosity measured by shear simulation to predicted effective viscosity as a function of connectivity, L/l_c . Inset: Same measurement for extensional simulations

In addition to changing the architecture and effective drag coefficient, we also validated the generality of our approximation by varying simulation size, medium viscosity, filament stiffness, and applied stress. We were able to find a slight trend that depended on filament stiffness as indicated in the difference between blue and red data points in Figure B.1. The deviation from our approximation and variability in results manifested itself more strongly when filaments were highly compliant. To investigate this effect further, we next performed a more detailed analysis of the creep response while varying filament compliances.

B.1.2 Effects of Filament Compliance

The effect of filament compliance on cross-linked networks under strain is a subject of active research at the moment [Sayantan]. Therefore, we wished to use our computational approach to extend our understanding of filament networks in the regime of non-negligible filament compliance.

In irreversibly cross-linked polymer networks, filament compliance is known to give rise to elastic deformation of the network as described in[78, 221].

During the initial affine deformation immediately after the application of an external stress, we see a rapid stretch of filaments, $\langle \delta L/L \rangle_0$, in response to the affine purely mechanical strain, γ_{xy} , which closely follows $\langle \delta L/L \rangle_0 = \gamma_{xy} \sin(\theta) \cos(\theta)$. As shown in Figure B.2, during the first phase in our simulations, the total network strain (solid) is described almost entirely by the strain of the filaments (dotted).

However, in the presence of cross-link slip, the filaments are not permanently constrained to remain at $\langle \delta L/L \rangle_0$. Interestingly, although the mean filament strain stays approximately constant, the distribution of individual filament strains broadens around the affine approximation as shown in the inset of Figure B.2.

During the period where crosslink slip allows changes in the filament length distribution, we also find a long-lived intermediate relaxation phase that deviates from both the initial purely elastic relaxation and the later purely viscous behavior of section B.1.1. In Panel B of Figure B.2, we show that the standard deviation of the filament stretch distribution continues to increase throughout the period that the strain rate is non constant.

Approximating this broadening as a normally distributed variation in filament stretched length throughout the network (\mathcal{N}) with a time varying standard deviation, $\sigma(t)$, we have $\delta L/L = \langle \delta L/L \rangle_0 + \sigma(t) \cdot \mathcal{N}$. This has an effect on the total mechanical energy stored in the network $\mathcal{H} \sim \langle \delta L/L \rangle^2 = \langle \delta L/L \rangle_0^2 + \sigma(t)^2$. Therefore, the network will deform further while some strain energy is being stored in the further stretching filaments.

Eventually the contribution from slow filament stretching will become negligible compared to that from pure cross-link slip on rigid rods. This occurs on a timescale

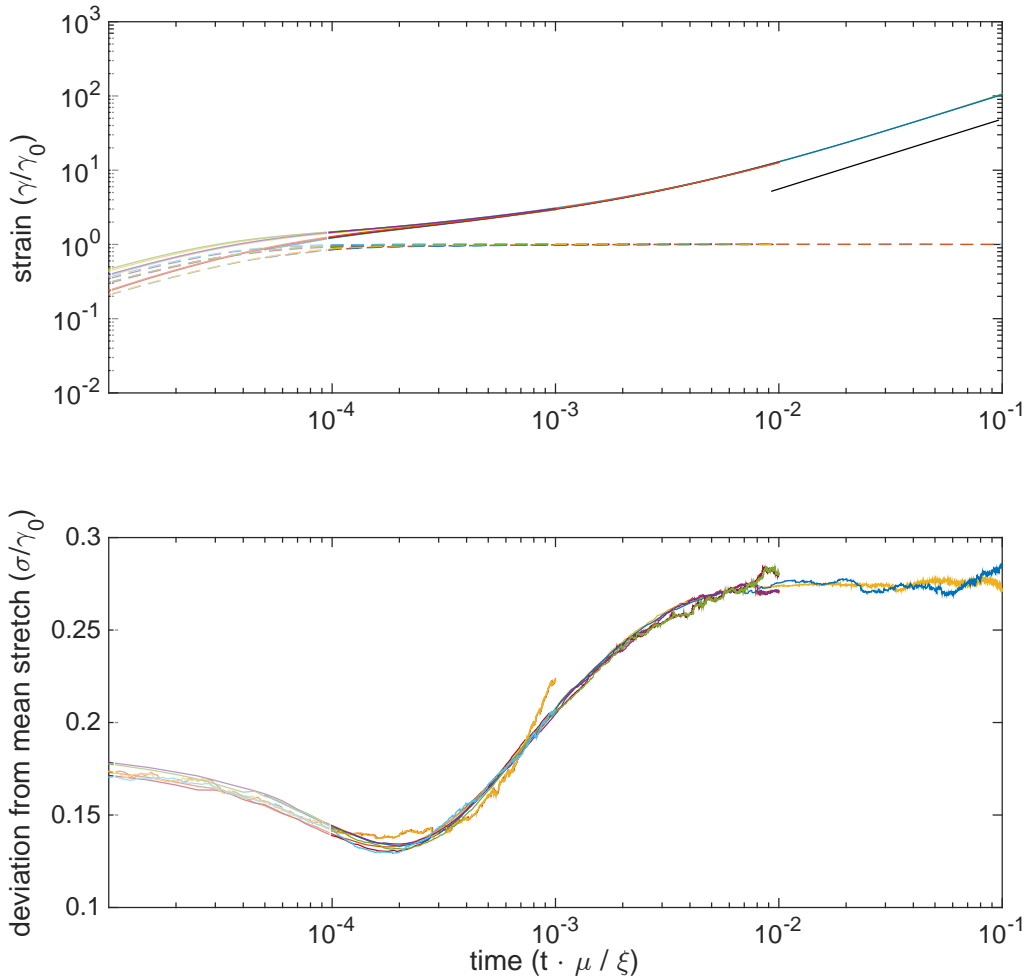


Figure B.2: Network and filament strain for different filament drag coefficient parameters. (top) Plot of total strain normalized by the final mean filament strain, $\delta L/L$. Dashed lines show the amount of strain from affine mechanical stretching. (bottom) Standard deviation of filament extension for the networks in A. Note that the creep compliance in A becomes constant (slope 1) only after the spread in filament extension in B stops increasing. Colors indicate unique experimental conditions.

similar to that of cross-link slip and causes the effective viscosity to decay back toward the rigid limit. This gives rise to a less-than-linear creep response during times after the initial elastic relaxation but before full filament relaxation from cross-link slip. As shown in Figure B.3, the transition begins to take place as network strain reaches

10 to 100 times the strain from pure mechanical stretching, $\gamma_0 = \delta L/L$, and this property is independent of the magnitude of the rate of strain.

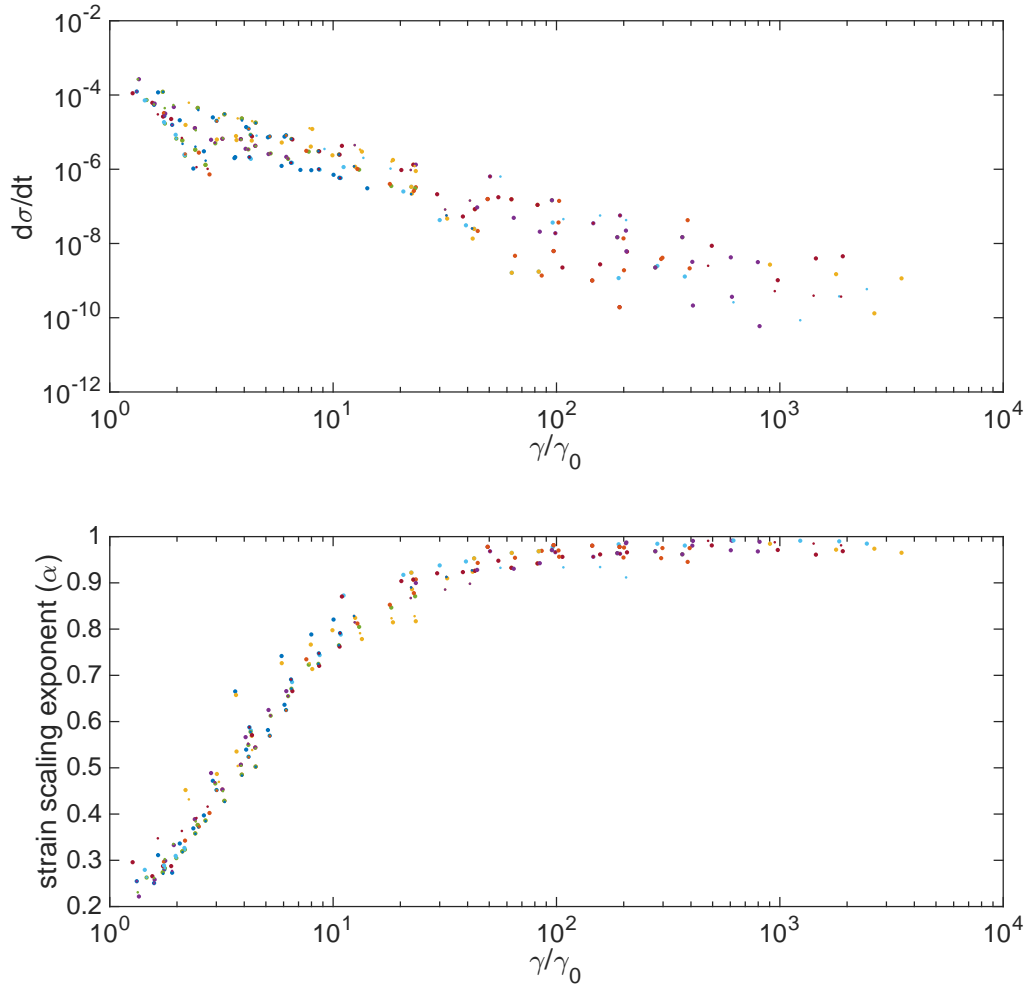


Figure B.3: Sublinear network strain ends as change in filament strain decays. (top) Change in standard deviation of filament strain, σ , as a function of strain relative to pure mechanical strain. (bottom) Dependence of strain rate exponent as a function of strain relative to pure mechanical strain, γ_0 . Colors indicate unique experimental conditions.

B.1.3 Alignment at High Strain and Network Tearing

Once the network is able to accumulate a large strain, the assumption of nearly uniform distributions of filament orientations begins to break down.

At this point the filament orientations become unevenly distributed $\langle \delta L/L \rangle \neq \gamma_{xy} \sin(\theta) \cos(\theta)$, with a larger number of filaments aligning in the direction of extension rather than compression. Filament alignment, conceptually, causes the formation of subdomains that no longer span the space of the network. To the authors' knowledge an exact derivation of the dependence of network connectedness on filament alignment has not been carried out, but Monte Carlo simulations have been used to show that alignment does indeed lead to lower connectedness[52].

We find that over time, the orientational distribution of the filaments begins to peak around 45 degrees as the large strain induces alignment. In Figure B.4, we see that as the angular standard deviation falls, this reorientation eventually leads to fewer bonds bridging the network perpendicular to the line of strain. As this connectivity begins to noticeably decrease, the observed effective viscosity decreases as well, giving rise to greater than linear creep. From the inset of Figure B.4 we can also see that the onset of phase D occurred before the network had completely reached phase C, leading to a rapid transition between sub-linear and super-linear creep. Finally, it should be noted that the end of this simulation resulted in the network tearing apart.

B.1.4 Phase Diagram of Dominant Behavior

In Figure B.5, we illustrate the four stereotyped phases of the general mechanical behavior that we observed in our networks. A deforming network typically undergoes a rapid filament stretching, a slower relaxation of elastic constraints, a phase of purely viscous cross-link slippage, and an eventual alignment and breakdown of network connectivity.

Finally, to explore the transitions between the various phases, we measured the creep response for a computationally tractable network ($L/l_c = 25$), as we varied the filament extensional modulus, μ , and the cross-link friction coefficient, ξ . In Figure

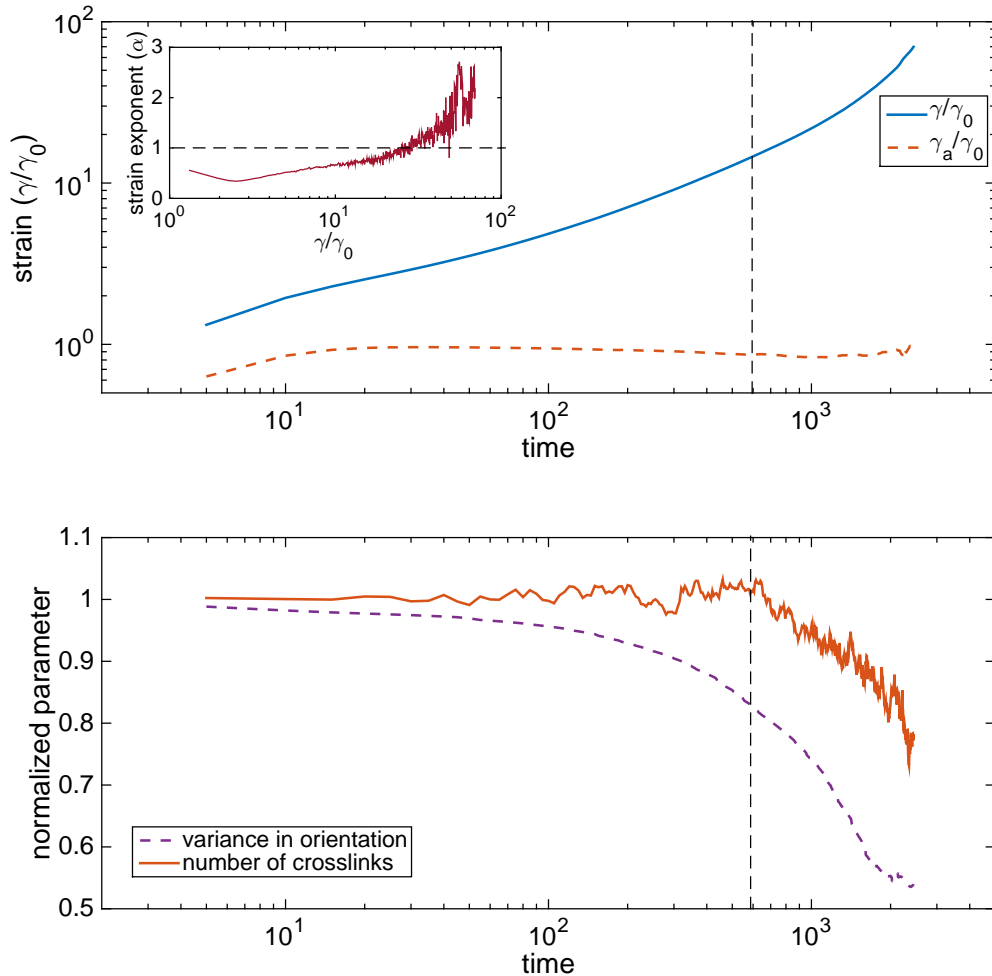


Figure B.4: Creep response of a network transitioning to phase D. (top) Strain curves for a network undergoing large scale deformation. Inset shows strain exponent as a function of strain (exponent passes 1). (bottom) Traces for the variance in filament orientation and number of cross links. Vertical dashed line shows the point where the strain exponent becomes greater than one.

B.6, we classified parameter sets based on their strain exponent. We can see the trends for the transitions between phases A, B, and C. The line for the transition to D is still speculative at this time.

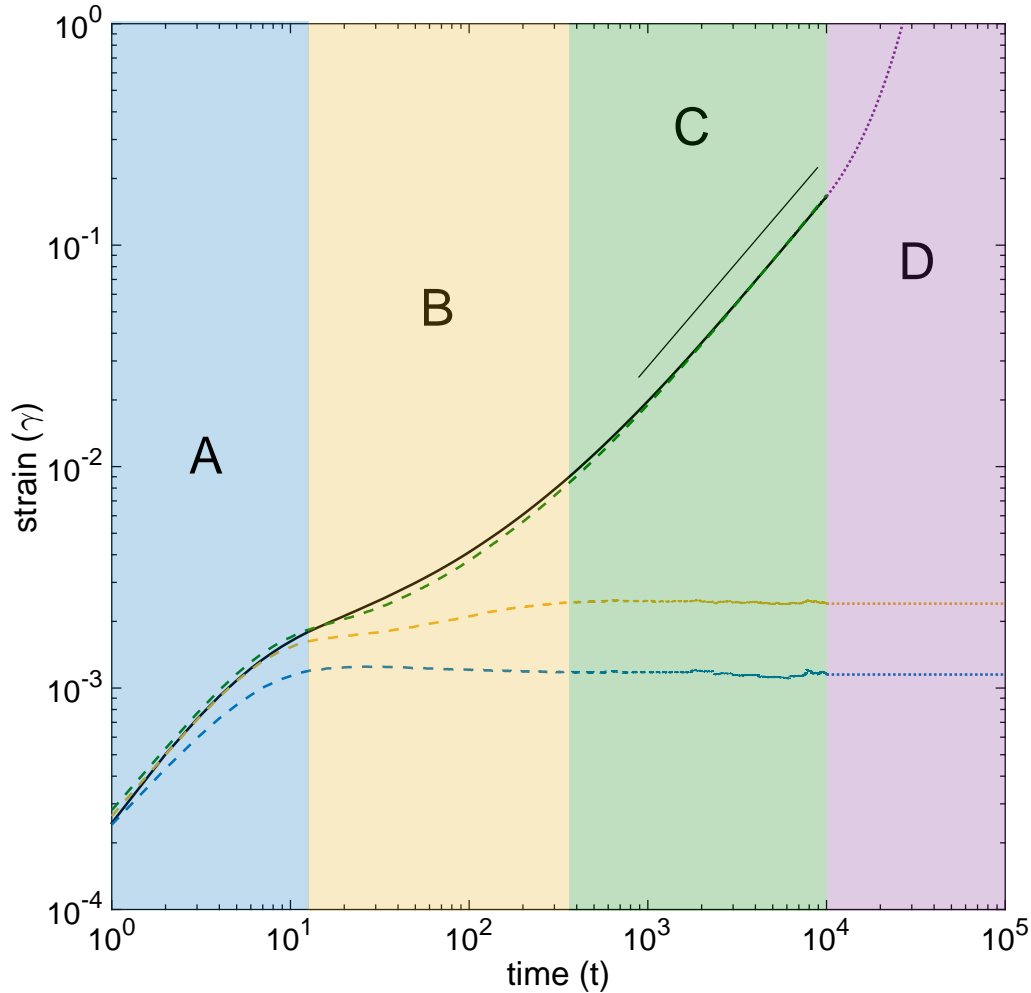


Figure B.5: Schematic of the general creep response of compliant filament networks illustrating the 4 phases of deformation: A) rapid mechanical response, B) combination of slow filament stretching and cross-link slip, C) cross-link slip dominated (line indicates slope of one), D) network tearing from filament alignment. Note that the portion of the curve in section D is only a hypothetical continuation of the actual data.

B.1.5 Frequency dependent modulus

This section will include a figure on the frequency dependent modulus once I get those.

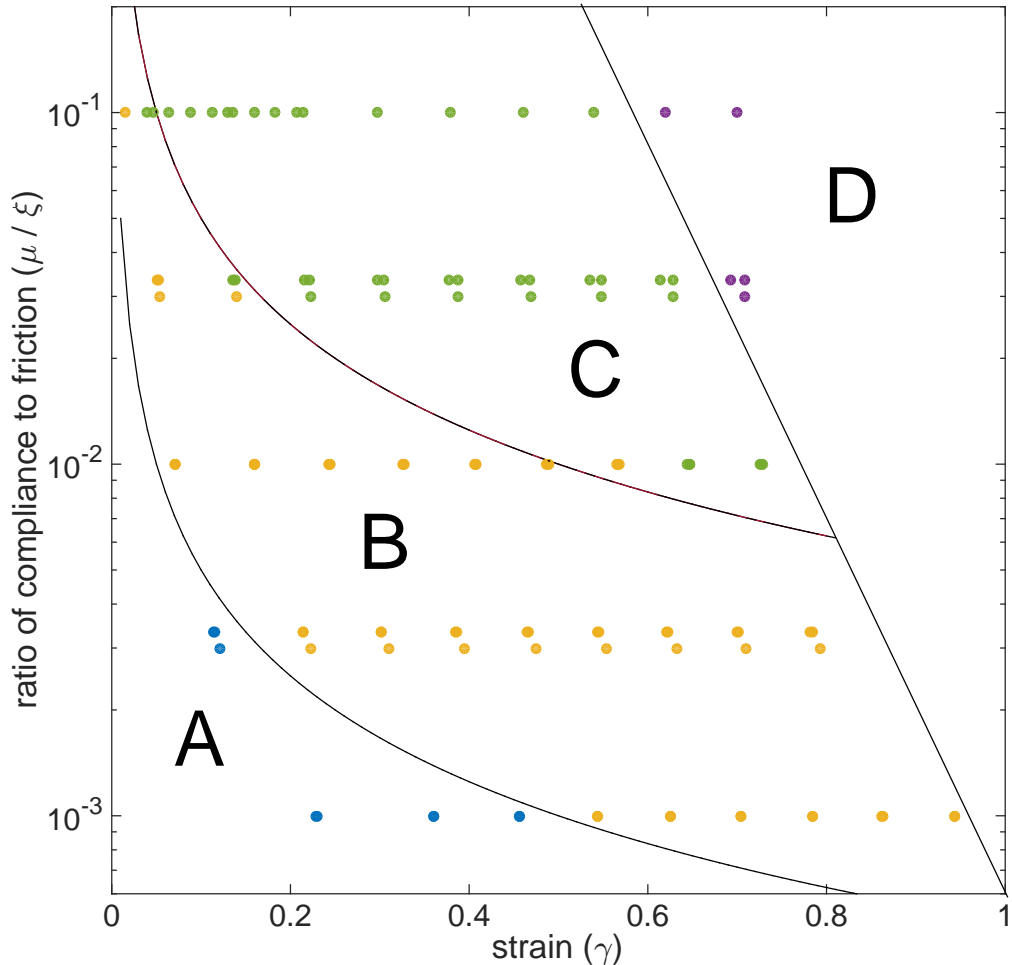


Figure B.6: phase diagram of creep response for different filament extension, μ and cross-link friction, ξ . Yellow, green, and purple dots correspond to creep measurements $\gamma \sim t^\alpha$ with $\alpha < 0.92$, $0.92 < \alpha < 0.98$, or $\alpha > 0.98$ respectively. Blue dots represent creep measurements where $\gamma_{total} < 2\gamma_{mechanical}$

B.1.6 Strain Memory

Finally, we found an interesting behavior when we introduced non-linear extensional stiffness into our filaments. When the network is allowed to relax to its unstrained state, there is generally a time comparable to the period of strain storage over which the energy in the network is relaxed away.

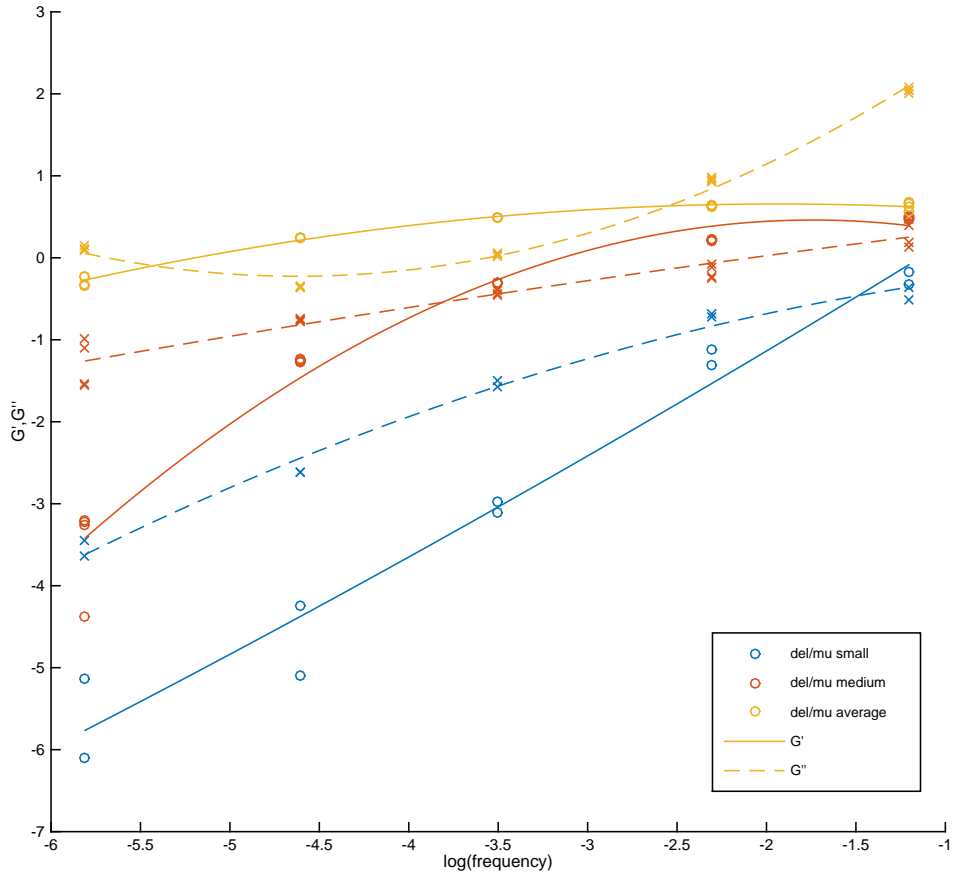


Figure B.7: Frequency dependent moduli for networks.

We observed deviations from this behavior by applying stepwise stress pulses to simulated networks, and observing whether the network behaves identically upon reversal of the applied stress direction. If the network has no strain memory then each reversal will result in an identically shaped creep curve. However, when we include nonlinear filament extension in our model, we find that the mechanical strain can be stored for longer periods of time than it took to entrain the network.

This behavior mimics recent experiments in filamin cross-linked networks. Filamin provides a high level of compliance to a network ($\gamma_0 > 0.5$) without substantial cross-link unbinding. This allows large scale rearrangements to take place without driving

very much cross-link slip, similar to the conditions in section B.1.2. However, if we force individual filaments to undergo a strongly nonlinear stiffening at strains above 5%, we find an interesting long term strain storage.

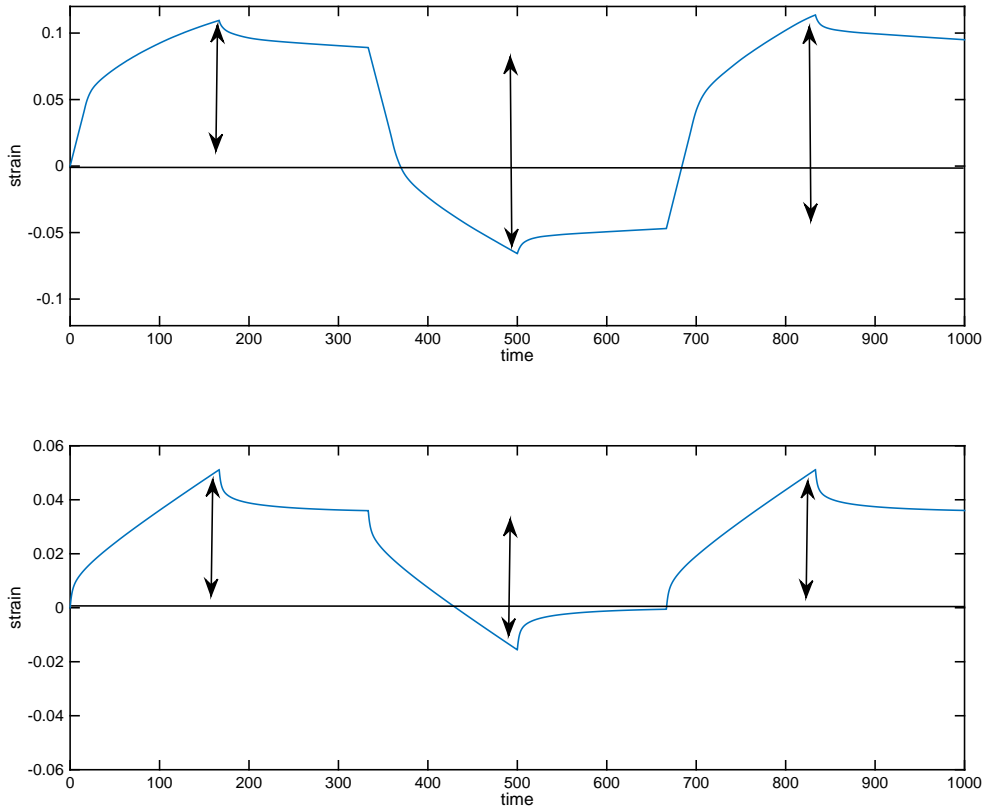


Figure B.8: Creep curves in the presence of reversing applied stress for (a) nonlinear extension or (b) linear extension. Note that for linear filaments the induced strain returns to approximately 0 after a complete cycle, while in the nonlinear case the cycle is not completely reversible.

Figure B.8 shows that the strain storage occurs, but I will need time for further study to build the full analytical picture of where when and why this happens in my model.

B.2 Summary and Conclusions

We have proposed a simplified effective friction model for understanding 2D cross-linked networks. Our model extends previous Mikado and lattice models to include effects of cross-link relaxation. We expect that our model can confer insights into mechanisms of network stress relaxation in quasi-2D networks such as those found in *in vitro* actin monolayer experiments[149] as well as in eukaryotic actomyosin cortices[138].

Our model is the first to address the plausible dependence of network effective viscosity on network structural properties. This led to a derivation of an estimate for the long timescale creep rate of networks under constant stress. Although this derivation neglects possible frequency dependence at short timescales, this finding offers a potential framework for addressing the dependence of network deformation rate on filament concentration and length.

Additionally, our simulations suggest that, in the presence of constant shear stress, cross-link friction will also produce a long-lived phase of sublinear creep as filaments relax from their affine stretched position. While this phase may transiently resemble more explicit 3D models such as [26], it is clear that our model differs by predicting that network will achieve a constant effective viscosity more rapidly. In particular, we predict that this relaxation will occur at a rate similar to that of rate of cross-link slip derived strain and will therefore be negligible after the network has slipped by roughly ten times the magnitude of the purely affine mechanical deformation.

In building our model we have neglected any other sources of potential mechanical relaxation in order to simplify our analysis. In the future, we hope to extend our model to include biochemically driven forms of relaxation such as filament turnover or regulated cross-link unbinding.

This model forms a basis for addressing 2D filament network deformation, and it proposes a simplified formulation of important qualitative properties. In this way we are able to address potentially general phases of network deformation and delineate what network properties may give rise to them. This may provide an important starting point for addressing the general importance of network structure in more

complex networks containing active elements.

B.3 Network Tearing under Extensional Stress

B.3.1 Extensional Thinning and Network Tearing

For moderate extensional stresses, the rigid filament approximation of the effective viscosity simply picks up a different geometrical factor out front.

However, at higher stress and in the presence of different things happen.

$$\frac{\partial l_c}{dt} = l_c \dot{\gamma} = \frac{l_c \sigma}{\eta} \sim l_c^3 \frac{\sigma}{L^2 \xi} \quad (\text{B.6})$$

We can see that the rate of network thinning accelerates as we would expect. When the network reaches some minimum connectivity we assume that it stops behaving as a continuum material and the network tears irreversibly.

$$\tau_{break} = \frac{\eta_{eff}}{2\sigma} \cdot \left(1 - \frac{l_c^2}{l_{break}^2} \right) \quad (\text{B.7})$$

This provides us with an estimate of the timescale of catastrophic breakdown for a network with a given initial architecture and molecular drag.

B.3.2 Tearing Events During Extensional Strain

This behavior is caused primarily by the low density network undergoing tearing events that interrupt global connectedness.

B.4 Deriving Molecular Drag Coefficients

Thus far, the idea of a molecular drag coefficient was taken as a phenomenological, measured parameter for a given experimental setup. While this is a sufficient pragmatic justification, it's useful to try to motivate the quantitative value of this drag coefficient by connecting it to the underlying cross-link properties of binding affinity, concentration, and extensibility.

To do this we'll imagine the simplified case of two cross linkers sliding past each other in one dimension. In this case, assume that we have an equilibrium number of bound cross-linkers, n_B , each of which is displaced from its equilibrium length by some distance x . Each cross linker unbinds with rate k_{off} and rebinds at it's relaxed position ($x = 0$) with rate k_{on} . At the same time, all the cross linkers are being pulled from their relaxed position at a rate, v , which is simply the rate at which the filaments are sliding past each other.

We can write the differential equation for the change in the density of cross-links, ρ , at displacement x as they are pulled upon, bind, and unbind.

$$\frac{\partial \rho}{\partial t} = -k_{off}\rho(x) - v\frac{\partial \rho}{\partial x} + k_{on}\delta(x) \quad (\text{B.8})$$

Recognizing that $\int \rho(x) dx = n_B$ implies $k_{on} = k_{off}n_B$, we can find the steady state solution

$$\rho(x) = \frac{n_b k_{off}}{v} \cdot \exp\left(-\frac{k_{off}}{v}x\right) \quad (\text{B.9})$$

If each cross-link has a spring constant μ_c , then we can equate the force on all cross-links to the applied force that is sliding the filaments past each other. Realistically, the spring constant and binding affinity would be functions of the cross-link stretch, but here we are taking them as approximately constant.

$$\int_0^\infty \rho(x)\mu_c x dx = v\frac{\mu_c n_B}{k_{off}} = F_{app} \quad (\text{B.10})$$

a

Therefore, the term next to v , (i.e. $\frac{\mu_c n_B}{k_{off}}$) would be equal to our molecular drag coefficient, ξ . Assuming approximately 1 cross link per filament overlap, and using parameter estimates culled from Ferrer et al., we build the following table of estimates for ξ .

This molecular description assumed both a constant off-rate and linear force extension of cross-links. In the event that binding kinetics are regulated by the state of extension, we would expect (based on Rf) to find a region that exhibits a stick-slip

| | | |
|--|-------------------|-----------|
| cross-linker type | α -actinin | filamin-A |
| dissociation constant (s^{-1}) | 0.4 | 0.6 |
| spring constant ($nN/\mu m$) | 455 | 820 |
| drag coefficient, ξ ($\frac{nN\cdot s}{\mu m}$) | 182 | 492 |

behavior instead of the smooth. Depending on the nature of any coupling between cross-links local stick-slip could either give rise to a global stick-slip behavior or a heterogenous mixture of stuck and sliding cross-links. It would be interesting to explore this topic further in the future, but in the present analysis, we choose to ignore complications from these nonlinear effects.

APPENDIX C

IMPACT OF FILAMENT RECYCLING ON CORTICAL FLOW IN ANIMAL CELLS

C.1 Active Fluid Model Fitting of Cortical Flow

Measurement in *C. elegans* embryos

To ascertain the manner in which active stress and effective viscosity depend upon actin and myosin densities, I studied cortical flow in the *C. elegans* single cell embryo during polarity maintenance phase. The single cell *C. elegans* embryo poses a viable model system wherein to determine how active stress and effective viscosity depend on constitutive properties of the cytoskeleton. During the *C. elegans* first division cycle, cell fate determinants and small regulatory GTPases are segregated between distinct anterior and posterior domains, and these asymmetries are actively sustained through regulatory feedback for 5 minutes during the polarity maintenance phase. [11] As displayed in Fig. C.1 this system is characterized by a spatially varying distribution of myosin motors in the presence of persistent unidirectional cortical flow from the posterior pole towards a band of cytoskeletal aggregation near the midline.

In addition to the steady state velocity profile, the *C. elegans* embryo provide a number of advantages that made these measurements easier. The events of polarization are highly stereotyped and reproducible, allowing for comparison between experiments. Transgenic strains expressing fluorescently-tagged variants of myosin-II and F-actin binding proteins (e.g. utrophin and moesin), allowing for simultaneous visualization of F-actin and myosin by fluorescence microscopy. In addition, the superficial cortical layer allows for high quality microscopy necessary for the experiments, and the cell geometry allows simplification to a 2D system. Finally, an important factor necessary for constraining the theory is a fine level of control over the densities

of both actin and myosin, which can be supplied in the *C. elegans* embryo by RNAi depletion of nearly any gene expressed in the germline. [12]

C.1.1 Obtaining spatially resolved simultaneous measurement of actin and myosin densities.

Rationale: Actin and myosin are assumed to be the drivers of cortical flow and their density profiles and gradients are therefore important variables necessary to parametrize the functions of active stress and effective viscosity upon which the theory is based.

To obtain the density profile, I used interleaved HILO microscopy timelapses to obtain simultaneous images of myosin and actin in the *C. elegans* embryo during the single celled polarity maintenance phase. Next, I coarse grained the image using image processing blurs or a fixed square bin so that microscopic inhomogeneity is removed from the measurement. Limiting the analysis to one dimension improved the measurement quality and made the mathematics simpler so an average density taken along cross section lines running perpendicular to the embryo AP axis was computed. The example in Fig. C.1 displays a typical fluorescence image of the myosin localization in the embryo along with the AP projection axis. The myosin fluorescence profile changes gradually over the course of five minutes with a period of particular stability lasting roughly two minutes.

C.1.2 Obtaining spatially resolved measurement of cortical flow velocities.

To obtain a flow profile, I analyzed the myosin interframe displacements with particle image velocimetry (PIV). I averaged a set of contiguous frames from the videos prior to blurring or binning in order to obtain a more clear image and provide a larger flow displacement between PIV analyzed frames. The PIV algorithm is assumed to maintain a nearly constant absolute margin of error so maximizing interframe flow distance while still maintaining consistent results minimizes relative error. I

selected a region of interest that remained consistent throughout all experiments and encompassed the entirety of the dilating and contracting regions.

The PIV algorithm was an FFT multipass with window deformation and a post-processing clean up that rejects and interpolates any velocity with a speed greater than 3 times the standard deviation.[13] Only the on axis motion is relevant at this time so the output velocity vectors will be projected onto a line parallel to the AP axis. This component of the flow velocity was averaged along the cross sections running perpendicular to the AP axis as before. The diagram below illustrates a typical PIV flow analysis on the left. On the right, the projection of the flow velocity onto the AP axis is shown to vary slowly in magnitude over the course of 5 minutes and to maintain the same overall shape.

C.1.3 Using the data to constrain a basic active fluid model

I compared these measurements to the theoretical predictions by setting up a few non-linear functional fits of the velocity, effective viscosity and active stress as a function of myosin density using a nonlinear least-squares fitting solver with the equation

$$v(x) = C_1 e^{x/l} + C_2 e^{-x/l} + \int_a^b \frac{\delta\mu}{\delta x} (e^{(x'-x)/l} + e^{(x-x')/l}) \quad (\text{C.1})$$

where l is a length scale of force falloff and the constants C_1 , C_2 are constrained by the boundary conditions at the points a and b in the embryo, $v(a) = v_a$ and $v(b) = v_b$. See [Bois et al] for more details on this equations derivation.

Data fitting was carried out in MATLAB by passing a starting guess for the fitting coefficients to lsqnonlin along with the function defined above.

The results of this analysis showed that, indeed, an active fluid function akin to that used in [Mayer and Grill] is capable of explaining the observed flow profiles in *C. elegans* embryos.

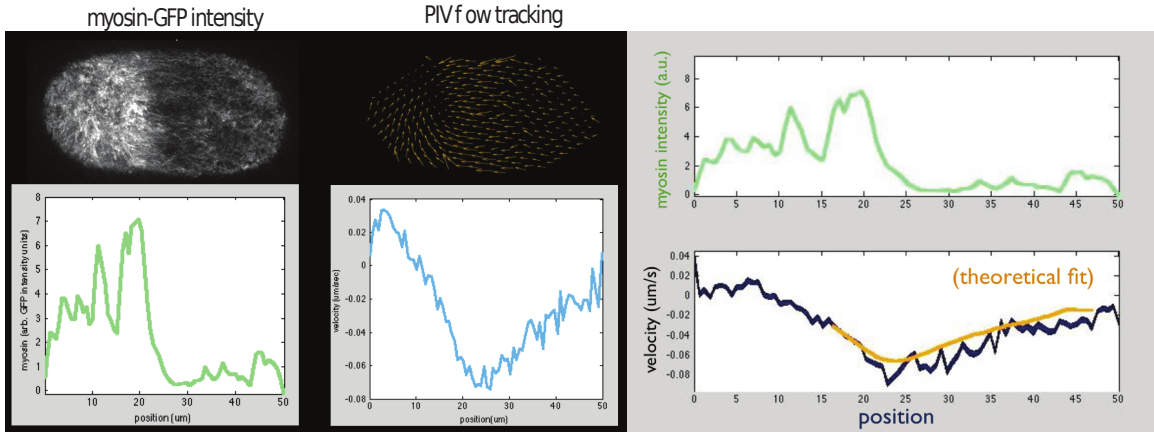


Figure C.1: Measurement of myosin intensity and flow profile. These measurements fit a theoretical model of active fluid flow.

C.1.4 Disruption of Flow by Myosin Depletion

The above experiment only sampled a limited region of myosin-actin state space if only analyzed in wild type. Using only data from this limited region does not uniquely determine the form of the functions that satisfy the equations of motion. I needed to test outside this range by varying the concentration of actin and myosin independently in order to adequately constrain the fitted equations of active stress and effective viscosity.

RNAi depletion is a common practice used to decrease the cellular concentration of endogenously expressed proteins in *C. elegans*. By feeding ssRNA containing *E. coli* to mother nematodes, the mRNA in the nematode germline is progressively silenced and the remaining protein decays away. I used this technique to lower the expression of myosin regulatory light chain kinase (MRCK), which is an upstream regulator of myosin. Overall myosin density decreases with a depletion of MRCK. We assume that the degree of depletion can be assessed by integrating the myosin density profile over the length of the cell.

Gene depleted embryos were imaged and processed in the exact same manner as described above for wild type.

As shown in Fig. C.2, the actin densities were largely unaffected. Nevertheless, the myosin density (not shown) and flow profile (Fig. C.2, right) were reduced.

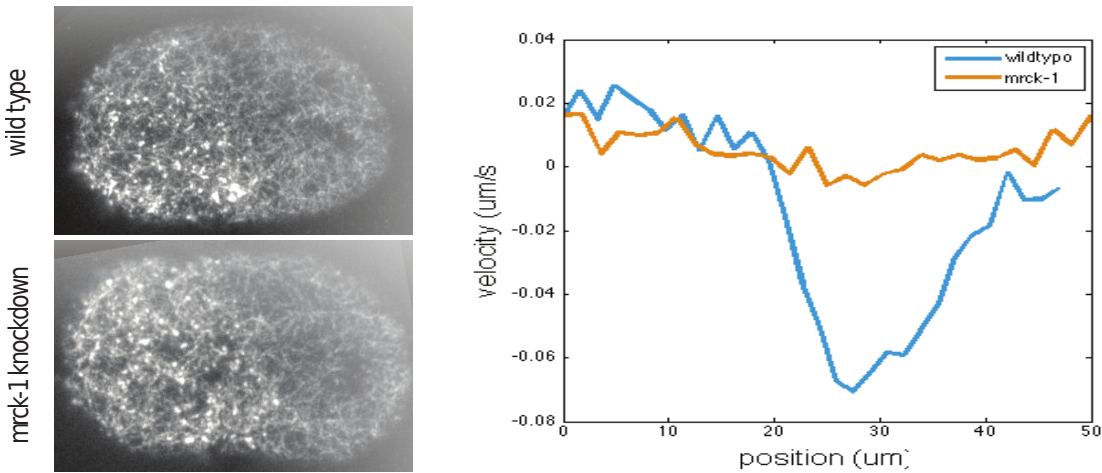


Figure C.2: Measurement of actin distributions and flow profiles for *mrck-1* knock-down embryos. MRCK-1 is an upstream regulator of myosin.

Progressive depletion of MRCK also showed a graded response to myosin depletion, indicating that myosin activity imparts internal force in a dose dependent manner.

C.2 Stabilization of Filament Turnover with Jasplakinolide Treatment

Jasplakinolide is a small molecule inhibitor of actin depolymerization. When treated with jasplakinolide, actin filaments can be stabilized to have very long filament lifetimes. To study the effect of filament stabilization on cortical flows, Jon Michaux treated embryos with jasplakinolide and imaged the actin cytoskeleton with utrophin::GFP. The results were striking, and clearly showed that loss of turnover resulted in disrupted flows. Moreover, in some cases, the treatment didn't just result in a stalling of flows, but also led to a tearing of the cortex followed by further transient contraction. Nevertheless, all embryos with jasplakinolide treatment eventually stalled and failed to continue with normal polarization and division.

I made an attempt to quantify the degree of contraction possible in jasplakinolide treated embryos using hand tracking of fiducial markers in Jon's videos. As can be seen in Fig. C.3, whether the cortex stalled or tore, the resulting strain asymptotically approached some limiting strain. This is in sharp contrast to the persistent strains

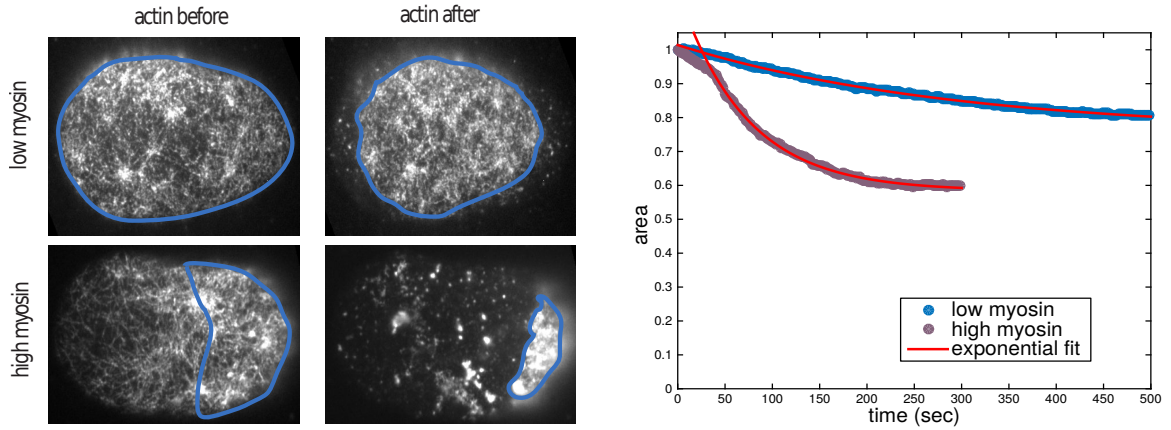


Figure C.3

$(\gamma > 1)$ possible in the steady state flows found when turnover is present.

APPENDIX D

ADDITIONAL INFORMATION ON PULSE MODEL

D.1 Motivation and experimental context

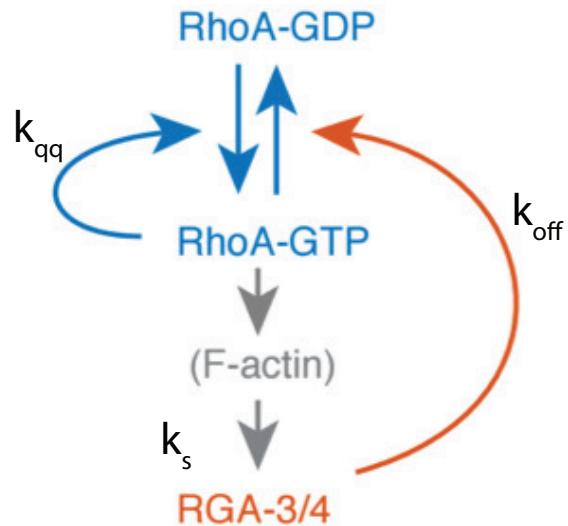


Figure D.1: Reaction pathway with labels for coefficients associated with feedback strengths.

In many systems, cortical flows are driven not by continuous contraction of active material, but by repeated rounds of pulsatile contraction. While it was once believed that these pulsatile behaviors could be an emergent property of actomyosin contractility itself, it is now more probably suspected that these behaviors are caused by upstream regulators of local actomyosin activity.

It is still unclear why so many systems exhibit this type of behavior, but it is nonetheless important to understand the origins of these behaviors and what differences may arise due to their presence or absence in a contractile system. Therefore,

we have begun exploring how to model both the upstream regulators that govern contractile systems as well as the downstream effects of coupling these to regulators to contractile flows themselves.

The majority of our data comes from the work of Francois Robin and Jon Michaux [173]. They have shown that upstream of both actin and myosin is a separate pulsatile biochemical circuit consisting of a combination of positive and negative feedback between a pair of proteins called Rho and RGA as depicted in Figure D.1.

To explain the dynamics I attempted to build ordinary differential equation models of local variation in active Rho and RGA concentrations. We found that many models are effectively equivalent at producing the qualitative results. However, this model in all of its forms is inconsistent with producing robust pulsatile behavior once the models were constrained by parameter fitting to the data.

D.2 A model for pulsatile actomyosin accumulation in *C. elegans*

I defined ρ as the concentration of Rho and r as the concentration of RGA, and generated association, dissociation and feedback parameters for the model.

$$\frac{d\rho}{dt} = k_{on}^\rho \left(1 + k_{on}^{\rho\rho} \frac{\rho^n}{\rho_0^n + \rho^n} \right) - (k_{off}^\rho + k_{off}^{\rho r})\rho \quad (\text{D.1})$$

$$\frac{dr}{dt} = k_{on}^{r\rho} \rho - k_{off}^r r \quad (\text{D.2})$$

Next we can nondimensionalize the equation with $q = \rho/\rho_0$, $s = k_{off}^{\rho r}/k_{off}^r$, and $\tau = k_{off}^r t$, and rename parameters for simplicity.

$$\frac{dq}{d\tau} = k_q \left(1 + k_{qq} \frac{q^n}{1 + q^n} \right) - (k_{off} + s)q \quad (\text{D.3})$$

$$\frac{ds}{d\tau} = k_s q - s \quad (\text{D.4})$$

D.2.1 Analyzing parameter space of the model

Just from analyzing the null-clines of this model we can gather a lot of information about the qualitative behavior of this model.

$$s_q = \frac{k_q}{q} \left(1 + k_{qq} \frac{q^n}{1 + q^n} \right) - k_{off} \quad (\text{D.5})$$

$$s_s = k_s q \quad (\text{D.6})$$

The s_q null-cline appears as an inverse relation between s and q , with a hump around $q = 1$ whose height is dictated by the strength of the q positive feedback, k_{qq} . The s_s null-cline is simply a straight line whose slope is governed by k_s . The dynamical system is only able to attain pulsatile behavior when the s_s null-cline runs parallel and to the left of the hump in the s_q null-cline. This gives two effective conditions on pulsatility: 1) If k_{qq} isn't much larger than 1, there will not be any hump, and so there cannot be any pulsatility. 2) If k_s and k_{off}

To test this prediction, I implemented an automated search of the model's parameter space. The test worked by adding perturbations of fixed strength to the equilibrium state, and observing whether the response of the system exceeded the perturbation. As shown in Figure D.2 for a number of simulation parameters, the response function could vary from having just a stable fixed point ($k_{off} = 10$ and $k_s = 25$) to having stable oscillations ($k_{off} = 10$ and $k_s = 63$) to having pulses ($k_{off} = 20$ and $k_s = 63$). Figure D.2 also shows the null-clines for each case, which can be used to interpret whether pulsation is possible.

Using this automated system, I was able to generate 1600 simulations and classify them automatically based on the ratio of the magnitude of the perturbation to maximum response (to determine if positive feedback drove excitation) and whether the maximum was attained multiple times (to differentiate pulses and stable oscillations). This resulted in a phase diagram of the behavior as shown in Figure D.3, with the three colors indicating the behavior of dynamical systems in that regime. The size and shape of the pulsing region of phase space was a direct result of the strength of

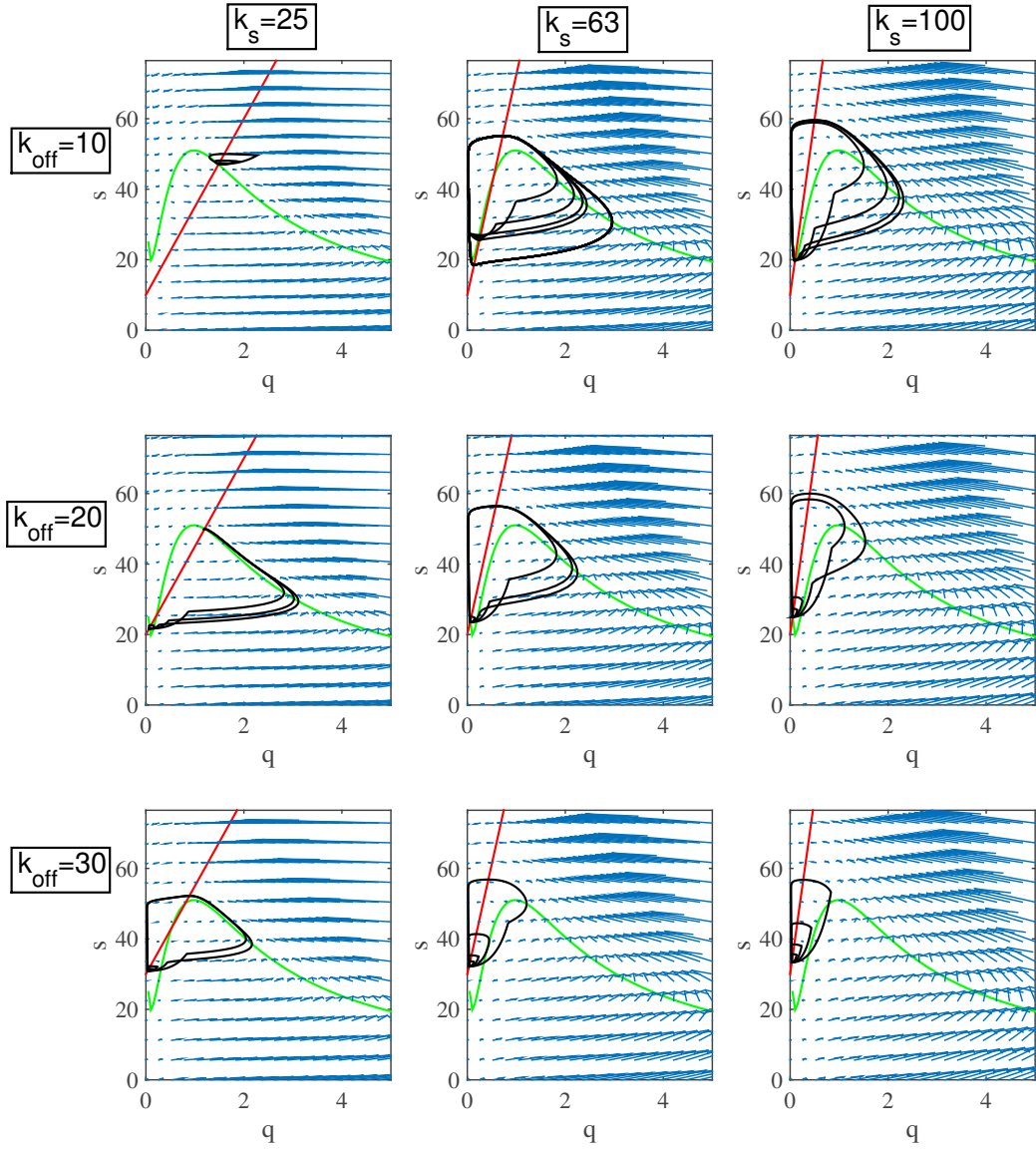


Figure D.2: Perturbation simulation results plotted on phase planes for a variety of parameters.

positive feedback (k_{qq}) with stronger feedback allowing more of phase space to permit pulsing and oscillations.

Finally, using this understanding of the phases behavior of the system, I implemented a stochastic dynamical equation to test the response to noise. As indicated

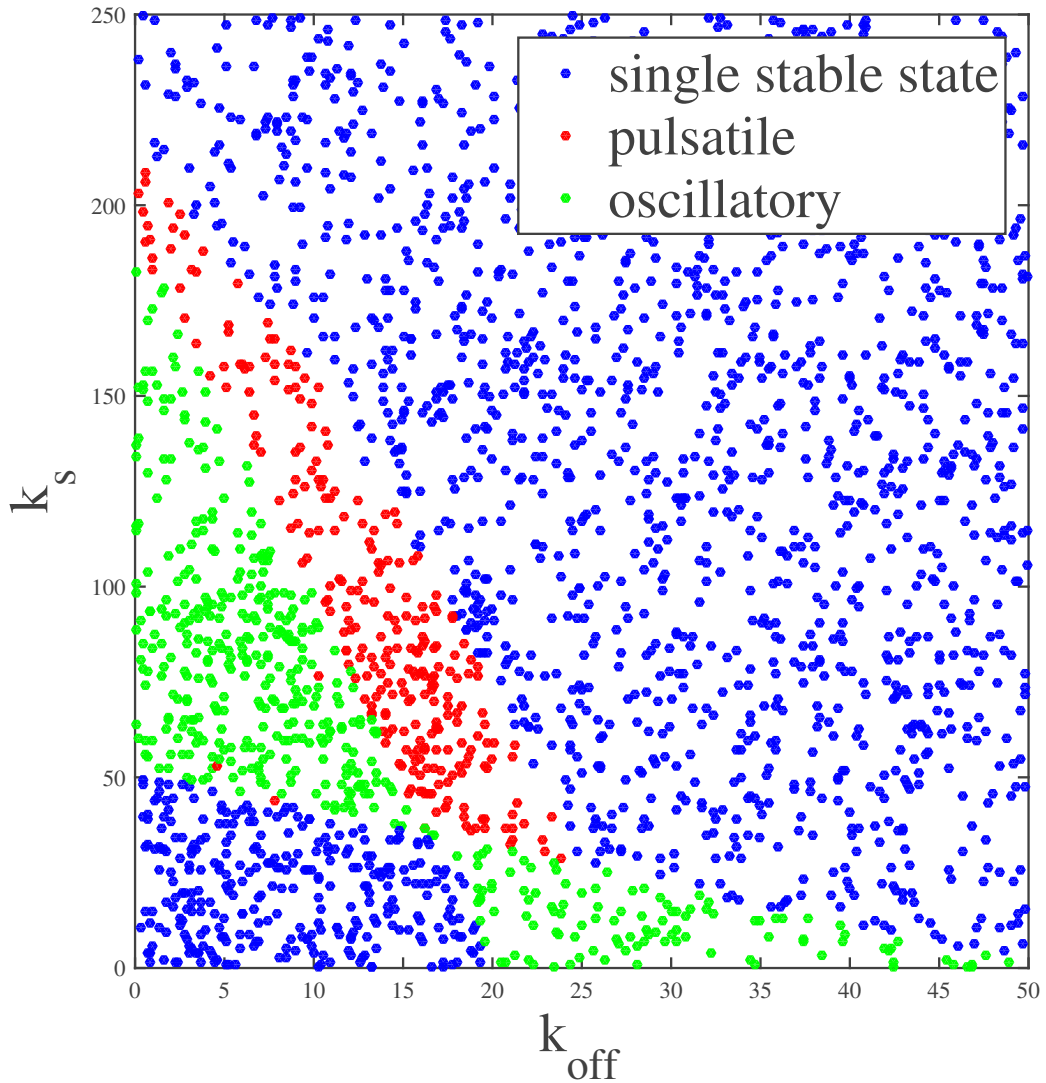


Figure D.3: Phase diagram of for $k_q = 1$ and $k_q q = 100$.

in Figure D.4, a basal level of noise was able to trigger robust pulses in both Rho and RGA for certain parameters. Taken together this analysis indicated that our biochemical reaction circuit for Rho and RGA feedback could in principle account for the excitable dynamics exhibited in the system.

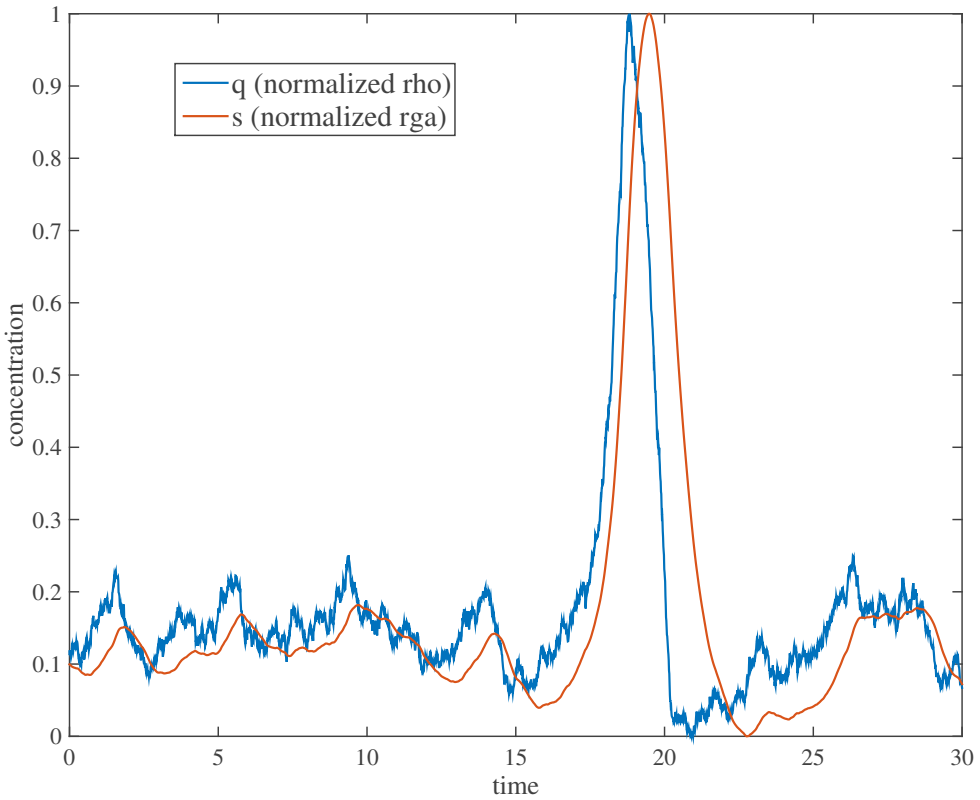


Figure D.4

D.3 Simplified model and data fitting

D.3.1 Fitting techniques

Although this model accounted for the qualitative behavior, we wished to determine whether it could be corroborated by fitting to the data presented in the paper. To experiment with fitting the normalized data, I created a reduced model, where the equilibrium concentration had been renormalized to 0 for both Rho and RGA, and the feedbacks between Rho and RGA are allowed to be non-linear.

$$\frac{dq}{d\tau} = \alpha \frac{q^n}{1 + q^n} - sq^k \quad (\text{D.7})$$

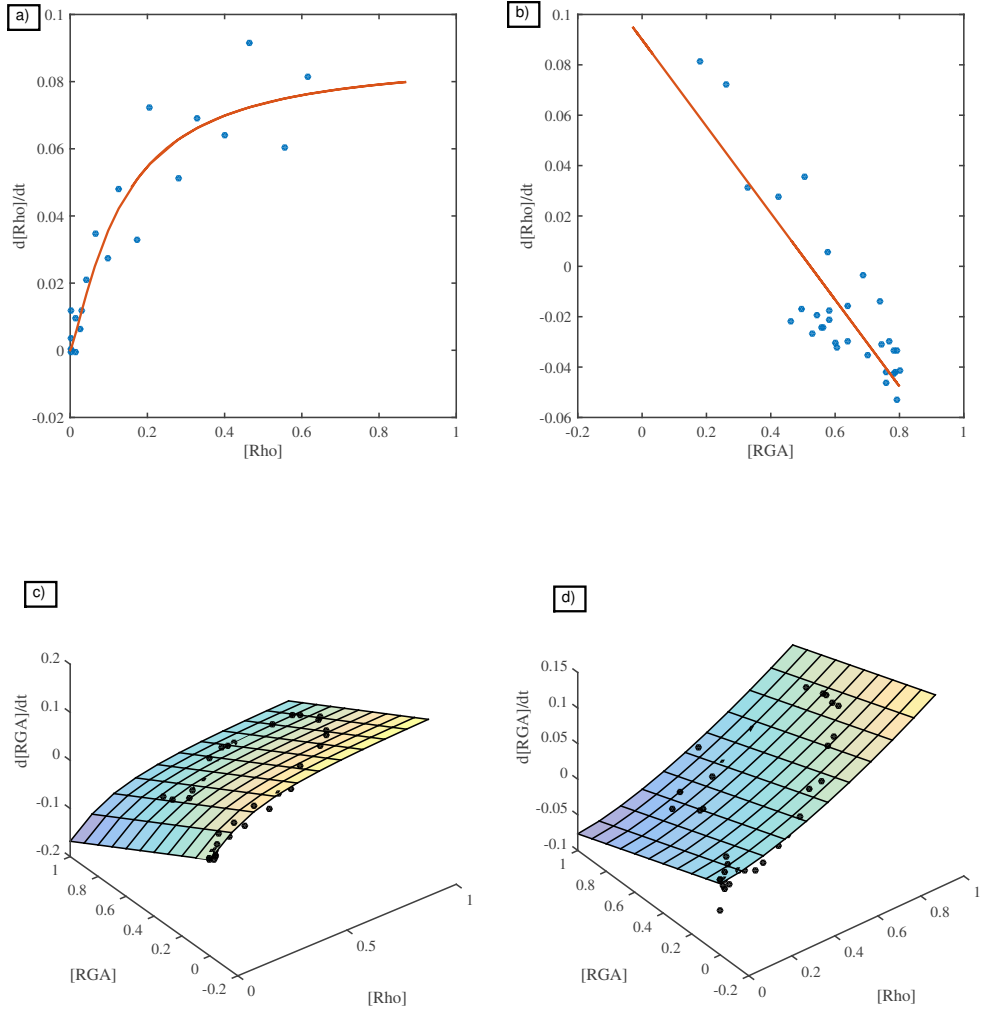


Figure D.5: Multiple methods of fitting.

$$\frac{ds}{d\tau} = \beta q^{(m-k)} - s \quad (\text{D.8})$$

These equations resulted in a family of models with different levels of feedback, depending on the values of n , m , and k . I fit models with a variety of exponents and found that any model with $k \approx 0$, $n > 1$, and $m \approx 2$ gave the best overall agreement with the greatest robustness. I used two different methods to fit the Rho and

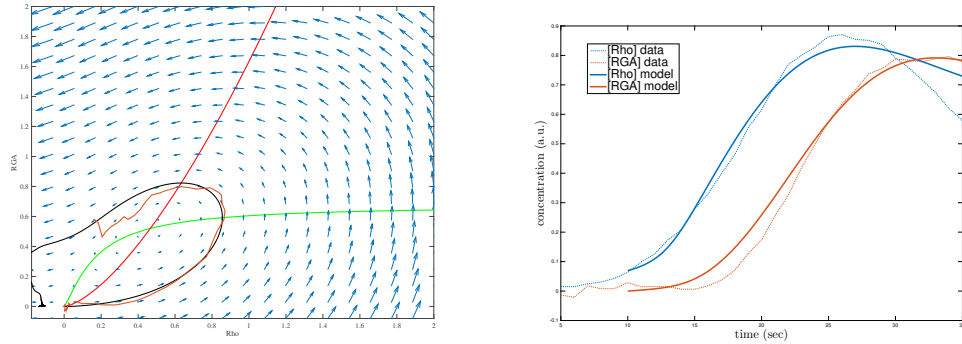


Figure D.6: Simulation results and fitted data for model with $m = 2$ and $k = 0$. Displaying simulation results and the data used to fit the simulation on a phase plane (left) and as pairs of time plots (right).

RGA data to determine the most appropriate model parameters. The first required subsecting the data to fit only datapoints where some terms in the equation were presumably close to constant (Figure D.5a,b). For example, as long as RGA concentration remained relatively small, the equation for Rho could be taken to consist of only the Rho self-feedback function. The second method allowed fitting all of the data the equations at once (Figure D.5c,d). The second method is clearly more accurate, but it comes at the cost of being slightly more difficult to explain to the lay-biologist.

The resulting fitted models could then be used to run simulations. As shown in Figure D.6, the models and fitted data were largely indistinguishable relative to the error in the data. Although the model was quite successful at recapitulating the original data, I found that the resulting models were not necessarily. For example by changing the value of the parameter α by 25% and rerunning the fits, I could tune the system from a stable system to pulsatility and into an oscillatory regime (Figure D.7). Therefore, it appears that this model is not incredibly robust to minor variations in parameters.

D.4 Conclusion

Ultimately, a model similar to D.1 and D.2 was utilized in the final paper in combination with at the 2D fitting routine outlined in Figure D.5c,d. In short, all models

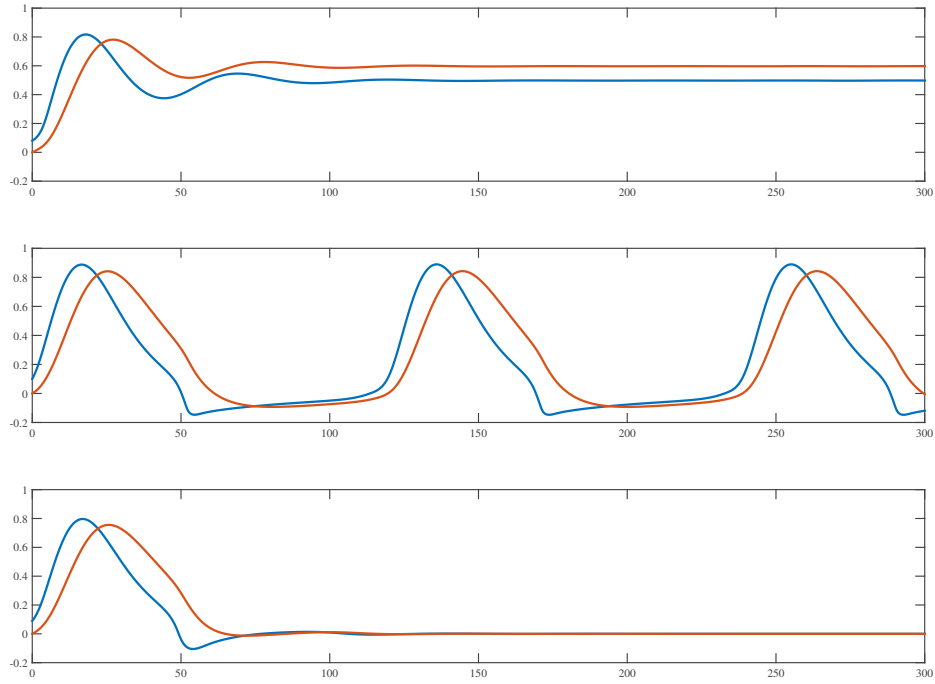


Figure D.7: Small variation in simulation parameters can have large qualitative effects.

performed fairly well at describing the qualitative features of the data, but none were very effective at generating a quantitative match with great robustness. We believe this is indicative of the need to perhaps extend to incorporating spatial effects in driving the dynamics of active material pulses. Based on the theoretical results of [19], we attempted to incorporate our upstream regulatory model into a 1D active fluid. This ongoing work will hopefully tie together the spatial and temporal interdependencies driving this system into its interesting non-equilibrium state.

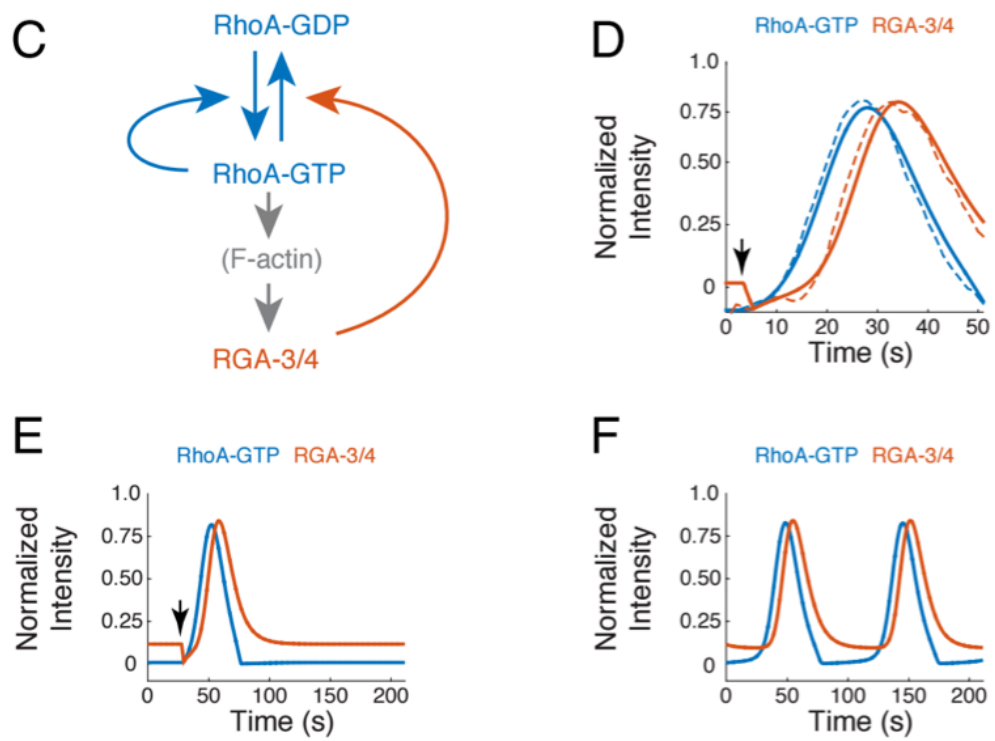


Figure D.8: Final figure as it appears in Reference [173].

APPENDIX E

REDUCING POWER CONSUMPTION IN HIGH PERFORMANCE COMPUTING

E.1 Introduction

Data centers in the US consume an estimated 91 billion kilowatt-hours yearly, equivalent to the annual output of 34 large coal-fired power plants.[46] These same estimates show that only 6-12% of the electricity is used for powering servers while the rest is used to keep machines idling, wasting resources and money in the process. Data center electricity is not inexpensive, costing American businesses \$13 billion annually in electricity bills.[46] Because cost is a strong motivating factor for businesses and universities, we consider data center energy efficiency in the context of cost savings for data center operations.

Demand response (DR) programs provide incentives to induce dynamic management of customers electricity load in response to power supply conditions, for example, reducing their power consumption in response to a request from the utility.[220] Anita can you add something around here that points out how demand response also increases the sustainability of the datacenter beyond just cost reduction. Many energy providers have Voluntary Load Response (VLR) programs, which encourage commercial consumers to reduce power demands during peak periods, such as particularly hot summer days. Participants are given between one and four hours notice of a request to shed some of their electric load, with two and eight hours of participation and the expectation to shed at least 10 kilowatts. We are interested in exploring more active ways in which to participate in electricity demand response programs while impacting the users minimally.

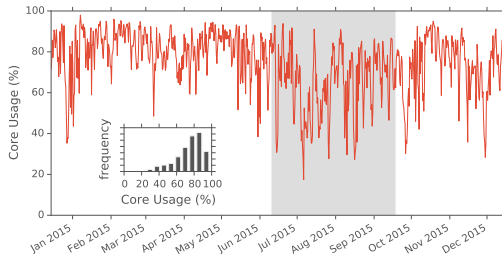


Figure E.1: Average core usage for a 244 node shared HPC partition in the Midway cluster. Insert shows usage statistics histogram.

In many university data centers, a significant portion of the data center is dedicated to high performance research computing which is typically Tier 1. While these jobs take longer periods of time to complete, they are less time sensitive and more flexible than systems which support core business functions such as the university's email. We wish to use the flexibility in scheduling of these jobs to reduce energy consumption of university data centers during periods of peak energy demand.

As shown in the example core usage data of Figure E.1, although the typical average usage during the school year is a fairly standard 80%, the averaged workload can fall to 65% of full capacity in the hottest summer months from June to September. These months also present the period of greatest electricity demand due largely to increased usage of air conditioning. This presents a valuable opportunity to potentially curtail electricity use in demand response scenarios by shifting load off of the peak periods of energy price. Toward this aim, this paper is our attempt to estimate the economic savings, feasibility, and any potential user impact from full or partial cluster shutdown during periods of increased energy demand.

E.1.1 Alternative Demand Response Options in Data Centers

Although we focus on load shifting for our study, we wish to point out prior work on alternative strategies for demand response.

Facility changes A study by Lawrence Berkeley National Laboratory (LBNL) found that 5% of the data center load can typically be shed in 5 minutes and 10% of the load can be shed in 15 minutes without changes to how the IT workload is handled, i.e., via temperature adjustment and other building management approaches[71]. Most data centers have local power due to a backup generator, which could also be used to absorb some load during peak time [121]. More recently, methods of energy storage have been proposed[153] in which UPS batteries are re-purposed for provisioning during periods of peak demand in addition to their primary purpose of backup power. However, these methods all entail manual intervention, with close monitoring and control.

Power capping is a strategy by which to run data center equipment within a set of constraints which assume the electricity draw for the data center as a whole cannot grow any larger. Some examples of this include and turning off or constraining CPU/GPU power consumption to values below the CPU Thermal Design Power (TDP) value, which requires less voltage. Many equipment manufacturers - including IBM, Intel and AMD - have implemented power capping technology that can be monitored at the processor level and applied at the rack level. One approach to power capping is Dynamic Voltage/Frequency Scaling (DVFS). However, as noted by Roundtree[175], no machine in the Top 500 list of supercomputers makes use of DVFS to save power or energy since the performance impact and the amount of power and energy saved was highly application dependent. Power capping doesn't necessarily equate to energy efficiency nor cost savings.

Schedulers Zhou et al[230] present a method for power-aware scheduling by using a combination of a scheduling window and 0-1 knapsack model, which shows promise. However, since SLURM is our scheduler, we decided to focus solely on SLURM. Bodas et al[18] demonstrate an integration of power capping into a power-aware scheduler, with the overall goal of maintaining average system power within a budget. Their work demonstrates that SLURMs auto mode can be used to maximize available power.

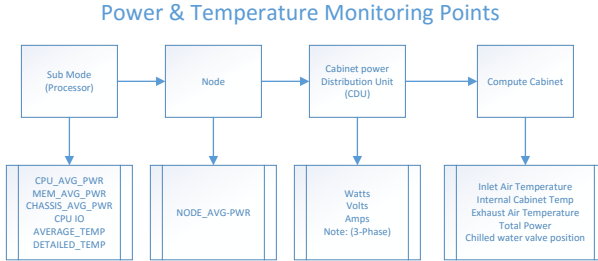


Figure E.2: Energy monitoring framework.

E.2 Problem Statement

Can load shifting of high performance computing tasks save universities money in energy demand response scenarios? To explore the relative costs of implementing load shifting in demand response scenarios, we have expressed the problem by modeling total dollar cost. We wish to use this framework to explore the optimization of price in the presence of various data center usage statistics and price fluctuation schemes.

E.2.1 Modeling Energy Costs

We generate a model total cost function composed of a fixed cost for purchasing and maintaining nodes plus a variable cost dependent on data center power usage and energy prices. We wish to minimize the cost function

$$C = p_n T n_{max} + \int_0^T dt \cdot p(t) \left(n(t) u(t) + u_w \frac{\Delta n(t)}{\Delta t} \right)$$

where $p(t)$ is the price of power at time t , $0 < n(t) < n_{max}$ is the number of running nodes, $u(t)$ is the average node power usage, u_w is the wasted power from turning on a node, p_n is the amortized lifetime cost of purchasing a node, and n_{max} is the total number of nodes in the cluster.

Based on our cluster usage statistics, we approximate that compute cycles are roughly interchangeable and that the main determiner of power usage is simply the CPU utilization of the node. In this case, node power usage takes the form

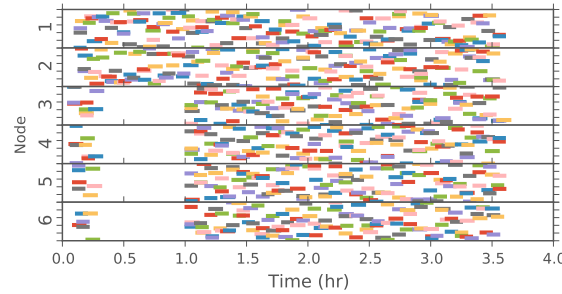


Figure E.3: Diagram of job scheduling during a four node temporary shutdown experiment. Each colored rectangle displays the execution time of a single LAMMPS test job running for approximately 5 minutes.

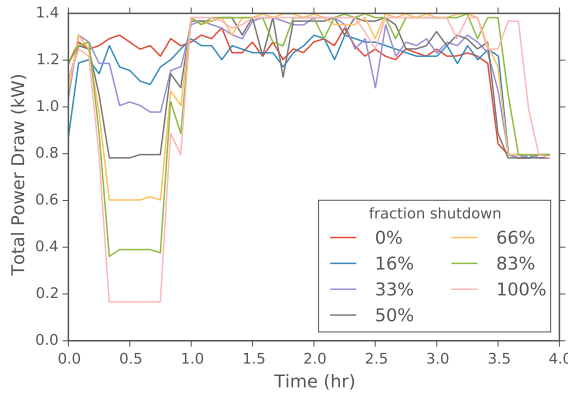


Figure E.4: Total power consumed during experiments where variable numbers of machines were shut down during simulated peak pricing.

$$u(t) = u_0 + u_v \cdot r(t)$$

where $0 < r(t) < 1$ is the fraction of CPU usage, u_0 is the cost of an idling node and u_v is the variable cost for doing r work on a machine.

We wish to minimize the cost function C subject to the constraint that the sum of the submitted CPU cycles, S , are all completed after a period T .

$$\int_0^T dt \cdot n(t)r(t) = S$$

E.2.2 Response to a Temporary Price Spike

In particular, we wish to use this framework to determine how to run our data center in the situation where every T days, we see a price spike from p_0 to p_s , lasting time period t_s . This condition is highly similar to the one facility managers face when utility providers impose usage tariffs during peak energy demand periods.

In this situation, the number of running machines will change stepwise between a high number of running machines, $n_H = n_{max}$, and a low number of running machines, n_L , and a high and low CPU utilization $r_H = 1$, r_L , with a corresponding u_H and u_L as defined above. The high usage will occur during the cheap energy supply, and the low usage will occur during the price spike. Therefore we can rewrite our cost function as

$$C = p_n n_H T + p_0(u_0 + u_v)n_H(T - t_s) + p_s(u_0 + u_v r_L)n_L t_s + p_0 u_w(n_H - n_L) \quad (\text{E.1})$$

with the constraint

$$n_H(T - t_s) + n_L r_L t_s = S \quad (\text{E.2})$$

Inserting the constraint into our cost function to replace r_L yields

$$C = p_s u_v S + n_L \cdot (p_s u_0 t_s - p_0 u_w t_w) + n_H \cdot (p_n T + p_0 u_w t_w - (\Delta p u_v - p_0 u_0)(T - t_s)) \quad (\text{E.3})$$

where we've introduce the price difference, $\Delta p = p_s - p_0$.

We can analyze the change in costs as a function of n_L and n_H to determine the optimal cluster setup for known variables, t_s , p_s , p_n , p_0 , u_0 , u_v , and u_w .

From this analysis, whenever $p_s u_0 t_s < p_0 u_w t_w$, the cost of powering off nodes exceeds the cost of running those nodes idle so $n_L = n_H$ and $r_L = S/n_H t_s - (T - t_s)/t_s$. Otherwise powering off nodes saves money so the nodes that remain on run at full capacity $r_L = 1$, and n_L is minimized subject to constraints giving $n_L = S/t_s -$

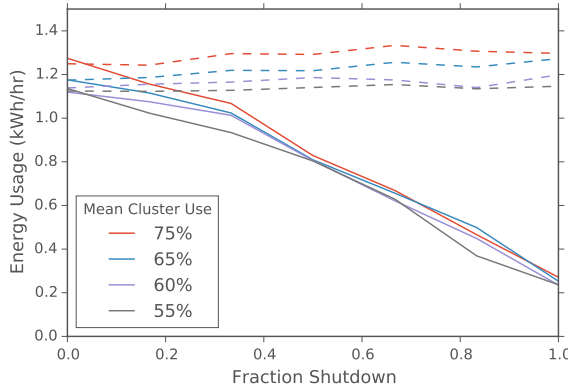


Figure E.5: Energy usage of test cluster during partial shutdown experiments. Solid lines indicate power usage during the shutdown, while dashed lines indicate power usage after returning to full operation.

$$n_H(T - t_s)/t_s.$$

If we can freely choose n_H to optimize cost, then whenever $(\Delta p u_v - p_0 u_0)(T - t_s) > p_n T + \min(p_0 u_w t_w, p_s u_0 t_s)$, we would increase n_H (i.e. buy more machines) until all the work is done during the cheap energy period. Therefore $n_H = S/(T - t_s)$ and either n_L or r_L is 0. Otherwise, the cost of new machines is more than any cost savings achieved from exploiting the price difference, and we would simply ignore the price spike (i.e. set $n_H = n_L = S/T$ and $r_L = 1$).

E.3 EDEALS: Electricity Demand-response Easy Adjusted Load Shifting

For a data center manager to use the above model to determine their cost savings, they must collect and analyze usage and power data on their system. We have built a cluster data processing pipeline, EDEALS, to assess the magnitude of potential savings available from a full or partial cluster shutdown. We combine SLURM job scheduling, node level IMM power and usage metrics, and cabinet level CDU measurements to determine the optimum magnitude of demand response cluster shutdowns.

Here we describe our data center instrumentation, so that we ensure accurate

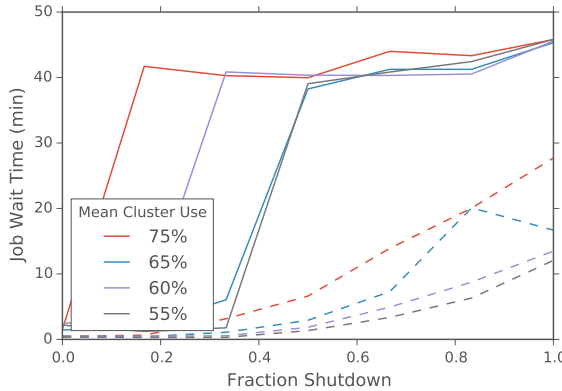


Figure E.6: Maximum (solid) and mean (dashed) job wait times during partial shutdown experiments.

measurements of performance of the workload management system and HPC cluster alone without the influence of extraneous components. Since our focus is the HPC cluster and SLURM manager, we need to ensure those components alone affect the reduced data center utility bill. As depicted in Figure E.2, we take measurements at the core, node, rack, and cabinet level. These data are combined to detect power losses at each step and to determine the correlation between the power measurements at the machine level and the true power draw at the facility level.

Combining this data with electricity pricing statistics from utility managers allows system administrators to determine when and by how much to reduce their power usage to save money. We have built a set of scripts particular to our system to implement machine level power down in response to predicted energy peaks. At the end of the peak energy period the machines automatically reboot and are added by to SLURMs available server pool. At this time, these power cycling scripts are manually executed by system administrators after evaluation of the likelihood of near-term energy demand peaks. However, as more data centers begin to implement smart metering, it will become possible to automate load shifting in response to real-time energy pricing indicators. We look forward to continuing this as future work.

E.4 Small-Scale Evaluation of EDEALS

To test our load shifting scheme, we launched a series of small-scale experiments on a 6 machine test cluster using SLURM batch management system to schedule jobs. We wished to compare the energy savings and job wait times during a full or partial cluster shutdown in response to an energy price spike.

E.4.1 Experimental Setup

We measured the total energy use over a 3.5 hour window of which the first 30 minutes comprised a partial cluster shutdown, followed by a 15 minute powerup routine. We explored the impact of shutting down between one and all six nodes during the 30 minute window. The shutdown was carried out by fully powering nodes off. We compared this to the energy usage without the partial shutdown.

Identical sample jobs were submitted to the cluster via SLURM scheduler at a constant rate to set the average cluster usage to approximately 55%, 60%, 65% and 75% capacity. We used custom state control commands to set the power states of individual machines in the test cluster. The SLURM scheduler automatically shifted queued jobs to run on the available machines, as shown in the example job schedule displayed Figure ?? from a four node shutdown experiment. We used our EDEALS data analysis pipeline to measure the changes in energy usage and job wait time in the queue.

E.4.2 Evaluation of Model Parameters

Importantly, EDEALS allowed us to determine appropriate power parameters, u_0 , u_v , and u_w for both our test rack as well as a larger partition of the University of Chicago’s Midway production cluster. Figure E.7 shows the measured relationship between CPU utilization and energy usage as determined from the machine level IPMI metric data.

To account for losses not measured at the IPMI level, we compare the sum IPMI power usage to the rack level power monitoring. This comparison revealed a correction

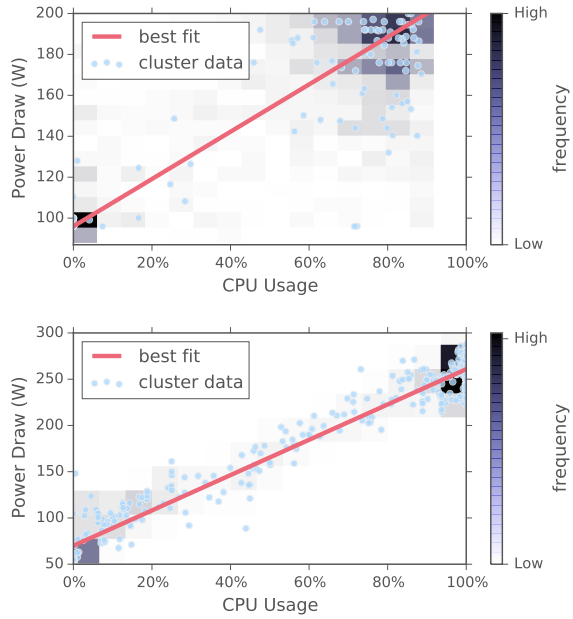


Figure E.7: Power data for test cluster (top) and production cluster (bottom) nodes in presence of variable usage. The slope and intercept of the line are used to determine u_v and u_0 respectively.

factor of 1.25 between the IPMI measurement and the total rack level energy draw. Using this corrected model, we were able to predict power consumption at the CDU level via CPU utilization under variable scheduler loads.

E.4.3 Relative Energy Savings and Max Wait Times

Our test cluster provided us with an important baseline in determining the effectiveness of a partial shutdown in reducing energy usage. As shown in Figure E.4, the total power draw from the test cluster was reduced dramatically during the shutdown period, and then returned to its baseline level.

These experiments were repeated with different job submission rates such that the average CPU usage varied from 55% to 75%. As shown in Figure E.5, the partial shutdowns reduced the total energy usage as measured at the CDU level. Not surprisingly, the power usage during cluster shutdown for all usage levels converged to roughly the same value at the point where all remaining operational machines reached

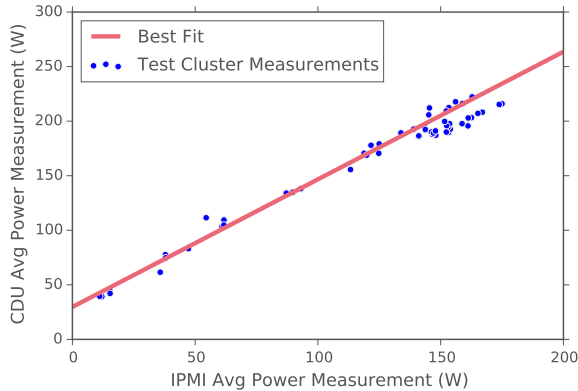


Figure E.8: Comparison between node level IPMI measurements and rack level CDU measurements. Best fit shows the model relationship used to convert IPMI data to estimated total power draw.

full capacity. Interestingly, the energy savings did not appear to be perfectly directly proportional to the fraction shut down. In particular, there was residual energy use associated with our machine’s low power state even when the cluster was entirely shut down.

We also measured the difference between job submission and start time, as depicted in Figure E.6. As one would expect, both mean and max wait times increased as the shutdown fraction grew and the effect was more pronounced when the cluster usage was higher. However, we were pleasantly surprised to find that max wait times topped out at 45 minutes, which was the duration of the entire cluster down period. This indicates that SLURM doesn’t add too much additional overhead, and therefore, the worst-case user wait times would not exceed the total period that the cluster was shut down.

E.5 Conclusion: Implication for An Operational HPC Datacenter

In an HPC datacenter, the variable cost to supply electricity to a facility can be decomposed into both a nominal cost per kilowatt-hour and a procurement cost from

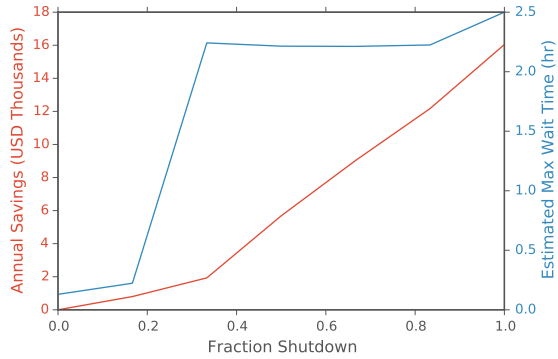


Figure E.9: Estimated savings from partial cluster shutdowns.

| T | t_s | p_0 | p_s |
|--------|-------|------------|-----------|
| 360 hr | 2 hr | \$0.03/kWh | \$6.5/kWh |

Table E.1: Model parameters estimated for medium scale HPC datacenter.

the supplier. Some suppliers impose a substantial procurement tariff based on electricity usage during the five, two hour long periods of highest demand in a year. In this scenario, the savings of load shedding can be orders of magnitude higher than the nominal price per kilowatt-hour. We estimate that by curtailing 1MW, 8 times per year, we can expect an annual savings of approximately \$100K, which in our case was roughly a 7

Combining these values with the power usage measurements from our production cluster, we can extrapolate the yearly savings based on fractional shutdowns of the data center. In addition, using the wait time statistics from our test cluster we can also estimate the worst-case impact on user wait-times that these cluster shutdowns will incur. We display this information in Figure E.9, as a function of the fraction of the cluster that we would be theoretically willing to shut down.

E.6 Acknowledgments

Special thanks goes out to Brandon for all his work getting our test cluster set up as well as for his useful input on machine pricing information. We also wish to thank

Matt Beach for his invaluable knowledge on energy pricing mechanisms and university power plans. Finally, we wish to thank Dr. Birali Runesha for his support in carrying out this project.

E.7 Availability

On our Github, we have provided all data collection scripts, analysis routines, and experimental setups, as well as detailed calculations and optimization methods for other price models.

<https://github.com/rcc-uchicago/datacenter>

APPENDIX F
ARTISTIC INTERPRETATIONS OF FILAMENT
RECYCLING

As part of a collaborative *Arts, Science and Culture* Grant sponsored by the University of Chicago's Institute for Molecular Engineering, Divisions of the Biological and Physical Sciences, the Humanities, and the Office of the Vice President for Research and for National Laboratories, I undertook an artistic collaboration project with MFA student at the Art Institute of Chicago, Keeley Haftner. the following is the text of our narrative proposal and the outcome images presented in our public talk.

Haftner is a Master of Fine Arts candidate in the Fiber and Material Studies department at the School of the Art Institute of Chicago, a department which focuses on the interdisciplinary study of the meaning and manipulation of materials through processes that involve politics, labour, gender, class and value. After meeting to discuss our specific areas of specialization and interest, however, it quickly became clear that our overlap was far more extensive and generative than general interests in the meaning and outcomes of manipulating material forms. Haftner is interested in value as it relates to materials, particularly the valueless. She transforms those materials into potentially valuable forms by employing a process of partial or complete transformation, which in a large part of her studio practice has involved taking waste plastics and transforming them into 3D printing filament with which to make sculptural multiples. McFadden, too, is fascinated by filament and renewal. In his work he studies how the cell's material properties give it the ability to change its own shape and migrate through its surroundings using its cytoskeletal structuring essentially a web-like sphere made from biopolymer filaments. He is also is focused on sustainability issues, emphasizing how biological materials can inspire new and sustainable technologies. This back and forth, combined with the link of the metaphorical and physical concept of filament, offers up extremely fertile ground for collaboration.

In terms of the physical manifestation of their collaboration, Haftner and McFadden have an overlapping material and technological interest that relates to both of their studies: 3D printing and polymer filament. PLA, or Polylactic Acid, is one of the most commonly used plastics in 3D printing. PLA is a naturally derived synthetic polymer which most additive manufacturers consider environmentally friendly because it purports to be compostable. This is important to many makers, since

opinions around the topic of 3D printing can be extreme articles often portray 3D printing as yet another elite frivolity producing unnecessary consumer garbage. PLA is a waste product from agricultural industry typically recouped from corn and sugar production. It is industrially compostable, which means exactly what it implies: that on an industrial scale, it can be composted. Industrial composting consists of mounding large-scale piles of organic matter and dirt, allowing these materials to combust and reach high temperatures. These piles are overturned and cycled with large-scale equipment until the matter has broken down entirely and become soil. PLA cannot be composted in backyards, it contaminates recycling streams when lumped in with other plastics, and it has the same (nearly infinite) lifespan as other plastics if it ends up in the landfill, the ocean, or as litter on the ground. These plastics rarely end up where they're meant to go, but they could, if people knew more.

Not only does the interesting material dilemma of PLA merge McFadden and Haftner's interests, but it is also rich research-based and metaphorical territory. The moment when industrial composting is in the process of biodegradation is the nexus of their research: Haftner's macro synthetic materials are broken down at the micro level by McFadden's microorganisms. The inorganic and the organic merge in a moment of decay that is both creation and destruction. This process takes into account the complexity of life, and starts to incorporate notions of Object Oriented Ontology from philosophy, a theory of the study of existence which purports that inorganic things are just as important and contingent as organic life, as well as poetical notions that gesture toward death and life cycles as they relate to existence in general. Anthropologist Tim Ingold speaks of materials as having their own life and trajectory, stating that the point of creation is simply a moment in time in which the scientist, artist, engineer or architect merely intervenes on material form. Both McFadden and Haftner seek to lend meaning to that intervention, in ways that encourage sustainable insights toward our stewardship of things in favour of collective re-examination.

The outcome of this collaboration will take the form of a series of sculptures made from both homemade filament from waste PLA plastics, and perhaps other plastic materials as they become relevant, with the possibility of using the filament extruder as the direct sculptural production site itself to make filament sculpture.

These filament sculptures could perhaps borrow from both the cytoskeletal forms at the heart of McFaddens research interests, and the conceptual interests that Haftner has in the idea of filament as a binder, a string, a connector, and an object of potential. The production, presentation, and documentation of both the process of making these sculptural multiples and the resultant multiples themselves will be the focus of this collaboration. The nature of this material investigation leaves plenty of room for unknown discoveries through the generative overlap of the pairs research and processes. As per the schedule for the work, Haftner and McFadden intend to purchase the new equipment as soon as possible and begin experimenting with materials on the previous model until it arrives. They will visit the compost facility in November, and meet once every two weeks for long sessions from November to May to research, play with materials, and experiment with conceptual and visual forms.

F.1 The ship of Theseus as a metaphor for life

The ship wherein Theseus and the youth of Athens returned from Crete had thirty oars, and was preserved by the Athenians down even to the time of Demetrius Phalereus, for they took away the old planks as they decayed, putting in new and stronger timber in their places, in so much that this ship became a standing example among the philosophers, for the logical question of things that grow; one side holding that the ship remained the same, and the other contending that it was not the same.
—Plutarch's Life of Theseus, as translated by John Dryden

F.2 Experiments with plastic filament sculpture



Figure F.1



Figure F.2

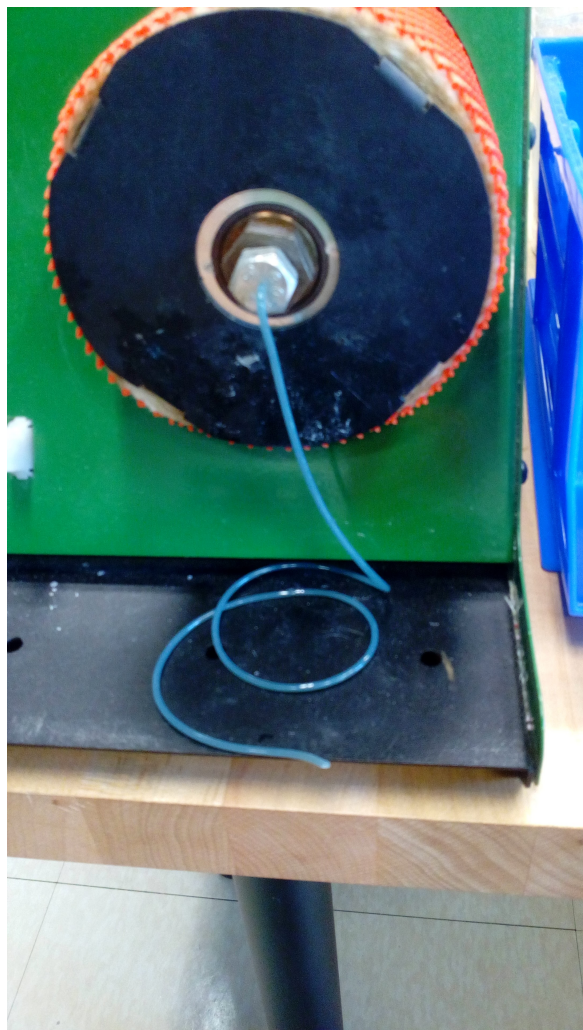


Figure F.3

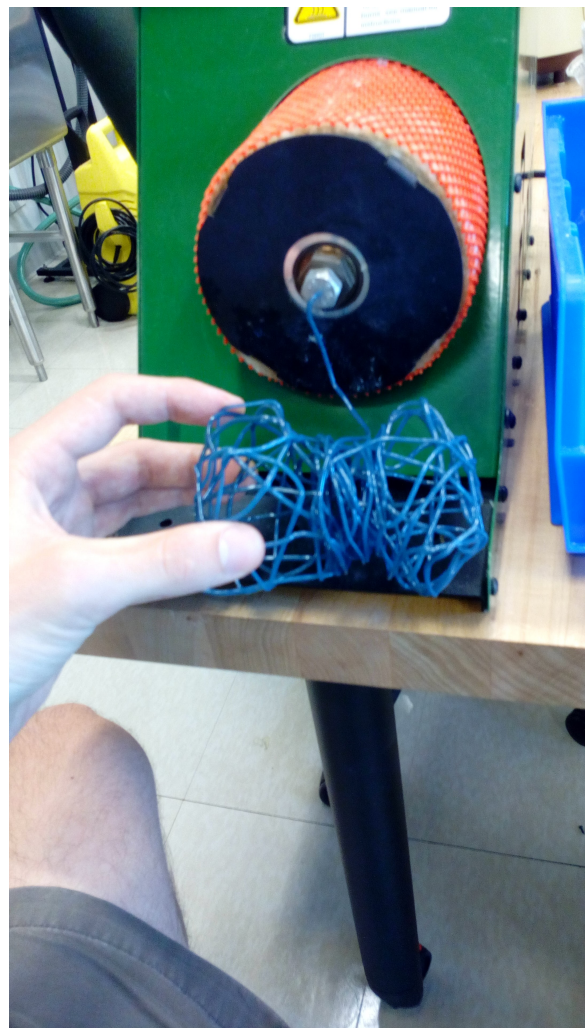


Figure F.4

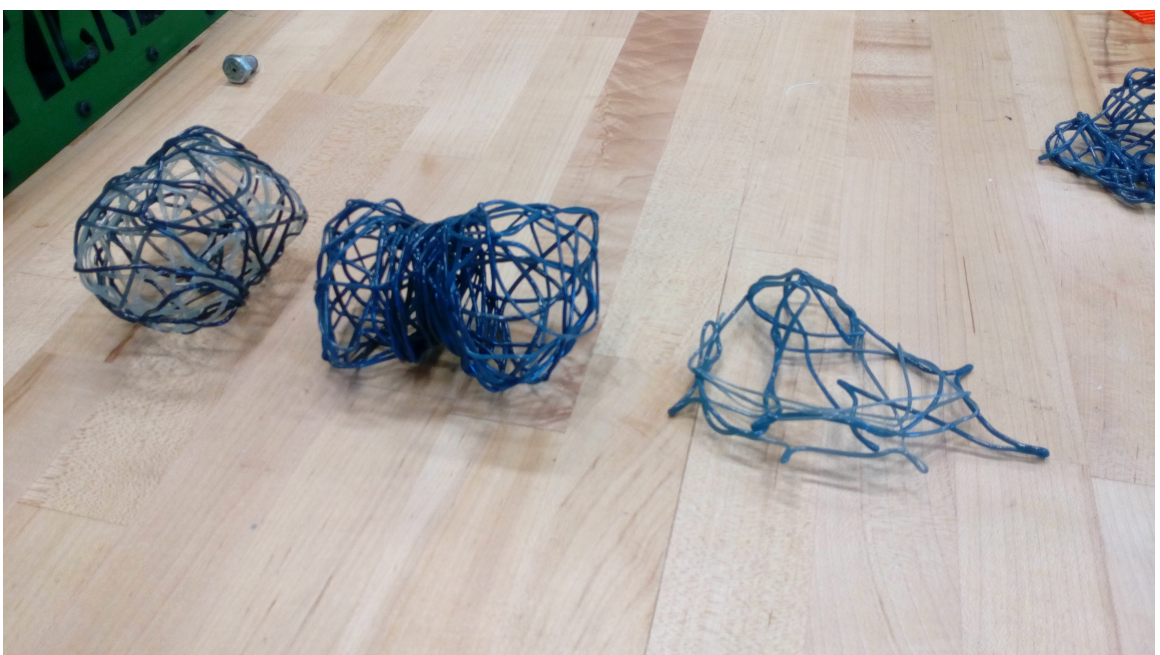


Figure F.5



Figure F.6



Figure F.7



Figure F.8

APPENDIX G
WORKSHOP ON MODELING IN BIOLOGY

G.1 Course syllabus

G.1.1 Course Objective

This course is designed to introduce a student with a reasonable understanding of biology to the basic techniques of mathematical modeling. Specifically, the student will be able to take a conceptual model of some biological system and transform it into an appropriate mathematical framework. The student will also be able to develop intuition based on their model and to interpret simulation results to draw conclusions.

G.1.2 Course Design

Content, Converse, Convey For each lesson in the course, the assignments will proceed in three parts. First, students will familiarize themselves with the content of that weeks lesson and take a short quiz to ensure that they have done the necessary reading. Second, the students will meet in class or use the online forum to converse on a problem related to the lesson. Finally, ever student will be given their own related problem to solve and convey their answer on our class wiki for other students to evaluate.

Programming Projects In addition to the weekly assignments, the students will also be synthesizing their knowledge of mathematical modeling concepts to build their own simple modeling projects. By the third week the students will be able to pick a biological system to study. They will work during a few of the hour long discussions to put together their own model of the system and explain it to the rest of the class. Finally, they will present an in-depth description of their project on the class wiki.

G.1.3 Assignments

Readings and Quizzes There are readings and lectures online for you to become introduced to the material before you come to class. There will be online quizzes on Chalk which will be due by Tuesday at midnight the day before new material is covered in class. These quizzes should resemble simple multiple choice exam questions; they

merely check whether you have viewed the material. However, in total these quizzes count towards 25% of your overall grade so take them seriously.

Class Forum Discussions Every week, the class will meet together to tackle a problem related to the lesson. The problems are frequently posed based on questions left unanswered by students in the previous year. The class should come to a reasonable consensus by the end of the session or they should follow up online to come to an agreement. I've designed the discussion sections so that you don't need to be the most boisterous student to participate in the discussion meaningfully. There will be an equal weight to valuable comments given in person as well as those on our online forum. In addition, our class discussions will often contain smaller discussions that allow for one-on-one interaction. Nevertheless, class discussion accounts for 25% of your grade so, whether in the forums or in person, your participation is required.

Wiki Articles Each student will be given a more in-depth problem for each lesson to be written up and posted to the group wiki. Here we are not just looking for a solution to the problem. We need an explanation of your approach and why it is right. Your peers will be evaluating your work to make sure that it makes sense to them. The writing and evaluation of these assignments will count for another 25% of your grade.

Final Project By the third week of this course, the student should start to have an understanding of what types of systems can be modeled with a differential equation. At this point in time, the students will select a biological system to model as their final project. The class during 4th week will involve every student briefly stating their problem area how they will model it. Please note that the system you are modeling does not have to be extremely complex, and the model you generate does not have to be perfectly accurate. The goal of this project is simply to show that you understand all of the steps in moving from an abstract idea to a mathematical model. By the end of the session you should have a reasonably involved computational model.

G.2 Post-class Student Survey

I asked the students to give me some feedback on their experience in the course and what could be improved. Feedback was generally positive and instructive in looking for ways to improve.

| | A lot | A little | Not at all | Did more harm than good |
|--|--------------|--------------|------------|-------------------------|
| ▼ This class clarified what biological models are good for. | 100.00% 2 | 0.00% 0 | 0.00% 0 | 0.00% 0 |
| ▼ The class examples were at the right pace for my level of understanding. | 50.00% 1 | 50.00% 1 | 0.00% 0 | 0.00% 0 |
| ▼ The information presented was well-motivated. | 100.00% 2 | 0.00% 0 | 0.00% 0 | 0.00% 0 |
| ▼ Expectations were clearly stated. | 0.00% 0 | 100.00% 2 | 0.00% 0 | 0.00% 0 |
| ▼ Class discussions were useful. | 50.00% 1 | 50.00% 1 | 0.00% 0 | 0.00% 0 |

Figure G.1: Responses from student survey. Only 2 of 5 students replied.

What are some questions you have about biological modeling that this class should have addressed. I think it might be good to emphasize presentation and interpretation of modeling results, both from the perspective of the experimenter and the reader. In other words, I think it would be good for people to become comfortable both reading theoretical papers and generating simple modeling figures. I know this wasn't the focus of the workshop, but it might be nice to briefly cover agent-based modeling to the point where someone could be conformable interpreting experiments.

It was a good foundation. Maybe how to interpret a model in a paper and evaluate it, if we did an example in class that would be helpful.

Describe how you would like to see this workshop structured to best promote your learning of the material It might be a good idea to have a list of things to model, so that people can still progress through the workshop even if the system they work on isn't amenable to modeling or isn't interesting to model. I liked the emphasis on students giving short presentations throughout.

A little more background on the basic calculus we needed. Also talking more about the reasoning behind what you're doing and less algebra on the board, it's kinda hard to follow but we can all probably do it.

G.3 Reflections and Future Ideas

In general, the students reacted positively to the framework that we established with its emphasis on the three C's outlined above. The student survey responses showed that the focus on classroom participation was welcome. In practice, the students were not required to complete any homework, and the course was not given for a grade. This led to many of the assignments being neglected entirely. However, despite all of the work being completely optional, many of the students completed a significant portion of the work voluntarily.

In the future, I will need to do a bit more preparation work to select a larger corpus of example systems for students to work with. And having more examples to work through together will also probably improve outcomes. On the other hand, I don't want to lose the student driven focus that I was hoping to attain. I may also want to establish a bit more authority so that students attend class with their assignments completed.

G.4 Course Materials

The course slides are available online at the following URL:

<https://drive.google.com/drive/folders/0B3gBL61483U8Z2h1b3JRUHZMQ1k?usp=sharing>

Below you can find the Q&A material used for quizzes or discussion prompts.

G.4.1 How mathematical models make sense of complex processes

G.4.2 Modeling biological systems with differential equations

Modelling biological systems is a significant task of systems biology and mathematical biology. It involves the use of computer simulations of biological systems, including cellular subsystems (such as the networks of metabolites and enzymes which comprise metabolism, signal transduction pathways and gene regulatory networks), to both analyze and visualize the complex connections of these cellular processes.”
—Wikipedia

Many types of models Biological models can work in many different ways: In general, models are made to focus on systems at a certain scale. We can choose from a wide variety of model types. Some work by modeling continuous values, such as concentration of a protein. Others work by modeling the discrete state of a system, such as a neuron being either on or off. Some models are deterministic, meaning that there is no randomness, while others add stochastic noise.

Focusing on Differential equations In our class we’re going to focus on probably the simplest and most widely used kind of mathematical model, differential equations. Differential equations are a continuous, deterministic model, they model real values with rules that describe exactly how those values change. Differential equations are very similar to the equations we learned about in our high school and college calculus courses.

What is a differential equation good for? A differential equation is a simple formula that describes how a system will change in time based on the state of the system right now. You can think of it like a very formal protocol for how concentrations of substances will change over time. For example, a differential equation

G.4.3 Visualizing equations with graphs

Why is it called differential? One could argue that differential equations could actually be called derivative equations. That's because the equation itself is really just a way of explicitly writing out the derivative of a variable. For those that don't remember a derivative is just a way to represent rate of change, that is - the amount by which a function is changing at one given point...it is the slope of the tangent line at a point on a graph.?

Equilibrium? Another important concept in diffeq is that of equilibrium. The meaning of equilibrium is simple once you have a rate equation to look at. When the net rates of change of all variables are equal to 0, then nothing can change anymore. The rates of production and destruction are balanced, and the concentrations of everything will remain constant forever. Not all systems reach equilibrium, but most do, and finding equilibria is the first step to understanding how many systems work. We will use equilibrium and steady state more or less interchangeably though there are subtle, pedantic differences.

Initial conditions and transient behaviors Even though most systems reach equilibrium after a long time, the system's initial conditions set the early "transient" behavior. The initial condition, or seed value, is simply the state of the system where we choose to start. The transient behavior is the way in which the system changes from the initial conditions to the steady state.

What are nullclines? If our rate equation has two variables that can change in it (i.e. not constants), then there is no longer a single value at which the rate equation will equal 0. Instead there will be a set of values that make the rate 0. This set of values defines a line, and this line is called a nullcline.

G.4.4 Simplifying models and starting simulations

Why simplify before simulating? There are a number of reasons to simplify your equations before you ever start a simulation. Here are my top three. 1) You won't be able to remember or adequately describe all the parameters that went into a given simulation when somebody asks you. If you have 20 parameters in a simulation there will always be a huge risk that you screwed one of them up and you will never be able to notice. 2) If you want to understand how your model works under many different conditions, then every time you add a parameter you have to do exponentially more work. In other words, when you are systematically checking how 3 parameters work together you may have to do 100^3 different simulations and analyze your results. If you add one more parameter you will have to do 100^4 simulation or 100 times more work. 3) Nobody wants to look at a disorganized giant equation. If you have a complicated equation most people will decide it isn't worth their time to pay attention to the modeling so none of your modeling work will count for anything anyway.

The parts of a differential equation model A differential equation model can be broken down into 3 parts: variables, parameters, and the form of the equation. Variables are the values (like concentration) that are changing in time. This is the physically ?real? stuff like the number of proteins or the size of your cell. Parameters are things like rate constants and diffusion coefficients. These are descriptive numbers that set the magnitudes of rates of change. Finally, the form of the equation determines how the variables and parameters fit together. This is the level at which we can see how each variable affects the other qualitatively, but it takes parameters to know by how much.

How do simulations work? The applied math behind solving differential equations with computers is rich and we certainly won't understand everything that has been done over the past 70 years to solve these problems. However we can get some intuition by looking at the simplest way of solving, called the Euler method. In this method you ?step? through time and change the value of your variables by a small amount using the rules defined in your differential equation (See wikipedia page for

more info). If you ever try this, you will get bored very fast because it is really annoying. But when computers do this, they can take very small steps and therefore ?solve? the system with arbitrary accuracy. There have been a bunch of modifications of this technique that significantly improve the accuracy vs timestep tradeoff.

G.4.5 Analyzing equations and understanding simulation output

(from wikipedia) **Nondimensionalization** is the partial or full removal of units from an equation involving physical quantities by a suitable substitution of variables. This technique can simplify and parameterize problems where measured units are involved. It is closely related to dimensional analysis. In some physical systems, the term scaling is used interchangeably with nondimensionalization, in order to suggest that certain quantities are better measured relative to some appropriate unit. These units refer to quantities intrinsic to the system, rather than units such as SI units. Nondimensionalization is not the same as converting extensive quantities in an equation to intensive quantities, since the latter procedure results in variables that still carry units.

Running simulations : The following two snippets of code is all you need to solve differential equations in MATLAB.

```
function dc = myode(t,p,a,b)
    p1 = p(1);
    p2 = p(2);
    dp1 = 1 - a*p2 - p1;
    dp2 = p1 - b*p2;
    dp = [dp1;dp2];
end

t = 0:0.1:10;      #timepoints for solution (1 to 10 increment of 0.1)
p0 = [1,0];         #initial conditions for the concentration of p1 and p2
a=1; b=1;           #optional constants a and b which will change behavior
```

```
[t, pt] = ode45(@myode,t,p0,[],a,b);           #this runs the simulation
plot(t,p(:,1)); hold on; plot(t,p(:,2));         #this plots the output
```

So now you can put whatever you want into the equation and change your parameters and run many simulations.

G.4.6 Explaining ever more complex systems

G.5 Quizzes and Project ideas

W2 Q1: Which is not a situation that is amenable to mathematical modeling? A metabolism, signal transduction pathways, gene regulatory networks, protein purification

Q2: Which is a category of biological mathematical model? A soft, prescient, discrete, topological

Q3: Which type of model is a differential equation? A continuous deterministic, discrete stochastic, continuous stochastic, discrete deterministic

Q4: What does a differential equation most closely resemble? A a protocol, a patent, a dissertation, a legume

W3 Q1: Which is the closest synonym for derivative in the context of diffeq? A Unoriginal, by-product, change, sum

Q2: Which is least similar to equilibrium? A balanced rates, constant concentrations, discrete probabilities, steady states

Q3: Which conditions set the transient behavior? A initial, parametric, hyperbolic, final

Q4: Nullclines are... A topographical, unimportant, lines, esoteric

W4 Q1: Number of simulations to run varies — with the number of free parameters. A quadratically, logarithmically, exponentially, combinatorially

Q2: Which is not a part of a differential equation model? A definitions, variables, parameters, the form of the equation

Q3: The Euler method gives exact solutions. A True, False, neither, depends who you ask

Q4: Who likes looking at a disorganized mess of an equation? A Your PI, your colleagues, your reviewer, nobody

W5 Q1: Once nondimensionalization is complete? A All variables have units of time, there are no more parameters left, equations are simpler to analyze, your solutions will fall on a line

Q2: In MATLAB — is the function for solving differential equations A ode23tb, ode113, ode45, ode15i

Q3: Which isn't necessary to solve a differential equation A An ode function, constants, initial conditions, timepoints for solution

REFERENCES

- [1] Force generation, transmission, and integration during cell and tissue morphogenesis. *Annual Review of Cell and Developmental Biology*, 27(1):157–184, 2011. PMID: 21740231.
- [2] Millius A, Watanabe N, and Weiner OD. Diffusion, capture and recycling of SCAR/wave and Arp2/3 complexes observed in cells by single-molecule imaging. *J Cell Sci. 2012 Mar 1;125(Pt 2)*, 2012.
- [3] Ponti A, Machacek M, Gupton SL, Waterman-Storer CM, and Danuser G. *Two distinct actin networks drive the protrusion of migrating cells*. Science, 2004.
- [4] Douglass AD and Vale RD. *Single-molecule microscopy reveals plasma membrane microdomains created by protein-protein networks that exclude or trap signaling molecules in T cells*. Cell, 2005.
- [5] Douglass AD and Vale RD. *Single-molecule imaging of fluorescent proteins*. Methods Cell Biol, 2008.
- [6] Wylie W. Ahmed and Timo Betz. Dynamic cross-links tune the solidfluid behavior of living cells. *Proceedings of the National Academy of Sciences*, 112(21):6527–6528, 2015.
- [7] Jun Allard and Alex Mogilner. Traveling waves in actin dynamics and cell motility. *Current opinion in cell biology*, 25(1):107–115, February 2013.
- [8] Jose Alvarado, Michael Sheinman, Abhinav Sharma, Fred C. MacKintosh, and Gijsje H. Koenderink. Molecular motors robustly drive active gels to a critically connected state. *Nat Phys*, 9(9):591–597, 09 2013.
- [9] Shiladitya Banerjee and M. Cristina Marchetti. Instabilities and oscillations in isotropic active gels. *Soft Matter*, 7:463–473, 2011.
- [10] Shiladitya Banerjee, M. Cristina Marchetti, and Kristian Müller-Nedebock. Motor-driven dynamics of cytoskeletal filaments in motility assays. *Phys. Rev. E*, 84:011914, Jul 2011.
- [11] Andreas R. Bausch, Florian Ziemann, Alexei A. Boulbitch, Ken Jacobson, and Erich Sackmann. Local measurements of viscoelastic parameters of adherent cell surfaces by magnetic bead microrheometry. *Biophysical Journal*, 75(4):2038 – 2049, 1998.

- [12] Martin Behrndt, Guillaume Salbreux, Pedro Campinho, Robert Hauschild, Felix Oswald, Julia Roensch, Stephan W. Grill, and Carl-Philipp Heisenberg. Forces driving epithelial spreading in zebrafish gastrulation. *Science*, 338(6104):257–260, 2012.
- [13] William M Bement, Marcin Leda, Alison M Moe, Angela M Kita, Matthew E Larson, Adriana E Golding, Courtney Pfeuti, Kuan-Chung Su, Ann L Miller, Andrew B Goryachev, and George von Dassow. Activator-inhibitor coupling between Rho signalling and actin assembly makes the cell cortex an excitable medium. *Nature cell biology*, 17(11):1471–1483, November 2015.
- [14] Poul M. Bendix, Gijsje H. Koenderink, Damien Cuvelier, Zvonimir Dogic, Bernard N. Koeleman, William M. Brieher, Christine M. Field, L. Mahadevan, and David A. Weitz. A quantitative analysis of contractility in active cytoskeletal protein networks. *Biophysical Journal*, 94(8):3126 – 3136, 2008.
- [15] Hélène A Benink, Craig A Mandato, and William M Bement. Analysis of cortical flow models in vivo. *Molecular Biology of the Cell*, 11(8):2553–2563, 08 2000.
- [16] W. Bing, A. Knott, and S. B. Marston. A simple method for measuring the relative force exerted by myosin on actin filaments in the in vitro motility assay: evidence that tropomyosin and troponin increase force in single thin filaments. *Biochem J*, 350(Pt 3):693–699, Sep 2000. 10970781[pmid].
- [17] G B Blanchard, S Murugesu, R J Adams, A Martinez-Arias, and N Gorfinkel. Cytoskeletal dynamics and supracellular organisation of cell shape fluctuations during dorsal closure. 137(16):2743–2752, July 2010.
- [18] Deva Bodas, Justin Song, Murali Rajappa, and Andy Hoffman. Simple power-aware scheduler to limit power consumption by hpc system within a budget. In *Proceedings of the 2Nd International Workshop on Energy Efficient Supercomputing*, E2SC ’14, pages 21–30, Piscataway, NJ, USA, 2014. IEEE Press.
- [19] Justin S. Bois, Frank Jülicher, and Stephan W. Grill. Pattern formation in active fluids. *Phys. Rev. Lett.*, 106:028103, Jan 2011.
- [20] Justin S Bois, Frank Jülicher, and Stephan W Grill. Pattern formation in active fluids. *Physical review letters*, 106(2):028103, January 2011.
- [21] M Bornens, M Paintrand, and C Celati. The cortical microfilament system of lymphoblasts displays a periodic oscillatory activity in the absence of microtubules: implications for cell polarity. *The Journal of cell biology*, 109(3):1071–1083, September 1989.

- [22] D Bray and JG White. Cortical flow in animal cells. *Science*, 239(4842):883–888, 1988.
- [23] S Brenner. The genetics of *Caenorhabditis elegans*. *Genetics*, 77(1):71–94, May 1974.
- [24] William Brieher. Mechanisms of actin disassembly. *Mol Biol Cell*, 24(15):2299–2302, Aug 2013.
- [25] C. P. Broedersz, C. Storm, and F. C. MacKintosh. Effective-medium approach for stiff polymer networks with flexible cross-links. *Phys. Rev. E*, 79:061914, Jun 2009.
- [26] Chase P. Broedersz, Martin Depken, Norman Y. Yao, Martin R. Pollak, David A. Weitz, and Frederick C. MacKintosh. Cross-link-governed dynamics of biopolymer networks. *Phys. Rev. Lett.*, 105:238101, Nov 2010.
- [27] P. Broedersz, C. and C. MacKintosh, F. Modeling semiflexible polymer networks. *Rev. Mod. Phys.*, 86:995–1036, Jul 2014.
- [28] Brian M Burkel, George von Dassow, and William M Bement. Versatile fluorescent probes for actin filaments based on the actin-binding domain of utrophin. *Cell Motility and the Cytoskeleton*, 64(11):822–832, November 2007.
- [29] Hoege C and Hyman AA. *Principles of PAR polarity in Caenorhabditis elegans embryos*. Nat Rev Mol Cell Biol, 2013.
- [30] Rappleye CA, Paredez AR, Smith CW, McDonald KL, and Aroian RV. *The coronin-like protein POD-1 is required for anterior-posterior axis formation and cellular architecture in the nematode caenorhabditis elegans*. Genes Dev, 1999.
- [31] Anders E Carlsson. Actin dynamics: From nanoscale to microscale. *Annual review of biophysics*, 39:91–110, 06 2010.
- [32] Ana Carvalho, Sara K Olson, Edgar Gutierrez, Kelly Zhang, Lisa B Noble, Esther Zanin, Arshad Desai, Alex Groisman, and Karen Oegema. Acute drug treatment in the early *C. elegans* embryo. *PloS one*, 6(9):e24656, 2011.
- [33] Preethi L. Chandran and Mohammad R. K. Mofrad. Averaged implicit hydrodynamic model of semiflexible filaments. *Phys. Rev. E*, 81:031920, Mar 2010.
- [34] Qian Chen, Shalini Nag, and Thomas D Pollard. Formins filter modified actin subunits during processive elongation. *Journal of structural biology*, 177(1):32–39, January 2012.

- [35] Priyamvada Chugh, Andrew G. Clark, Matthew B. Smith, Davide A. D. Cas-sani, Guillaume Charras, Guillaume Salbreux, and Ewa K. Paluch. Nanoscale organization of the actomyosin cortex during the cell cycle. *Biophysical Journal*, 110(3):198a, 2016/07/18 2016.
- [36] Waterman-Storer CM, Desai A, Bulinski JC, and Salmon ED. *Fluorescent speckle microscopy*. a method to visualize the dynamics of protein assemblies in living cells, 1998.
- [37] Martine Coué, Stephen L. Brenner, Ilan Spector, and Edward D. Korn. Inhi-bition of actin polymerization by latrunculin a. *FEBS Letters*, 213(2):316–318, 1987.
- [38] J Crocker and D G Grier. Methods of digital video microscopy for colloidal studies. 179(1):298–310, 1996.
- [39] CC Cunningham, JB Gorlin, DJ Kwiatkowski, JH Hartwig, PA Janmey, HR By-ers, and TP Stossel. Actin-binding protein requirement for cortical stability and efficient locomotion. *Science*, 255(5042):325–327, 1992.
- [40] Christian J. Cyron, Kei W. Müller, Andreas R. Bausch, and Wolfgang A. Wall. Micromechanical simulations of biopolymer networks with finite elements. *Journal of Computational Physics*, 244(0):236 – 251, 2013. Multi-scale Modeling and Simulation of Biological Systems.
- [41] Nilushi L. Dasanayake and Anders E. Carlsson. Stress generation by myosin minifilaments in actin bundles. *Phys Biol*, 10(3):036006–036006, Jun 2013. 23595157[pmid].
- [42] Daryl J V David, Alisa Tishkina, and Tony J C Harris. The PAR complex regulates pulsed actomyosin contractions during amnioserosa apical constriction in Drosophila. 137(10):1645–1655, May 2010.
- [43] Enrique M De La Cruz. How cofilin severs an actin filament. *Biophysical reviews*, 1(2):51–59, 05 2009.
- [44] Enrique M. De La Cruz and Margaret L. Gardel. Actin mechanics and frag-mentation. *Journal of Biological Chemistry*, 290(28):17137–17144, 07 2015.
- [45] Enrique M De La Cruz and Margaret L Gardel. Actin Mechanics and Fragmen-tation. *The Journal of biological chemistry*, 290(28):17137–17144, July 2015.
- [46] Pierre Delforge and Josh Whitney. Data center efficiency assessment: Scaing up energy efficiency across the data center industry: Evaluating key drivers and barriers. Technical report, National Resources Defense Council, August 2014.

- [47] Kai Dierkes, Angughali Sumi, Jérôme Solon, and Guillaume Salbreux. Spontaneous oscillations of elastic contractile materials with turnover. *Phys. Rev. Lett.*, 113:148102, Oct 2014.
- [48] Kai Dierkes, Angughali Sumi, Jérôme Solon, and Guillaume Salbreux. Spontaneous oscillations of elastic contractile materials with turnover. *Physical review letters*, 113(14):148102, October 2014.
- [49] Dickinson DJ, Ward JD, Reiner DJ, and Goldstein B. Engineering the *Caenorhabditis* genome using Cas9-triggered homologous recombination. *Nat Methods*. 2013 Oct;10(10):1028-34. doi:, 10., 2013.
- [50] M. Doi and S. F. Edwards. *The Theory of Polymer Dynamics*. Oxford University Press, USA, November 1986.
- [51] Burnette DT et al. *A role for actin arcs in the leading-edge advance of migrating cells*. Nat Cell Biol, 2011.
- [52] Fangming Du, John E. Fischer, and Karen I. Winey. Effect of nanotube alignment on percolation conductivity in carbon nanotube/polymer composites. *Phys. Rev. B*, 72:121404, Sep 2005.
- [53] Janet C Effler, Yee-Seir Kee, Jason M Berk, Minhchau N Tran, Pablo A Iglesias, and Douglas N Robinson. Mitosis-specific mechanosensing and contractile-protein redistribution control cell shape. *Current biology : CB*, 16(19):1962–1967, October 2006.
- [54] Hajar Ennmani, Gaëlle Letort, Christophe Guérin, Jean-Louis Martiel, Wenxiang Cao, François Nédélec, Enrique M. De La Cruz, Manuel Théry, and Laurent Blanchoin. Architecture and connectivity govern actin network contractility. *Current Biology*, 26(5):616 – 626, 2016.
- [55] Sako Y et al. *Live cell single-molecule detection in systems biology*. 2012.
- [56] E Evans and A Yeung. Apparent viscosity and cortical tension of blood granulocytes determined by micropipet aspiration. *Biophysical Journal*, 56(1):151–160, 07 1989.
- [57] Bird A. F. and Bird J. *The structure of nematodes*. Academic Press, California, 1991.
- [58] Persson F, Lindn M, Unoson C, and Elf J. *Extracting intracellular diffusive states and transition rates from single-molecule tracking data*. Nat Methods, 2013.

- [59] Rodrigo Fernandez-Gonzalez, Sérgio de Matos Simoes, Jens-Christian Röper, Suzanne Eaton, and Jennifer A Zallen. Myosin II dynamics are regulated by tension in intercalating cells. *Developmental cell*, 17(5):736–743, November 2009.
- [60] A. E. Filippov, J. Klafter, and M. Urbakh. Friction through dynamical formation and rupture of molecular bonds. *Phys. Rev. Lett.*, 92:135503, Mar 2004.
- [61] Daniel A. Fletcher and R. Dyche Mullins. Cell mechanics and the cytoskeleton. *Nature*, 463(7280):485–492, 01 2010.
- [62] Marco Fritzsche, Christoph Erlenkämper, Emad Moeendarbary, Guillaume Charras, and Karsten Kruse. Actin kinetics shapes cortical network structure and mechanics. *Science Advances*, 2(4), 2016.
- [63] Marco Fritzsche, Alexandre Lewalle, Tom Duke, Karsten Kruse, and Guillaume Charras. Analysis of turnover dynamics of the submembranous actin cortex. *Molecular Biology of the Cell*, 24(6):757–767, 03 2013.
- [64] Marco Fritzsche, Alexandre Lewalle, Tom Duke, Karsten Kruse, and Guillaume Charras. Analysis of turnover dynamics of the submembranous actin cortex. *Molecular Biology of the Cell*, 24(6):757–767, 2013.
- [65] Danuser G and Waterman-Storer CM. *Quantitative fluorescent speckle microscopy of cytoskeleton dynamics*. Annu Rev Biophys Biomol Struct, 2006.
- [66] Giannone G, Hosy E, Levet F, Constals A, Schulze K, Sobolevsky AI, Rosconi MP, Gouaux E, Tamp R, Choquet D, and Cognet L. *Dynamic superresolution imaging of endogenous proteins on living cells at ultra-high density*. Biophys J, 2010.
- [67] Salbreux G, Charras G, and Paluch E. *Actin cortex mechanics and cellular morphogenesis*. Trends Cell Biol, 2012.
- [68] M. L. Gardel, F. Nakamura, J. Hartwig, J. C. Crocker, T. P. Stossel, and D. A. Weitz. Stress-dependent elasticity of composite actin networks as a model for cell behavior. *Phys. Rev. Lett.*, 96:088102, Mar 2006.
- [69] M. L. Gardel, F. Nakamura, J. H. Hartwig, J. C. Crocker, T. P. Stossel, and D. A. Weitz. Prestressed f-actin networks cross-linked by hinged filamins replicate mechanical properties of cells. *Proceedings of the National Academy of Sciences of the United States of America*, 103(6):1762–1767, 2006.
- [70] M. L. Gardel, J. H. Shin, F. C. MacKintosh, L. Mahadevan, P. Matsudaira, and D. A. Weitz. Elastic behavior of cross-linked and bundled actin networks. *Science*, 304(5675):1301–1305, 2004.

- [71] Girish Ghatikar, Venkata Ganti, Nance Matson, and Mary Ann Piette. Demand response opportunities and enabling technologies for data centers: Findings from field studies. 2012.
- [72] Albert Goldbeter. *Biochemical Oscillations and Cellular Rhythms: The Molecular Bases of Periodic and Chaotic Behavior*. Cambridge Univ. Press, Cambridge, UK, 1996.
- [73] Nicole Gorfinkiel. From actomyosin oscillations to tissue-level deformations. *Developmental dynamics : an official publication of the American Association of Anatomists*, 245(3):268–275, March 2016.
- [74] Nicole Gorfinkiel and Guy B Blanchard. Dynamics of actomyosin contractile activity during epithelial morphogenesis. *Current Opinion in Cell Biology*, 23(5):531 – 539, 2011. Cell-to-cell contact and extracellular matrix.
- [75] Minakshi Guha, Mian Zhou, and Yu-li Wang. Cortical actin turnover during cytokinesis requires myosin ii. *Current Biology*, 15(8):732–736, 2016/12/15 2016.
- [76] Danielle R Hamill, Aaron F Severson, J Clayton Carter, and Bruce Bowerman. Centrosome maturation and mitotic spindle assembly in C. elegans require SPD-5, a protein with multiple coiled-coil domains. *Developmental cell*, 3(5):673–684, November 2002.
- [77] Kimihide Hayakawa, Hitoshi Tatsumi, and Masahiro Sokabe. Actin filaments function as a tension sensor by tension-dependent binding of cofilin to the filament. *The Journal of cell biology*, 195(5):721–727, November 2011.
- [78] David A. Head, Alex J. Levine, and F. C. MacKintosh. Deformation of cross-linked semiflexible polymer networks. *Phys. Rev. Lett.*, 91:108102, Sep 2003.
- [79] Carl-Philipp Heisenberg and Yohanns Bellaïche. Forces in tissue morphogenesis and patterning. *Cell*, 153(5):948 – 962, 2013.
- [80] Claus Heussinger, Boris Schaefer, and Erwin Frey. Nonaffine rubber elasticity for stiff polymer networks. *Phys. Rev. E*, 76:031906, Sep 2007.
- [81] T. Hiraiwa and G. Salbreux. Role of turn-over in active stress generation in a filament network. *ArXiv e-prints*, July 2015.
- [82] S N Hird and J G White. Cortical and cytoplasmic flow polarity in early embryonic cells of caenorhabditis elegans. *The Journal of Cell Biology*, 121(6):1343–1355, 1993.

- [83] Robert M Hochmuth. Micropipette aspiration of living cells. *Journal of Biomechanics*, 33(1):15 – 22, 2000.
- [84] Jonathon Howard, Stephan W. Grill, and Justin S. Bois. Turing’s next steps: the mechanochemical basis of morphogenesis. *Nat Rev Mol Cell Biol*, 12(6):392–398, Jun 2011.
- [85] A. F. HUXLEY and R. NIEDERGERKE. Structural changes in muscle during contraction: Interference microscopy of living muscle fibres. *Nature*, 173(4412):971–973, May 1954.
- [86] Tatsuo Iwazumi. *Mechanics of the Sarcomere*, pages 13–22. Springer Japan, Tokyo, 1989.
- [87] Eugene M Izhikevich. *Dynamical systems in neuroscience : the geometry of excitability and bursting*. Computational neuroscience. MIT Press, Cambridge, Mass., London, 2007.
- [88] Aron B Jaffe and Alan Hall. Rho GTPases: biochemistry and biology. *Annual review of cell and developmental biology*, 21(1):247–269, 2005.
- [89] L W Janson, J Kolega, and D L Taylor. Modulation of contraction by gelation/solation in a reconstituted motile model. *The Journal of Cell Biology*, 114(5):1005–1015, 1991.
- [90] Jaqaman K et al. *Robust single-particle tracking in live-cell time-lapse sequences*. Nat Methods, 2008.
- [91] Jaqaman K et al. *Cytoskeletal control of CD36 diffusion promotes its receptor and signaling function*. Cell, 2011.
- [92] Ravi S Kamath, Andrew G Fraser, Yan Dong, Gino Poulin, Richard Durbin, Monica Gotta, Alexander Kanapin, Nathalie Le Bot, Sergio Moreno, Marc Sohrmann, David P Welchman, Peder Zipperlen, and Julie Ahringer. Systematic functional analysis of the *Caenorhabditis elegans* genome using RNAi. *Nature*, 421(6920):231–237, January 2003.
- [93] Maryna Kapustina, Timothy C Elston, and Ken Jacobson. Compression and dilation of the membrane-cortex layer generates rapid changes in cell shape. *The Journal of cell biology*, 200(1):95–108, January 2013.
- [94] Maryna Kapustina, Gabriel E Weinreb, Nancy Costigliola, Zenon Rajfur, Ken Jacobson, and Timothy C Elston. Mechanical and biochemical modeling of cortical oscillations in spreading cells. *Biophysical journal*, 94(12):4605–4620, June 2008.

- [95] Elena Kassianidou and Sanjay Kumar. A biomechanical perspective on stress fiber structure and function. *Biochimica et Biophysica Acta (BBA) - Molecular Cell Research*, 1853(11, Part B):3065 – 3074, 2015. Mechanobiology.
- [96] K. E. Kasza, C. P. Broedersz, G. H. Koenderink, Y. C. Lin, W. Messner, E. A. Millman, F. Nakamura, T. P. Stossel, F. C. MacKintosh, and D. A. Weitz. Actin filament length tunes elasticity of flexibly cross-linked actin networks. *Biophysical Journal*, 99(4):1091–1100, 2015/03/12.
- [97] Karen E Kasza and Jennifer A Zallen. Dynamics and regulation of contractile actin-myosin networks in morphogenesis. *Current opinion in cell biology*, 23(1):30–38, February 2011.
- [98] Kinneret Keren, Patricia T. Yam, Anika Kinkhabwala, Alex Mogilner, and Julie A. Theriot. Intracellular fluid flow in rapidly moving cells. *Nat Cell Biol*, 11(10):1219–1224, 10 2009.
- [99] Hye Young Kim and Lance A Davidson. Punctuated actin contractions during convergent extension and their permissive regulation by the non-canonical Wnt-signaling pathway. *Journal of cell science*, 124(Pt 4):635–646, February 2011.
- [100] Taeyoon Kim, Margaret L. Gardel, and Ed Munro. Determinants of fluid-like behavior and effective viscosity in cross-linked actin networks. *Biophysical Journal*, 106(3):526 – 534, 2014.
- [101] Taeyoon Kim, Wonmuk Hwang, and Roger D Kamm. Dynamic role of cross-linking proteins in actin rheology. *Biophysical Journal*, 101(7):1597–1603, 10 2011.
- [102] Gijsje H Koenderink, Zvonimir Dogic, Fumihiro Nakamura, Poul M Bendix, Frederick C MacKintosh, John H Hartwig, Thomas P Stossel, and David A Weitz. An active biopolymer network controlled by molecular motors. *Proceedings of the National Academy of Sciences of the United States of America*, 106(36):15192–15197, 09 2009.
- [103] Simone Köhler and Andreas R. Bausch. Contraction mechanisms in composite active actin networks. *PLoS ONE*, 7(7):e39869, 07 2012.
- [104] Sarita Koride, Li He, Li-Ping Xiong, Ganhui Lan, Denise J Montell, and Sean X Sun. Mechanochemical regulation of oscillatory follicle cell dynamics in the developing Drosophila egg chamber. *Molecular biology of the cell*, 25(22):3709–3716, November 2014.
- [105] Kumfer KT, Cook SJ, Squirrell JM, Eliceiri KW, Peel N, O'Connell KF, and White JG. *CGEF-1 and CHIN-1 regulate CDC-42 activity during asymmetric division in the Caenorhabditis elegans embryo*. Mol Biol Cell, 2010.

- [106] K Vijay Kumar, Justin S Bois, Frank Jülicher, and Stephan W Grill. Pulsatory Patterns in Active Fluids. *Physical review letters*, 112(20):208101 EP –, May 2014.
- [107] Niu L and Yu J. *Investigating intracellular dynamics of FtsZ cytoskeleton with photoactivation single-molecule tracking*. Biophys J, 2008.
- [108] Frank PL Lai, Małgorzata Szczodrak, Jennifer Block, Jan Faix, Dennis Breitsprecher, Hans G Mannherz, Theresia EB Stradal, Graham A Dunn, J Victor Small, and Klemens Rottner. Arp2/3 complex interactions and actin network turnover in lamellipodia. *The EMBO Journal*, 27(7):982–992, 04 2008.
- [109] Martin Lenz. Geometrical origins of contractility in disordered actomyosin networks. *Phys. Rev. X*, 4:041002, Oct 2014.
- [110] Martin Lenz, Margaret L Gardel, and Aaron R Dinner. Requirements for contractility in disordered cytoskeletal bundles. *New Journal of Physics*, 14(3):033037, 2012.
- [111] Romain Levayer and Thomas Lecuit. Biomechanical regulation of contractility: spatial control and dynamics. *Trends in cell biology*, 22(2):61–81, February 2012.
- [112] Romain Levayer and Thomas Lecuit. Oscillation and polarity of E-cadherin asymmetries control actomyosin flow patterns during morphogenesis. *Developmental cell*, 26(2):162–175, July 2013.
- [113] O. Lieleg and A. R. Bausch. Cross-linker unbinding and self-similarity in bundled cytoskeletal networks. *Phys. Rev. Lett.*, 99:158105, Oct 2007.
- [114] O. Lieleg, M. M. A. E. Claessens, Y. Luan, and A. R. Bausch. Transient binding and dissipation in cross-linked actin networks. *Phys. Rev. Lett.*, 101:108101, Sep 2008.
- [115] O. Lieleg, M. M. A. E. Claessens, Y. Luan, and A. R. Bausch. Transient binding and dissipation in cross-linked actin networks. *Phys. Rev. Lett.*, 101:108101, Sep 2008.
- [116] O. Lieleg, K. M. Schmoller, M. M. A. E. Claessens, and A. R. Bausch. Cytoskeletal polymer networks: Viscoelastic properties are determined by the microscopic interaction potential of cross-links. *Biophysical Journal*, 96(11):4725–4732, 6 2009.
- [117] Oliver Lieleg, Mireille M. A. E. Claessens, and Andreas R. Bausch. Structure and dynamics of cross-linked actin networks. *Soft Matter*, 6:218–225, 2010.

- [118] Oliver Lieleg, Mireille M. A. E. Claessens, and Andreas R. Bausch. Structure and dynamics of cross-linked actin networks. *Soft Matter*, 6:218–225, 2010.
- [119] Yi-Chia Lin, Chase P. Broedersz, Amy C. Rowat, Tatjana Wedig, Harald Herrmann, Frederick C. MacKintosh, and David A. Weitz. Divalent cations crosslink vimentin intermediate filament tail domains to regulate network mechanics. *Journal of Molecular Biology*, 399(4):637 – 644, 2010.
- [120] J. Liu, G. H. Koenderink, K. E. Kasza, F. C. MacKintosh, and D. A. Weitz. Visualizing the strain field in semiflexible polymer networks: Strain fluctuations and nonlinear rheology of *f*-actin gels. *Phys. Rev. Lett.*, 98:198304, May 2007.
- [121] Zhenhua Liu, Adam Wierman, Yuan Chen, Benjamin Razon, and Niangjun Chen. Data center demand response: Avoiding the coincident peak via workload shifting and local generation. *SIGMETRICS Perform. Eval. Rev.*, 41(1):341–342, June 2013.
- [122] T. B. Liverpool, M. C. Marchetti, J.-F. Joanny, and J. Prost. Mechanical response of active gels. *EPL (Europhysics Letters)*, 85(1):18007, 2009.
- [123] Andy Loria, Katrina M Longhini, and Michael Glotzer. The RhoGAP domain of CYK-4 has an essential role in RhoA activation. *Current biology : CB*, 22(3):213–219, February 2012.
- [124] C H Luo and Y Rudy. A model of the ventricular cardiac action potential. Depolarization, repolarization, and their interaction. *Circulation research*, 68(6):1501–1526, June 1991.
- [125] Tianzhi Luo, Krithika Mohan, Vasudha Srivastava, Yixin Ren, Pablo A Iglesias, and Douglas N Robinson. Understanding the cooperative interaction between myosin II and actin cross-linkers mediated by actin filaments during mechanosensation. *Biophysical journal*, 102(2):238–247, January 2012.
- [126] Beers M and Kemphues K. *Depletion of the co-chaperone CDC-37 reveals two modes of PAR-6 cortical association in C. elegans embryos*. Development, 2006.
- [127] Sarov M et al. *A genome-scale resource for in vivo tag-based protein function exploration in C. elegans*. Cell, 2012.
- [128] Tokunaga M, Imamoto N, and Sakata-Sogawa K. *Highly inclined thin illumination enables clear single-molecule imaging in cells*. Nat Methods, 2008.
- [129] Ueda M, Sako Y, Tanaka T, Devreotes P, and Yanagida T. *Single-molecule analysis of chemotactic signaling in Dictyostelium cells*. Science, 2001.

- [130] P F Machado, G B Blanchard, J Duque, and N Gorfinkel. Cytoskeletal turnover and Myosin contractility drive cell autonomous oscillations in a model of Drosophila Dorsal Closure. *The European Physical Journal Special Topics*, 223(7):1391–1402, June 2014.
- [131] A S Maddox. Distinct roles for two *C. elegans* anillins in the gonad and early embryo. 132(12):2837–2848, June 2005.
- [132] Michael Mak, Taeyoon Kim, Muhammad H. Zaman, and Roger D. Kamm. Multiscale mechanobiology: computational models for integrating molecules to multicellular systems. *Integr Biol (Camb)*, 7(10):1093–1108, Oct 2015. 26019013[pmid].
- [133] Michael Mak, Muhammad H. Zaman, Roger D. Kamm, and Taeyoon Kim. Interplay of active processes modulates tension and drives phase transition in self-renewing, motor-driven cytoskeletal networks. *Nat Commun*, 7, 01 2016.
- [134] M. C. Marchetti, J. F. Joanny, S. Ramaswamy, T. B. Liverpool, J. Prost, Madan Rao, and R. Aditi Simha. Hydrodynamics of soft active matter. *Rev. Mod. Phys.*, 85:1143–1189, Jul 2013.
- [135] John F. Marko and Eric D. Siggia. Stretching dna. *Macromolecules*, 28(26):8759–8770, 1995.
- [136] Adam C Martin, Matthias Kaschube, and Eric F Wieschaus. Pulsed contractions of an actin-myosin network drive apical constriction. *Nature*, 457(7228):495–499, January 2009.
- [137] Frank M Mason, Shicong Xie, Claudia G Vasquez, Michael Tworoger, and Adam C Martin. RhoA GTPase inhibition organizes contraction during epithelial morphogenesis. *The Journal of cell biology*, 214(5):603–617, August 2016.
- [138] Mirjam Mayer, Martin Depken, Justin S. Bois, Frank Julicher, and Stephan W. Grill. Anisotropies in cortical tension reveal the physical basis of polarizing cortical flows. *Nature*, 467(7315):617–621, 09 2010.
- [139] N.G. McCrum, C.P. Buckley, and C.B. Bucknall. *Principles of Polymer Engineering*. Oxford science publications. Oxford University Press, 1997.
- [140] W. M. McFadden, P. M. McCall, and E. M. Munro. Filament turnover is essential for continuous long range contractile flow in a model actomyosin cortex. *ArXiv e-prints*, December 2016.
- [141] David C. Morse. Viscoelasticity of concentrated isotropic solutions of semiflexible polymers. 2. linear response. *Macromolecules*, 31(20):7044–7067, 1998.

- [142] Fumio Motegi and Asako Sugimoto. Sequential functioning of the ECT-2 RhoGEF, RHO-1 and CDC-42 establishes cell polarity in *Caenorhabditis elegans* embryos. *Nature cell biology*, 8(9):978–985, September 2006.
- [143] Kei W. Müller, Robijn F. Bruinsma, Oliver Lieleg, Andreas R. Bausch, Wolfgang A. Wall, and Alex J. Levine. Rheology of semiflexible bundle networks with transient linkers. *Phys. Rev. Lett.*, 112:238102, Jun 2014.
- [144] Akankshi Munjal, Jean-Marc Philippe, Edwin Munro, and Thomas Lecuit. A self-organized biomechanical network drives shape changes during tissue morphogenesis. *Nature*, 524(7565):351–355, August 2015.
- [145] Edwin Munro, Jeremy Nance, and James R. Priess. Cortical flows powered by asymmetrical contraction transport {PAR} proteins to establish and maintain anterior-posterior polarity in the early *c. elegans* embryo. *Developmental Cell*, 7(3):413 – 424, 2004.
- [146] Edwin Munro, Jeremy Nance, and James R Priess. Cortical flows powered by asymmetrical contraction transport PAR proteins to establish and maintain anterior-posterior polarity in the early *C. elegans* embryo. *Developmental cell*, 7(3):413–424, September 2004.
- [147] Michael Murrell and Margaret L. Gardel. Actomyosin sliding is attenuated in contractile biomimetic cortices. *Molecular Biology of the Cell*, 25(12):1845–1853, 2014.
- [148] Michael Murrell, Patrick W. Oakes, Martin Lenz, and Margaret L. Gardel. Forcing cells into shape: the mechanics of actomyosin contractility. *Nat Rev Mol Cell Biol*, 16(8):486–498, 08 2015.
- [149] Michael P. Murrell and Margaret L. Gardel. F-actin buckling coordinates contractility and severing in a biomimetic actomyosin cortex. *Proceedings of the National Academy of Sciences*, 109(51):20820–20825, 2012.
- [150] Kausalya Murthy and Patricia Wadsworth. Myosin-II-dependent localization and dynamics of f-actin during cytokinesis. *Current Biology*, 15(8):724–731, 2016/12/15 2016.
- [151] Monnier N, Guo SM, Mori M, He J, Lnrt P, and Bathe M. *Bayesian approach to MSD-based analysis of particle motion in live cells*. Biophys J, 2012.
- [152] Watanabe N and Mitchison TJ. *Single-molecule speckle analysis of actin filament turnover in lamellipodia*. Science, 2002.

- [153] Lyswarya Narayanan, Di Wang, Abdullah-Al Mamun, Anand Sivasubramanian, and Hosam K. Fathy. Should we dual-purpose energy storage in datacenters for power backup and demand response? In *6th Workshop on Power-Aware Computing and Systems (HotPower 14)*, Broomfield, CO, 2014. USENIX Association.
- [154] F. J. Nedelec, T. Surrey, A. C. Maggs, and S. Leibler. Self-organization of microtubules and motors. *Nature*, 389(6648):305–308, 09 1997.
- [155] Goehring NW, Hoege C, Grill SW, and Hyman AA. *PAR proteins diffuse freely across the anterior-posterior boundary in polarized C. elegans embryos*, 2011.
- [156] Shigeo Okabe and Nobutaka Hirokawa. Actin dynamics in growth cones. *Journal of Neuroscience*, 11(7):1918–1929, 1991.
- [157] Sara K Olson, Garrett Greenan, Arshad Desai, Thomas Müller-Reichert, and Karen Oegema. Hierarchical assembly of the eggshell and permeability barrier in *C. elegans*. *The Journal of cell biology*, 198(4):731–748, August 2012.
- [158] Ewa Paluch, Matthieu Piel, Jacques Prost, Michel Bornens, and Cécile Sykes. Cortical actomyosin breakage triggers shape oscillations in cells and cell fragments. *Biophysical journal*, 89(1):724–733, July 2005.
- [159] Vincent Pelletier, Naama Gal, Paul Fournier, and Maria L Kilfoil. Microrheology of Microtubule Solutions and Actin-Microtubule Composite Networks. 102(18):188303 EP–, May 2009.
- [160] Alisa J Piekny and Michael Glotzer. Anillin is a scaffold protein that links RhoA, actin, and myosin during cytokinesis. *Current biology : CB*, 18(1):30–36, January 2008.
- [161] Alisa J Piekny, Jacque-Lynne F Johnson, Gwendolyn D Cham, and Paul E Mains. The *Caenorhabditis elegans* nonmuscle myosin genes *nmy-1* and *nmy-2* function as redundant components of the *let-502/Rho*-binding kinase and *mel-11/myosin* phosphatase pathway during embryonic morphogenesis. 130(23):5695–5704, December 2003.
- [162] Alisa J Piekny and Paul E Mains. Rho-binding kinase (LET-502) and myosin phosphatase (MEL-11) regulate cytokinesis in the early *Caenorhabditis elegans* embryo. *Journal of cell science*, 115(Pt 11):2271–2282, June 2002.
- [163] Christian Pohl, Michael Tiongson, Julia L Moore, Anthony Santella, and Zhirong Bao. Actomyosin-based self-organization of cell internalization during *C. elegans* gastrulation. *BMC biology*, 10(1):94, 2012.

- [164] Kathleen E Rankin and Linda Wordeman. Long astral microtubules uncouple mitotic spindles from the cytokinetic furrow. *The Journal of cell biology*, 190(1):35–43, July 2010.
- [165] Matteo Rauzi, Pierre-Francois Lenne, and Thomas Lecuit. Planar polarized actomyosin contractile flows control epithelial junction remodelling. *Nature*, 468(7327):1110–1114, Dec 2010.
- [166] Matteo Rauzi, Pierre-François Lenne, and Thomas Lecuit. Planar polarized actomyosin contractile flows control epithelial junction remodelling. *Nature*, 468(7327):1110–1114, December 2010.
- [167] William Razzell, Will Wood, and Paul Martin. Recapitulation of morphogenetic cell shape changes enables wound re-epithelialisation. *Development (Cambridge, England)*, 141(9):1814–1820, May 2014.
- [168] Yixin Ren, Janet C Effler, Melanie Norstrom, Tianzhi Luo, Richard A Firtel, Pablo A Iglesias, Ronald S Rock, and Douglas N Robinson. Mechanosensing through cooperative interactions between myosin II and the actin crosslinker cortexillin I. *Current biology : CB*, 19(17):1421–1428, September 2009.
- [169] Anne-Cécile Reymann, Rajaa Boujemaa-Paterski, Jean-Louis Martiel, Christophe Guérin, Wenxiang Cao, Harvey F. Chin, Enrique M. De La Cruz, Manuel Théry, and Laurent Blanchoin. Actin network architecture can determine myosin motor activity. *Science*, 336(6086):1310–1314, 2012.
- [170] Cheeks RJ, Canman JC, Gabriel WN, Meyer N, Strome S, and Goldstein B. *C. elegans PAR proteins function by mobilizing and stabilizing asymmetrically localized protein complexes*. *Curr Biol*, 2004.
- [171] Francois B Robin, William M McFadden, Baixue Yao, and Edwin M Munro. Single-molecule analysis of cell surface dynamics in *caenorhabditis elegans* embryos. *Nat Meth*, 11(6):677–682, 06 2014.
- [172] François B Robin, William M McFadden, Baixue Yao, and Edwin M Munro. Single-molecule analysis of cell surface dynamics in *Caenorhabditis elegans* embryos. 11(6):677–682, June 2014.
- [173] François B Robin, Jonathan B Michaux, William M McFadden, and Edwin M Munro. Excitable rhoa dynamics drive pulsed contractions in the early *c. elegans* embryo. *bioRxiv*, 2016.
- [174] Ralf Ross, Helmut Jonuleit, Matthias Bros, Xiao-Lan Ross, Alexander H. Enk, Jrgen Knop, Angelika B. Reske-Kunz, Shigeko Yamashiro, and Fumio Matsumura. Expression of the actin-bundling protein fascin in cultured human den-

- dritic cells correlates with dendritic morphology and cell differentiation. *Journal of Investigative Dermatology*, 115(4):658 – 663, 2000.
- [175] Barry Rountree, Dong H. Ahn, Bronis R. de Supinski, David K. Lowenthal, and Martin Schulz. Beyond dvfs: A first look at performance under a hardware-enforced power bound. *2013 IEEE International Symposium on Parallel & Distributed Processing, Workshops and Phd Forum*, 0:947–953, 2012.
 - [176] Manley S et al. *High-density mapping of single-molecule trajectories with photoactivated localization microscopy*. Nat Methods, 2008.
 - [177] G Salbreux, J F Joanny, J Prost, and P Pullarkat. Shape oscillations of non-adhering fibroblast cells. *Physical biology*, 4(4):268–284, December 2007.
 - [178] G. Salbreux, J. Prost, and J. F. Joanny. Hydrodynamics of cellular cortical flows and the formation of contractile rings. *Phys. Rev. Lett.*, 103:058102, Jul 2009.
 - [179] Guillaume Salbreux, Guillaume Charras, and Ewa Paluch. Actin cortex mechanics and cellular morphogenesis. *Trends in Cell Biology*, 22(10):536 – 545, 2012.
 - [180] Guillaume Salbreux, Guillaume Charras, and Ewa Paluch. Actin cortex mechanics and cellular morphogenesis. *Trends in Cell Biology*, 22(10):536 – 545, 2012.
 - [181] Tim Sanchez, Daniel T. N. Chen, Stephen J. DeCamp, Michael Heymann, and Zvonimir Dogic. Spontaneous motion in hierarchically assembled active matter. *Nature*, 491(7424):431–434, 11 2012.
 - [182] Eric S Schiffhauer, Tianzhi Luo, Krithika Mohan, Vasudha Srivastava, Xuyu Qian, Eric R Griffis, Pablo A Iglesias, and Douglas N Robinson. Mechanoacumulative Elements of the Mammalian Actin Cytoskeleton. *Current biology : CB*, 26(11):1473–1479, June 2016.
 - [183] Cornelia Schmutz, Julia Stevens, and Anne Spang. Functions of the novel RhoGAP proteins RGA-3 and RGA-4 in the germ line and in the early embryo of *C. elegans*. *Development (Cambridge, England)*, 134(19):3495–3505, October 2007.
 - [184] Stephanie Schonegg, Alexandru T Constantinescu, Carsten Hoege, and Anthony A Hyman. The Rho GTPase-activating proteins RGA-3 and RGA-4 are required to set the initial size of PAR domains in *Caenorhabditis elegans* one-cell embryos. *Proceedings of the National Academy of Sciences of the United States of America*, 104(38):14976–14981, September 2007.

- [185] Stephanie Schonegg and Anthony A Hyman. CDC-42 and RHO-1 coordinate acto-myosin contractility and PAR protein localization during polarity establishment in *C. elegans* embryos. *Development (Cambridge, England)*, 133(18):3507–3516, September 2006.
- [186] Jakub Sedzinski, Maté Biro, Annelie Oswald, Jean-Yves Tinevez, Guillaume Salbreux, and Ewa Paluch. Polar actomyosin contractility destabilizes the position of the cytokinetic furrow. *Nature*, 476(7361):462–466, August 2011.
- [187] Aaron F Severson, David L Baillie, and Bruce Bowerman. A Formin Homology protein and a profilin are required for cytokinesis and Arp2/3-independent assembly of cortical microfilaments in *C. elegans*. *Current biology : CB*, 12(24):2066–2075, December 2002.
- [188] Lord SJ, Lee HL, and Moerner WE. Single-molecule spectroscopy and imaging of biomolecules in living cells. 2010.
- [189] Jérôme Solon, Aynur Kaya-Copur, Julien Colombelli, and Damian Brunner. Pulsed forces timed by a ratchet-like mechanism drive directed tissue movement during dorsal closure. *Cell*, 137(7):1331–1342, June 2009.
- [190] Evan Spruijt, Joris Sprakel, Marc Lemmers, Martien A. Cohen Stuart, and Jasper van der Gucht. Relaxation dynamics at different time scales in electrostatic complexes: Time-salt superposition. *Phys. Rev. Lett.*, 105:208301, Nov 2010.
- [191] Dimitrije Stamenovic. Cell mechanics: Two regimes, maybe three? *Nat Mater*, 5(8):597–598, 08 2006.
- [192] Cornelis Storm, Jennifer J. Pastore, F. C. MacKintosh, T. C. Lubensky, and Paul A. Janmey. Nonlinear elasticity in biological gels. *Nature*, 435(7039):191–194, 05 2005.
- [193] Steven Strogatz. Nonlinear dynamics and chaos with applications to physics, biology, chemistry, and engineering, January 1994.
- [194] Thomas Surrey, François Nédélec, Stanislas Leibler, and Eric Karsenti. Physical properties determining self-organization of motors and microtubules. *Science*, 292(5519):1167–1171, 2001.
- [195] Uyemura T, Takagi H, and Yanagida T. *Sako Y Single-molecule analysis of epidermal growth factor signaling that leads to ultrasensitive calcium response*. Biophys J, 2005.
- [196] Xia T, Li N, and Fang X. *Single-molecule fluorescence imaging in living cells*. Annu Rev Phys Chem, 2013.

- [197] Pollard TD. *Mechanics of cytokinesis in eukaryotes*. Curr Opin Cell Biol, 2010.
- [198] R. Tharmann, M. M. A. E. Claessens, and A. R. Bausch. Viscoelasticity of isotropically cross-linked actin networks. *Phys. Rev. Lett.*, 98:088103, Feb 2007.
- [199] Julie A. Theriot and Timothy J. Mitchison. Actin microfilament dynamics in locomoting cells. *Nature*, 352(6331):126–131, Jul 1991.
- [200] D'Arcy Wentworth Thompson. *On growth and form / by D'Arcy Wentworth Thompson*. Cambridge :University Press ;, 1945. <http://www.biodiversitylibrary.org/bibliography/6462>.
- [201] L Timmons, D L Court, and A Fire. Ingestion of bacterially expressed dsRNAs can produce specific and potent genetic interference in *Caenorhabditis elegans*. *Gene*, 263(1-2):103–112, January 2001.
- [202] Makio Tokunaga, Naoko Imamoto, and Kumiko Sakata-Sogawa. Highly inclined thin illumination enables clear single-molecule imaging in cells. *5(2):159–161*, January 2008.
- [203] Yu Chung Tse, Alisa Piekny, and Michael Glotzer. Anillin promotes astral microtubule-directed cortical myosin polarization. *Molecular biology of the cell*, 22(17):3165–3175, September 2011.
- [204] Yu Chung Tse, Michael Werner, Katrina M Longhini, Jean-Claude Labbe, Bob Goldstein, and Michael Glotzer. RhoA activation during polarization and cytokinesis of the early *Caenorhabditis elegans* embryo is differentially dependent on NOP-1 and CYK-4. *Molecular biology of the cell*, 23(20):4020–4031, October 2012.
- [205] Hervé Turlier, Basile Audoly, Jacques Prost, and Jean-François Joanny. Furrow constriction in animal cell cytokinesis. *Biophysical Journal*, 106(1):114 – 123, 2014.
- [206] Michael J. Unterberger and Gerhard A. Holzapfel. Advances in the mechanical modeling of filamentous actin and its cross-linked networks on multiple scales. *Biomechanics and Modeling in Mechanobiology*, 13(6):1155–1174, 2014.
- [207] Pelletier V, Gal N, Fournier P, and Kilfoil ML. *Microrheology of microtubule solutions and actin-microtubule composite networks*. Phys Rev Lett, 2009.
- [208] Pascal Vallotton, Stephanie L Gupton, Clare M Waterman-Storer, and Gaudenz Danuser. Simultaneous mapping of filamentous actin flow and turnover in migrating cells by quantitative fluorescent speckle microscopy. *Proceedings of the National Academy of Sciences of the United States of America*, 101(26):9660–9665, June 2004.

- [209] David Van Goor, Callen Hyland, Andrew W Schaefer, and Paul Forscher. The role of actin turnover in retrograde actin network flow in neuronal growth cones. *PLoS ONE*, 7(2):e30959, 2012.
- [210] Andrea Vanossi, Nicola Manini, Michael Urbakh, Stefano Zapperi, and Erio Tosatti. *Colloquium : Modeling friction: From nanoscale to mesoscale*. *Rev. Mod. Phys.*, 85:529–552, Apr 2013.
- [211] Claudia G Vasquez, Mike Tworoger, and Adam C Martin. Dynamic myosin phosphorylation regulates contractile pulses and tissue integrity during epithelial morphogenesis. *The Journal of cell biology*, 206(3):435–450, August 2014.
- [212] D.H. Wachsstock, W.H. Schwarz, and T.D. Pollard. Cross-linker dynamics determine the mechanical properties of actin gels. *Biophysical Journal*, 66(3, Part 1):801 – 809, 1994.
- [213] Yu-Li Wang. Exchange of actin subunits at the leading edge of living fibroblasts: possible role of treadmilling. *The Journal of cell biology*, 101(2):597–602, 1985.
- [214] Andrew Ward, Feodor Hilitski, Walter Schwenger, David Welch, A. W. C. Lau, Vincenzo Vitelli, L. Mahadevan, and Zvonimir Dogic. Solid friction between soft filaments. *Nat Mater*, advance online publication:–, 03 2015.
- [215] Sabine M. Volkmer Ward, Astrid Weins, Martin R. Pollak, and David A. Weitz. Dynamic viscoelasticity of actin cross-linked with wild-type and disease-causing mutant alpha-actinin-4. *Biophysical Journal*, 95(10):4915 – 4923, 2008.
- [216] Naoki Watanabe and Timothy J. Mitchison. Single-molecule speckle analysis of actin filament turnover in lamellipodia. *Science*, 295(5557):1083–1086, 2002.
- [217] Naoki Watanabe and Timothy J Mitchison. Single-molecule speckle analysis of actin filament turnover in lamellipodia. *Science (New York, N.Y.)*, 295(5557):1083–1086, February 2002.
- [218] Orion D Weiner, William A Marganski, Lani F Wu, Steven J Altschuler, and Marc W Kirschner. An actin-based wave generator organizes cell motility. *PLoS biology*, 5(9):e221, September 2007.
- [219] Michael Werner, Ed Munro, and Michael Glotzer. Astral signals spatially bias cortical myosin recruitment to break symmetry and promote cytokinesis. *Current biology : CB*, 17(15):1286–1297, August 2007.
- [220] A. Wierman, Zhenhua Liu, I. Liu, and H. Mohsenian-Rad. Opportunities and challenges for data center demand response. In *Green Computing Conference (IGCC), 2014 International*, pages 1–10, Nov 2014.

- [221] Jan Wilhelm and Erwin Frey. Elasticity of stiff polymer networks. *Phys. Rev. Lett.*, 91:108103, Sep 2003.
- [222] Cyrus A. Wilson, Mark A. Tsuchida, Greg M. Allen, Erin L. Barnhart, Kathryn T. Applegate, Patricia T. Yam, Lin Ji, Kinneret Keren, Gaudenz Danuser, and Julie A. Theriot. Myosin ii contributes to cell-scale actin network treadmilling through network disassembly. *Nature*, 465(7296):373–377, 05 2010.
- [223] M. Wyart, H. Liang, A. Kabla, and L. Mahadevan. Elasticity of floppy and stiff random networks. *Phys. Rev. Lett.*, 101:215501, Nov 2008.
- [224] Nakayama Y, Shivas JM, Poole DS, Squirrell JM, Kulkoski JM, Schleede JB, and Skop AR. Dynamin participates in the maintenance of anterior polarity in the *Caenorhabditis elegans* embryo. *Dev Cell*. 2009 Jun;16(6):889-900. doi:, 10., 2009.
- [225] Norman Y. Yao, Daniel J. Becker, Chase P. Broedersz, Martin Depken, Frederick C. MacKintosh, Martin R. Pollak, and David A. Weitz. Nonlinear viscoelasticity of actin transiently cross-linked with mutant alpha-actinin-4. *Journal of Molecular Biology*, 411(5):1062 – 1071, 2011.
- [226] Shigehiko Yumura, Go Itoh, Yumi Kikuta, Takeomi Kikuchi, Toshiko Kitanishi-Yumura, and Masatsune Tsujioka. Cell-scale dynamic recycling and cortical flow of the actin-myosin cytoskeleton for rapid cell migration. *Biology Open*, 2(2):200–209, 2013.
- [227] Ronen Zaidel-Bar, Shalev Itzkovitz, Avi Ma’ayan, Ravi Iyengar, and Benjamin Geiger. Functional atlas of the integrin adhesome. *Nat Cell Biol*, 9(8):858–867, Aug 2007.
- [228] Esther Zanin, Arshad Desai, Ina Poser, Yusuke Toyoda, Cordula Andree, Claudia Moebius, Marc Bickle, Barbara Conradt, Alisa Piekny, and Karen Oegema. A conserved RhoGAP limits M phase contractility and coordinates with microtubule asters to confine RhoA during cytokinesis. *Developmental cell*, 26(5):496–510, September 2013.
- [229] Donglei Zhang and Michael Glotzer. The RhoGAP activity of CYK-4/MgcRacGAP functions non-canonically by promoting RhoA activation during cytokinesis. *eLife*, 4:204, 2015.
- [230] Zhou Zhou, Zhiling Lan, Wei Tang, and Narayan Desai. Reducing energy costs for ibm blue gene/p via power-aware job scheduling. In Narayan Desai and Walfredo Cirne, editors, *Job Scheduling Strategies for Parallel Processing*, volume 8429 of *Lecture Notes in Computer Science*, pages 96–115. Springer Berlin Heidelberg, 2014.

- [231] Alexander Zumdieck, Karsten Kruse, Henrik Bringmann, Anthony A. Hyman, and Frank Jülicher. Stress generation and filament turnover during actin ring constriction. *PLoS ONE*, 2(8):e696, 08 2007.